REGULATION OF ERYTHROID-SPECIFIC AMINOLEVULINIC ACID SYNTHASE IN PORPHYRIA AND ANEMIA

by

JASON ROBERT MARCERO

(Under the Direction of Harry A. Dailey and Amy E. Medlock)

ABSTRACT

Aminolevulinic acid synthase 2 (ALAS2) is the rate-limiting enzyme of heme synthesis in the mammalian erythroid compartment and controls the production of approximately 400 billion hemoglobin molecules per second in adult human bone marrow. The *ALAS2* gene is induced late in erythropoiesis when numerous red cell precursors are intimately associated with a central macrophage which facilitates differentiation in niches known as erythroblastic islands. Based largely on structure-function and kinetic studies on recombinant human ALAS2 and analysis of erythroid progenitor metabolism in culture, we have proposed explanations here for ALAS2 enzyme behavior in various blood disorders, including X-linked protoporphyria (XLP), X-linked sideroblastic anemia (XLSA), and anemia of chronic disease (inflammation). Notably, we have found that the eukaryotic-specific C-terminal extension of human ALAS2 demonstrates an autoinhibitory mechanism that is disrupted in XLP and enhanced in XLSA, resulting in gain- and loss-of function enzymes, respectively. We have also elucidated the metabolic fate of the immunoactivated macrophage compound itaconic acid in red cell progenitors and have developed a new model for terminal erythropoiesis in the erythroblastic island during an

inflammatory response. In particular, we show that itaconyl-CoA is produced by erythroblasts from imported itaconate and that itaconyl-CoA competitively inhibits ALAS2 catalysis. We therefore implicate macrophage-derived itaconate as a key factor in states of inflammatory anemia. Finally and perhaps most importantly, we have used the knowledge gained from these studies to identify small-molecule antagonists of ALAS2, including itaconate, that may one day be used to treat XLP or other conditions involving porphyrin accumulation.

INDEX WORDS: Aminolevulinic acid, ALAS2, Heme, Itaconic acid, Porphyria, Anemia

REGULATION OF ERYTHROID-SPECIFIC AMINOLEVULINIC ACID SYNTHASE IN PORPHYRIA AND ANEMIA

by

JASON ROBERT MARCERO

B.S., Alma College, 1996

M.A.T., University of South Carolina, 2003

A Dissertation Submitted to the Graduate Faculty of The University of Georgia in Partial Fulfillment of the Requirements for the Degree

DOCTOR OF PHILOSOPHY

ATHENS, GEORGIA

2020

REGULATION OF ERYTHROID-SPECIFIC AMINOLEVULINIC ACID SYNTHASE IN PORPHYRIA AND ANEMIA

by

JASON ROBERT MARCERO

Major Professor:	Harry A. Dailey, Jr.
Co-Major Professor:	Amy E. Medlock
Committee:	Stephen Dalton
	Lianchun Wang

Electronic Version Approved:

Ron Walcott
Interim Dean of the Graduate School
The University of Georgia
August 2020

DEDICATION

This dissertation is for my beautiful wife, Kelsey, and my three wonderful children, Isaac, Wren, and Luke. They are the definition of a devoted family and my greatest achievement. Knowing that I would come home to them every day regardless of how good or bad life was in lab has made all the difference. Without their unwavering love, support, and sacrifice, none of this would have been possible.

ACKNOWLEDGEMENTS

This list starts with my major professor, Dr. Harry Dailey. While he is not part of "The Greatest Generation", his core values of honor, self-discipline, and forthrightness are indistinguishable from those who are (and were). He is an avid and skilled storyteller and teacher, and I thank him here not only for his lessons on science, but those on life, death, and of course basketball (according to John Wooden) as well. I also would like to acknowledge his late wife, Dr. Tammy Dailey. She not only taught me the valuable trade of molecular biology before she passed, but also how to manage a lab and to remain steadfast in the face of countless failed experiments. I miss her laugh the most. Next I would like to thank Dr. Amy Medlock. With three kids of her own, she demonstrated daily how it is possible to be both a good scientist and a good spouse and parent. Dr. Medlock always focused on the positive and helped me through the toughest of times in lab. I would also like to thank Bob Piel, whose love of science and sports made for engaging conversations in lab and at the gym. Most of what I broke along the way, Bob fixed. Next is Sophia Weerth. Sophia is the pragmatic but "Angry German" (she literally wrote this on her shaker) who kept the lab on course so many times after Tammy was gone. Finally, I would like to thank my other committee members, Dr. Stephen Dalton and Dr. Lianchun Wang. Dr. Dalton always provided helpful and often humbling feedback at my committee meetings and has had much more of an impact on me than he knows. Dr. Wang's lab is where I worked during my first lab rotation. After being out of a research lab for 10 years, he and his postdoc Dr. Hong Qiu made the transition back a smooth one. Their knowledge, patience, and trust in me were largely responsible for my early success at UGA.

TABLE OF CONTENTS

PAGE

CHAPTER 1

INTRODUCTION AND LITERATURE REVIEW

1.1 Characterization and Quantitation of Heme

Heme is a tetrapyrrole macrocycle (porphyrin) with a central iron ion coordinated to nitrogen atoms of the pyrrole rings and is planar in the unbound state. Heme is an ancient molecule found in all kingdoms of life and is essential for almost all aerobic organisms in a protein-bound state, while paradoxically being cytotoxic in an unbound state (1). The heterocyclic porphyrin component of heme is a so-called "pigment of life" (porphyrin means "purple" in Greek) and bears multiple rings with conjugated heteroatoms (monopyrroles) that provide a foundation for the rich redox chemistry of heme (2). Multiple types of heme are found in nature (e.g., heme *a*, heme *b*, heme *c*, heme *o*), each variant with unique porphyrin ring substituent(s). Heme *b*, also known as iron protoporphyrin IX or protoheme, has vinyl side groups on its A and B rings and propionate groups on its C and D rings (Figure 1). Heme *b* is the precursor for all other heme types and is the molecular sibling of other key metalloporphyrins in eukaryotic organisms, including chlorophyll and cyanocobalamin (vitamin B_{12}) (3,4). Hereafter in this dissertation, heme *b* will simply be referred to as "heme".

De novo heme biosynthesis appeared early in bacterial evolution (5). Most organisms in general synthesize heme from 5- or δ-aminolevulinic acid (ALA), although there are some parasitic prokaryotes (e.g., *Streptococcus* species) and eukaryotes (e.g., *Boophilus microplus* and nematodes such as *Caenorhabditis elegans*) that are heme auxotrophs and instead have evolved

heme uptake machinery (6-8). Animals, fungi, and photosynthetic proteobacteria synthesize ALA from glycine and succinyl-CoA by the C_4 (Shemin) pathway (9), while archaea, higher plants, and other bacteria use the more ancient C_5 (glutamate) pathway, which utilizes α-ketoglutarate (5). *Euglena gracilis* is the only known species to utilize both pathways (10). A more comprehensive review of the Shemin pathway for heme synthesis in mammals will be provided later in this dissertation (Section 1.2).

Once made or taken up, heme is utilized as both a prosthetic group and a signaling molecule in diverse pathways and cellular compartments in eukaryotes. Heme as a cofactor is involved in such processes as in diatomic gas production (e.g., nitric oxide synthases), transportation (e.g., hemoglobin), and storage (e.g., myoglobin), as well as xenobiotic detoxification (e.g., cytochromes P450 (CYPs)), redox catalysis (e.g., catalases and peroxidases), and electron transfer (e.g., respiration cytochromes) (11-16). Most relevant to this dissertation and perhaps most notably in general, heme is synthesized and utilized in human erythroid tissue as the oxygen-carrying cofactor for more than 300 million hemoglobin molecules (four hemes per hemoglobin) in each of approximately 2-3 million human red cells released into circulation per second (17). Heme also functions as a signaling molecule when it binds to heme-responsive proteins such as transcription factors, kinases, and microRNA processing proteins (14,16,18,19). Heme oxygenases (HOs), namely heme-inducible heme oxygenase 1 (HO-1) and constitutive HO-2 in mammals, are the rate-limiting enzymes in heme degradation and sources of another important signaling molecule: carbon monoxide (CO) (20). "Free heme", or heme released from proteins to which is noncovalently bound is a redox active molecule due to several biologically relevant oxidations states of its iron center. Ferric and ferrous iron are the most common, though Fe^{4+} and Fe^{5+} states are also possible (21,22). Free heme is capable of generating reactive

oxygen species (ROS) through NAPH oxidases (23) and Fenton chemistry (24). ROS, like free heme itself, function as signaling molecules under homeostatic conditions but are cytotoxic at elevated levels. Directly or indirectly, heme is involved in cell signaling processes that include oxygen sensing, iron homeostasis, oxidative stress response, mitochondrial respiration and biogenesis, mitophagy, apoptosis, circadian rhythm, and cell cycle progression and proliferation (11,16,23,25-32).

The quantitation of heme and hemoproteins is not only necessary in a medical setting to diagnose various pathological states such as anemia and polycythemia vera associated with aberrant hemoglobin levels, but to further investigate and elucidate the impacts of heme as a free and protein-bound molecule across numerous systems. Clinically, heme is most commonly assessed as hemoglobin on a per cell basis using Drabkin's method (33-35). In basic research, heme concentrations are typically determined in processed biological samples using other colorimetric approaches, particularly the pyridine hemochromogen assay (36-38), fluorescence analysis (39,40), reverse-phase high performance liquid chromatography (HPLC) (41,42) or radiolabeling with solvent extraction (43-45). One exception is the direct quantitation of heme in whole cells (i.e., turbid samples) with a rapid scanning monochromator and integrating cavity absorption meter (RSM-ICAM) (46), as detailed in Chapter 2 of this dissertation.

Spectroscopic assays of heme in biological samples have been carried out for nearly a century and were originally conducted to quantitate hemoglobin. Oxyhemoglobin produces three characteristic heme absorbance peaks, known as α, β, and γ (Soret peak) (Figure 2A), each resulting from distinct π-π^* electron transitions in the porphyrin with contributions from the iron dπ orbitals (47). Drabkin's method involves the oxidation of all hemoglobin species (except sulfhemoglobin) to methemoglobin with alkaline potassium ferricyanide, followed by

derivatization of the methemoglobin intermediate to cyanmethemoglobin by potassium cyanide (33,34). The result is a single, broad, baselined peak centered at 540 nm that is directly proportional to hemoglobin concentration (Figure 2B). The pyridine hemochromogen assay (36-38) quantitates heme specifically, using concentrated NaOH to release noncovalently bound heme from hemoproteins before axial coordination of the heme iron by two pyridine molecules. Potassium ferricyanide is often added as well to ensure that all heme iron is initially oxidized to the ferric state. Samples are then split and treated with sodium dithionite (reducing agent) or water and absorbance differences between reduced (ferrous heme) and oxidized (ferric heme) samples at 557 nm and 540 nm, respectively, are measured (Figure 2B). Finally, a fluorescence-based assay may be used quantitate heme. This extremely sensitive technique relies on detection of porphyrin fluorescence (405 nm excitation, 608 nm or 662 nm emission) in samples following removal of the heme iron center with oxalic acid and boiling (39,40). Both boiled and unboiled aliquots of samples are analyzed, where fluorescence readings from the latter are subtracted from the former to remove the contribution of any endogenous porphyrin. Due to the inherent limitations of fluorescence spectroscopy, including the variability and impact of environmental factors such as temperature and bulb life, a real-time linear dynamic range must be obtained with tissue-specific assay parameters and fresh standards (i.e., the Beer-Lambert law, which is not applicable) (48).

Other established approaches for heme quantitation rely on separation of heme from the sample prior to spectroscopic analysis and therefore provide a more accurate, albeit more time-intensive, assessment of heme species. The "gold standard" method is reverse-phase HPLC, as detailed elsewhere (41,42). Briefly, heme (and heme synthesis intermediates and degradation products) are extracted with acid-acetone solution (~75-80% recovery) and separated on a C18

column, with analyte detection by absorbance at 405 nm or fluorescence as described above. Analysis of *de novo* heme levels by radiolabeling (e.g., with ^{59}Fe) can be conducted after acid-acetone and ethyl ether extraction from tissue samples (43-45). Though extensive acid washing of ethyl ether extracts has been reported to remove contaminant species and provide an accurate assessment of heme concentration, HPLC analysis of such extracts has shown otherwise (49).

1.2 Heme Biosynthesis via the Shemin Pathway

Synthesis of Aminolevulinic Acid

Heme biosynthesis in mammals, like in all other non-plant eukaryotic organisms, follows the Shemin pathway (9) and requires eight steps and one nuclear-encoded enzyme per step, beginning with the production of ALA (Figure 3) (50). ALA is a non-proteinogenic amino acid and is the universal precursor for all tetrapyrroles, including chlorophylls, cobalamin, siroheme and coenzyme F_{430} (3). ALA synthesis occurs via the condensation of glycine (51) and succinyl-CoA (52-54) in the first committed and rate-limiting step of mammalian heme biosynthesis (50). This reaction is catalyzed by ALA synthase (ALAS), a pyridoxal 5' phosphate (PLP)-dependent enzyme, in the mitochondrial matrix and yields CoA and CO_2 in addition to ALA (Figure 3). ALAS is thought to have evolved from glutamate-1-semialdehyde aminotransferase (GSAT) (55), the PLP-dependent enzyme used to synthesize ALA in the C_5 pathway in higher plants (5). In this section, a general overview of ALAS will be provided. A more comprehensive review of mammalian ALAS will be presented later in this dissertation (Section 1.3).

In animals, ALAS is unique among other heme biosynthesis enzymes in that it has two isozymes encoded by two separate nuclear-encoded genes: *ALAS1* (or *ALASN*, on human chromosome 3) and *ALAS2* (or *ALASE*, on the X chromosome) (56). *ALAS1* and *ALAS2* likely

diverged after a duplication event that occurred between the branching of cephalochordates and early vertebrates, with *Opsanus tau* (toadfish) being the earliest species known to synthesize both isozymes (57). Tissue-specific expression of ALAS1 and ALAS2 was first elucidated with *ALAS* cDNA clones obtained from chicken liver and erythroid cells (58). ALAS2 is expressed in erythroid tissues (e.g., bone marrow) during terminal differentiation of red cell precursors and massive upregulation of heme and globin synthesis, while ALAS1 is the housekeeping isozyme that controls heme synthesis in all other instances. *ALAS2* transcription is controlled largely by GATA binding factor 1 (GATA1) while *ALAS1* is regulated by glucose (59) and heme (28,60). Both *ALAS1* and *ALAS2* express multiple splice variants in humans and rodents (61,62). The post-transcriptional forms of the two genes are distinct in that *ALAS2* but not *ALAS1* contains an iron-responsive element (IRE) in its 5' untranslated region (UTR) that is bound by iron-responsive proteins (IRPs) in low-iron conditions, effectively blocking translation of the protein (63,64). Interestingly, the human ALAS1 and ALAS2 isozymes maintain only 59% amino acid identity (no homology in the N-terminal region) and have greater similarity to the their respective isozymes in other species than to each other (65).

Structural and protein-protein interaction data have contributed significantly to the understanding of the human isozymes. ALAS structures obtained from the α-proteobacterium *Rhodobacter capsulatus* (66) and *Saccharomyces cerevisiae* (67) have a high degree of sequence homology to the human protein core. Eukaryotic ALAS contains an N-terminal mitochondrial targeting sequence (MTS) that is cleaved after localizing the mature protein to the matrix. Mammalian ALAS1 and ALAS2 also have N-terminal heme regulatory motifs (HRMs) in their respective presequences and mature proteins, though only ALAS1 has demonstrated conclusive evidence for heme-inhibited protein translocation into the mitochondria (68,69). While human

ALAS2 (hsALAS2) binds the ATP-specific succinyl-CoA synthetase (SCS-A) beta subunit (SUCLA2), a proposed source of succinyl-CoA substrate, hsALAS1 forms no such interaction (70,71). A more recent study from our lab (72) has identified α-ketoglutarate dehydrogenase (αKGDH) as another protein partner and the primary source of succinyl-CoA during terminal erythroid differentiation. ALAS2 has further been shown to bind the other two matrix heme synthesis enzymes, protoporphyrinogen (proto'gen) oxidase (PPOX) and ferrochelatase (FECH) (73). While functional roles for PPOX- and FECH-ALAS2 interactions are yet to be clarified, the complex formed by ALAS2 and caseinolytic mitochondrial matrix peptidase chaperone subunit X (CLPX), an AAA+ unfoldase, has been reported to regulate ALAS biochemistry at multiple levels, including cofactor loading and enzyme degradation (74-76). ALAS1 has been shown to pair with CLPX as well as Lon peptidase 1 (LONP1), a mitochondrial ATP-dependent serine peptidase, and subject to turnover by these two proteins (76).

No known mutations of *ALAS1* have been identified to date, but two human diseases have been associated with loss- and gain-of-function *ALAS2* mutations resulting in X-linked sideroblastic anemia (XLSA) (77-79) and X-linked protoporphyria (XLP) (78,80,81), respectively (Table 1). XLSA, which can occur due to the limitation of ALA synthesis, leads to mismatched iron and porphyrin supplies for heme synthesis. The results are decreased heme and hemoglobin production and microcytic anemia, as well as iron overload as evidenced around the nuclei of affected cells (77,78). XLP mutations also cause unmatched iron and porphyrin levels, but with protoporphyrin (PPIX) excess rather than iron due to accelerated ALA synthesis (78,80,81). XLP is a phenocopy of "classic" erythropoietic protoporphyria (EPP), caused by loss-of-function mutations in FECH. Distinct from EPP, however, XLP patients maintain elevated ZnPPIX due to nonspecific metallation of some of the accumulating PPIX (Table 1).

The associated XLP (and EPP) symptoms of non-blistering cutaneous photosensitivity and infrequent liver damage are believed to be caused by leaking PPIX from circulating red blood cells and its accumulation in the dermis (where it reacts with sunlight) and hepatic tissue (where it crystallizes), respectively (78,81-84). Only bone marrow transplant is curative for XLP (85,86), though melanin-stimulating therapies have been shown to mitigate the exposure of porphyrin-loaded dermal capillaries to sunlight (87-90).

Tetrapyrrole Macrocycle Synthesis

Once ALA is released from ALAS, it is transported out of the mitochondria by a hereto undefined mechanism and made available to the cytosolic metalloenzyme porphobilinogen (PBG) synthase (PBGS, formerly known as ALA dehydratase) (Figure 3). ALA transport may involve solute carrier 25A38 (SLC25A38) (91) and/or SLC25A39 (92) across the inner membrane (IMM) and then simple diffusion through porins in the outer membrane. SLC25A38 has also been linked to the mitochondrial import of glycine (an ALAS substrate) (93), and SLC25A39 may be involved in iron-sulfur cluster biogenesis (92). In the cytosol, two ALA molecules undergo a condensation reaction catalyzed by PBGS. This second step of the heme synthesis pathway yields one molecule of the PBG monopyrrole and two molecules of water (Figure 3). Unlike ALAS, PBGS and the remaining human heme biosynthesis enzymes are encoded by a single gene. *PBGS* (chromosome 9) does contain erythroid and housekeeping splice variants, though the only difference is an additional 5' UTR (94). Thus the final protein product is identical in both erythroid and nonerythroid tissues.

The PBGS structure was first characterized in yeast (95) and subsequently in humans (96,97) and defined as a symmetrical homooctomer (tetramer of homodimers), where ALA binds to the enzyme via a Schiff base to a conserved lysine in the active site. The homooctomer is the

predominant quaternary structure, but allosteric changes may cause the homodimers to dissociate and reassemble in part as a lower activity, homohexameric morpheein (97). Zinc (one ion per monomer) and reduced cysteine thiol groups are required for enzyme activity. While only four of the eight zinc ions are required for maximal catalysis, the other four are involved in tertiary stability of the enzyme (78).

Loss-of-function PBGS occurs in lead poisoning and the autosomal recessive disorder, ALAD deficiency porphyria (ALADP). In lead poisoning, lead ions (Pb^{2+}) displace the zinc ion cofactors of PBGS and strongly inhibit enzyme activity and cause ALA to accumulate (98,99). ALADP, the rarest of all porphyrias, has been called a "conformational disease" because *PBGS* mutations have been shown to lower PBGS activity by stabilizing a homohexameric morpheein of PBGS (97,100), also leading to ALA buildup (Table 1). The neurological symptoms associated with lead poisoning and ALADP have been attributed to the interaction of ALA, a structural analog of the neurotransmitter γ-aminobutyric acid (GABA), and the GABA receptor (101).

Following PBG synthesis, hydoxymethylbilane synthase (HMBS, previously called PBG deaminase, or PBGD) catalyzes the third step in the heme biosynthesis pathway. The reaction involves the deamination and condensation of four PBG molecules in a head-to-tail arrangement to produce a linear tetrapyrrole, HMB, and four molecules of ammonia (Figure 3) (78). Like *PBGS*, human *HMBS* (chromosome 11) has distinct erythroid and housekeeping promoter regions and splice variants. The erythroid promoter, located upstream of exon 2, contains GATA1 and nuclear factor, erythroid 2 (NFE2) sites not found in the housekeeping promoter, located upstream of exon 1 (102). Unlike *PBGS*, human *HMBS* contains erythroid and housekeeping splice variants that do not result in an identical enzyme product. Instead, the

erythroid HMBS translational initiation start site is exon 3, while that of the housekeeping isoform is exon 1 due to another in-frame AUG codon located 51 bp upstream of the erythroid mRNA. The result is an additional 17 amino acids at the N-terminus of the housekeeping enzyme (103).

Structural data for the HMBS has been obtained from both human (104) and bacterial (105) enzymes. HMBS is functional as a monomer, but the human form has been crystallized as a two-subunit species with a weak dimer interface (104). Moreover, affinity purification studies indicate that HMBS may exist as a homodimer in erythroid tissue (73). Interestingly, HMBS is synthesized as an apoprotein and produces its own covalent dipyrromethane cofactor that binds to the active site and catalyzes the addition of four PBG molecules to yield a hexameric linear tetrapyrrole (106). The distal tetrapyrrole of the hexamer is subsequently cleaved, leaving behind an enzyme-bound dipyrromethane for future catalytic cycles.

Deficiencies in HMBS can cause an accumulation of ALA and PBG and acute intermittent porphyria (AIP), the second most common form of porphyria (107). AIP is an autosomal dominant disorder characterized by neurological symptoms and severe abdominal pain (Table 1). However, clinical manifestation of the disease is sporadic and often occurs with precipitating factors such as drugs, diet, and hormones that induce ALAS1 and heme production for synthesis of CYPs needed for xenodetoxification in the liver (50). For this reason, exogenous hemin (for severe attacks) and glucose supplementation may be used to limit ALA synthesis via ALAS1 (59,108).

In the fourth step of the heme synthesis pathway, the HMB linear tetrapyrrole is cyclized to form a porphyrin macrocycle via uroporphyrinogen (uro'gen) III synthase (UROS), generating the uro'gen III isomer and a water molecule (Figure 3). Like *PBGS*, the human *UROS* gene

(chromosome 10) has erythroid and housekeeping splice variants that are ultimately translated to identical proteins (109).

UROS is a highly flexible, monomeric protein devoid of a cofactor, as determined from crystal structures for both bacterial (110) and human (111) enzymes. The catalytic reaction involves a spiro inversion of the D ring of HMB (112). HMB does cyclize nonenzymatically in the absence UROS but without the D ring inversion, forming the uro'gen I structural isomer. Uro'gen I can be decarboxylated by the next enzyme in the pathway, uro'gen carboxylase (UROD), to form the coproporphyrinogen (copro'gen) I isomer, but cannot be metabolized further (78,113).

Mutations in *UROS* cause congenital porphyria (CEP), an extremely rare autosomal recessive disease with clinical symptoms of blistering photosensitivity and hemolytic anemia due to the accumulation of cytotoxic uro'gen I and copro'gen I in erythroid cells (Table 1). Teeth are usually stained brown and fluoresce pink, as does urine, beginning at a very young age (50). Additionally, a more severe CEP phenotype has been observed in a female patient also carrying a gain-of-function *ALAS2* mutation (114). To date, only bone marrow transplant has been shown to be curative. Interestingly, some *UROS* mutations yield a protein that is catalytically active but triggers premature proteosomal degradation. A CEP mouse model with one of these mutations has been successfully treated with proteosomal inhibitors such as bortezomib (115).

Tetrapyrrole Side Chain Modifications

Once uro'gen III is released from UROS, it is metabolized by the final cytosolic and fifth overall enzyme in the pathway, uro'gen decarboxylase (UROD). More specifically, the UROD enzyme decarboxylates the four acetate side groups of uro'gen III to produce copro'gen III and four carbon dioxide molecules. UROD is also capable of decarboxylating uro'gen I, though it

prefers uro'gen III, which explains the elevated levels of this compound in CEP (Table 1). Human *UROD* is mapped to chromosome 1 and contains two transcriptional start sites used in equal proportions across all tissues, with the upstream (and major) start site adding a small, 15-bp 5'-UTR to the mRNA (116). Contrary to other heme synthesis enzymes, the *UROD* gene does not appear to have any splice variants.

UROD functions as a homodimeric enzyme with no cofactors (117), and evidence suggests that it decarboxylates the uro'gen acetate groups in a preferred order: D, A, B, and then C, in a clockwise fashion (118). Surprisingly, there is no evidence of direct protein-protein interactions among any of the cytosolic heme synthesis enzymes (UROD, PBGS, HMBS, and UROS) (73) despite the theoretical need for substrate channeling of reactive porphyrin intermediates before transport back into the mitochondria.

Enzymatic deficiency of UROD results in either porphyria cutanea tarda (PCT), an autosomal dominant disease, or hepatoerythropoietic porphyria (HEP), an extremely rare homozygous form of PCT (Table 1). PCT is the most common porphyria and develops when UROD activity decreases to approximately 20% wild-type activity in the liver (107). PCT is the only form of porphyria that is sporadic, and only ~25% of cases are caused by mutations at the *UROD* locus (119,120). Even though PCT is an autosomal dominant disease, it is incompletely penetrant because 50% enzyme activity is sufficient for normal metabolism. Most cases of PCT develop as a result of environmental factors such as alcohol use, smoking, and hepatitis C virus infection (121). However, unlike in ALADP and AIP, risk factors that induce ALAS1 rarely cause PCT (122). Interestingly, a potent endogenous inhibitor of UROD is uroporphomethene, a product of uro'gen oxidation, which can also trigger symptoms. The mechanism for uroporphomethene generation is unclear, but CYPs may play a role (123). The classic PCT

phenotype is chronic blistering photosensitivity, often complicated by infection and resulting in skin fragility and scarring over time, with only minor liver anomalies and no neurological symptoms (50). HEP UROD has as low as 5% of wild-type activity in erythroid tissue (homozygous null alleles are embryonic lethal) (124). As a result, the HEP phenotype largely mimics that of CEP, and ZnPPIX accumulates in erythroid tissue as in ALADP and XLP (50).

In animals, copro'gen III it is transported by a currently unidentified mechanism into the intermembrane space (IMS) of the mitochondria and to the antepenultimate pathway enzyme, copro'gen oxidase (CPOX) (Figure 3) (125). ATP binding cassette subfamily B member 6 (ABCB6) may play a role (126), as it has demonstrated the ability transport planar (but not nonplanar) coproporphyrin molecules (127,128). Copro'gen III is oxidized by CPOX, producing a proto'gen IX molecule, two carbon dioxide molecules, and two water molecules in the IMS (Figure 3). The catalytic reaction is specific to the copro'gen III isomer and involves an unusual stepwise oxidative decarboxylation of the propionate groups on the A and B rings to vinyl groups (78). The human *CPOX* gene (chromosome 3) contains a GC-rich promoter region that includes GATA1 and Sp1-like sites, as well as a unique *CPOX* gene promoter regulatory element (CPRE) (129). Synergistic activation of GATA1, Sp1-like, and CPRE elements has been shown to be necessary for *CPOX* expression in differentiating murine erythroid precursor cells, while the GATA1 site is not required in nonerythroid cells (130). Interestingly, *CPOX* mRNA levels appear to increase during terminal erythroid differentiation while enzyme activity decreases (131,132). In addition, heterologous *CPOX* expression in erythroid-induced cells increases heme synthesis levels (133) and coproporphyrin accumulates during *in situ* erythropoiesis (134), perhaps questioning the role of ALAS2 as the rate-limiting enzyme at certain stages of red cell differentiation.

While it has been established that CPOX is a mitochondrial protein in higher organisms (125), CPOX is cytosolic in yeast (135). A recently developed proteomic mapping strategy has specifically localized the N-terminus of mammalian CPOX to the IMS-facing side of the IMM (136). Mature CPOX functions as a homodimer without a cofactor (78), and the crystal structure has been solved for yeast (137) and human (138) proteins. The mechanism of CPOX action is unusual in that the two decarboxylations occur at the same active site in the homodimer (139,140).

Most loss-of-function *CPOX* mutations result in hereditary coproporphyria (HCP) (Table 1), an autosomal dominant disorder with variable penetrance much like AIP and PCT that includes asymptomatic heterozygotes (141). HCP is manifested in neurovisceral and skin symptoms akin to AIP and PCT, respectively, and risk factors (e.g., alcohol use) and treatments (e.g., exogenous hemin) for HCP are the same as for AIP (50). A particular set of CPOX mutations results in harderoporphyria (Table 1), a variant of HCP caused by the release of 2-vinyl-4,6,7-tripropionic acid porphyrin (a tricarboxyl porphyrin) after decarboxylation of the A ring and before decarboxylation of the B ring. The term "harderoporphyrinogen" for which the disease is named is actually a misnomer, as the porphyrin secreted from the Harderian gland is actually a glycoconjugate, protoporphyrin-1-O-acyl-β-xyloside (142). The increased levels of the 2-vinyl-4,6,7-tripropionic acid porphyrin result in a similar phenotype to HCP, with the exception that hemolytic anemia is observed at birth but resolves with age (140).

Formation of Protoporphyrin IX and Iron Insertion

Once proto'gen IX is made, it is transported through the IMM and into the mitochondrial matrix by a hereto undefined mechanism (Figure 3). Data from yeast indicate that the adenine

nucleotide translocator (ANT) is involved (143), while proto'gen IX transport in erythroid tissue appears to rely on transmembrane protein 14C (TMEM14C) (92,144). Association of both CPOX and PPOX to opposite sides of the IMM could also indicate a simple and direct transfer across the lipid bilayer.

In the matrix, proto'gen IX is oxidized to protoporphyrin IX (PPIX) via proto'gen oxidase (PPOX) in the penultimate step of heme biosynthesis (50). The reaction requires three oxygen molecules and produces three molecules of hydrogen peroxide per PPIX molecule (Figure 3). Interestingly, the hydrogen peroxide byproduct is an ROS whose oxidized products of superoxide and hydroxyl radicals are particularly cytotoxic, but this is postulated to be controlled in non-disease states by cellular catalases, peroxidases, superoxide dismutases, and reductases (5,145). Human *PPOX* has been mapped to chromosome 1 and, like the *CPOX* gene, contains tissue-specific promoter elements (146). Two GATA1 sites in the *PPOX* promoter region are activated specifically in erythroid tissue and cause a four-fold increase in *PPOX* expression in differentiating human erythrocyte precursors (147).

PPOX structural and interaction data are relatively plentiful. Crystals have been solved for plant (148), bacterial (149,150), and human (151) forms and in each case the enzyme has been shown to function as a homodimer with one flavin adenine dinucleotide (FAD) molecule cofactor per monomer. Unlike CPOX, the PPOX pre-protein requires N-terminal and internal targeting sequences to localize to the mitochondrial matrix (152). Aside from the previously noted interactions with ALAS2, CPOX, and FECH, mature PPOX is also a protein partner of manganese superoxide dismutase (MnSOD) (73). The PPOX-MnSOD interaction may help explain stable ROS levels despite hydrogen peroxide production during PPOX catalysis. Finally, mature PPOX also binds TMEM14C (144) and associates with a complex made up of FECH,

ATP Binding Cassette Subfamily B Member 10 (ABCB10), and mitoferrin-1 (MFN1) (153), though the particular role of PPOX in these complexes has not yet been clarified.

Human PPOX deficiency results in variegate porphyria (VP), an autosomal dominant disease that behaves much like HCP (Table 1). However, blistering photosensitivity and associated skin lesions are more prevalent in VP than HCP (50). This characteristic may be due in part to the accumulation of ROS in VP, perhaps due to both increased levels of porphyrin precursors and decreased activity of antioxidant heme-dependent proteins such as catalase and glutathione peroxidase (GPx) (145,154). Increased levels of ALA and PBG in both HCP and VP indicate that HMBS may become rate-limiting in these disease states. Indeed, it has been shown that copro'gen III and proto'gen IX allosterically inhibit HMBS in transformed lymphoblasts from VP patients (155). Symptomatic VP patients are treated in the same manner as those with HCP and AIP (50).

The eighth and final step of heme biosynthesis involves the iron metallation of the PPIX macrocycle by FECH, a homodimeric protein on the matrix-facing side of the IMM to produce heme (Figure 3) (156). The iron is believed to be sourced from the endocytosis of extracellular diferric transferrin (TFN), bound to Tf receptor 1 (TFNR1) (157). Ferric iron is released from TFN upon endosomal acidification (158) and reduced to the ferrous state by six-transmembrane epithelial antigen of the prostate 3 (STEAP3) metalloreductase (159). Ferrous iron is then loaded onto divalent metal transporter 1 (DMT1) (160) and released either 1) into the cytosol, forming a chelatable "labile iron pool" in which iron is redox-inactive and allocated for storage (i.e., in ferritin) or cellular distribution (161); or 2) directly into mitochondria according to the "kiss and run" hypothesis (162,163). The latter is thought only to occur during late erythropoiesis when iron demand is greatest. Iron transport across the IMM to FECH is carried out by mitoferrin

(MFN) 1 and MFN2 in erythroid and nonerythroid cells, respectively (164,165). The single *FECH* gene (chromosome 18) contains housekeeping Sp1 and erythroid-specific NFE2 and GATA1 elements (166). Two *FECH* variants with differing polyadenylation sites exist and are putatively generated in a tissue-specific manner, as suggested by the predominance of the larger mRNA in murine erythroid precursors (50,167). Another *FECH* splice variant is devoid of exon 2 and results in the translation of a truncated, inactive enzyme. Interestingly, the amount of this variant has been shown to be correlated with heme levels (168). Finally, alternative splicing of *FECH* pre-mRNA can result in the inclusion of an intronic sequence that contains a premature termination codon (PTC). Wild-type *FECH* is spliced this way in 10-20% of transcripts, while a polymorphism in intron 3 (IVS3-48C>T) results in more than double the percentage of aberrant mRNA (169,170).

Like PPOX, much is known about the structural and protein binding nature of FECH. FECH crystals for *Bacillus subtilis* (171) and human (156) proteins have been solved, including characterization of a conserved pi-helix switch involved in heme release (172). Human FECH is a homodimer with a [2Fe-2S] cluster in each subunit, bound to a cysteine-rich C-terminal region that is lacking in yeast and plants (173,174). The [2Fe-2S] cluster cofactor for mammalian FECH is required for enzyme activity, though it is apparently uninvolved in the catalytic mechanism. Iron-sulfur clusters are ancient structures with diverse redox chemistries, and evidence suggests they are important for FECH protein stability (175). It has been postulated that the [2Fe-2S] clusters in FECH may act as sensors of nitric oxide (which destroys the cluster) (176), mitochondrial iron status (175), and/or redox or mitochondrial membrane potential (177). In addition, unlike other heme synthesis enzymes, post-translational phosphorylation of FECH has been demonstrated to impact enzyme activity in human and murine erythroid precursors as

well as zebrafish (178). More specifically, phosphorylation of a conserved threonine near the FECH active site pocket by protein kinase A (PKA) is required for full FECH activity during terminal erythropoiesis. As previously discussed, FECH has multiple protein partners (e.g., ALAS2, CPOX, PPOX, ABCB10, MFN1) involved in heme biosynthesis and mitochondrial iron supply (73,153). Furthermore, data indicate that FECH also interacts with α-ketoglutarate dehydrogenase (αKGDH) and SUCLA2 (72,73), both potential sources of succinyl-CoA for ALAS, indicating possible regulation upstream of committed heme synthesis.

Loss-of-function mutations in human *FECH* result in the third most common porphyria, erythropoietic protoporphyria (EPP) (107) (Table 1). This disease is classified as autosomal recessive, as heterozygous individuals demonstrate 50% enzyme activity and overt disease appears only when enzyme activity decreases to less than ~30% of normal (78). Of note, more than 90% of EPP patients have FECH mutations in *trans* with the aforementioned low-expression FECH polymorphism (IVS3-48C), which skews aberrant splicing (169). As previously mentioned, the EPP phenotype of ubiquitous nonblistering skin photosensitivity and an increased risk of liver disease mirrors that of XLP. XLP treatments of UVB therapy and α-melanocyte-stimulating hormone (α-MSH) are also applicable to EPP. However, while iron supplementation has been shown to improve XLP (179), evidence suggests that it may not ameliorate EPP. The model that iron stimulates ALAS2 synthesis (63,180) combined with the possibility that the IVS3-48C polymorphism is unresponsive to iron-mediated increases in proper *FECH* splicing (181) may lead to exacerbation of the disease in EPP patients (179).

1.3 Aminolevulinate Synthase in Mammals

Enzyme Structure and Mechanism

Until our most recent study (Chapter 3, ref (182)), structural knowledge of mammalian ALAS has been limited to modeling conserved domains after crystal data from *R. capsulatus* (rcALAS, PDB 2BWN, 2BWO, and 2BWP, solved to 2.1-2.9 Å) (66) and *S. cerevisiae* (scALAS, PDB 5TXR and 5TXT, 2.7 Å) (67), as well as computational hypotheses (183). Sequence alignments of rcALAS, scALAS, and the human ALAS isozymes (Figure 4) show that the bacterial protein has a significantly shorter N-terminal region and lacks a C-terminal (Ct)-extension of ~40-55 amino acids common to eukaryotes. The rcALAS core, however, is highly homologous to human and yeast ALAS proteins, exhibiting ~50% amino acid identity and ~70% similarity. The rcALAS (Figure 5A) and scALAS (Figure 5D) structures both indicate a tightly interlocked homodimer whose monomer subunits are made up of three distinct domains, all of which contribute to the dimer interface: a variable N-terminal domain, a conserved catalytic domain, and a regulatory C-terminal domain (Figures 5A, 5D).

The N-terminal regions of eukaryotic ALAS pro-enzymes are highly variable but all have an amphipathic MTS (Figure 4) that is proteolyzed following targeting of the protein to the matrix, first demonstrated for ALAS1 from rat liver *in vitro* (184). The length of the MTS is 56 amino acid residues in hsALAS1 (185) and 57 residues in scALAS, although evidence suggests that the yeast presequence is not required for mitochondrial import (186,187). The ALAS2 MTS is less well defined and is reportedly homologous to either the ALAS1 MTS and 49 residues in length (185) or the ornithine transcarbamylase MTS and 78 residues (188). As shown in the rcALAS structure (66), the overlapping N-terminal regions of prokaryotic and eukaryotic ALAS enzymes are very similar and include an arginine (Arg21 in rcALAS and Arg91 in scALAS) that

forms a salt bridge with succinyl-CoA and an acidic residue (Glu17 in rcALAS and Asp87 in scALAS) that stabilizes enzyme conformation following succinyl-CoA binding (Figure 5B).

The ALAS catalytic domain contains a PLP cofactor bound as a Schiff base to either an active site lysine (Lys248 in rcALAS and Lys337 in scALAS) or glycine substrate and stabilized by an adjacent histidine (His217 in rcALAS and His284 in scALAS) and aspartate (Asp214 in rcALAS and Asp281 in scALAS) (Figures 5B, 5C, 5E). These histidine and aspartate residues are responsible for the PLP specificity of the enzyme via hydrogen bonding and salt bridge formation, respectively. A conserved glycine-rich region exists within a conserved loop in this region and is necessary for succinyl-CoA substrate binding. Another histidine (His142 in rcALAS and His 209 in scALAS) is positioned directly above the active site and drives the decarboxylation step of catalysis (189), as described in further detail below.

The bacterial and eukaryotic C-terminal domains share two conserved loops, where the more downstream of these loops covers the active site and likely controls substrate binding and product release by an induced-fit mechanism (Figure 6A). When this loop is shifted outward, the enzyme adopts an "open" conformation in which the active site is widened (Figures 5C, 6A). The loop moves inward and locks the enzyme in a "closed" conformation when 1) a conserved threonine (Thr365 in rcALAS and Thr452 in scALAS) in the loop noncovalently binds to a) the carboxylate group of succinyl-CoA and the previously mentioned N-terminal arginine (Arg21 in rcALAS and Arg91 in scALAS) and an isoleucine (Ile361 rcALAS and Ile448 in scALAS) and methionine (Met190 in rcALAS and Met257 in scALAS) in the active site; and 2) a conserved arginine (Arg368 in rcALAS and Arg455 in scALAS) interacts with the amino-terminal residues Glu17 in rcALAS (Figure 5B) or Asp87 in scALAS via a salt bridge (Figure 5F).

The eukaryotic-specific Ct-extension provides an additional level of regulation on ALAS activity, as first evidenced by mutations in this region of hsALAS2 with XLSA and XLP human disease states (71,80). This region was further shown to confer an autoinhibitory effect on enzyme activity with stable transgenic expression of hsALAS2 with and without the Ct-extension in a nonerythroid human cell line (190). Based on the scALAS structure, the Ct-extension wraps around the homodimer, allowing the Ser543 residue to hydrogen bond to an arginine (Arg151) within the glycine-rich stretch on the same subunit and to Glu164, both proximal to the active site of the opposite subunit (Figure 5F). Importantly, the Ct-extension in scALAS is ~15 amino acids longer than the same region in its vertebrate counterparts, packing into a hydrophobic groove and against a unique 22-residue insertion in the catalytic domain of the same subunit (Figures 4, 5E), and appears to stabilize the opposite active site. Deletion of the scALAS Ct-extension results in decreased enzyme activity (67), suggesting that the regulatory role of this region is distinct in hsALAS2 and does not explain the post-translational impacts of XLSA and XLP mutations. It is worth noting here that differences in the structures of yeast and human Ct-extensions have been verified with the recently solved hsALAS2 structure by our collaborators in the UK (PBD 6HRH, 2.3 Å resolution), and the corresponding published work (ref (182), see Chapter 3) from our labs comprises Chapter 3 of this dissertation. While specific details will be discussed therein, we have indeed been able to demonstrate that the Ct-extension of hsALAS2 (Figure 4) confers an autoinhibitory mechanism distinct from that of the yeast enzyme.

ALAS is a member of the α-oxoamine synthase family of PLP-dependent enzymes (191), all of which require PLP as a cofactor to catalyze the condensation of acid-CoA thioesters and small amino acids. ALAS follows an ordered Bi Bi mechanism in which glycine is bound before

succinyl-CoA, and ALA is released from the enzyme in the final step of the catalytic cycle (192). The enzyme has a strict requirement for L-glycine, although mutant murine ALAS2 has been shown to metabolize L-serine as well (193). ALAS is more promiscuous regarding the succinyl-CoA substrate, as several CoA esters have been found to act as alternative substrates (194). Unusually, ALAS behaves as both an aminotransferase and decarboxylase and involves the cleavage of two amino acid α-carbon bonds, one from the glycine substrate and the other from the ALA precursor (189). The catalytic cycle of ALA production via ALAS has been previously elucidated through positional labeling experiments, structural studies, and interrogations of pre-steady state kinetics with stopped-flow spectroscopy (66,193,195-197) (Figure 6B). Briefly, the cycle is initiated when ALAS is in the open conformation, with the conserved active site lysine (e.g., Lys248 in rcALAS) (Figure 4) bound to the PLP cofactor via a Schiff base, forming an internal aldimine (Figures 5C, 6B). PLP is displaced from the enzyme and forms a Schiff base with L-glycine once this substrate enters the active site, yielding an external aldimine (Figures 5E and 6B). The pro-*R*-hydrogen of glycine is then stereospecifically abstracted by the active site lysine, the first α-carbon cleavage, producing a carbanion and the first of two quinonoid intermediates. After succinyl-CoA enters the active site, the enzyme adopts the closed conformation (Figures 5B and 6B), and the carbanion attacks the electrophilic carbonyl of succinyl-CoA. The result is a transient tetrahedral intermediate that quickly transforms to a 2-amino-3-ketoadipate intermediate with the loss of CoA. Subsequent decarboxylation of the 2-amino-3-ketoadipate is catalyzed by a conserved histidine (His142 in rcALAS and His209 in scALAS) that sits atop the active site (Figures, 5B, 5C, 5F, 6B), resulting in an enolic compound in equilibrium with the second quinoid intermediate and the ALA-bound external aldimine. Finally, proton abstraction by the catalytic lysine causes cleavage of the second α-carbon in the

reaction and release of ALA product. This step is accompanied by a return to the open enzyme conformation (Figures 5B, 5F, 6B).

Regulation of Enzyme Synthesis and Localization

Synthesis of mammalian ALAS isozymes is differentially controlled in a cell- and time-specific manner from transcription through translation. The housekeeping *hsALAS1* gene was first isolated from a human adult liver cDNA library and localized to chromosome 3 (3p21.2) (56,198,199), where it is ~17 kb in length and contains 12 total exons (10 protein-coding and two noncoding exons in its 5'-UTR) (61). In the promoter region of *ALAS1*, transcription is stimulated by a complex of factors consisting of peroxisome proliferator-activated receptor γ coactivator 1α (PGC1α), nuclear respiratory factor 1 (NRF1), and forkhead box protein O1 (FOXO1) (Figure 7A) (59). Assembly of this complex is limited by glucose and heme by distinct mechanisms. In short, sufficiently elevated glucose levels result in the phosphorylation of FOXO1 and disruption of the PGC1α-NRF1-FOXO1 activating complex (59), which explains why diet can be a precipitating factor in the hepatic porphyrias (50). In addition, PGC1α transcription is suppressed by heme-loaded nuclear hormone receptor protein REV-ERBα, a mediator of circadian rhythm (Figure 7A) (62). Elevated heme concentrations also diminish *ALAS1* transcription via growth response 1 (EGR1) (60). In mice, Egr1 was found to interact with NGFI-A Binding Proteins 1 and 2 (Nab1 and Nab2) and subsequently bind to a heme responsive element (HRE) in the proximal promoter region of Alas1 to repress transcription (Figure 7A) (60). The *hsALAS1* gene is unique to other mammals in that it contains two transcription start sites that are tissue-specific (61). Interestingly, a single TATA start site is used in hepatocytes where ALAS1 and heme synthesis are sensitive to xenobiotics, while initiation at a second site upstream of the TATA box also occurs in tissues like brain where

ALAS1 is only weakly inducible. Furthermore, it is likely that use of the single transcription start site in liver is associated with a drug-responsive enhancer element in the *ALAS1* 5'-UTR, upon which heterodimers of the nuclear receptors constitutive androstane receptor (CAR) and retinoid X receptor (RXR) assemble and promote ALAS1 and ultimately heme synthesis (Figure 7A) in much the same manner they induce the production of CYPs (200).

Like transcription, *ALAS1* mRNA translation and protein localization to the mitochondria are also controlled by heme-dependent mechanisms. Humans and rodents have been shown to produce two alternatively spliced *ALAS1* mRNA variants in similar relative amounts across all tissues, where the minor variant contains an additional exon (1B) in the 5'-UTR (61). Only the major variant appears to be sensitive to heme, as exon 1B in the minor variant forms a stable stem loop structure that inhibits translation and limits the ALAS1 protein synthesis required for heme-mediated mRNA decay (201). Heme also increases the rate of *ALAS1* mRNA degradation in chicken liver embryos (202). As previously mentioned, ALAS1 is translated as a proenzyme with a 56-residue N-terminal MTS that is cleaved by an unknown protease following localization of the mature protein sequence to the mitochondrial matrix (185). Although MTSs are poorly conserved and have less than 25% identity between ALAS1 and ALAS2, both pre-proteins harbor multiple N-terminal HRMs consisting of cysteine-proline (CP) dipeptides (Figure 4) (68). ALAS1 contains two CP motifs in its MTS, and heme-dependent inhibition of mitochondrial localization of rat ALAS1 proenzyme (Figure 7A) in quail fibroblasts was observed and eliminated upon mutation of the CP cysteines to serines (69). It has been hypothesized that when these CP motifs are bound by heme, the anchoring hydrophobic interactions of the ALAS MTS with an inner mitochondrial importer such as TOM20 are disrupted (203).

Unlike ALAS1, regulation of ALAS2 synthesis and localization is less dependent on heme, which is not surprising given the large quantities of heme required for hemoglobin synthesis in differentiating erythroid tissue. A definitive switch from *ALAS1* to *ALAS2* expression occurs during the proerythroblast stage of mammalian erythropoiesis (204-206), following stimulation of terminal differentiation by the essential hormone erythropoietin (EPO) (207) (detailed further in Section 1.4). The *hsALAS2* gene was first cloned from a human fetal liver library and mapped to the X chromosome (Xp11.21) (56), where it is ~22 kb and contains 11 exons (10 coding exons and a single 5'-UTR exon) (208). Initial studies on transcriptional regulation of the murine *Alas2* gene expressed in various cell lines revealed that the proximal promoter region within ~720 bp of the transcription start site (TSS) contains several regulatory elements specific to the transcription factors GATA1 (two binding sites), nuclear factor erythroid 2 (NFE2), Sp1, erythroid Krüppel-like factor (EKLF), and hypoxia inducible factor 1 (HIF1) (Figure 7B) (209). HIF1 is interesting in that while it is known to upregulate several other genes essential for erythroid differentiation (e.g., *EPO* and *TFNR1*), the putative hypoxia-responsive element (HRE) in the proximal ALAS2 promoter was found to be insensitive to mutation (210). More recently, however, it was found that three HREs ~600-750 bp downstream of the hsALAS2 gene bind HIF1α protein and upregulate *ALAS2* expression (211). Additionally, introns 1 and 8 of the *hsALAS2* gene include enhancer elements that are functional during erythropoiesis (212). Both introns contain GATA motifs, though CRISPR-Cas9 knockout experiments in murine erythroid model cells indicate that the intron 1 site is more important for normal terminal differentiation (213). Most recently, the intron 1 enhancer has been modeled as an anchor connecting GATA sites in intron 8 and the proximal promoter in a long-distance loop that

increases *ALAS2* expression via a complex including GATA1, RNA polymerase II, and other factors (214).

The fate of *ALAS2* mRNA is governed by alternative splicing, post-translational modification of a translational initiation kinase, and an IRE in the 5'-UTR that is absent in *ALAS1* (Figure 7B) (62,215,216). Splicing of *ALAS2* mRNA results in two main isoforms, one lacking exon 4 (37 N-terminal amino acids) that results in an enzyme with ~30% wild-type activity, along with three additional variants that comprise less than 15% of all transcripts and are of little known physiological consequence (62). Along with other proteins during erythropoiesis, *ALAS2* translation is reportedly controlled by the heme-regulated eukaryotic initiation factor 2 alpha (eIF2α) kinase (HRI), where HRI is activated by heme deficiency and oxidative stress and subsequently phosphorylates eIF2α to decrease uncoordinated globin synthesis and ROS levels, respectively (Figure 7B) (217,218).

The presence of IREs and their associated stem loop structure can either be inhibitory or stimulatory depending on their location in the transcript. The 5'-IRE present in both *ALAS2* isoforms is bound by one of two IRPs (IRP1 or IRP2, encoded by paralogs *IREB1* and *IREB2*, respectively) when iron levels are low, effectively blocking attachment of the ribosomal pre-initiation complex and peptide chain elongation (215,216,219,220). The same regulatory mechanism has been observed for ferritin (220), an iron storage protein. Conversely, the presence of an IRE in the 3'-UTR of a transcript stimulates translation by limiting RNAse-mediated degradation of the transcript (221). Examples of genes relevant to iron homeostasis and erythropoiesis whose mRNA contain 3'-IREs are *TFNR1* (222) and *DMT1* (223). The specific impacts of IRP1 and IRP2 on *ALAS2* mRNA translation are dependent on iron (and perhaps heme iron), oxygen levels, and the stage of red cell development (219,224,225).

Mammalian IRP1 and IRP2 are ~60% identical in primary structure and bind the *ALAS2* 5'-IRE stem loop and inhibit translation by distinct mechanisms (224,226). Briefly, IRP1 obtains a 4Fe-4S cluster and functions as a cytosolic aconitase that is unable to interact with the 5'-IRE of *ALAS2* at sufficient cellular iron concentrations. In iron deficiency, however, the cluster is lost and a conformational change results in the conversion of the aconitase form of IRP1 to an IRE-binding protein. Hypoxia inhibits disassembly of the IRP1 aconitase (221). IRP2 has an unusual 73-amino acid insertion in the N-terminal domain that is absent in IRP1 but contains three homologous iron-binding cysteine residues (227). IRP2 does not utilize an Fe-S cluster and has no aconitase activity. IRP2 is a stable IRE-binding protein at low iron and/or hypoxic conditions and is ubiquitinated and degraded as part of a larger complex when iron and oxygen levels rise (224). Notably, earlier work identified an HRM in the IRP2 protein that is oxidized by heme and also results in ubiquitination and subsequent degradation of IRP2 (228). Although Irp2 has been reported to be the primary physiological Irp in mice (229), animals with impaired Fe-S cluster biosynthesis demonstrate decreased heme synthesis without porphyria due to IRP1-mediated inhibition of ALAS2 synthesis (64,230). Evidence from an *Irp2*$^{-/-}$ mouse model demonstrating microcytic anemia and porphyrin overproduction suggests that the IRE-IRP system is critical for normal erythropoiesis in mammals (63). However, others indicate that the IRE-IRP system may be overwhelmed and decoupled from iron levels when massive upregulation of *ALAS2* and iron utilization occurs late in erythroid differentiation (63,219,225,231). One group has provided clear evidence that heme-dependent HRI controls translation far greater than the iron-dependent IRE-IRP system late in terminal erythropoiesis (231). The aforementioned "kiss and run" model of direct iron transport from the plasmalemmal to mitochondrial membrane (162,163) may also indicate that the cytosolic iron pool and thus IRE-IRP regulation are bypassed in these cells.

Like hsALAS1, translated hsALAS2 pre-protein contains multiple CP dipeptides in its MTS of reportedly 49 or 78 amino acids in length (Figure 4) (185,188,232). Predictably, ALAS2 has been shown to be bound by heme at its two most N-terminal CP motifs and blocked from translocating into the mitochondrial matrix in the same manner as ALAS1 (68,203). However, in the same cell culture model in which the import of heterologous rat Alas1 was shown to be inhibited by heme in quail fibroblasts, rat Alas2 was not affected (69). These contending data have yet to be resolved (Figure 7B), although it has been postulated that the ALAS2-specific association with SUCLA2 may be relevant in the mitochondrial localization of mammalian ALAS2 (70).

Regulation of Mature Enzyme Stability and Activity

In the mitochondrial matrix, the abundance and enzymatic activity of mature mammalian ALAS1 and ALAS2 are regulated via several mechanisms, most of which are associated with protein-protein interactions and proteolysis (72,75,76,210). ALAS1 and ALAS2 have half-lives on the order of hours (232,233). One variable that controls ALAS enzyme turnover is protein oxidation, where hydroxylation of proline within the ALAS2-specific C-terminal LXXLAP motif (Figure 4) targets ALAS2 for ubiquitination and proteosomal degradation (234). This study showed that hypoxia left the proline unmodified and thus stabilized the mature ALAS2 for 2- to 7-fold greater than the half-life of the protein in normoxia. A later investigation of oxidative stress caused by disorders such as β-thalassemia found that ALAS2 enzyme activity decreases in the presence of ROS and heme as a protective measure in erythroid model cells (235). Mitochondrial LONP1, an ATP-dependent serine peptidase, has also been described as a key player in heme-dependent ALAS1 oxidation and protein turnover in human liver cell models (233). Another group provided further evidence that LONP1 accelerates ALAS1 degradation

following hemin-mediated oxidation of ALAS1 and/or heme binding to the remaining CP motif in the mature ALAS1 N-terminal domain (Figures 4, 7A) (76). In the associated pull down experiments, heme-bound ALAS1 also paired with CLPX, and was proteolyzed by the mitochondrial proteasomal complex, CLPXP, made up of CLPX and caseinolytic mitochondrial matrix peptidase proteolytic subunit (CLPP) (Figure 7A). Other work in yeast and zebrafish have shown that mitochondrial ClpX also interacts with a specific region of the ALAS N-terminal domain to enhance PLP incorporation and ALA synthesis (Figures 7A, 7B) (74). In the same study, knockdown of ClpX in zebrafish resulted in a sideroblastic anemia phenotype that could be rescued with ALA supplementation. The most recent paper from this group indicates that PLP loading of ALAS follows the partial unfolding of a ClpX subdomain extending from the PLP binding site to its active site (236). The apparently paradoxical roles of CLPX in ALAS biochemistry were made clearer in mammalian erythroid precursor cells and EPP patients harboring *CLPX* (not *FECH*) mutations (75). Here, heterozygous erythroid precursors expressing wild-type CLPX and the active site mutant found in an EPP family maintained PLP incorporation at wild-type levels but were unable to function normally as part of the CLPXP degradation complex in murine erythroid cells (Figure 7B), resulting in ALAS2 protein and PPIX accumulation (75). Finally, ALAS2 binds the terminal heme synthesis enzymes PPOX and FECH *in vitro* as part of a heme metabolon (4,73). It is feasible in this context that the initial and final steps of the pathway are interregulated to maintain prevent accumulation of cytotoxic porphyrin intermediates, though conclusive evidence for this hypothesis is currently lacking.

Substrate-level control of ALAS activity was at the forefront of research in porphyrin synthesis more than 50 years ago (52,54,237) but has again gained interest in the last 20 years due largely to evidence for protein-protein interactions involving ALAS (70-72). Glycine is

abundant in plasma (~250 μM) and can be readily obtained by the cell by glycine transporter 1 (GLYT1), which is essential for normal hemoglobinization to occur in erythroid precursors (238-240). While the mitochondrial import mechanism is not clear, data indicate that SLC25A38 transports glycine as well as ALA (91,93). The possibility that glycine for ALA synthesis may be derived intracellularly from serine metabolism cannot be excluded, particularly in nonerythroid cells. The primary source of succinyl-CoA, a highly reactive molecule, has long been presumed to be the TCA cycle (52,54,70,71,237), although whether primarily from αKGDH or SCS has been debated and linked to the cellular context of ALAS, including protein interactions. For example, early experiments in hemolysates from chicken demonstrated that α-ketoglutarate is the source of succinyl-CoA when intact cellular "particles" were assayed (54), whereas succinate filled this role when these particles were freeze-dried before use and sufficient ATP was provided (52). A later study indicated α-ketoglutarate to be an important supplier of heme carbon, as αKGDH deficiency in a diabetic family resulted in anemia (241). The strongest argument for succinyl-CoA being derived from SCS during erythropoiesis comes from evidence that the SUCLA2 subunit of SCS-A binds ALAS2, and in particular the mammalian Ct-extension, but not ALAS1 (70,71). Again, this would require large quantities of ATP, beyond what is needed to drive basal oxidative phosphorylation, to supply sufficient levels of succinyl-CoA for the mass production of heme synthesis. In addition, data indicate that neither *Sucla2*$^{+/-}$ mice (242) nor human patients with SUCLA2 deficiency (MIM #612073) exhibit anemia.

Recent work in our lab supports α-ketoglutarate as the primary source of heme carbon based on mRNA, protein, and activity levels of TCA cycle enzymes, as well as stable isotope metabolomics and protein-protein interactions during mammalian erythropoiesis (72). Briefly, we found that SCS and αKGDH activities decrease and increase with erythroid differentiation in

murine erythroleukemia (MEL) cells, respectively. These data correlate with the known changes in message and protein levels of SCS and αKGDH in this same window (206,243,244). In addition, pull down experiments in MEL cells overexpressing *hsALAS2* have revealed an ALAS2 interaction with all three subunits (E1, E2, and E3) of αKGDH, where the E1-ALAS2 pair in particular has been verified by protein affinity chromatography and western blot (Figure 7B). Perhaps most importantly, stable isotope metabolomics revealed that the largest source of heme carbon is glutamine, not succinate, in erythroid precursors. Thus, we have proposed that α-ketoglutarate produced from glutamine via glutamate is metabolized by a distinct pool of αKGDH enzyme operating outside the TCA cycle that supplies succinyl-CoA to ALAS2 specifically for heme synthesis. Alternative roles of the SUCLA2-ALAS2 interaction include facilitation of ALAS2 mitochondrial localization (70), apoenzyme stabilization, or sequestration of succinyl-CoA from SCS early in differentiation (before SCS-A levels decrease). Post-translational modification of ALAS2 via succinylation is also plausible (245,246), although proteomic data of succinylated proteins during erythropoiesis are lacking.

Mutations and Human Disease

To date, no disease-causing mutations have been found in *hsALAS1*, while dozens of mutations in *hsALAS2* have been chronicled and are associated with aberrant erythropoiesis (50). As previously mentioned, loss-of-function and gain-of-function mutations in hsALAS2 result in XLSA or XLP diseases, respectively (Table 1). As X-linked disorders, the inheritance pattern of XLSA and XLP precludes father-to-son transmission. Males are fully symptomatic while females are variably affected based on the random nature of X-chromosome inactivation and lyonization (247,248).

XLSA is characterized by microcytic hypochromic anemia, often with intracellular iron overload, and patient symptoms include dizziness, fatigue, and decreased capacity for physical activity (249). Most XLSA mutations are located in translated exons of *hsALAS2* and are the result of single nucleotide substitutions, with the exceptions of a premature stop, frameshift, and a lysine codon deletion at amino acid positions 204, 506, and 535, respectively (250). Evidence for XLSA stemming from mutations in the 5'-noncoding region of *hsALAS2* also exists (251,252). A structural analysis of many XLSA mutations has been completed based on the crystallized rcALAS protein (66), and mutations found in exon 9 of the *hsALAS2* gene and other regions that contribute to the integrity of the PLP binding site are treatable with pyridoxine, the alcohol form of vitamin B_6 (PLP is the aldehyde form). In contrast, mutations affecting substrate binding or protein stability tend to be pyridoxine-refractory. Several pyridoxine-responsive missense XLSA mutations located in the Ct-extension of hsALAS2 have been identified (Figure 8) and abrogate SUCLA2 binding (71). Of note, the ALAS2-SUCLA2 interaction is also lost in the pyridoxine-refractory D190V mutant (N-terminal domain) (70). Regardless of whether XLSA patients are pyridoxine-responsive, however, management of iron overload with chelation therapy (e.g., desferrioxamine) or phlebotomy may be required (232).

XLP is caused by the accumulation of PPIX due to hyperactive ALAS2 and rate-limiting iron incorporation via FECH in the final step of heme biosynthesis (80). The ALAS2 gain of function is caused by multiple frameshift mutations in the eukaryotic Ct-extension (Figure 8) and loss of the associated autoinhibitory regulation (80,253,254), likely increasing the rate of ALA release from the active site (255). Uniquely, the Y586F mutation has only been observed in CEP patients where increased ALA synthesis via the ALAS2 mutant exacerbates the accumulation of uro'gen I and copro'gen I and the associated symptoms of porphyria (114). XLP phenocopies

EPP, in which FECH deficiency also results in elevated PPIX levels. However, the biochemical profile of XLP is usually distinct from EPP in that a large fraction of the PPIX is converted to ZnPPIX, presumably due to promiscuous FECH activity in the absence of sufficient iron to match accumulating free PPIX (81). In XLP and EPP, free PPIX accumulates in red cells and putatively leaks into circulating plasma, where it fluoresces upon irradiation with sunlight (specific excitation wavelength ~405 nm) in the upper dermal capillaries and generates ROS (82,83). Furthermore, ROS (the hydroxyl radical in particular) induce lipid membrane peroxidation, complement activation, and mast cell degranulation in the surrounding tissue. Thus, patients with protoporphyria experience acute, nonblistering photosensitivity characterized by painful itching, tingling, and burning of the skin (81). Liver complications also develop in less than 10% of XLP and EPP patients, most commonly later in life, due to the accumulation of birefringent porphyrin crystals in hepatic tissue following enterohepatic circulation (81,84). The only known cure for XLP is bone marrow transplant, though this procedure has only been completed to avoid or to complement liver transplantation (85,86). The use of melanin-stimulating prophylaxes such as narrow-band ultraviolet B (UVB) therapy (82) and an α-MSH analog (83-85) have been shown to diminish photosensitivity significantly. Iron supplementation may also be a possible XLP therapy due to iron-limited heme synthesis in this disease (179). Isonicotinic acid hydrazide (INH), an FDA-approved anti-tuberculosis drug and PLP antagonist, was unfortunately ineffective in decreasing PPIX levels in physiological doses (256). Finally, inhibition of ATP Binding Cassette Subfamily G Member 2 (ABCG2), a putative porphyrin efflux transporter, was demonstrated to significantly decrease free PPIX release from red cells to the skin in an EPP mouse model (257), and thus ABCG2 antagonists such as febuxostat (258) could potentially be used in the future to treat XLP and EPP in the future.

1.4 Terminal Erythroid Differentiation and Inflammatory Response

From Colony-Forming Units to Erythrocytes

Adult humans generate approximately 2-3 million new mature erythroid cells per second from bone marrow tissue to maintain homeostatic oxygen levels throughout the body (17). "Definitive" erythropoiesis, which follows "primitive" erythropoiesis early in embryonic development, occurs via the stepwise differentiation of hematopoietic stem cells (HSCs) in the fetal liver until birth (or three weeks postnatal birth in mice) and in the bone marrow thereafter (259,260). An exception to this is when so-called "stress erythropoiesis" occurs (e.g., due to hypoxia or inflammation) when marrow alone cannot supply a sufficient number of circulating erythrocytes. In this case, erythropoiesis in the spleen provides a bolus of new erythrocytes by synchronizing the differentiation of resident HSCs (261). Definitive erythropoiesis in bone marrow or spleen progresses from HSCs to reticulocytes, with final erythrocyte maturation occurring in circulation (Figure 9) (262). The marrow niche where erythropoiesis occurs is characterized by oxygen levels as low as 1% (263). Each stage is characterized by several cell surface markers, notably cluster of differentiation (CD) 34 (CD34) in HSCs and early differentiation, and CD36 (fatty acid translocase/platelet glycoprotein 4), CD71 (TFNR1), and CD235 (glycophorin A) late in differentiation (206,264). The proliferation and differentiation capacities of HSCs are controlled by multiple cytokines (e.g., stem cell factor (SCF), granulocyte colony-stimulating factor (G-CSF)), transcription factors (e.g., GATA1, GATA2), and cell-cell contacts (265). In addition, erythropoiesis has been associated with increases in mitochondrial biogenesis, oxidative phosphorylation, and fatty acid oxidation (266).

Differentiating HSCs give rise to two pluripotent progenitors in succession, namely the common myeloid progenitor (CMP) and megakaryocyte erythrocyte progenitor (MEP), before

beginning terminal erythropoiesis. In MEP cells, induction of *GATA1*, the so-called master transcription factor of red cell differentiation, and downregulation of *GATA2* occurs in what is known as the "GATA switch" (267). The transition from GATA2 to GATA1 involves hypomethylation of the *GATA1* promoter region, allowing GATA2 to bind and transactivate *GATA1* expression. GATA1, in turn, suppresses *GATA2* expression by displacing GATA2 from its own upstream enhancer element (268). This process is not instantaneous, as GATA1 activity does not supersede that of GATA2 until after MEP cells differentiate into the earliest erythroid-committed progenitors: burst-forming unit-erythroid (BFU-E) and colony-forming unit-erythroid (CFU-E) cells (Figure 9) (262,267,268).

Most BFU-E and CFU-E cells can be sorted from the upstream MEP population based on decreasing expression of CD34 and increasing expression of CD36 and CD71 markers (269). CFU-E is considered the first stage of terminal erythroid differentiation. Unlike BFU-E progenitors, CFU-E are unable to self-renew (270). While human BFU-E cells require approximately 14 days (7 days in mice) to form more than a thousand RBCs, CFU-E need 7 days (only 2 days in mice) to divide 4-5 times and generate 16-32 mature erythroid cells (260). Aside from GATA1, the other critical factor at this point of erythropoiesis is EPO, which promotes the survival, proliferation, and differentiation. EPO is produced in the kidney and transcriptionally upregulated there in response to hypoxia, driven by HIF2 stabilization and loss of GATA2 repressor (271). CFU-E are extremely sensitive to EPO as its cognate receptor (*EPOR*) gene is highly upregulated at this stage (Figure 9) (272). EPOR activation triggers the JAK/STAT, PI3K, and MAPK cascades responsible for propagating anti-apoptotic and differentiation signals (271,273). For example, growth arrest–specific gene 6 (Gas6) is a vitamin K-dependent protein that is synthesized and secreted by murine CFU-Es in response to Epo and acts in an autocrine

manner via Gas6 receptor (Gas6R) to enhance EpoR signaling via PI3K (274). BFU-E colony formation has also been shown by others to be dependent on EPO, though only in combination with SCF and other cytokines (269,275). Notably, during conditions of stress erythropoiesis the number of marrow CFU-E cells cannot replenish RBCs at the required rate despite higher levels of circulating EPO. In response, a large quantity of splenic HSCs differentiate simultaneously to produce more CFU-Es (269).

Immediately downstream of CFU-E progenitors are proerythroblasts (ProEBs). ProEBs are smaller than CFU-Es at 20-25 μm in humans (8-13 μm in mice) with RNA-loaded cytosol and a single nucleus that occupies ~75-80% of the cell volume (276). Human ProEB cells divide three times to yield mature erythroid cells in less than three days. ProEBs maintain high levels of CD36 and CD71 markers like CFU-E cells, but also begin expressing CD235 (206). Perhaps most significantly, CFU-Es and ProEBs associate with a central, or "nurse", macrophage (CM) which promotes terminal differentiation to the reticulocyte stage in fetal liver, postnatal bone marrow, and the spleen (277,278). This union between erythrocyte precursor and macrophage, characterized by physical attachment and various forms of cell-cell communication and metabolite transfer, forms a microniche known as an "erythroblastic island" (EBI) (276,279) (Figure 9). ProEBs are sensitive to EPO, though to a lesser extent than CFU-Es (271). GATA1 and other transcription factors such as EKLF are also required at this stage (280). The GATA switch is complete and GATA1 is required by ProEBs to avoid apoptosis (281). Paradoxically, overexpression of GATA1 at this stage blocks further differentiation, as it has been suggested that caspase-mediated degradation is involved in downregulation of GATA1 activity (267). It was later discovered by another group that EPOR signaling in ProEBs is involved in the process of regulating GATA1 and apoptosis via the hematopoietic cell kinase (HCK) (273). This work

demonstrated that phosphorylation of HCK upstream of PI3K/AKT and MAPK pathways decreases *GATA1* message levels while increasing expression of the B-cell lymphoma-extra large (*BCL-XL*) anti-apoptotic gene. As previously noted, *ALAS2* transcription is enhanced by GATA1 via a long-range loop between introns 1 and 8 (214). Murine *Alas2* is induced in the ProEB stage (205,206,282). *Alas2* expression here is required for induction of downstream heme- and globin-synthesizing enzymes, although the manner in which this occurs has been described as "sequential" (40), "biphasic" (i.e., *PPOX*, *FECH*, and globin genes are upregulated separately from the early heme synthesis enzymes and only after sufficient intracellular heme levels are reached) (132), and "simultaneous" (283) in different systems and is yet to be clarified *in vivo*.

Interestingly, exogenous ALA can stimulate terminal differentiation in MEL cells (284) but not when *ALAS2* is knocked out in these cells (132). In addition, overexpression of *hsALAS2* and ALA supplementation both rescued erythroid differentiation in MEL cells with *Abcb10* deficiency, but only the former did so in *abcb10* zebrafish mutants (285). In the mammalian liver, exogenous ALA increases the production of heme, which in turn stimulates HO-1 synthesis by binding to the BTB and CNC homology 1 (BACH1) transcriptional repressor and causing it to disengage the *HMOX1* proximal promoter region (286,287). With upregulation of ALAS2 and ALA synthesis in ProEBs, however, *HMOX1* and *HMOX2* message levels decrease ~50% (205).

ProEBs mature to basophilic erythroblasts (BasoEBs), where human *ALAS2* and heme synthesis are induced (282). BasoEBs are so named because of their similarity in color to basophils (purple-blue) with Giemsa staining, caused by the elevated concentration of ribosomes required to synthesize hemoglobin (276). BasoEBs are significantly smaller (16-18 μm in

humans, 6-11 μm in mice) than ProEBs and are the first differentiating erythroid cell to show distinct heterochromatin formation and decreased EPOR expression (Figure 9) (276,288). This observed decrease in size continues for the remainder of terminal differentiation and has been attributed to specific cyclin-dependent kinases (CDKs) identified in mouse knockout experiments (289). In addition to heme and globins, BasoEBs produce high levels of CD36, CD71, and CD235, and show increasing levels of Band 3 (SLC4A1) at the cell surface (206,276). GATA1 levels continue to decrease here as they do throughout the rest of terminal maturation (267,273).

In mice and humans, globin synthesis lags behind heme synthesis (78,205). It is widely believed that the delay in globin production is due to the requirement for sufficient heme to bind BACH1 repressor at the β-globin locus control region (LCR) and activate globin synthesis, much in the same manner *HMOX1* transcription is stimulated by heme in nonerythroid tissues (290). Two mechanisms have been identified that may mitigate free heme synthesis and the associated oxidative stress when heme and globin levels are disproportionate: 1) excess heme is exported via feline leukemia virus subgroup C receptors 1a (plasmalemmal FLVCR1) and FLVCR1b (mitochondrial) (291,292), and 2) the previously mentioned HRI protein negatively impacts general translation until sufficient heme levels are sensed (217).

BasoEBs differentiate to polychromatophilic (or polychromatic) erythroblasts (PolyEBs). PolyEBs are 12-15 μm and 5-8 μm in human and mouse cells, respectively, and display large clusters of heterochromatin, as well as a pink-tinted cytoplasm (for which they are named) due to accumulating hemoglobin (Figure 9) (276). CD36, CD71, and CD235 remain abundant, and Band 3 levels continue to increase (206). In mice, the formation and differentiation of PolyEBs

is enhanced by G-CSF, which has also been shown to act synergistically with EPO to improve myelodysplastic syndromes (293).

In the final cell division of erythropoiesis, PolyEBs differentiate to orthochromatophilic (or orthochromatic) erythroblasts (OrthoEBs). OrthoEBs are the smallest red cell progenitors (10-15 μm in humans, 8-13 μm in mice) and the last to contain nuclei, which are at this point are filled with aggregates of heterochromatin (Figure 9) (276). In addition, the orthoEB cytosol has the coloration of eosinophils (bright pink) with Giemsa staining due to the extremely high levels of hemoglobin. CD71 levels begin to decline, while those for Band 3 increase further (206). Expulsion of the pyknotic orthoEB nucleus results in the formation of two species, the pyrenocyte (nucleus surrounded by a thin layer of cytoplasm and plasma membrane) and the reticulocyte (Figure 9) (262). The process of enucleation is a complex process involving microtubule and membrane reorganization that is specific to mammals (260,294). Once extruded, pyrenocytes present phosphatidylserine on their cell surface and are subsequently consumed by the of the erythroblastic island (pyrenophagocytosis) (295). Nascent reticulocytes are only 8-10 μm in humans and 6-8 μm in mice and are named for the net-like (reticular) appearance of ribosomal RNA aggregates with staining. Reticulocytes spend approximately 48 additional hours in the marrow undergoing autophagy (and mitophagy), exocytosis, and further membrane remodeling as they clear organelles and change their cell morphology from multilobulated to a biconcave disc (260). Reticulocytes enter blood circulation via pseudopods that penetrate the marrow capillary walls (296), a process which is promoted by G-CSF (297).

Mature mammalian erythrocytes (RBCs) develop from reticulocytes ~24-48 hours after entering circulation (276). The unique anchoring of an elastic network of cytoskeletal proteins to the cholesterol-phospholipid bilayer permits the mature erythrocyte to distort shape as needed

during their repeated passaging through narrow blood capillaries (298). The average lifespans of circulating mouse and human RBCs are 45 and 120 days, respectively (260). With age, RBCs progressively lose surface area and volume but maintain hemoglobin content. When changes such as the Band 3 surface marker occur (299), splenic macrophages ingest and clear the senescent RBCs as part of the reticuloendothelial system (260). Notably, the main function of the RBC is to transport oxygen and carbon dioxide gases to and from tissues peripheral to the alveolar capillaries of the lung, respectively. In short, oxygen molecules (O_2) bind to axial iron positions among the four hemes in erythrocyte hemoglobin with homotropic positive cooperativity at pH 7.4 in the lungs (Bohr effect) (300). Increasing carbon dioxide (CO_2) and decreasing pH in peripheral tissues result in carbamylation of the free hemoglobin amino groups and protonation of specific globin residues, respectively, both of which promote oxygen dissociation via stabilization of the deoxygenated tertiary and quaternary structures of hemoglobin by salt bridge formation (301). Increasing pH and oxygen levels upon return of the RBC to the pulmonary capillaries disrupts the salt bridge interactions and promotes O_2 binding and the release of CO_2 gas for exhalation (Haldane effect) (302,303).

The Erythroblastic Island

The erythroblastic island (EBI) is a niche found in mammalian fetal liver, postnatal bone marrow, and the spleen consisting of a CM surrounded by 5-48 developing erythroblasts, from CFU-E/ProEBs to immature reticulocytes (277,278,304). Scanning electron microscopy (SEM) of rat bone marrow illustrates the EBI with intimate cell-cell contacts between erythroblasts and the CM (Figure 9) as well as among the erythroblasts themselves (305). Histological work in human marrow depicts the EBI as a rosette in which each erythroblast maintains close contact with the CM cytoplasm (306). Whether EBIs are essential for normal erythropoiesis, however, is

not clear. For example, one mouse study involving the depletion of the $CD169^{+}$ macrophages by diptheria toxin showed a reduced number of erythroblasts but no anemia (307). Other *in vivo* experiments in which marrow and splenic CM levels were reduced by chemical means showed decreased blood and cellular hemoglobin levels without effect on RBC counts, though responses to stress erythropoiesis were negatively impacted and polycythemia RBC numbers were normalized (308). Interestingly, other studies indicate that the treatment of mice and humans with the G-CSF cytokine diminishes marrow macrophage levels and increases the number of ProEBs and/or decreases reticulocyte and RBC counts (309,310). However, these effects were not observed in the mouse spleen, as EBI formation and erythropoiesis were actually enhanced there by G-CSF (309).

CMs are a heterogeneous population of macrophages that invariably express only a handful of cell surface markers, including CD163, CD169 (sialoadhesin), and vascular cell adhesion protein 1 (VCAM1) (Figure 9) (262,311). Recent SEM experiments on rodent marrow show two distinct morphological classes of EBIs, identified as “flat” or “domed” based on the appearance of the CM (312). The “flat” classification embodies the classic depiction of the EBI, wherein cytoplasmic arms from the CM extend and envelope the red cell precursors. Unlike splenic macrophages, the CM does not phagocytose entire erythroid cells in unperturbed systems (276). Beyond these observations, little known about the mammalian CM phenotypes and how distinct they are from the other, more well-defined macrophage lineages.

Developing erythroblasts communicate with CMs on multiple levels. For example, cell-cell contact is mediated by protein interactions, notably erythroblast integrins and macrophage VCAM1 (313), erythroblast intercellular adhesion molecule 4 (ICAM4) and macrophage integrins (314), and erythroblast macrophage proteins (EMPs) present on both erythroblast and

macrophage cell surfaces (Figure 9) (315). Of these, only EMP has been shown to be dispensable for normal erythropoiesis (316).

In addition to direct physical contacts, several other interactions have been identified between erythroblasts and CMs in the EBI and linked to the process of red cell differentiation. The first and perhaps most important is iron delivery (276). *In vivo* data suggest that iron for heme synthesis in mammalian erythrocyte precursors is provided solely by diferric transferrin (holo-TFN) and internalized for use via TFNR-mediated endocytosis and direct endosomal transfer to mitochondria (157,162,163). Clinically, patients with atransferrinemia suffer hypochromic microcytic anemia (317). However, *in vitro* experimental evidence suggests that ferritin is an alternative source of iron for developing erythroid progenitors that involves the CM. Specifically, co-cultures of human peripheral macrophages and erythroblasts have demonstrated ferritin synthesis and exocytosis by the macrophages in TFN-free media (318). In a separate and much earlier work, erythroblasts were able to take up iron-loaded ferritin via micropinocytosis (319). While integration of these data provides a putative model for erythroblast iron acquisition in the EBI, the systems in which the data were collected lacked key systemic iron regulators such as hepcidin and erythroferrone. Briefly, hepcidin is a cysteine-rich peptide that diminishes systemic iron levels by inhibiting iron absorption from the gut and release from the liver and macrophages (320). Hepcidin also binds the iron transporter ferroportin (FPN), inducing its subsequent endocytosis and degradation and systemic iron deficiency. ERFE is an erythroblast-derived hormone that inhibits hepcidin mRNA and protein synthesis but is apparently only a significant player during stress erythropoiesis (321). Without such key iron regulators accounted for *in vitro*, ferritin transfer from CMs to developing erythroblasts may simply be artificial and irrelevant *in vivo* (279).

Perhaps the best described impacts of CMs on terminal erythropoiesis involve the essential processes of pyrenocyte engulfment (pyrenophagocytosis) and destruction (pyrenocytolysis) following the formation of immature reticulocytes. Pyrenophagocytosis is initiated by the display of phosphatidylserine ("eat me" signal) on the surface of pyrenocytes, which is subsequently recognized by the CM receptors T-cell immunoglobulin mucin protein 4 (TIM4) (322) and c-mer proto-oncogene tyrosine kinase (MERTK) (323). Interestingly, CMs do not phagocytose nucleated erythroblasts except in cases of hemophagocytic lymphohistiocytosis (276). Pyrenocytolysis was first observed in transgenic mice expressing a green fluorescent protein (GFP)-histone fusion protein, which was degraded within fetal liver CMs following phagocytosis (324). Pyrenocyte heme contained within the thin cytoplasmic layer surrounding the nucleus is believed to be metabolized by HO-1 in the CM. Mice with decreased *Hmox1* expression have dysfunctional EBIs exhibiting an abnormally domed morphology and interacting with only a limited number of erythroblasts (325). Finally, it has been suggested that CM heme may be transported to (and perhaps recycled to) developing red cells in EBIs (279). Studies have shown that macrophages export heme via FLVCR1a (291,292) and that erythroblasts express heme-responsive gene 1 (HRG1) (326), a plasmalemmal heme transporter. However, *in vivo* evidence is currently lacking as models such as an FLVCR1a knockout mouse are not yet available (279).

The most recently described erythroblast-CM interaction involves EPOR (327,328). More specifically, EPOR has been found to be expressed in more than 90% of CMs, and EPO treatment increases the number of erythroblasts interacting with CMs in the EBI (327). As previously established, CFU-E/ProEBs in EBIs express EPOR and the response to EPO impacts GATA1 and other differentiation factors (272,273). Thus, it can be hypothesized that EPO,

widely used in the treatment of anemia, increases red cell counts by affecting both progenitor cell differentiation and the physiological integrity of the EBI niche.

Finally, soluble factors such as Gas6 (274), insulin-like growth factor 1 (IGF1) (329), and the FAS ligand (FASL) also regulate erythroid differentiation in EBIs. In particular, Gas6 is produced and secreted by both murine erythroblasts and CMs and enhances EPO effects by autocrine and paracrine signaling mechanisms (274). In humans, IGF1 is synthesized in CMs and promotes BFU-E and CFU-E growth in the early stages of EBI-facilitated erythropoiesis (329). The FAS transmembrane glycoprotein "death" receptor is expressed in all developing erythroblasts during terminal differentiation, but FASL is synthesized and secreted only by orthoEBs (278). Interestingly, FASL-activated caspase activity promotes both apoptosis and differentiation at basal EPO levels in mammals (330).

Anemia of Inflammation

Anemia is defined by a decrease in RBC count, hemoglobin, or hematocrit (i.e., volume of packed RBCs). Anemia of inflammation (AI), also known as anemia of chronic disease (ACD), is most commonly caused by infections, autoimmune diseases, cancer, or chronic kidney disease (CKD) (331). ACD is second only to iron-deficiency anemia (IDA) as the most common form of anemia (332), where both AI and IDA patients are hypoferremic and exhibit symptoms of fatigue, inability to tolerate exercise, and decreased cognitive function (331). ACD demonstrates as either normochromic normocytic or hypochromic microcytic anemia, the latter of which is observed in IDA (333). Two serological parameters, however, distinguish ACD from IDA: serum ferritin (high in ACD but low in IDA) and serum transferrin (low in ACD, high in IDA) (331). ACD develops following a systemic acute-phase reaction to infection that results in elevated levels of numerous inflammatory cytokines, complement factors, and small

molecules associated with an immune response (331). These endogenous substances make up part of a general host defense strategy to limit iron and/or heme iron in order to stunt the propagation of pathogens or malignant cells by so called "nutritional immunity" (334,335) and to decrease iron/heme-associated ROS in inflamed tissues (336). Moreover, there is an inverse relationship between hemoglobin levels and established markers for inflammation (i.e., erythrocyte sedimentation rate (ESR) and C-reactive protein (CRP)) in disease states such as rheumatoid arthritis (RA) (337).

ACD pathogenesis is complex but can be characterized by decreased erythroid survival rates and diminished erythropoiesis (Table 2) (331). For example, tumor necrosis factor alpha (TNFα) been shown to enhance erythrophagocytosis in the spleen and the liver and hence decreasing average erythrocyte lifespan (322). TNFα and other cytokines negatively affect early and terminal erythroid differentiation, both before and after EBI formation (262,331) (Figure 9). While a complete analysis of inflammatory cytokines and their modes of action during erythropoiesis is beyond the scope of this dissertation, the effects of TNFα, interferon gamma (IFNγ), interleukin 1-beta (IL1β), interleukin 6 (IL6), and interleukin-10 (IL10) will be discussed. Each of these factors is produced and secreted by activated leukocytes, including macrophages, and negatively impact the spectrum of erythroid differentiation (262). TNFα, IL1β, and IFNγ are characterized as type I proinflammatory cytokines and are active at the outset of infection. However, IL6 is a type II proinflammatory cytokine that is most impactful later in the response (both type I and type II are considered acute-phase factors). On the other hand, IL10 is categorized as anti-inflammatory cytokine. IL10 is usually involved in the resolution of the acute phase, but is known to be a source of pathogenesis in underlying ACD disorders such as irritable bowel syndrome (IBS) (338). Upstream of EBI assembly, IFNγ impairs CMP

development in mice by inducing synthesis of the PU.1 transcription factor in these cells and diverting them toward the myeloid lineage (339). TNFα, produced mainly in macrophages via toll-like receptor 4 (TLR4) stimulation (340), also negatively affects erythropoiesis prior to CFU-E and EBI formation (341). This cytokine has been linked with decreased BFU-E colony formation in RA, likely by inducing pro-apoptotic signals via its cognate receptor, TNFR (342). Interestingly, anti-IL6 antibody treatment of RA cells *in vitro* stunts differentiation at the BFU-E stage, indicating that IL6 is stimulatory at this point unless masked by other cytokines (e.g., TNFα) *in vivo* (337).

During terminal differentiation, cytokines are supplied to EBIs by plasma seeping into the marrow as well as by immunoactivated CMs within EBIs themselves. The phenotypes of CMs before and after immune stimulation by antigens like lipopolysaccharide (LPS), the classic proinflammatory trigger found in the outer membrane of invading Gram-negative bacteria, have remained elusive. Traditionally, macrophage phenotypes have been designated as naïve (M0), proinflammatory (M1), or anti-inflammatory (M2). However, the unperturbed CM population is heterogeneous in nature, as evidenced by an array of cells surface markers and shapes (276,311). One model of CMs derived from human $CD34^+$ cells has an M2c-like phenotype (343). Classically-activated M1 macrophages produce and secrete the proinflammatory TNFα, IL1β, and IL6 cytokines (but not IFNγ). M2 macrophages are sources of anti-inflammatory cytokines, including IL10. All of these M1 and M2 cytokines are known to be generated in activated CMs as well (Figure 10) (262,278).

Inflammatory cytokines negatively impact terminal erythropoiesis at many levels. *In vivo*, diminished red cell differentiation in the EBI starts with the restriction of EPO supply from the kidneys by TNFα and IL1β (262). These cytokines both block renal EPO synthesis by

enhancing GATA1, GATA2, and nuclear factor kappa-light-chain-enhancer of activated B cells (NFκβ) (344,345). NFκβ is an established proinflammatory signaling factor that binds the *EPO* promoter region and represses EPO transcription. IFNγ directly antagonizes CFU-E differentiation by downregulating EPOR synthesis (346) and promoting FAS receptor expression (347). In addition, IFNγ stimulates macrophage and erythroblast synthesis and secretion of TNF-related apoptosis-inducing ligand (TRAIL), which slows erythroid differentiation via the MAP/ERK signaling pathway and ultimately diminish the production of orthoEBs (262,348). INFγ has also been shown to impede CFU-E colony formation by a ROS-induced, caspase-dependent mechanism, though this was only observed in peripheral blood cultures and not the marrow (349). In the EPO-sensitive human TF-1 erythroid cell line, IL6 treatment disrupts mitochondrial integrity and diminishes hemoglobinization and terminal erythropoiesis without any impact on message levels of heme synthesis enzymes or globins (350). EPO-independent inhibition of differentiation has been observed in MEL cells (ProEB models) when treated with conditioned media from LPS-stimulated RAW264.7 cells (an immortalized murine macrophage line) (351). This work specifically showed that MEL cell hemoglobin levels decrease with increasing activated macrophage media in a dose-dependent manner.

The signature systemic response to infection is to limit iron, including heme iron, putatively to deprive invading pathogens and/or to avoid complicating inflammation-derived ROS production (334,336). Factors such as LPS and associated proinflammatory cytokines IL1β and IL6 contribute to systemic iron deprivation by diminishing *TFN* expression in the liver (331). TNFα, IL1β, IL6, and IL10 stimulate iron sequestration in macrophages by upregulation and exocytosis of ferritin (318), as well as enhancement of *DMT1* expression and the associated process of TFNR-driven endocytosis in these cells (352). Most notably, IL6 upregulates the

synthesis of the acute-phase peptide hepcidin, the “master regulator of iron homeostasis”, in the liver and macrophages (353) and reportedly contributes to ACD in rheumatoid arthritis (354) (Figure 9). Hepcidin blocks the export of iron from the gut, liver, and macrophages by binding and degrading FPN in these tissues (320). ERFE produced in erythroblasts could neutralize hepcidin activity in the EBI, as has been established in stress erythropoiesis (321). However, ERFE synthesis requires strong EPOR signaling usually absent in ACD patients. In addition to restricted EPO from the kidney, hepcidin-mediated intracellular iron loss via TfnR2 (but not TfnR1) catabolism has been shown to negatively impact EpoR cell surface localization in mice (355).

Iron sequestration is detrimental to terminal erythroid differentiation and hemoglobin production because iron is required for chelation of PPIX to form heme. Early ferrokinetic experiments in rats point to decreased functional TFNR in erythroid progenitors during infection (356), likely due to decreased EPO levels (357) that derail increased (63) or unaltered (225) TFNR synthesis observed during normal differentiation. ALAS2 levels may also be diminished via the IRE-IRP system in inflammatory disease states demonstrating hypoferremia. In addition, nitric oxide (NO) may further activate the IRE-IRP system because NO from NO synthase (NOS) expressed in immunostimulated macrophages (358) can activate IRP1 (359) and IRP2 (360) and thus indirectly inhibit hsALAS2 translation (361). The FECH Fe-S cluster is also susceptible to NO-associated destabilization (362), and so NO may also facilitate coordination of porphyrin and iron supply during an inflammatory response, as shown in rat liver overexpressing NOS2 (363). However, the IRE-IRP and NOS systems may not be relevant across the temporal spectrum of terminal erythroid differentiation or inflammation (225,231,364) and so another acute-phase factor could be involved in limiting ALA synthesis as well. In LPS treated mice,

terminal erythropoiesis is effectively blocked at the ProEB/BasoEB level (365), coincidentally the point at which ALAS2 synthesis is induced. Several investigations have previously indicated that unimpaired ALAS2 activity is essential for complete erythropoiesis (132,283,366,367). In particular, differentiated MEL cells (132) and murine embryonic stem (ES) cells (283) lacking *ALAS2* showed stunted hemoglobin synthesis and erythroid differentiation. A zebrafish XLSA model (*sau*) with mild Alas2 deficiency (i.e., no iron overload/ring sideroblasts) demonstrates delayed erythropoiesis and aberrant RBCs with greater mean corpuscular volume (MCV) and less aggregated chromatin than their wild-type counterparts (366). Primitive and definitive differentiation of *Alas2*-null mouse embryos and adult mice chimeric for *Alas2*-null cells, respectively, were also negatively impacted despite the differential effects of iron in these animals (367). Perhaps most importantly, bone marrow aspirates and purified erythroblasts from RA patients show loss of ALAS2 activity without any alterations in FECH activity (368) or cellular iron supply (369,370).

Strategies used to counter the innate and chronic immune responses to inflammation include the use of erythropoiesis-stimulating agents (ESAs) and iron regulatory therapies (331). The potential benefits of recombinant EPO and oral or intravenous (IV) iron to ameliorate anemia in ACD are straightforward. Recent approaches to control iron levels involve antagonists of hepcidin and IL6 production (371). Application of positive modulators of ACD such as Gas6 and ALA also holds promise. Overexpression of Gas6R and Gas6, which synergizes with EPO in the EBI milieu to stimulate survival and differentiation, has been shown to diminish inflammatory TNFα, IL1β, IL6, and IL10 cytokine synthesis in murine bone marrow-derived macrophages (BMDM) (274). With similar results, ALA treatment of RAW264.7 cells induced HO-1 synthesis and subsequently inhibited the production of NO, TNFα, IL1β, and IL6 (372).

ALA has also been used in photodynamic therapy (PDT) to ablate tumor cells for decades and so may be particularly useful in treating ACD stemming from cancers (373).

1.5 Itaconic Acid

Industrial Building Block and Antimicrobial Agent

Itaconic acid (methylenesuccinic acid) is an unsaturated dicarboxylic acid with implications in both industrial technology and eukaryotic biochemistry. Itaconic acid was first produced from the distillation of citric acid in 1836 and a few years later the decarboxylation of *cis*-aconitic acid, from which its name is derived as an anagram (374). Since 1932, itaconic acid has been isolated from several filamentous fungi, the first identified as *Aspergillus itaconicus* (375). Itaconic acid serves these organisms as an antibiotic compound (376). Today, itaconic acid has become a key industrial building block due to its reactive methylene group and associated ability to participate in many chemical transformations, including polymerizations (377). The global industrial production of itaconic acid is currently about 80,000 tons annually (sold at ~$1 per pound) and could more than double over the next five years (378). Unlike its fossil fuel analogs acrylic and methacrylic acids, itaconic acid is currently mass produced from *Aspergillus terreus* (379) and constitutes a "green" alternative to petroleum feedstocks. Less than a decade ago, itaconic acid was also found to be an important mammalian metabolite synthesized by macrophages during the innate inflammatory response (380,381). In addition to its role as an antimicrobial agent, itaconic acid (or itaconate, the dianionic form at physiological pH) has demonstrated immunological functions akin to the cytokines correlated with its synthesis (382).

Itaconic acid is capable of participating in homo- (forming polyitaconic acid) and heteropolymerizations by free-radical and condensation reactions to produce plastics, resins, and fibers (374). In 1945, the Pfizer Co. was the first to patent the fermentation process of *A. terreus* to produce itaconic acid on an industrial scale (383). The current manufacturing process involves batch fermentation of *A. terreus* at 37ºC with glucose or pretreated starch as substrates under aerobic, acidic, and phosphate-limiting conditions, generating up to 86 g/L culture (374,384,385). Large-scale aeration requires high energy investments but is necessary to maintain mycelia integrity, adequate ATP production, and oxidation of NADH, an inhibitor of the glycolytic and TCA cycle enzymes required for the generation of itaconic acid from glucose (374). *A. terreus* synthesizes itaconic acid from cis-aconitic acid, a TCA cycle intermediate that is exported from the mitochondria to the cytosol where cis-aconitic acid decarboxylase (CAD) catalyzes the conversion and releases carbon dioxide (386,387). The *A. terreus CAD1* gene contains two exons and encodes for a 490-amino acid, 55-kDa monomeric protein. Interestingly, itaconate inhibits the growth of *A. terreus* and thus limits product yield (388,389). Genetically-modified strains of *A. terreus* that generate more itaconate and are less sensitive to this form of feedback inhibition are typically used in industrial applications (374,390).

The antimicrobial properties of itaconic acid are associated with its ability to inhibit three important metabolic pathways in bacterial pathogens: the glyoxylate shunt, the methylcitrate cycle, and the citramalate cycle (374). The glyoxylate shunt circumvents two steps of acetyl-CoA decarboxylation in the TCA cycle and instead converts isocitric acid directly to succinic acid and glyoxylic acid by isocitrate lyase (ICL), where glyoxylic acid is further metabolized to malic acid by malate synthase. This two-for-one payoff (i.e., succinic acid and malic acid molecules are generated from one isocitric acid molecule) allows pathogens such as

Mycobacterium tuberculosis (391,392) and *Salmonella enterica* (393) to shift the carbon source for the TCA cycle to odd-chain fatty acids and cholesterol when glucose levels are low. Itaconic acid inhibits ICL activity by acting as a competitive inhibitor for the succinic acid product and subsequently reduces the proliferation rate of the invading species (394). Notably, the ICL enzyme is functional in microbes including fungi but does not appear to play a role in vertebrate metabolism, making it a putative drug target (374,395).

Itaconic acid has also been shown to downregulate the methylcitrate cycle and citramalate cycles in *M. tuberculosis* (392) and *Rhodosprillum rubrum* (396), respectively. The methylcitrate cycle is essential in *M. tuberculosis* because it is required for propionyl-CoA detoxification via TCA cataplerosis (oxaloacetate) and anaplerosis (succinic acid and pyruvic acid) (397). Itaconic acid inhibits methylisocitrate lyase (MCL) and the associated catabolic conversion of methylisocitric acid to pyruvic acid and succinic acid (374). According to another study (392), the growth of *M. tuberculosis* during macrophage infection is curbed significantly by host-derived itaconate due to its negative impacts on both ICL and MCL proteins. The citramalate cycle is an anaplerotic pathway for acetate assimilation and involves carboxylation of propionyl-CoA to methylmalonyl-CoA via propionyl-CoA carboxylase (PCC). Evidence that itaconate inhibits PCC has been obtained from *R. rubrum*, which lacks ICL but not MCL (396). Contrary to work on *M. tuberculosis*, this study showed that the growth of *R. rubrum* is unimpeded by itaconate, possibly due to secretion or metabolism of the itaconate.

Itaconate may act also as an endogenous antimicrobial agent by deactivating host B_{12} and depriving invading species of this essential nutrient (398,399). *M. tuberculosis* is known to scavenge B_{12} from its host (400) and to be less active in patients suffering from B_{12} deficiency disorders (401). Recent work (399) has provided a viable explanation for the latter observation.

Briefly, immunoactivated macrophages synthesize itaconate (Figure 10) and its CoA derivative, itaconyl-CoA, which effectively traps the naturally-occurring B_{12} radical by suicide inhibition. As a result, growth of invading *M. tuberculosis* is significantly reduced by itaconyl-CoA inactivation of host B_{12} (398) as well as direct itaconate inhibition of pathogen ICL and MCL enzymes (392).

Unsurprisingly, some pathogens have evolved detoxification mechanisms for itaconate (402). In *Pseudomonas aeruginosa* and *Yersinia pestis*, itaconate is metabolized in a three-step process catalyzed by separate enzymes encoded in nonhomologous operons (402,403). In certain *Pseudomonas* and *Salmonella* species, itaconate detoxification occurs as follows: 1) itaconate is converted to itaconyl-CoA by an itaconyl-CoA transferase, 2) itaconyl-CoA is hydrated to (*S*)-citramalyl-CoA by itaconyl-CoA hydratase, and 3) (*S*)-citramalyl-CoA is cleaved to yield acetyl-CoA and pyruvate by (S)-citramalyl-CoA lyase (403). Notably, itaconyl-CoA has two isomers, 2-methylenesuccinyl-CoA and 3-methylenesuccinyl-CoA, the latter of which is regarded as the biologically active form. In *Y. pestis*, the ripABC operon codes for an itaconyl-CoA transferase (RipA), an itaconyl-CoA hydratase (RipB), and an (S)-citramalyl-CoA lyase (RipC) (402). Importantly, an analogous metabolic pathway has been proposed for itaconate metabolism in mammals (404,405) (Figure 11), though not all enzymes required for this process have been verified.

Mammalian Metabolism

The first publication identifying itaconate as a mammalian metabolite dates back to the late 1930s, when it was shown that itaconate could be generated from methylated four-carbon dicarboxylic acids unable to undergo fatty acid oxidation due to the methyl group at the β-position (406). This seminal study concluded that itaconate is only a transient intermediate and

rapidly degraded, as it was not detected in urine from animals. In 1947, an investigation on the effects of oral and IV administration of various itaconate salts on adult feline metabolism revealed that itaconate is a relatively inert species, with no systemic toxicity and little impact on RBC profiles in these animals in doses up to 1 g/kg (407). In 1949, it was discovered that itaconate inhibits succinate dehydrogenase (SDH), a TCA cycle enzyme and Complex II of the electron transport chain (ETC) in a competitive manner (408). Two years later, diminished growth rates of weanling rats fed itaconate-loaded chow were attributed to this inhibitory action of itaconate on succinate oxidation, as these animals demonstrated increased urinary excretion of succinate (409).

In the late 1950s and early 1960s, another group provided evidence that itaconate is oxidized in guinea pig liver mitochondria like other TCA-cycle intermediates such as succinate, fumarate, and malate despite lacking a hydrogen at the β-position and inhibiting SDH (404). This group further showed that isolated mammalian liver mitochondria could metabolize itaconate in a similar manner to *Pseudomonas* and *Y. pestis* in the presence of Mg^{2+}, ATP, and CoA: 1) itaconate to itaconyl-CoA by SCS; 2) itaconyl-CoA to citramalyl-CoA by methyl glutaconase (MGTK, or methylglutaconyl-CoA hydratase); and 3) cleavage of citramalyl-CoA to acetyl-CoA and pyruvate by citramalyl-CoA lyase (CYLBL) (398). It is worth mentioning here that despite the production of itaconyl-CoA in liver mitochondria with ATP, MgCl2, and CoA addition (404), there is still no direct evidence for SCS catalysis of this process. Speculatively, there may be other requirements such as SCS protein partners (73,410), assumed to be conserved in whole mitochondria, that must be in engaged in order for SCS to metabolize itaconate to itaconyl-CoA. Alternatively, another CoA transferase, succinyl-CoA:glutarate-CoA transferase (SUGCT) (encoded by the *C7ORF10* gene) has been found in human liver and other tissues

(411) and is capable of metabolizing itaconate to itaconyl-CoA *in vitro* using glutaryl-CoA or succinyl-CoA as substrate (412).

Interest in itaconate metabolism in mammals subsequently waned until the last decade, after itaconate was found in lung tissue of mice infected with *M. tuberculosis* (413). Around the same time, it was discovered that murine macrophages polarize to the M1 phenotype by LPS-activated Tlr4 receptor and, like *A. terreus*, produce itaconate via the decarboxylation of *cis*-aconitate from the TCA cycle (380). A metabolomics study further showed that itaconate generated in LPS-induced RAW264.7 macrophage models is secreted and accumulates in the growth media (381). Seminally, another group reported that immunoactivated RAW264.7 macrophages synthesize itaconate from *cis*-aconitate in the mitochondria and effectively break the TCA cycle using aconitate decarboxylase (Acod), or immune-responsive gene 1 (Irg1) protein (392). In this same study, it was determined that *Irg1* transcription in these cells is massively upregulated shortly after LPS treatment and results in up to 8 mM intracellular itaconate within 10 hours of infection, presumably to enlist its antimicrobial properties.

From this point, numerous studies have evolved and further described the role of itaconate as both a pro- and anti-inflammatory agent during the acute-phase of an inflammatory response. Initially, proinflammatory macrophages exhibit a Warburg-like phenotype, attenuating oxidative phosphorylation (OXPHOS) and promoting aerobic glycolysis to provide sufficient ATP for biogenesis (414). Concomitantly, succinate levels increase, resulting in murine Hif1α stabilization via succinate-mediated product inhibition of prolyl hydroxylase domain (PHD) enzyme in the cytosol. Hif1α subsequently enhances the transcription of IL1β, among other proinflammatory targets (415). Increased oxidation of accumulating succinate by SDH in the mitochondria is a major source of ROS, another marker of M1 macrophage polarization, by

reverse electron transport (RET) through Complex I (416). Surprisingly, itaconate appears to counter this action of succinate despite being at least partially responsible for its accumulation by decreasing SDH activity. Itaconate inhibition of SDH (K_i = 0.22 mM, succinate K_m = 0.29 mM) (417) hypothetically abrogates RET-driven ROS accumulation by blocking succinate oxidation (418). The SDH inhibitor dimethyl malonate prevented RET-driven ROS formation and brain injury during reperfusion in a mouse ischemia model (419), suggesting that itaconate may have a similar effect (Figure 10). In addition, RA model mouse tissue and human fibroblast cells accumulate measurable itaconate only in the presence of TNFα and the proinflammatory state (420), while immunoactivated murine *Irg1*$^{-/-}$ BMDM treated with dimethyl itaconate (cell-permeable form of itaconate) sustain decreases in proinflammatory factors Hif1α, Il1β, Il6, and NO (417). A caveat of the latter study is that dimethyl itaconate is not de-esterified to itaconate in LPS-activated macrophages (421) and participates in enhanced and perhaps nonphysiological itaconate biochemistry such as cysteine modification due to its strong electrophilic character (422).

Subsequent studies (422-425) have elucidated alternative mechanisms by which itaconate modulates oxidative stress. For example, itaconate has been shown to allosterically inhibit liver fructose-6-phosphate 2-kinase (F6P2Kinase), or phosphofructokinase 2 (PFK2) (425), part of a bifunctional enzyme complex with fructose bisphosphatase 2 (FBPase2). Here itaconate allosterically inhibits PFK2 and slows glycolysis, putatively shunting glucose-6-phosphate through the pentose phosphate pathway and diminishing ROS formation via NADPH and glutathione production (426). Dimethyl itaconate and 4-octyl itaconate (a cell-permeable form of itaconate that is metabolized to itaconate in activated macrophages) decrease ROS in murine LPS-stimulated BMDMs by stimulating production of nuclear factor erythroid 2–related factor 2

(Nrf2) and its downstream target, *Hmox1* (423). More specifically, tandem mass spectrometry experiments have inferred that itaconate alkylation (i.e., itaconylation) of Kelch-like ECH associated protein 1 (Keap1) cysteine residues by Michael addition reduces Keap1-Nrf2 binding and proteosomal degradation of Nrf2 in mice. The same study further revealed that augmentation of the Nrf2 signaling pathway downregulates the production of Il1β, interferon beta (Ifnβ), and ultimately itaconate itself, as Ifnβ was shown to enhance *Irg1* expression. Interestingly, more recent work describes a similar mechanism in models of mammalian liver reperfusion, wherein the upregulated IRG1 stimulates the itaconate-KEAP1-NRF2 axis during recovery and decreases synthesis of proinflammatory cytokines such as IL6 (424). Data from another group further verify the anti-inflammatory impact of itaconate in mice via Keap1-mediated oxidative stress, but at the same time infer that endogenous itaconate and its esterified derivatives downregulate the Iκβζ transcription factor and the associated secondary inflammatory response (follows initial Tlr4 induction of factors such as Tnfα and Nfκβ) independent of the Nrf2 signaling pathway (422). Instead, Iκβζ protein and its known *Il6* gene target (427) were found to be negatively impacted by itaconate through activating transcription factor 3 (Atf3). In contrast to its effect on Nrf2-mediated responses, dimethyl itaconate inhibition of Iκβζ activity was positively correlated with cellular ROS levels, putatively due to the inactivation of GSH by alkylation of its cysteine moiety (422).

Looking beyond redox implications during macrophage inflammation, one study sought to elucidate the impact of itaconate metabolism on cellular biogenesis (418). Unlike the results from more than 50 years previous (404,405), this group found that itaconate could not support respiration and that its reported oxidation may have been an *in vitro* artifact. Instead, itaconate facilitates the Warburg-like shift in metabolism from mitochondrial OXPHOS to aerobic

glycolysis by blocking substrate-level phosphorylation (SLP) in murine BMDMs. Whether the observed abrogation of SLP and succinyl-CoA metabolism was due to succinate increases attributable to SDH inhibition by itaconate (428) or anaplerosis via glutamine or the GABA shunt has not been resolved. In agreement with the older data (404,405), the possibility that itaconate is converted to itaconyl-CoA, a veritable "CoA trap" that consumes ATP and decreases upstream succinyl-CoA synthesis in the TCA cycle (Figure 11), may also provide an explanation for decreased SLP during inflammation (418). Other recent studies suggest that itaconyl-CoA can also impact the odd-chain fatty acid oxidation and metabolism of the essential pathogen nutrient B_{12} in adipose tissue and inflamed macrophages (398,399). More specifically, itaconyl-CoA was shown to enhance homolytic cleavage of the B_{12} cobalt-carbon bond and subsequent formation of a B_{12}-itaconyl-CoA adduct within the active site of methylmalonyl mutase (MUT), irreversibly inhibiting MUT and depleting the host macrophages of functional B_{12} (Figure 11). The predicted consequence is toxic propionyl-CoA/propionate accumulation and stunting of cholesterol-dependent growth of pathogens such as *M. tuberculosis* (399). This process is reportedly exacerbated by citrate lyase beta-like (CLYBL) protein deficiency (398). Notably, the associated accumulation of methylmalonic acid and propionate would be matched by decreases in the MUT product succinyl-CoA, perhaps explaining another route by which SLP could be diminished.

The intercellular implications of itaconate in mammalian cell physiology are also worthy of discussion here. It is well known that itaconate accumulates within cells at up to millimolar levels via IRG1 (392,428). An early metabolomics study on LPS-stimulated macrophages (381) revealed that itaconate is secreted by these cells as well. More recently, itaconate was shown to increase in the media to only 5-10 μM over the same time period intracellular accumulations

reached 5-10 mM in RAW264.7 and murine BMDM cultures (429). In addition, metabolomic tracing experiments have revealed that itaconate can be imported by mammalian cells (398), including polarized macrophages (430), but that this is a slow process (421). Large differences between intracellular and extracellular itaconate imply that passive diffusion could be the only mode of transport. *In vitro* studies have revealed that itaconate serves as an alternative substrate for murine mitochondrial dicarboxylate transporters such as Slc25a10 (cognate succinate transporter), Slc25a11 (α-ketoglutarate), and Slc25a1 (citrate) (423). Transport across the cell membrane via their plasmalemmal counterparts, Slc13a3, Slc13a5 (or a plasmalemmal isoform of Slc25a1), and Slc13a2, respectively, is therefore plausible though data supporting such promiscuity remain elusive. The apparently sluggish transport of itaconate likely explains the inability to detect itaconate in the circulating plasma of septic patients (429). However, itaconate has been detected and shown to increase inversely to CRP and ESR in the plasma of RA patients three months after treatment with the anti-rheumatic drug methotrexate (431). In contrast, itaconate accumulation earlier in local tissues of an RA mouse model (420) and sepsis patients (429) correlates directly with disease progression and CRP levels.

The antimicrobial character of itaconate may be important both locally and systemically in mammals, but the data as a whole suggest that itaconate plays a multifunctional cytokine-like role during inflammation states in an autocrine-paracrine fashion (382). One way itaconate might impact intercellular metabolism is by modulating succinate signaling and/or transport, as has already been described for the cases of SDH inhibition (417,428) and a shared mitochondrial transporter (SLC25A10) (423). It has also been shown that succinate import by the *S. cerevisiae* dicarboxylic acid transporter is strongly antagonized by itaconate due to a hydrophobic patch proximal to the dicarboxylate binding site that promotes van der Waals interactions with the

itaconate methylene group (432). In addition, the succinate cognate G-protein coupled receptor 91 (GPR91, or SUCNR1) activates both calcium and inositol triphosphate (IP3) signaling pathways when human HEK293 cells overexpressing mouse or human GPR91 are treated with succinate or itaconate (433). Curiously, despite the availability of much of this information at the time of publication, two recent studies detailing the autocrine and paracrine effects of succinate accumulation and secretion in inflamed macrophages (434,435) failed to address the possible role of itaconate in these processes.

Finally, the autocrine-paracrine effects of itaconate may be relevant in EBIs. CMs are in close proximity of numerous developing erythrocytes (262,276) in EBIs, with close contacts established between cell membranes (306). CMs have a heterogenous and poorly defined phenotype (276,311). However, given that BMDM cultures include CMs (436) and upregulate itaconate synthesis and secretion with immunoactivation, we have hypothesized that itaconate metabolism alters erythropoiesis during inflammation. For instance, EPO-induced $CD34^{+}$ progenitors and TF1 erythroid model cells express SUCNR1 (437), and thus erythroblasts could be subject to the succinate-itaconate inflammatory axis during an infection. Like in activated macrophages, erythroblast itaconate may also activate the Nrf2-KEAP1 antioxidant pathway to counter inflammation-derived ROS. Itaconate transferred from activated CMs to erythroid progenitors by an unknown mechanism could be metabolized to itaconyl-CoA in the erythroblasts. We have shown that itaconyl-CoA, a putative inhibitor or alternative substrate of ALAS2, results in diminished or aberrant porphyrin synthesis (Figure 11, see details in Chapter 4). As detailed earlier in this review, ALAS2 deficiency has been implicated in stunted erythroid differentiation (132,283,366,367). The significance of itaconate-driven attenuation of ALA synthesis and erythropoiesis in the context of inflammatory hepcidin and systemic hypoferremia

is speculative at this point. However, the literature suggests that IRE-IRP coordination of iron and ALAS2 levels may be less relevant during terminal differentiation (225,231). Thus it is reasonable to predict that itaconyl-CoA serves to decrease ALAS2 activity and the associated differentiation protocol to limit acute-phase heme iron availability from invading pathogens. Additionally, plasma itaconate and itaconyl-CoA plasma recently observed in ACD conditions such as RA (431) may explain the observed ALAS2-linked downregulation of heme synthesis in this disease (368). Founded on our contributions to the biochemical knowledge base on heme (Chapter 2) and mammalian ALAS2 (Chapter 3), our most recent work (Chapter 4) explores the putative impacts of itaconate metabolism on erythroid ALA and heme synthesis in the context of inflammation (Chapter 4).

1.6 References

1. Kumar, S., and Bandyopadhyay, U. (2005) Free heme toxicity and its detoxification systems in human. *Toxicol Lett* **157**, 175-188

2. Mauzerall, D. C. (1998) Evolution of porphyrins. *Clin Dermatol* **16**, 195-201

3. Dailey, H. A. (2013) Illuminating the black box of B12 biosynthesis. *Proc Natl Acad Sci U S A* **110**, 14823-14824

4. Swenson, S. A., Moore, C. M., Marcero, J. R., Medlock, A. E., Reddi, A. R., and Khalimonchuk, O. (2020) From Synthesis to Utilization: The Ins and Outs of Mitochondrial Heme. *Cells* **9**

5. Dailey, H. A., Dailey, T. A., Gerdes, S., Jahn, D., Jahn, M., O'Brian, M. R., and Warren, M. J. (2017) Prokaryotic Heme Biosynthesis: Multiple Pathways to a Common Essential Product. *Microbiol Mol Biol Rev* **81**

6. Meehan, M., Burke, F. M., Macken, S., and Owen, P. (2010) Characterization of the haem-uptake system of the equine pathogen Streptococcus equi subsp. equi. *Microbiology* **156**, 1824-1835

7. Rao, A. U., Carta, L. K., Lesuisse, E., and Hamza, I. (2005) Lack of heme synthesis in a free-living eukaryote. *Proc Natl Acad Sci U S A* **102**, 4270-4275

8. Braz, G. R., Coelho, H. S., Masuda, H., and Oliveira, P. L. (1999) A missing metabolic pathway in the cattle tick Boophilus microplus. *Curr Biol* **9**, 703-706

9. Shemin, D., and Russell, C. S. (1953) δ-Aminolevulinic Acid, Its Role In The Biosynthesis Of Porphyrins And Purines. *Journal of the American Chemical Society* **75**, 4873-4874

10. Iida, K., Mimura, I., and Kajiwara, M. (2002) Evaluation of two biosynthetic pathways to delta-aminolevulinic acid in Euglena gracilis. *Eur J Biochem* **269**, 291-297

11. Ponka, P. (1999) Cell biology of heme. *Am J Med Sci* **318**, 241-256

12. Severance, S., and Hamza, I. (2009) Trafficking of heme and porphyrins in metazoa. *Chem Rev* **109**, 4596-4616

13. Reddi, A. R., and Hamza, I. (2016) Heme Mobilization in Animals: A Metallolipid's Journey. *Acc Chem Res* **49**, 1104-1110

14. Tsiftsoglou, A. S., Tsamadou, A. I., and Papadopoulou, L. C. (2006) Heme as key regulator of major mammalian cellular functions: molecular, cellular, and pharmacological aspects. *Pharmacol Ther* **111**, 327-345

15. Kim, H. J., Khalimonchuk, O., Smith, P. M., and Winge, D. R. (2012) Structure, function, and assembly of heme centers in mitochondrial respiratory complexes. *Biochim Biophys Acta* **1823**, 1604-1616

16. Mense, S. M., and Zhang, L. (2006) Heme: a versatile signaling molecule controlling the activities of diverse regulators ranging from transcription factors to MAP kinases. *Cell Res* **16**, 681-692

17. Smith, D. W. (1980) The molecular biology of mammalian hemoglobin synthesis. *Ann Clin Lab Sci* **10**, 116-122

18. Faller, M., Matsunaga, M., Yin, S., Loo, J. A., and Guo, F. (2007) Heme is involved in microRNA processing. *Nat Struct Mol Biol* **14**, 23-29

19. Quick-Cleveland, J., Jacob, J. P., Weitz, S. H., Shoffner, G., Senturia, R., and Guo, F. (2014) The DGCR8 RNA-binding heme domain recognizes primary microRNAs by clamping the hairpin. *Cell Rep* **7**, 1994-2005

20. Kikuchi, G., Yoshida, T., and Noguchi, M. (2005) Heme oxygenase and heme degradation. *Biochem Biophys Res Commun* **338**, 558-567

21. Ogura, T., Hirota, S., A., P. D., K., S., S., Y., and T., K. (1996) Time-resolved resonance Raman evidence for tight coupling between electron transfer and proton pumping of cytochrome c oxidase upon the change from the Fe-V oxidation level to the Fe-IV oxidation level. *Journal of the American Chemical Society* **118**, 5443-5449

22. Dey, A., and Ghosh, A. (2002) "True" iron (V) and iron (VI) porphyrins: A first theoretical exploration. *Journal of the American Chemical Society* **124**, 3206-3207

23. Barcellos-de-Souza, P., Moraes, J. A., de-Freitas-Junior, J. C., Morgado-Diaz, J. A., Barja-Fidalgo, C., and Arruda, M. A. (2013) Heme modulates intestinal epithelial cell activation: involvement of NADPHox-derived ROS signaling. *Am J Physiol Cell Physiol* **304**, C170-179

24. Prousek, J. (2007) Fenton chemistry in biology and medicine. *Pure and Applied Chemistry* **79**, 2325-2338

25. Hamza, I., and Dailey, H. A. (2012) One ring to rule them all: trafficking of heme and heme synthesis intermediates in the metazoans. *Biochim Biophys Acta* **1823**, 1617-1632

26. Igarashi, K., and Sun, J. (2006) The heme-Bach1 pathway in the regulation of oxidative stress response and erythroid differentiation. *Antioxid Redox Signal* **8**, 107-118

27. Haldar, M., Kohyama, M., So, A. Y., Kc, W., Wu, X., Briseno, C. G., Satpathy, A. T., Kretzer, N. M., Arase, H., Rajasekaran, N. S., Wang, L., Egawa, T., Igarashi, K., Baltimore, D., Murphy, T. L., and Murphy, K. M. (2014) Heme-mediated SPI-C induction promotes monocyte differentiation into iron-recycling macrophages. *Cell* **156**, 1223-1234

28. Raghuram, S., Stayrook, K. R., Huang, P., Rogers, P. M., Nosie, A. K., McClure, D. B., Burris, L. L., Khorasanizadeh, S., Burris, T. P., and Rastinejad, F. (2007) Identification of heme as the ligand for the orphan nuclear receptors REV-ERBalpha and REV-ERBbeta. *Nat Struct Mol Biol* **14**, 1207-1213

29. Chiabrando, D., Vinchi, F., Fiorito, V., Mercurio, S., and Tolosano, E. (2014) Heme in pathophysiology: a matter of scavenging, metabolism and trafficking across cell membranes. *Front Pharmacol* **5**, 61

30. Keel, S. B., Doty, R. T., Yang, Z., Quigley, J. G., Chen, J., Knoblaugh, S., Kingsley, P. D., De Domenico, I., Vaughn, M. B., Kaplan, J., Palis, J., and Abkowitz, J. L. (2008) A heme export protein is required for red blood cell differentiation and iron homeostasis. *Science* **319**, 825-828

31. Dutra, F. F., and Bozza, M. T. (2014) Heme on innate immunity and inflammation. *Front Pharmacol* **5**, 115

32. Desmard, M., Boczkowski, J., Poderoso, J., and Motterlini, R. (2007) Mitochondrial and cellular heme-dependent proteins as targets for the bioactive function of the heme oxygenase/carbon monoxide system. *Antioxid Redox Signal* **9**, 2139-2155

33. Drabkin, D. L., and Austin, J. H. (1935) Spectrophotometric studies II. Preparations from washed blood cells; nitric oxide hemoglobin and sulfhemoglobin. *Journal of Biological Chemistry* **112**, 51-65

34. Waterman, M. R. (1978) Spectral characterization of human hemoglobin and its derivatives. *Methods Enzymol* **52**, 456-463

35. Whitehead, R. D., Jr., Mei, Z., Mapango, C., and Jefferds, M. E. D. (2019) Methods and analyzers for hemoglobin measurement in clinical laboratories and field settings. *Ann N Y Acad Sci* **1450**, 147-171

36. Paul, K. G., Theorell, H., and Akeson, A. (1953) The molar light absorption of pyridine ferroprotoporphyrin (pyridine haemochromogen). *Acta Chemica Scandinavica* **7**, 1284-1287

37. Furhop, J. H., and Smith, K. M. (1975) *Laboratory methods in porphyrin and metalloporphyrin research*, Elsevier Science LTD, Amerstdam, Netherlands

38. Berry, E. A., and Trumpower, B. L. (1987) Simultaneous determination of hemes a, b, and c from pyridine hemochrome spectra. *Anal Biochem* **161**, 1-15

39. Morrison, G. R. (1965) Fluorometric Microdetermination of Heme Protein. *Anal Chem* **37**, 1124-1126

40. Sassa, S. (1976) Sequential induction of heme pathway enzymes during erythroid differentiation of mouse Friend leukemia virus-infected cells. *J Exp Med* **143**, 305-315

41. Bonkovsky, H. L., Wood, S. G., Howell, S. K., Sinclair, P. R., Lincoln, B., Healey, J. F., and Sinclair, J. F. (1986) High-performance liquid chromatographic separation and quantitation of tetrapyrroles from biological materials. *Anal Biochem* **155**, 56-64

42. Jacobs, J. M., Sinclair, P. R., Gorman, N., Jacobs, N. J., Sinclair, J. F., Bement, W. J., and Walton, H. (1992) Effects of diphenyl ether herbicides on porphyrin accumulation by cultured hepatocytes. *J Biochem Toxicol* **7**, 87-95

43. Healey, J. F., Bonkowsky, H. L., Sinclair, P. R., and Sinclair, J. F. (1981) Conversion of 5-aminolaevulinate into haem by liver homogenates. Comparison of rat and chick embryo. *Biochem J* **198**, 595-604

44. Jacobs, J. M., Sinclair, P. R., Sinclair, J. F., Gorman, N., Walton, H. S., Wood, S. G., and Nichols, C. (1998) Formation of zinc protoporphyrin in cultured hepatocytes: effects of ferrochelatase inhibition, iron chelation or lead. *Toxicology* **125**, 95-105

45. Taketani, S., Immenschuh, S., Go, S., Sinclair, P. R., Stockert, R. J., Liem, H. H., and Muller Eberhard, U. (1998) Hemopexin from four species inhibits the association of heme with cultured hepatoma cells or primary rat hepatocytes exhibiting a small number of species specific hemopexin receptors. *Hepatology* **27**, 808-814

46. Marcero, J. R., Piel Iii, R. B., Burch, J. S., and Dailey, H. A. (2016) Rapid and sensitive quantitation of heme in hemoglobinized cells. *Biotechniques* **61**, 83-91

47. Dayer, M. R., Moosavi-Movahedi, A. A., and Dayer, M. S. (2010) Band assignment in hemoglobin porphyrin ring spectrum: using four-orbital model of Gouterman. *Protein Pept Lett* **17**, 473-479

48. Bashford, C. L., and Harris, D. A. (1987) *Spectrophotometry & spectrofluorimetry : a practical approach*, IRL Press, Oxford ; Washington DC

49. Sinclair, P. R., Gorman, N., and Jacobs, J. M. (2001) Measurement of heme concentration. *Curr Protoc Toxicol* **Chapter 8**, Unit 8 3

50. Phillips, J. D. (2019) Heme biosynthesis and the porphyrias. *Mol Genet Metab* **128**, 164-177

51. Shemin, D., and Rittenberg, D. (1946) The biological utilization of glycine for the synthesis of the protoporphyrin of hemoglobin. *J Biol Chem* **166**, 621-625

52. Gibson, K. D., Laver, W. G., and Neuberger, A. (1958) Initial stages in the biosynthesis of porphyrins. 2. The formation of delta-aminolaevulic acid from glycine and succinyl-coenzyme A by particles from chicken erythrocytes. *Biochem J* **70**, 71-81

53. Shemin, D., and Kikuchi, G. (1958) Enzymatic synthesis of sigma-aminolevulinic acid. *Ann N Y Acad Sci* **75**, 122-128

54. Gibson, K. D., Laver, W. G., and Neuberger, A. (1958) Initial stages in the biosynthesis of porphyrins. 1. The formation of delta-aminolaevulic acid by particles from chicken erythrocytes. *Biochem J* **70**, 4-14

55. Schulze, J. O., Schubert, W. D., Moser, J., Jahn, D., and Heinz, D. W. (2006) Evolutionary relationship between initial enzymes of tetrapyrrole biosynthesis. *J Mol Biol* **358**, 1212-1220

56. Bishop, D. F., Henderson, A. S., and Astrin, K. H. (1990) Human delta-aminolevulinate synthase: assignment of the housekeeping gene to 3p21 and the erythroid-specific gene to the X chromosome. *Genomics* **7**, 207-214

57. Duncan, R., Faggart, M. A., Roger, A. J., and Cornell, N. W. (1999) Phylogenetic analysis of the 5-aminolevulinate synthase gene. *Mol Biol Evol* **16**, 383-396

58. Riddle, R. D., Yamamoto, M., and Engel, J. D. (1989) Expression of delta-aminolevulinate synthase in avian cells: separate genes encode erythroid-specific and nonspecific isozymes. *Proc Natl Acad Sci U S A* **86**, 792-796

59. Handschin, C., Lin, J., Rhee, J., Peyer, A. K., Chin, S., Wu, P. H., Meyer, U. A., and Spiegelman, B. M. (2005) Nutritional regulation of hepatic heme biosynthesis and porphyria through PGC-1alpha. *Cell* **122**, 505-515

60. Gotoh, S., Nakamura, T., Kataoka, T., and Taketani, S. (2011) Egr-1 regulates the transcriptional repression of mouse delta-aminolevulinic acid synthase 1 by heme. *Gene* **472**, 28-36

61. Roberts, A. G., and Elder, G. H. (2001) Alternative splicing and tissue-specific transcription of human and rodent ubiquitous 5-aminolevulinate synthase (ALAS1) genes. *Biochim Biophys Acta* **1518**, 95-105

62. Cox, T. C., Sadlon, T. J., Schwarz, Q. P., Matthews, C. S., Wise, P. D., Cox, L. L., Bottomley, S. S., and May, B. K. (2004) The major splice variant of human 5-aminolevulinate synthase-2 contributes significantly to erythroid heme biosynthesis. *Int J Biochem Cell Biol* **36**, 281-295

63. Cooperman, S. S., Meyron-Holtz, E. G., Olivierre-Wilson, H., Ghosh, M. C., McConnell, J. P., and Rouault, T. A. (2005) Microcytic anemia, erythropoietic protoporphyria, and neurodegeneration in mice with targeted deletion of iron-regulatory protein 2. *Blood* **106**, 1084-1091

64. Chung, J., Anderson, S. A., Gwynn, B., Deck, K. M., Chen, M. J., Langer, N. B., Shaw, G. C., Huston, N. C., Boyer, L. F., Datta, S., Paradkar, P. N., Li, L., Wei, Z., Lambert, A. J., Sahr, K., Wittig, J. G., Chen, W., Lu, W., Galy, B., Schlaeger, T. M., Hentze, M. W., Ward, D. M., Kaplan, J., Eisenstein, R. S., Peters, L. L., and Paw, B. H. (2014) Iron regulatory protein-1 protects against mitoferrin-1-deficient porphyria. *J Biol Chem* **289**, 7835-7843

65. Bishop, D. F. (1990) Two different genes encode delta-aminolevulinate synthase in humans: nucleotide sequences of cDNAs for the housekeeping and erythroid genes. *Nucleic Acids Res* **18**, 7187-7188

66. Astner, I., Schulze, J. O., van den Heuvel, J., Jahn, D., Schubert, W. D., and Heinz, D. W. (2005) Crystal structure of 5-aminolevulinate synthase, the first enzyme of heme biosynthesis, and its link to XLSA in humans. *EMBO J* **24**, 3166-3177

67. Brown, B. L., Kardon, J. R., Sauer, R. T., and Baker, T. A. (2018) Structure of the Mitochondrial Aminolevulinic Acid Synthase, a Key Heme Biosynthetic Enzyme. *Structure* **26**, 580-589 e584

68. Lathrop, J. T., and Timko, M. P. (1993) Regulation by heme of mitochondrial protein transport through a conserved amino acid motif. *Science* **259**, 522-525

69. Munakata, H., Sun, J. Y., Yoshida, K., Nakatani, T., Honda, E., Hayakawa, S., Furuyama, K., and Hayashi, N. (2004) Role of the heme regulatory motif in the heme-mediated inhibition of mitochondrial import of 5-aminolevulinate synthase. *J Biochem* **136**, 233-238

70. Furuyama, K., and Sassa, S. (2000) Interaction between succinyl CoA synthetase and the heme-biosynthetic enzyme ALAS-E is disrupted in sideroblastic anemia. *J Clin Invest* **105**, 757-764

71. Bishop, D. F., Tchaikovskii, V., Hoffbrand, A. V., Fraser, M. E., and Margolis, S. (2012) X-linked sideroblastic anemia due to carboxyl-terminal ALAS2 mutations that cause loss of binding to the beta-subunit of succinyl-CoA synthetase (SUCLA2). *J Biol Chem* **287**, 28943-28955

72. Burch, J. S., Marcero, J. R., Maschek, J. A., Cox, J. E., Jackson, L. K., Medlock, A. E., Phillips, J. D., and Dailey, H. A., Jr. (2018) Glutamine via alpha-ketoglutarate dehydrogenase provides succinyl-CoA for heme synthesis during erythropoiesis. *Blood* **132**, 987-998

73. Medlock, A. E., Shiferaw, M. T., Marcero, J. R., Vashisht, A. A., Wohlschlegel, J. A., Phillips, J. D., and Dailey, H. A. (2015) Identification of the Mitochondrial Heme Metabolism Complex. *PLoS One* **10**, e0135896

74. Kardon, J. R., Yien, Y. Y., Huston, N. C., Branco, D. S., Hildick-Smith, G. J., Rhee, K. Y., Paw, B. H., and Baker, T. A. (2015) Mitochondrial ClpX Activates a Key Enzyme for Heme Biosynthesis and Erythropoiesis. *Cell* **161**, 858-867

75. Yien, Y. Y., Ducamp, S., van der Vorm, L. N., Kardon, J. R., Manceau, H., Kannengiesser, C., Bergonia, H. A., Kafina, M. D., Karim, Z., Gouya, L., Baker, T. A., Puy, H., Phillips, J. D., Nicolas, G., and Paw, B. H. (2017) Mutation in human CLPX elevates levels of delta-aminolevulinate synthase and protoporphyrin IX to promote erythropoietic protoporphyria. *Proc Natl Acad Sci U S A* **114**, E8045-E8052

76. Kubota, Y., Nomura, K., Katoh, Y., Yamashita, R., Kaneko, K., and Furuyama, K. (2016) Novel Mechanisms for Heme-dependent Degradation of ALAS1 Protein as a Component of Negative Feedback Regulation of Heme Biosynthesis. *J Biol Chem* **291**, 20516-20529

77. Cotter, P. D., Baumann, M., and Bishop, D. F. (1992) Enzymatic defect in "X-linked" sideroblastic anemia: molecular evidence for erythroid delta-aminolevulinate synthase deficiency. *Proc Natl Acad Sci U S A* **89**, 4028-4032

78. Dailey, H. A., and Meissner, P. N. (2013) Erythroid heme biosynthesis and its disorders. *Cold Spring Harb Perspect Med* **3**, a011676

79. Bottomley, S. S., May, B. K., Cox, T. C., Cotter, P. D., and Bishop, D. F. (1995) Molecular defects of erythroid 5-aminolevulinate synthase in X-linked sideroblastic anemia. *J Bioenerg Biomembr* **27**, 161-168

80. Whatley, S. D., Ducamp, S., Gouya, L., Grandchamp, B., Beaumont, C., Badminton, M. N., Elder, G. H., Holme, S. A., Anstey, A. V., Parker, M., Corrigall, A. V., Meissner, P. N., Hift, R. J., Marsden, J. T., Ma, Y., Mieli-Vergani, G., Deybach, J. C., and Puy, H. (2008) C-terminal deletions in the ALAS2 gene lead to gain of function and cause X-linked dominant protoporphyria without anemia or iron overload. *Am J Hum Genet* **83**, 408-414

81. Balwani, M. (2019) Erythropoietic Protoporphyria and X-Linked Protoporphyria: pathophysiology, genetics, clinical manifestations, and management. *Mol Genet Metab* **128**, 298-303

82. Goldstein, B. D., and Harber, L. C. (1972) Erythropoietic protoporphyria: lipid peroxidation and red cell membrane damage associated with photohemolysis. *J Clin Invest* **51**, 892-902

83. Schneider-Yin, X., Gouya, L., Meier-Weinand, A., Deybach, J. C., and Minder, E. I. (2000) New insights into the pathogenesis of erythropoietic protoporphyria and their impact on patient care. *Eur J Pediatr* **159**, 719-725

84. Bloomer, J. R. (1988) The liver in protoporphyria. *Hepatology* **8**, 402-407

85. Rand, E. B., Bunin, N., Cochran, W., Ruchelli, E., Olthoff, K. M., and Bloomer, J. R. (2006) Sequential liver and bone marrow transplantation for treatment of erythropoietic protoporphyria. *Pediatrics* **118**, e1896-1899

86. Butler, D. F., Ginn, K. F., Daniel, J. F., Bloomer, J. R., Kats, A., Shreve, N., and Myers, G. D. (2015) Bone marrow transplant for X-linked protoporphyria with severe hepatic fibrosis. *Pediatr Transplant* **19**, E106-110

87. Langendonk, J. G., Balwani, M., Anderson, K. E., Bonkovsky, H. L., Anstey, A. V., Bissell, D. M., Bloomer, J., Edwards, C., Neumann, N. J., Parker, C., Phillips, J. D., Lim, H. W., Hamzavi, I., Deybach, J. C., Kauppinen, R., Rhodes, L. E., Frank, J., Murphy, G. M., Karstens, F. P. J., Sijbrands, E. J. G., de Rooij, F. W. M., Lebwohl, M., Naik, H.,

Goding, C. R., Wilson, J. H. P., and Desnick, R. J. (2015) Afamelanotide for Erythropoietic Protoporphyria. *N Engl J Med* **373**, 48-59

88. Minder, E. I. (2010) Afamelanotide, an agonistic analog of alpha-melanocyte-stimulating hormone, in dermal phototoxicity of erythropoietic protoporphyria. *Expert Opin Investig Drugs* **19**, 1591-1602

89. Wensink, D., Wagenmakers, M., Barman-Aksozen, J., Friesema, E. C. H., Wilson, J. H. P., van Rosmalen, J., and Langendonk, J. G. (2020) Association of Afamelanotide With Improved Outcomes in Patients With Erythropoietic Protoporphyria in Clinical Practice. *JAMA Dermatol*

90. Warren, L. J., and George, S. (1998) Erythropoietic protoporphyria treated with narrow-band (TL-01) UVB phototherapy. *Australas J Dermatol* **39**, 179-182

91. Guernsey, D. L., Jiang, H., Campagna, D. R., Evans, S. C., Ferguson, M., Kellogg, M. D., Lachance, M., Matsuoka, M., Nightingale, M., Rideout, A., Saint-Amant, L., Schmidt, P. J., Orr, A., Bottomley, S. S., Fleming, M. D., Ludman, M., Dyack, S., Fernandez, C. V., and Samuels, M. E. (2009) Mutations in mitochondrial carrier family gene SLC25A38 cause nonsyndromic autosomal recessive congenital sideroblastic anemia. *Nat Genet* **41**, 651-653

92. Nilsson, R., Schultz, I. J., Pierce, E. L., Soltis, K. A., Naranuntarat, A., Ward, D. M., Baughman, J. M., Paradkar, P. N., Kingsley, P. D., Culotta, V. C., Kaplan, J., Palis, J., Paw, B. H., and Mootha, V. K. (2009) Discovery of genes essential for heme biosynthesis through large-scale gene expression analysis. *Cell Metab* **10**, 119-130

93. Lunetti, P., Damiano, F., De Benedetto, G., Siculella, L., Pennetta, A., Muto, L., Paradies, E., Marobbio, C. M., Dolce, V., and Capobianco, L. (2016) Characterization of Human and Yeast Mitochondrial Glycine Carriers with Implications for Heme Biosynthesis and Anemia. *J Biol Chem* **291**, 19746-19759

94. Kaya, A. H., Plewinska, M., Wong, D. M., Desnick, R. J., and Wetmur, J. G. (1994) Human delta-aminolevulinate dehydratase (ALAD) gene: structure and alternative splicing of the erythroid and housekeeping mRNAs. *Genomics* **19**, 242-248

95. Erskine, P. T., Senior, N., Awan, S., Lambert, R., Lewis, G., Tickle, I. J., Sarwar, M., Spencer, P., Thomas, P., Warren, M. J., Shoolingin-Jordan, P. M., Wood, S. P., and Cooper, J. B. (1997) X-ray structure of 5-aminolaevulinate dehydratase, a hybrid aldolase. *Nat Struct Biol* **4**, 1025-1031

96. Lawrence, S. H., Ramirez, U. D., Selwood, T., Stith, L., and Jaffe, E. K. (2009) Allosteric inhibition of human porphobilinogen synthase. *J Biol Chem* **284**, 35807-35817

97. Jaffe, E. K., and Lawrence, S. H. (2012) Allostery and the dynamic oligomerization of porphobilinogen synthase. *Arch Biochem Biophys* **519**, 144-153

98. Tsukamoto, I., Yoshinaga, T., and Sano, S. (1979) The role of zinc with special reference to the essential thiol groups in delta-aminolevulinic acid dehydratase of bovine liver. *Biochim Biophys Acta* **570**, 167-178

99. Warren, M. J., Cooper, J. B., Wood, S. P., and Shoolingin-Jordan, P. M. (1998) Lead poisoning, haem synthesis and 5-aminolaevulinic acid dehydratase. *Trends Biochem Sci* **23**, 217-221

100. Breinig, S., Kervinen, J., Stith, L., Wasson, A. S., Fairman, R., Wlodawer, A., Zdanov, A., and Jaffe, E. K. (2003) Control of tetrapyrrole biosynthesis by alternate quaternary forms of porphobilinogen synthase. *Nat Struct Biol* **10**, 757-763

101. Muller, W. E., and Snyder, S. H. (1977) delta-Aminolevulinic acid: influences on synaptic GABA receptor binding may explain CNS symptoms of porphyria. *Ann Neurol* **2**, 340-342

102. Mignotte, V., Eleouet, J. F., Raich, N., and Romeo, P. H. (1989) Cis- and trans-acting elements involved in the regulation of the erythroid promoter of the human porphobilinogen deaminase gene. *Proc Natl Acad Sci U S A* **86**, 6548-6552

103. Grandchamp, B., De Verneuil, H., Beaumont, C., Chretien, S., Walter, O., and Nordmann, Y. (1987) Tissue-specific expression of porphobilinogen deaminase. Two isoenzymes from a single gene. *Eur J Biochem* **162**, 105-110

104. Gill, R., Kolstoe, S. E., Mohammed, F., Al, D. B. A., Mosely, J. E., Sarwar, M., Cooper, J. B., Wood, S. P., and Shoolingin-Jordan, P. M. (2009) Structure of human porphobilinogen deaminase at 2.8 A: the molecular basis of acute intermittent porphyria. *Biochem J* **420**, 17-25

105. Louie, G. V., Brownlie, P. D., Lambert, R., Cooper, J. B., Blundell, T. L., Wood, S. P., Warren, M. J., Woodcock, S. C., and Jordan, P. M. (1992) Structure of porphobilinogen deaminase reveals a flexible multidomain polymerase with a single catalytic site. *Nature* **359**, 33-39

106. Jordan, P. M., and Warren, M. J. (1987) Evidence for a dipyrromethane cofactor at the catalytic site of E. coli porphobilinogen deaminase. *FEBS Lett* **225**, 87-92

107. Ramanujam, V. S., and Anderson, K. E. (2015) Porphyria Diagnostics-Part 1: A Brief Overview of the Porphyrias. *Curr Protoc Hum Genet* **86**, 17 20 11-17 20 26

108. Podvinec, M., Handschin, C., Looser, R., and Meyer, U. A. (2004) Identification of the xenosensors regulating human 5-aminolevulinate synthase. *Proc Natl Acad Sci U S A* **101**, 9127-9132

109. Aizencang, G., Solis, C., Bishop, D. F., Warner, C., and Desnick, R. J. (2000) Human uroporphyrinogen-III synthase: genomic organization, alternative promoters, and erythroid-specific expression. *Genomics* **70**, 223-231

110. Schubert, H. L., Phillips, J. D., Heroux, A., and Hill, C. P. (2008) Structure and mechanistic implications of a uroporphyrinogen III synthase-product complex. *Biochemistry* **47**, 8648-8655

111. Mathews, M. A., Schubert, H. L., Whitby, F. G., Alexander, K. J., Schadick, K., Bergonia, H. A., Phillips, J. D., and Hill, C. P. (2001) Crystal structure of human uroporphyrinogen III synthase. *EMBO J* **20**, 5832-5839

112. Battersby, A. R., Fookes, C. J., Matcham, G. W., and McDonald, E. (1980) Biosynthesis of the pigments of life: formation of the macrocycle. *Nature* **285**, 17-21

113. Elder, G. H., and Roberts, A. G. (1995) Uroporphyrinogen decarboxylase. *J Bioenerg Biomembr* **27**, 207-214

114. To-Figueras, J., Ducamp, S., Clayton, J., Badenas, C., Delaby, C., Ged, C., Lyoumi, S., Gouya, L., de Verneuil, H., Beaumont, C., Ferreira, G. C., Deybach, J. C., Herrero, C., and Puy, H. (2011) ALAS2 acts as a modifier gene in patients with congenital erythropoietic porphyria. *Blood* **118**, 1443-1451

115. Blouin, J. M., Duchartre, Y., Costet, P., Lalanne, M., Ged, C., Lain, A., Millet, O., de Verneuil, H., and Richard, E. (2013) Therapeutic potential of proteasome inhibitors in congenital erythropoietic porphyria. *Proc Natl Acad Sci U S A* **110**, 18238-18243

116. Romana, M., Dubart, A., Beaupain, D., Chabret, C., Goossens, M., and Romeo, P. H. (1987) Structure of the gene for human uroporphyrinogen decarboxylase. *Nucleic Acids Res* **15**, 7343-7356

117. Phillips, J. D., Whitby, F. G., Kushner, J. P., and Hill, C. P. (2003) Structural basis for tetrapyrrole coordination by uroporphyrinogen decarboxylase. *EMBO J* **22**, 6225-6233

118. Lewis, C. A., Jr., and Wolfenden, R. (2008) Uroporphyrinogen decarboxylation as a benchmark for the catalytic proficiency of enzymes. *Proc Natl Acad Sci U S A* **105**, 17328-17333

119. Elder, G. H. (1998) Porphyria cutanea tarda. *Semin Liver Dis* **18**, 67-75

120. Ajioka, R. S., Phillips, J. D., and Kushner, J. P. (2006) Biosynthesis of heme in mammals. *Biochim Biophys Acta* **1763**, 723-736

121. Jalil, S., Grady, J. J., Lee, C., and Anderson, K. E. (2010) Associations among behavior-related susceptibility factors in porphyria cutanea tarda. *Clin Gastroenterol Hepatol* **8**, 297-302, 302 e291

122. Barzilay, D., Orion, E., and Brenner, S. (2001) Porphyria cutanea tarda triggered by a combination of three predisposing factors. *Dermatology* **203**, 195-197

123. Phillips, J. D., Bergonia, H. A., Reilly, C. A., Franklin, M. R., and Kushner, J. P. (2007) A porphomethene inhibitor of uroporphyrinogen decarboxylase causes porphyria cutanea tarda. *Proc Natl Acad Sci U S A* **104**, 5079-5084

124. Phillips, J. D., Jackson, L. K., Bunting, M., Franklin, M. R., Thomas, K. R., Levy, J. E., Andrews, N. C., and Kushner, J. P. (2001) A mouse model of familial porphyria cutanea tarda. *Proc Natl Acad Sci U S A* **98**, 259-264

125. Grandchamp, B., Phung, N., and Nordmann, Y. (1978) The mitochondrial localization of coproporphyrinogen III oxidase. *Biochem J* **176**, 97-102

126. Krishnamurthy, P. C., Du, G., Fukuda, Y., Sun, D., Sampath, J., Mercer, K. E., Wang, J., Sosa-Pineda, B., Murti, K. G., and Schuetz, J. D. (2006) Identification of a mammalian mitochondrial porphyrin transporter. *Nature* **443**, 586-589

127. Ulrich, D. L., Lynch, J., Wang, Y., Fukuda, Y., Nachagari, D., Du, G., Sun, D., Fan, Y., Tsurkan, L., Potter, P. M., Rehg, J. E., and Schuetz, J. D. (2012) ATP-dependent mitochondrial porphyrin importer ABCB6 protects against phenylhydrazine toxicity. *J Biol Chem* **287**, 12679-12690

128. Fukuda, Y., Cheong, P. L., Lynch, J., Brighton, C., Frase, S., Kargas, V., Rampersaud, E., Wang, Y., Sankaran, V. G., Yu, B., Ney, P. A., Weiss, M. J., Vogel, P., Bond, P. J., Ford, R. C., Trent, R. J., and Schuetz, J. D. (2016) The severity of hereditary porphyria is modulated by the porphyrin exporter and Lan antigen ABCB6. *Nat Commun* **7**, 12353

129. Takahashi, S., Furuyama, K., Kobayashi, A., Taketani, S., Harigae, H., Yamamoto, M., Igarashi, K., Sasaki, T., and Hayashi, N. (2000) Cloning of a coproporphyrinogen oxidase promoter regulatory element binding protein. *Biochem Biophys Res Commun* **273**, 596-602

130. Takahashi, S., Taketani, S., Akasaka, J. E., Kobayashi, A., Hayashi, N., Yamamoto, M., and Nagai, T. (1998) Differential regulation of coproporphyrinogen oxidase gene between erythroid and nonerythroid cells. *Blood* **92**, 3436-3444

131. Conder, L. H., Woodard, S. I., and Dailey, H. A. (1991) Multiple mechanisms for the regulation of haem synthesis during erythroid cell differentiation. Possible role for coproporphyrinogen oxidase. *Biochem J* **275 (Pt 2)**, 321-326

132. Lake-Bullock, H., and Dailey, H. A. (1993) Biphasic ordered induction of heme synthesis in differentiating murine erythroleukemia cells: role of erythroid 5-aminolevulinate synthase. *Mol Cell Biol* **13**, 7122-7132

133. Taketani, S., Furukawa, T., and Furuyama, K. (2001) Expression of coproporphyrinogen oxidase and synthesis of hemoglobin in human erythroleukemia K562 cells. *Eur J Biochem* **268**, 1705-1711

134. Woodard, S. I., and Dailey, H. A. (2000) Multiple regulatory steps in erythroid heme biosynthesis. *Arch Biochem Biophys* **384**, 375-378

135. Camadro, J. M., Chambon, H., Jolles, J., and Labbe, P. (1986) Purification and properties of coproporphyrinogen oxidase from the yeast Saccharomyces cerevisiae. *Eur J Biochem* **156**, 579-587

136. Rhee, H. W., Zou, P., Udeshi, N. D., Martell, J. D., Mootha, V. K., Carr, S. A., and Ting, A. Y. (2013) Proteomic mapping of mitochondria in living cells via spatially restricted enzymatic tagging. *Science* **339**, 1328-1331

137. Phillips, J. D., Whitby, F. G., Warby, C. A., Labbe, P., Yang, C., Pflugrath, J. W., Ferrara, J. D., Robinson, H., Kushner, J. P., and Hill, C. P. (2004) Crystal structure of the oxygen-dependant coproporphyrinogen oxidase (Hem13p) of Saccharomyces cerevisiae. *J Biol Chem* **279**, 38960-38968

138. Lee, D. S., Flachsova, E., Bodnarova, M., Demeler, B., Martasek, P., and Raman, C. S. (2005) Structural basis of hereditary coproporphyria. *Proc Natl Acad Sci U S A* **102**, 14232-14237

139. Elder, G. H., Evans, J. O., Jackson, J. R., and Jackson, A. H. (1978) Factors determining the sequence of oxidative decarboxylation of the 2- and 4-propionate substituents of coproporphyrinogen III by coproporphyrinogen oxidase in rat liver. *Biochem J* **169**, 215-223

140. Nordmann, Y., Grandchamp, B., de Verneuil, H., Phung, L., Cartigny, B., and Fontaine, G. (1983) Harderoporphyria: a variant hereditary coproporphyria. *J Clin Invest* **72**, 1139-1149

141. Besur, S., Hou, W., Schmeltzer, P., and Bonkovsky, H. L. (2014) Clinically important features of porphyrin and heme metabolism and the porphyrias. *Metabolites* **4**, 977-1006

142. Gorchein, A., Danton, M., and Lim, C. K. (2005) Harderoporphyrin: a misnomer. *Biomed Chromatogr* **19**, 565-569

143. Azuma, M., Kabe, Y., Kuramori, C., Kondo, M., Yamaguchi, Y., and Handa, H. (2008) Adenine nucleotide translocator transports haem precursors into mitochondria. *PLoS One* **3**, e3070

144. Yien, Y. Y., Robledo, R. F., Schultz, I. J., Takahashi-Makise, N., Gwynn, B., Bauer, D. E., Dass, A., Yi, G., Li, L., Hildick-Smith, G. J., Cooney, J. D., Pierce, E. L., Mohler, K., Dailey, T. A., Miyata, N., Kingsley, P. D., Garone, C., Hattangadi, S. M., Huang, H., Chen, W., Keenan, E. M., Shah, D. I., Schlaeger, T. M., DiMauro, S., Orkin, S. H., Cantor, A. B., Palis, J., Koehler, C. M., Lodish, H. F., Kaplan, J., Ward, D. M., Dailey, H. A., Phillips, J. D., Peters, L. L., and Paw, B. H. (2014) TMEM14C is required for erythroid mitochondrial heme metabolism. *J Clin Invest* **124**, 4294-4304

145. Ferrer, M. D., Tauler, P., Sureda, A., Romaguera, D., Llompart, I., Palacin, C., Orfila, J., Tur, J. A., and Pons, A. (2009) Enzyme antioxidant defences and oxidative damage in red blood cells of variegate porphyria patients. *Redox Rep* **14**, 69-74

146. Dailey, T. A., McManus, J. F., and Dailey, H. A. (2002) Characterization of the mouse protoporphyrinogen oxidase gene. *Cell Mol Biol (Noisy-le-grand)* **48**, 61-69

147. de Vooght, K. M., van Wijk, R., and van Solinge, W. W. (2008) GATA-1 binding sites in exon 1 direct erythroid-specific transcription of PPOX. *Gene* **409**, 83-91

148. Koch, M., Breithaupt, C., Kiefersauer, R., Freigang, J., Huber, R., and Messerschmidt, A. (2004) Crystal structure of protoporphyrinogen IX oxidase: a key enzyme in haem and chlorophyll biosynthesis. *EMBO J* **23**, 1720-1728

149. Corradi, H. R., Corrigall, A. V., Boix, E., Mohan, C. G., Sturrock, E. D., Meissner, P. N., and Acharya, K. R. (2006) Crystal structure of protoporphyrinogen oxidase from Myxococcus xanthus and its complex with the inhibitor acifluorfen. *J Biol Chem* **281**, 38625-38633

150. Qin, X., Sun, L., Wen, X., Yang, X., Tan, Y., Jin, H., Cao, Q., Zhou, W., Xi, Z., and Shen, Y. (2010) Structural insight into unique properties of protoporphyrinogen oxidase from Bacillus subtilis. *J Struct Biol* **170**, 76-82

151. Qin, X., Tan, Y., Wang, L., Wang, Z., Wang, B., Wen, X., Yang, G., Xi, Z., and Shen, Y. (2011) Structural insight into human variegate porphyria disease. *FASEB J* **25**, 653-664

152. von und zu Fraunberg, M., Nyroen, T., and Kauppinen, R. (2003) Mitochondrial targeting of normal and mutant protoporphyrinogen oxidase. *J Biol Chem* **278**, 13376-13381

153. Chen, W., Dailey, H. A., and Paw, B. H. (2010) Ferrochelatase forms an oligomeric complex with mitoferrin-1 and Abcb10 for erythroid heme biosynthesis. *Blood* **116**, 628-630

154. Ferrer, M. D., Tauler, P., Sureda, A., Palacin, C., Tur, J. A., and Pons, A. (2013) Antioxidants restore protoporphyrinogen oxidase in variegate porphyria patients. *Eur J Clin Invest* **43**, 668-678

155. Meissner, P., Adams, P., and Kirsch, R. (1993) Allosteric inhibition of human lymphoblast and purified porphobilinogen deaminase by protoporphyrinogen and coproporphyrinogen. A possible mechanism for the acute attack of variegate porphyria. *J Clin Invest* **91**, 1436-1444

156. Medlock, A., Swartz, L., Dailey, T. A., Dailey, H. A., and Lanzilotta, W. N. (2007) Substrate interactions with human ferrochelatase. *Proc Natl Acad Sci U S A* **104**, 1789-1793

157. Iacopetta, B. J., and Morgan, E. H. (1983) The kinetics of transferrin endocytosis and iron uptake from transferrin in rabbit reticulocytes. *J Biol Chem* **258**, 9108-9115

158. Morgan, E. H. (1983) Effect of pH and iron content of transferrin on its binding to reticulocyte receptors. *Biochim Biophys Acta* **762**, 498-502

159. Ohgami, R. S., Campagna, D. R., Greer, E. L., Antiochos, B., McDonald, A., Chen, J., Sharp, J. J., Fujiwara, Y., Barker, J. E., and Fleming, M. D. (2005) Identification of a ferrireductase required for efficient transferrin-dependent iron uptake in erythroid cells. *Nat Genet* **37**, 1264-1269

160. Fleming, M. D., Romano, M. A., Su, M. A., Garrick, L. M., Garrick, M. D., and Andrews, N. C. (1998) Nramp2 is mutated in the anemic Belgrade (b) rat: evidence of a role for Nramp2 in endosomal iron transport. *Proc Natl Acad Sci U S A* **95**, 1148-1153

161. Jacobs, A. (1977) Low molecular weight intracellular iron transport compounds. *Blood* **50**, 433-439

162. Sheftel, A. D., Zhang, A. S., Brown, C., Shirihai, O. S., and Ponka, P. (2007) Direct interorganellar transfer of iron from endosome to mitochondrion. *Blood* **110**, 125-132

163. Kafina, M. D., and Paw, B. H. (2017) Intracellular iron and heme trafficking and metabolism in developing erythroblasts. *Metallomics* **9**, 1193-1203

164. Shaw, G. C., Cope, J. J., Li, L., Corson, K., Hersey, C., Ackermann, G. E., Gwynn, B., Lambert, A. J., Wingert, R. A., Traver, D., Trede, N. S., Barut, B. A., Zhou, Y., Minet, E., Donovan, A., Brownlie, A., Balzan, R., Weiss, M. J., Peters, L. L., Kaplan, J., Zon, L. I., and Paw, B. H. (2006) Mitoferrin is essential for erythroid iron assimilation. *Nature* **440**, 96-100

165. Paradkar, P. N., Zumbrennen, K. B., Paw, B. H., Ward, D. M., and Kaplan, J. (2009) Regulation of mitochondrial iron import through differential turnover of mitoferrin 1 and mitoferrin 2. *Mol Cell Biol* **29**, 1007-1016

166. Tugores, A., Magness, S. T., and Brenner, D. A. (1994) A single promoter directs both housekeeping and erythroid preferential expression of the human ferrochelatase gene. *J Biol Chem* **269**, 30789-30797

167. Chan, R. Y., Schulman, H. M., and Ponka, P. (1993) Expression of ferrochelatase mRNA in erythroid and non-erythroid cells. *Biochem J* **292 (Pt 2)**, 343-349

168. Sakaino, M., Kataoka, T., and Taketani, S. (2009) Post-transcriptional regulation of the expression of ferrochelatase by its variant mRNA. *J Biochem* **145**, 733-738

169. Gouya, L., Martin-Schmitt, C., Robreau, A. M., Austerlitz, F., Da Silva, V., Brun, P., Simonin, S., Lyoumi, S., Grandchamp, B., Beaumont, C., Puy, H., and Deybach, J. C. (2006) Contribution of a common single-nucleotide polymorphism to the genetic predisposition for erythropoietic protoporphyria. *Am J Hum Genet* **78**, 2-14

170. Gouya, L., Puy, H., Robreau, A. M., Bourgeois, M., Lamoril, J., Da Silva, V., Grandchamp, B., and Deybach, J. C. (2002) The penetrance of dominant erythropoietic protoporphyria is modulated by expression of wildtype FECH. *Nat Genet* **30**, 27-28

171. Al-Karadaghi, S., Hansson, M., Nikonov, S., Jonsson, B., and Hederstedt, L. (1997) Crystal structure of ferrochelatase: the terminal enzyme in heme biosynthesis. *Structure* **5**, 1501-1510

172. Medlock, A. E., Dailey, T. A., Ross, T. A., Dailey, H. A., and Lanzilotta, W. N. (2007) A pi-helix switch selective for porphyrin deprotonation and product release in human ferrochelatase. *J Mol Biol* **373**, 1006-1016

173. Dailey, H. A., Finnegan, M. G., and Johnson, M. K. (1994) Human ferrochelatase is an iron-sulfur protein. *Biochemistry* **33**, 403-407

174. Gora, M., Grzybowska, E., Rytka, J., and Labbe-Bois, R. (1996) Probing the active-site residues in Saccharomyces cerevisiae ferrochelatase by directed mutagenesis. In vivo and in vitro analyses. *J Biol Chem* **271**, 11810-11816

175. Crooks, D. R., Ghosh, M. C., Haller, R. G., Tong, W. H., and Rouault, T. A. (2010) Posttranslational stability of the heme biosynthetic enzyme ferrochelatase is dependent on iron availability and intact iron-sulfur cluster assembly machinery. *Blood* **115**, 860-869

176. Sellers, V. M., Johnson, M. K., and Dailey, H. A. (1996) Function of the [2FE-2S] cluster in mammalian ferrochelatase: a possible role as a nitric oxide sensor. *Biochemistry* **35**, 2699-2704

177. Shah, D. I., Takahashi-Makise, N., Cooney, J. D., Li, L., Schultz, I. J., Pierce, E. L., Narla, A., Seguin, A., Hattangadi, S. M., Medlock, A. E., Langer, N. B., Dailey, T. A., Hurst, S. N., Faccenda, D., Wiwczar, J. M., Heggers, S. K., Vogin, G., Chen, W., Chen, C., Campagna, D. R., Brugnara, C., Zhou, Y., Ebert, B. L., Danial, N. N., Fleming, M. D., Ward, D. M., Campanella, M., Dailey, H. A., Kaplan, J., and Paw, B. H. (2012) Mitochondrial Atpif1 regulates haem synthesis in developing erythroblasts. *Nature* **491**, 608-612

178. Chung, J., Wittig, J. G., Ghamari, A., Maeda, M., Dailey, T. A., Bergonia, H., Kafina, M. D., Coughlin, E. E., Minogue, C. E., Hebert, A. S., Li, L., Kaplan, J., Lodish, H. F., Bauer, D. E., Orkin, S. H., Cantor, A. B., Maeda, T., Phillips, J. D., Coon, J. J., Pagliarini, D. J., Dailey, H. A., and Paw, B. H. (2017) Erythropoietin signaling regulates heme biosynthesis. *Elife* **6**

179. Landefeld, C., Kentouche, K., Gruhn, B., Stauch, T., Rossler, S., Schuppan, D., Whatley, S. D., Beck, J. F., and Stolzel, U. (2016) X-linked protoporphyria: Iron supplementation improves protoporphyrin overload, liver damage and anaemia. *Br J Haematol* **173**, 482-484

180. Barman-Aksozen, J., Minder, E. I., Schubiger, C., Biolcati, G., and Schneider-Yin, X. (2015) In ferrochelatase-deficient protoporphyria patients, ALAS2 expression is enhanced and erythrocytic protoporphyrin concentration correlates with iron availability. *Blood Cells Mol Dis* **54**, 71-77

181. Barman-Aksozen, J., Beguin, C., Dogar, A. M., Schneider-Yin, X., and Minder, E. I. (2013) Iron availability modulates aberrant splicing of ferrochelatase through the iron- and 2-oxoglutarate dependent dioxygenase Jmjd6 and U2AF(65.). *Blood Cells Mol Dis* **51**, 151-161

182. Bailey, H. J., Bezerra, G. A., Marcero, J. R., Padhi, S., Foster, W. R., Rembeza, E., Roy, A., Bishop, D. F., Desnick, R. J., Bulusu, G., Dailey, H. A., Jr., and Yue, W. W. (2020) Human aminolevulinate synthase structure reveals a eukaryotic-specific autoinhibitory loop regulating substrate binding and product release. *Nat Commun* **11**(1), 1-12

183. Na, I., Catena, D., Kong, M. J., Ferreira, G. C., and Uversky, V. N. (2018) Anti-Correlation between the Dynamics of the Active Site Loop and C-Terminal Tail in Relation to the Homodimer Asymmetry of the Mouse Erythroid 5-Aminolevulinate Synthase. *Int J Mol Sci* **19**

184. Yamauchi, K., Hayashi, N., and Kikuchi, G. (1980) Cell-free synthesis of rat liver delta-aminolevulinate synthase and possible occurrence of processing of the enzyme protein in the course of its translocation from the cytosol into the mitochondrial matrix. *FEBS Lett* **115**, 15-18

185. Srivastava, G., Borthwick, I. A., Maguire, D. J., Elferink, C. J., Bawden, M. J., Mercer, J. F., and May, B. K. (1988) Regulation of 5-aminolevulinate synthase mRNA in different rat tissues. *J Biol Chem* **263**, 5202-5209

186. Vogtle, F. N., Wortelkamp, S., Zahedi, R. P., Becker, D., Leidhold, C., Gevaert, K., Kellermann, J., Voos, W., Sickmann, A., Pfanner, N., and Meisinger, C. (2009) Global analysis of the mitochondrial N-proteome identifies a processing peptidase critical for protein stability. *Cell* **139**, 428-439

187. Volland, C., and Urban-Grimal, D. (1988) The presequence of yeast 5-aminolevulinate synthase is not required for targeting to mitochondria. *J Biol Chem* **263**, 8294-8299

188. Schoenhaut, D. S., and Curtis, P. J. (1986) Nucleotide sequence of mouse 5-aminolevulinic acid synthase cDNA and expression of its gene in hepatic and erythroid tissues. *Gene* **48**, 55-63

189. Hunter, G. A., and Ferreira, G. C. (2009) 5-aminolevulinate synthase: catalysis of the first step of heme biosynthesis. *Cell Mol Biol (Noisy-le-grand)* **55**, 102-110

190. Kadirvel, S., Furuyama, K., Harigae, H., Kaneko, K., Tamai, Y., Ishida, Y., and Shibahara, S. (2012) The carboxyl-terminal region of erythroid-specific 5-aminolevulinate synthase acts as an intrinsic modifier for its catalytic activity and protein stability. *Exp Hematol* **40**, 477-486 e471

191. Grishin, N. V., Phillips, M. A., and Goldsmith, E. J. (1995) Modeling of the spatial structure of eukaryotic ornithine decarboxylases. *Protein Sci* **4**, 1291-1304

192. Fanica-Gaignier, M., and Clement-Metral, J. (1973) 5-Aminolevulinic-acid synthetase of Rhodopseudomonas spheroides Y. Purification and some properties. *Eur J Biochem* **40**, 13-18

193. Stojanovski, B. M., Hunter, G. A., Jahn, M., Jahn, D., and Ferreira, G. C. (2014) Unstable reaction intermediates and hysteresis during the catalytic cycle of 5-aminolevulinate synthase: implications from using pseudo and alternate substrates and a promiscuous enzyme variant. *J Biol Chem* **289**, 22915-22925

194. Shoolingin-Jordan, P. M., LeLean, J. E., and Lloyd, A. J. (1997) Continuous coupled assay for 5-aminolevulinate synthase. *Methods Enzymol* **281**, 309-316

195. Kaufholz, A. L., Hunter, G. A., Ferreira, G. C., Lendrihas, T., Hering, V., Layer, G., Jahn, M., and Jahn, D. (2013) Aminolaevulinic acid synthase of Rhodobacter capsulatus: high-resolution kinetic investigation of the structural basis for substrate binding and catalysis. *Biochem J* **451**, 205-216

196. Hunter, G. A., and Ferreira, G. C. (1999) Pre-steady-state reaction of 5-aminolevulinate synthase. Evidence for a rate-determining product release. *J Biol Chem* **274**, 12222-12228

197. Zaman, Z., Jordan, P. M., and Akhtar, M. (1973) Mechanism and stereochemistry of the 5-aminolaevulinate synthetase reaction. *Biochem J* **135**, 257-263

198. Bawden, M. J., Borthwick, I. A., Healy, H. M., Morris, C. P., May, B. K., and Elliott, W. H. (1987) Sequence of human 5-aminolevulinate synthase cDNA. *Nucleic Acids Res* **15**, 8563

199. Sutherland, G. R., Baker, E., Callen, D. F., Hyland, V. J., May, B. K., Bawden, M. J., Healy, H. M., and Borthwick, I. A. (1988) 5-Aminolevulinate synthase is at 3p21 and thus not the primary defect in X-linked sideroblastic anemia. *Am J Hum Genet* **43**, 331-335

200. Fraser, D. J., Zumsteg, A., and Meyer, U. A. (2003) Nuclear receptors constitutive androstane receptor and pregnane X receptor activate a drug-responsive enhancer of the murine 5-aminolevulinic acid synthase gene. *J Biol Chem* **278**, 39392-39401

201. Roberts, A. G., Redding, S. J., and Llewellyn, D. H. (2005) An alternatively-spliced exon in the 5'-UTR of human ALAS1 mRNA inhibits translation and renders it resistant to haem-mediated decay. *FEBS Lett* **579**, 1061-1066

202. Drew, P. D., and Ades, I. Z. (1989) Regulation of the stability of chicken embryo liver delta-aminolevulinate synthase mRNA by hemin. *Biochem Biophys Res Commun* **162**, 102-107

203. Goodfellow, B. J., Dias, J. S., Ferreira, G. C., Henklein, P., Wray, V., and Macedo, A. L. (2001) The solution structure and heme binding of the presequence of murine 5-aminolevulinate synthase. *FEBS Lett* **505**, 325-331

204. Pishesha, N., Thiru, P., Shi, J., Eng, J. C., Sankaran, V. G., and Lodish, H. F. (2014) Transcriptional divergence and conservation of human and mouse erythropoiesis. *Proc Natl Acad Sci U S A* **111**, 4103-4108

205. Doty, R. T., Phelps, S. R., Shadle, C., Sanchez-Bonilla, M., Keel, S. B., and Abkowitz, J. L. (2015) Coordinate expression of heme and globin is essential for effective erythropoiesis. *J Clin Invest* **125**, 4681-4691

206. Gautier, E. F., Ducamp, S., Leduc, M., Salnot, V., Guillonneau, F., Dussiot, M., Hale, J., Giarratana, M. C., Raimbault, A., Douay, L., Lacombe, C., Mohandas, N., Verdier, F., Zermati, Y., and Mayeux, P. (2016) Comprehensive Proteomic Analysis of Human Erythropoiesis. *Cell Rep* **16**, 1470-1484

207. Lin, C. S., Lim, S. K., D'Agati, V., and Costantini, F. (1996) Differential effects of an erythropoietin receptor gene disruption on primitive and definitive erythropoiesis. *Genes Dev* **10**, 154-164

208. Conboy, J. G., Cox, T. C., Bottomley, S. S., Bawden, M. J., and May, B. K. (1992) Human erythroid 5-aminolevulinate synthase. Gene structure and species-specific differences in alternative RNA splicing. *J Biol Chem* **267**, 18753-18758

209. Kramer, M. F., Gunaratne, P., and Ferreira, G. C. (2000) Transcriptional regulation of the murine erythroid-specific 5-aminolevulinate synthase gene. *Gene* **247**, 153-166

210. Hofer, T., Wenger, R. H., Kramer, M. F., Ferreira, G. C., and Gassmann, M. (2003) Hypoxic up-regulation of erythroid 5-aminolevulinate synthase. *Blood* **101**, 348-350

211. Zhang, F. L., Shen, G. M., Liu, X. L., Wang, F., Zhao, H. L., Yu, J., and Zhang, J. W. (2011) Hypoxic induction of human erythroid-specific delta-aminolevulinate synthase mediated by hypoxia-inducible factor 1. *Biochemistry* **50**, 1194-1202

212. Surinya, K. H., Cox, T. C., and May, B. K. (1998) Identification and characterization of a conserved erythroid-specific enhancer located in intron 8 of the human 5-aminolevulinate synthase 2 gene. *J Biol Chem* **273**, 16798-16809

213. Tanimura, N., Miller, E., Igarashi, K., Yang, D., Burstyn, J. N., Dewey, C. N., and Bresnick, E. H. (2016) Mechanism governing heme synthesis reveals a GATA factor/heme circuit that controls differentiation. *EMBO Rep* **17**, 249-265

214. Zhang, Y., Zhang, J., An, W., Wan, Y., Ma, S., Yin, J., Li, X., Gao, J., Yuan, W., Guo, Y., Engel, J. D., Shi, L., Cheng, T., and Zhu, X. (2017) Intron 1 GATA site enhances ALAS2 expression indispensably during erythroid differentiation. *Nucleic Acids Res* **45**, 657-671

215. Dandekar, T., Stripecke, R., Gray, N. K., Goossen, B., Constable, A., Johansson, H. E., and Hentze, M. W. (1991) Identification of a novel iron-responsive element in murine and human erythroid delta-aminolevulinic acid synthase mRNA. *EMBO J* **10**, 1903-1909

216. Melefors, O., Goossen, B., Johansson, H. E., Stripecke, R., Gray, N. K., and Hentze, M. W. (1993) Translational control of 5-aminolevulinate synthase mRNA by iron-responsive elements in erythroid cells. *J Biol Chem* **268**, 5974-5978

217. Chen, J. J. (2014) Translational control by heme-regulated eIF2alpha kinase during erythropoiesis. *Curr Opin Hematol* **21**, 172-178

218. Chiabrando, D., Mercurio, S., and Tolosano, E. (2014) Heme and erythropoieis: more than a structural role. *Haematologica* **99**, 973-983

219. Hentze, M. W., and Kuhn, L. C. (1996) Molecular control of vertebrate iron metabolism: mRNA-based regulatory circuits operated by iron, nitric oxide, and oxidative stress. *Proc Natl Acad Sci U S A* **93**, 8175-8182

220. Gray, N. K., and Hentze, M. W. (1994) Iron regulatory protein prevents binding of the 43S translation pre-initiation complex to ferritin and eALAS mRNAs. *EMBO J* **13**, 3882-3891

221. Rouault, T. A. (2006) The role of iron regulatory proteins in mammalian iron homeostasis and disease. *Nat Chem Biol* **2**, 406-414

222. Casey, J. L., Hentze, M. W., Koeller, D. M., Caughman, S. W., Rouault, T. A., Klausner, R. D., and Harford, J. B. (1988) Iron-responsive elements: regulatory RNA sequences that control mRNA levels and translation. *Science* **240**, 924-928

223. Gunshin, H., Mackenzie, B., Berger, U. V., Gunshin, Y., Romero, M. F., Boron, W. F., Nussberger, S., Gollan, J. L., and Hediger, M. A. (1997) Cloning and characterization of a mammalian proton-coupled metal-ion transporter. *Nature* **388**, 482-488

224. Wang, J., and Pantopoulos, K. (2011) Regulation of cellular iron metabolism. *Biochem J* **434**, 365-381

225. Schranzhofer, M., Schifrer, M., Cabrera, J. A., Kopp, S., Chiba, P., Beug, H., and Mullner, E. W. (2006) Remodeling the regulation of iron metabolism during erythroid differentiation to ensure efficient heme biosynthesis. *Blood* **107**, 4159-4167

226. Guo B, Y. Y., Leibold EA. (1994) Iron regulates cytoplasmic levels of a novel iron-responsive element-binding protein without aconitase activity. *J Biol Chem* **269**, 24252-24260

227. Dupuy, J., Volbeda, A., Carpentier, P., Darnault, C., Moulis, J. M., and Fontecilla-Camps, J. C. (2006) Crystal structure of human iron regulatory protein 1 as cytosolic aconitase. *Structure* **14**, 129-139

228. Ishikawa, H., Kato, M., Hori, H., Ishimori, K., Kirisako, T., Tokunaga, F., and Iwai, K. (2005) Involvement of heme regulatory motif in heme-mediated ubiquitination and degradation of IRP2. *Mol Cell* **19**, 171-181

229. Galy, B., Ferring, D., Minana, B., Bell, O., Janser, H. G., Muckenthaler, M., Schumann, K., and Hentze, M. W. (2005) Altered body iron distribution and microcytosis in mice deficient in iron regulatory protein 2 (IRP2). *Blood* **106**, 2580-2589

230. Rodriguez-Manzaneque, M. T., Tamarit, J., Belli, G., Ros, J., and Herrero, E. (2002) Grx5 is a mitochondrial glutaredoxin required for the activity of iron/sulfur enzymes. *Mol Biol Cell* **13**, 1109-1121

231. Zhang, S., Macias-Garcia, A., Ulirsch, J. C., Velazquez, J., Butty, V. L., Levine, S. S., Sankaran, V. G., and Chen, J. J. (2019) HRI coordinates translation necessary for protein homeostasis and mitochondrial function in erythropoiesis. *Elife* **8**

232. May, A., and Bishop, D. F. (1998) The molecular biology and pyridoxine responsiveness of X-linked sideroblastic anaemia. *Haematologica* **83**, 56-70

233. Tian, Q., Li, T., Hou, W., Zheng, J., Schrum, L. W., and Bonkovsky, H. L. (2011) Lon peptidase 1 (LONP1)-dependent breakdown of mitochondrial 5-aminolevulinic acid synthase protein by heme in human liver cells. *J Biol Chem* **286**, 26424-26430

234. Abu-Farha, M., Niles, J., and Willmore, W. G. (2005) Erythroid-specific 5-aminolevulinate synthase protein is stabilized by low oxygen and proteasomal inhibition. *Biochem Cell Biol* **83**, 620-630

235. De Franceschi, L., Bertoldi, M., De Falco, L., Santos Franco, S., Ronzoni, L., Turrini, F., Colancecco, A., Camaschella, C., Cappellini, M. D., and Iolascon, A. (2011) Oxidative stress modulates heme synthesis and induces peroxiredoxin-2 as a novel cytoprotective response in beta-thalassemic erythropoiesis. *Haematologica* **96**, 1595-1604

236. Kardon, J. R., Moroco, J. A., Engen, J. R., and Baker, T. A. (2020) Mitochondrial ClpX activates an essential biosynthetic enzyme through partial unfolding. *Elife* **9**

237. Labbe, R. F., Kurumada, T., and Onisawa, J. (1965) The role of succinyl-CoA synthetase in the control of heme biosynthesis. *Biochim Biophys Acta* **111**, 403-415

238. Garcia-Santos, D., Schranzhofer, M., Bergeron, R., Sheftel, A. D., and Ponka, P. (2017) Extracellular glycine is necessary for optimal hemoglobinization of erythroid cells. *Haematologica* **102**, 1314-1323

239. Matte, A., Federti, E., Winter, M., Koerner, A., Harmeier, A., Mazer, N., Tomka, T., Di Paolo, M. L., De Falco, L., Andolfo, I., Beneduce, E., Iolascon, A., Macias-Garcia, A., Chen, J. J., Janin, A., Lebouef, C., Turrini, F., Brugnara, C., and De Franceschi, L. (2019) Bitopertin, a selective oral GLYT1 inhibitor, improves anemia in a mouse model of beta-thalassemia. *JCI Insight* **4**

240. Schranzhofer, M., Bergeron, R., and Ponka, P. (2011) Glycine Transporter 1 Plays a Crucial Role in Hemoglobinization. *Blood* **118**, 345-345

241. Abboud, M. R., Alexander, D., and Najjar, S. S. (1985) Diabetes mellitus, thiamine-dependent megaloblastic anemia, and sensorineural deafness associated with deficient alpha-ketoglutarate dehydrogenase activity. *J Pediatr* **107**, 537-541

242. Kacso, G., Ravasz, D., Doczi, J., Nemeth, B., Madgar, O., Saada, A., Ilin, P., Miller, C., Ostergaard, E., Iordanov, I., Adams, D., Vargedo, Z., Araki, M., Araki, K., Nakahara, M., Ito, H., Gal, A., Molnar, M. J., Nagy, Z., Patocs, A., Adam-Vizi, V., and Chinopoulos, C. (2016) Two transgenic mouse models for beta-subunit components of succinate-CoA ligase yielding pleiotropic metabolic alterations. *Biochem J* **473**, 3463-3485

243. Kingsley, P. D., Greenfest-Allen, E., Frame, J. M., Bushnell, T. P., Malik, J., McGrath, K. E., Stoeckert, C. J., and Palis, J. (2013) Ontogeny of erythroid gene expression. *Blood* **121**, e5-e13

244. Zhen, R., Moo, C., Zhao, Z., Chen, M., Feng, H., Zheng, X., Zhang, L., Shi, J., and Chen, C. (2020) Wdr26 regulates nuclear condensation in developing erythroblasts. *Blood* **135**, 208-219

245. Lin, H., Su, X., and He, B. (2012) Protein lysine acylation and cysteine succination by intermediates of energy metabolism. *ACS Chem Biol* **7**, 947-960

246. Du, J., Zhou, Y., Su, X., Yu, J. J., Khan, S., Jiang, H., Kim, J., Woo, J., Kim, J. H., Choi, B. H., He, B., Chen, W., Zhang, S., Cerione, R. A., Auwerx, J., Hao, Q., and Lin, H. (2011) Sirt5 is a NAD-dependent protein lysine demalonylase and desuccinylase. *Science* **334**, 806-809

247. Aivado, M., Gattermann, N., Rong, A., Giagounidis, A. A., Prall, W. C., Czibere, A., Hildebrandt, B., Haas, R., and Bottomley, S. S. (2006) X-linked sideroblastic anemia associated with a novel ALAS2 mutation and unfortunate skewed X-chromosome inactivation patterns. *Blood Cells Mol Dis* **37**, 40-45

248. Brancaleoni, V., Balwani, M., Granata, F., Graziadei, G., Missineo, P., Fiorentino, V., Fustinoni, S., Cappellini, M. D., Naik, H., Desnick, R. J., and Di Pierro, E. (2016) X-chromosomal inactivation directly influences the phenotypic manifestation of X-linked protoporphyria. *Clin Genet* **89**, 20-26

249. Camaschella, C. (2009) Hereditary sideroblastic anemias: pathophysiology, diagnosis, and treatment. *Semin Hematol* **46**, 371-377

250. Harigae, H., and Furuyama, K. (2010) Hereditary sideroblastic anemia: pathophysiology and gene mutations. *Int J Hematol* **92**, 425-431

251. Campagna, D. R., de Bie, C. I., Schmitz-Abe, K., Sweeney, M., Sendamarai, A. K., Schmidt, P. J., Heeney, M. M., Yntema, H. G., Kannengiesser, C., Grandchamp, B., Niemeyer, C. M., Knoers, N. V., Swart, S., Marron, G., van Wijk, R., Raymakers, R. A., May, A., Markianos, K., Bottomley, S. S., Swinkels, D. W., and Fleming, M. D. (2014) X-linked sideroblastic anemia due to ALAS2 intron 1 enhancer element GATA-binding site mutations. *Am J Hematol* **89**, 315-319

252. Bekri, S., May, A., Cotter, P. D., Al-Sabah, A. I., Guo, X., Masters, G. S., and Bishop, D. F. (2003) A promoter mutation in the erythroid-specific 5-aminolevulinate synthase (ALAS2) gene causes X-linked sideroblastic anemia. *Blood* **102**, 698-704

253. Bishop, D. F., Tchaikovskii, V., Nazarenko, I., and Desnick, R. J. (2013) Molecular expression and characterization of erythroid-specific 5-aminolevulinate synthase gain-of-function mutations causing X-linked protoporphyria. *Mol Med* **19**, 18-25

254. Ducamp, S., Schneider-Yin, X., de Rooij, F., Clayton, J., Fratz, E. J., Rudd, A., Ostapowicz, G., Varigos, G., Lefebvre, T., Deybach, J. C., Gouya, L., Wilson, P., Ferreira, G. C., Minder, E. I., and Puy, H. (2013) Molecular and functional analysis of the C-terminal region of human erythroid-specific 5-aminolevulinic synthase associated with X-linked dominant protoporphyria (XLDPP). *Hum Mol Genet* **22**, 1280-1288

255. Fratz, E. J., Clayton, J., Hunter, G. A., Ducamp, S., Breydo, L., Uversky, V. N., Deybach, J. C., Gouya, L., Puy, H., and Ferreira, G. C. (2015) Human Erythroid 5-Aminolevulinate Synthase Mutations Associated with X-Linked Protoporphyria Disrupt the Conformational Equilibrium and Enhance Product Release. *Biochemistry* **54**, 5617-5631

256. Parker, C. J., Desnick, R. J., Bissel, M. D., Bloomer, J. R., Singal, A., Gouya, L., Puy, H., Anderson, K. E., Balwani, M., and Phillips, J. D. (2019) Results of a pilot study of isoniazid in patients with erythropoietic protoporphyria. *Mol Genet Metab* **128**, 309-313

257. Wang, P., Sachar, M., Lu, J., Shehu, A. I., Zhu, J., Chen, J., Liu, K., Anderson, K. E., Xie, W., Gonzalez, F. J., Klaassen, C. D., and Ma, X. (2019) The essential role of the transporter ABCG2 in the pathophysiology of erythropoietic protoporphyria. *Sci Adv* **5**, eaaw6127

258. Miyata, H., Takada, T., Toyoda, Y., Matsuo, H., Ichida, K., and Suzuki, H. (2016) Identification of Febuxostat as a New Strong ABCG2 Inhibitor: Potential Applications and Risks in Clinical Situations. *Front Pharmacol* **7**, 518

259. Al-Drees, M. A., Yeo, J. H., Boumelhem, B. B., Antas, V. I., Brigden, K. W., Colonne, C. K., and Fraser, S. T. (2015) Making Blood: The Haematopoietic Niche throughout Ontogeny. *Stem Cells Int* **2015**, 571893

260. Palis, J. (2014) Primitive and definitive erythropoiesis in mammals. *Front Physiol* **5**, 3

261. Paulson, R. F., Ruan, B., Hao, S., and Chen, Y. (2020) Stress Erythropoiesis is a Key Inflammatory Response. *Cells* **9**

262. Hom, J., Dulmovits, B. M., Mohandas, N., and Blanc, L. (2015) The erythroblastic island as an emerging paradigm in the anemia of inflammation. *Immunol Res* **63**, 75-89

263. Chow, D. C., Wenning, L. A., Miller, W. M., and Papoutsakis, E. T. (2001) Modeling pO(2) distributions in the bone marrow hematopoietic compartment. II. Modified Kroghian models. *Biophys J* **81**, 685-696

264. Mao, B., Huang, S., Lu, X., Sun, W., Zhou, Y., Pan, X., Yu, J., Lai, M., Chen, B., Zhou, Q., Mao, S., Bian, G., Zhou, J., Nakahata, T., and Ma, F. (2016) Early Development of Definitive Erythroblasts from Human Pluripotent Stem Cells Defined by Expression of Glycophorin A/CD235a, CD34, and CD36. *Stem Cell Reports* **7**, 869-883

265. Zhu, J., and Emerson, S. G. (2002) Hematopoietic cytokines, transcription factors and lineage commitment. *Oncogene* **21**, 3295-3313

266. Oburoglu, L., Romano, M., Taylor, N., and Kinet, S. (2016) Metabolic regulation of hematopoietic stem cell commitment and erythroid differentiation. *Curr Opin Hematol* **23**, 198-205

267. Ferreira, R., Ohneda, K., Yamamoto, M., and Philipsen, S. (2005) GATA1 function, a paradigm for transcription factors in hematopoiesis. *Mol Cell Biol* **25**, 1215-1227

268. Lentjes, M. H., Niessen, H. E., Akiyama, Y., de Bruine, A. P., Melotte, V., and van Engeland, M. (2016) The emerging role of GATA transcription factors in development and disease. *Expert Rev Mol Med* **18**, e3

269. Li, J., Hale, J., Bhagia, P., Xue, F., Chen, L., Jaffray, J., Yan, H., Lane, J., Gallagher, P. G., Mohandas, N., Liu, J., and An, X. (2014) Isolation and transcriptome analyses of human erythroid progenitors: BFU-E and CFU-E. *Blood* **124**, 3636-3645

270. Gregory, C. J., and Eaves, A. C. (1978) Three stages of erythropoietic progenitor cell differentiation distinguished by a number of physical and biologic properties. *Blood* **51**, 527-537

271. Jelkmann, W. (2011) Regulation of erythropoietin production. *J Physiol* **589**, 1251-1258

272. Gregory, C. J. (1976) Erythropoietin sensitivity as a differentiation marker in the hemopoietic system: studies of three erythropoietic colony responses in culture. *J Cell Physiol* **89**, 289-301

273. Roversi, F. M., Pericole, F. V., Machado-Neto, J. A., da Silva Santos Duarte, A., Longhini, A. L., Corrocher, F. A., Palodetto, B., Ferro, K. P., Rosa, R. G., Baratti, M. O., Verjovski-Almeida, S., Traina, F., Molinari, A., Botta, M., and Saad, S. T. (2017) Hematopoietic cell kinase (HCK) is a potential therapeutic target for dysplastic and leukemic cells due to integration of erythropoietin/PI3K pathway and regulation of erythropoiesis: HCK in erythropoietin/PI3K pathway. *Biochim Biophys Acta Mol Basis Dis* **1863**, 450-461

274. Angelillo-Scherrer, A., Burnier, L., Lambrechts, D., Fish, R. J., Tjwa, M., Plaisance, S., Sugamele, R., DeMol, M., Martinez-Soria, E., Maxwell, P. H., Lemke, G., Goff, S. P., Matsushima, G. K., Earp, H. S., Chanson, M., Collen, D., Izui, S., Schapira, M., Conway, E. M., and Carmeliet, P. (2008) Role of Gas6 in erythropoiesis and anemia in mice. *J Clin Invest* **118**, 583-596

275. Lodish, H., Flygare, J., and Chou, S. (2010) From stem cell to erythroblast: regulation of red cell production at multiple levels by multiple hormones. *IUBMB Life* **62**, 492-496

276. Yeo, J. H., Lam, Y. W., and Fraser, S. T. (2019) Cellular dynamics of mammalian red blood cell production in the erythroblastic island niche. *Biophys Rev* **11**, 873-894

277. Bessis, M. (1958) L'ilot erythroblastique. Unite functionelle de la moelle osseuse. *Rev Hematol.* **13**, 8-11

278. Chasis, J. A., and Mohandas, N. (2008) Erythroblastic islands: niches for erythropoiesis. *Blood* **112**, 470-478

279. Korolnek, T., and Hamza, I. (2015) Macrophages and iron trafficking at the birth and death of red cells. *Blood* **125**, 2893-2897

280. Hattangadi, S. M., Wong, P., Zhang, L., Flygare, J., and Lodish, H. F. (2011) From stem cell to red cell: regulation of erythropoiesis at multiple levels by multiple proteins, RNAs, and chromatin modifications. *Blood* **118**, 6258-6268

281. Fujiwara, Y., Browne, C. P., Cunniff, K., Goff, S. C., and Orkin, S. H. (1996) Arrested development of embryonic red cell precursors in mouse embryos lacking transcription factor GATA-1. *Proc Natl Acad Sci U S A* **93**, 12355-12358

282. An, X., Schulz, V. P., Li, J., Wu, K., Liu, J., Xue, F., Hu, J., Mohandas, N., and Gallagher, P. G. (2014) Global transcriptome analyses of human and murine terminal erythroid differentiation. *Blood* **123**, 3466-3477

283. Yin, X., and Dailey, H. A. (1998) Erythroid 5-aminolevulinate synthase is required for erythroid differentiation in mouse embryonic stem cells. *Blood Cells Mol Dis* **24**, 41-53

284. Fujiwara, T., Okamoto, K., Niikuni, R., Takahashi, K., Okitsu, Y., Fukuhara, N., Onishi, Y., Ishizawa, K., Ichinohasama, R., Nakamura, Y., Nakajima, M., Tanaka, T., and Harigae, H. (2014) Effect of 5-aminolevulinic acid on erythropoiesis: a preclinical in vitro characterization for the treatment of congenital sideroblastic anemia. *Biochem Biophys Res Commun* **454**, 102-108

285. Seguin, A., Takahashi-Makise, N., Yien, Y. Y., Huston, N. C., Whitman, J. C., Musso, G., Wallace, J. A., Bradley, T., Bergonia, H. A., Kafina, M. D., Matsumoto, M., Igarashi, K., Phillips, J. D., Paw, B. H., Kaplan, J., and Ward, D. M. (2017) Reductions in the mitochondrial ABC transporter Abcb10 affect the transcriptional profile of heme biosynthesis genes. *J Biol Chem* **292**, 16284-16299

286. Anderson, K. E., Drummond, G. S., Freddara, U., Sardana, M. K., and Sassa, S. (1981) Porphyrogenic effects and induction of heme oxygenase in vivo by delta-aminolevulinic acid. *Biochim Biophys Acta* **676**, 289-299

287. Ogawa, K., Sun, J., Taketani, S., Nakajima, O., Nishitani, C., Sassa, S., Hayashi, N., Yamamoto, M., Shibahara, S., Fujita, H., and Igarashi, K. (2001) Heme mediates

derepression of Maf recognition element through direct binding to transcription repressor Bach1. *EMBO J* **20**, 2835-2843

288. Wu, H., Liu, X., Jaenisch, R., and Lodish, H. F. (1995) Generation of committed erythroid BFU-E and CFU-E progenitors does not require erythropoietin or the erythropoietin receptor. *Cell* **83**, 59-67

289. Jayapal, S. R., Wang, C. Q., Bisteau, X., Caldez, M. J., Lim, S., Tergaonkar, V., Osato, M., and Kaldis, P. (2015) Hematopoiesis specific loss of Cdk2 and Cdk4 results in increased erythrocyte size and delayed platelet recovery following stress. *Haematologica* **100**, 431-438

290. Igarashi, K., Hoshino, H., Muto, A., Suwabe, N., Nishikawa, S., Nakauchi, H., and Yamamoto, M. (1998) Multivalent DNA binding complex generated by small Maf and Bach1 as a possible biochemical basis for beta-globin locus control region complex. *J Biol Chem* **273**, 11783-11790

291. Quigley, J. G., Yang, Z., Worthington, M. T., Phillips, J. D., Sabo, K. M., Sabath, D. E., Berg, C. L., Sassa, S., Wood, B. L., and Abkowitz, J. L. (2004) Identification of a human heme exporter that is essential for erythropoiesis. *Cell* **118**, 757-766

292. Khan, A. A., and Quigley, J. G. (2011) Control of intracellular heme levels: heme transporters and heme oxygenases. *Biochim Biophys Acta* **1813**, 668-682

293. Negrin, R. S., Stein, R., Vardiman, J., Doherty, K., Cornwell, J., Krantz, S., and Greenberg, P. L. (1993) Treatment of the anemia of myelodysplastic syndromes using recombinant human granulocyte colony-stimulating factor in combination with erythropoietin. *Blood* **82**, 737-743

294. Ji, P., Murata-Hori, M., and Lodish, H. F. (2011) Formation of mammalian erythrocytes: chromatin condensation and enucleation. *Trends Cell Biol* **21**, 409-415

295. Yoshida, H., Kawane, K., Koike, M., Mori, Y., Uchiyama, Y., and Nagata, S. (2005) Phosphatidylserine-dependent engulfment by macrophages of nuclei from erythroid precursor cells. *Nature* **437**, 754-758

296. Bessis, M., and Weed, R. I. (1973) The structure of normal and pathologic erythrocytes. *Adv Biol Med Phys* **14**, 35-91

297. Chen, T. L., Chiang, Y. W., Lin, G. L., Chang, H. H., Lien, T. S., Sheh, M. H., and Sun, D. S. (2018) Different effects of granulocyte colony-stimulating factor and erythropoietin on erythropoiesis. *Stem Cell Res Ther* **9**, 119

298. Mohandas, N., and Gallagher, P. G. (2008) Red cell membrane: past, present, and future. *Blood* **112**, 3939-3948

299. Low, P. S. (1991) Role of hemoglobin denaturation and band 3 clustering in initiating red cell removal. *Adv Exp Med Biol* **307**, 173-183

300. Bohr, C., Hasselbalch, K. and Krogh, A. (1904) Ueber einen in biologischer Beziehung wichtigen Einfluss, den die Kohlensäurespannung des Blutes auf dessen Sauerstoffbindung übt 1. *Skandinavisches Archiv Für Physiologie* **16**, 402-412

301. Russo, R., Benazzi, L., and Perrella, M. (2001) The Bohr effect of hemoglobin intermediates and the role of salt bridges in the tertiary/quaternary transitions. *J Biol Chem* **276**, 13628-13634

302. Christiansen, J., Douglas, C. G., and Haldane, J. S. (1914) The absorption and dissociation of carbon dioxide by human blood. *J Physiol* **48**, 244-271

303. Teboul, J. L., and Scheeren, T. (2017) Understanding the Haldane effect. *Intensive Care Med* **43**, 91-93

304. Lee, S. H., Crocker, P. R., Westaby, S., Key, N., Mason, D. Y., Gordon, S., and Weatherall, D. J. (1988) Isolation and immunocytochemical characterization of human bone marrow stromal macrophages in hemopoietic clusters. *J Exp Med* **168**, 1193-1198

305. Bessis, M., Mize, C., and Prenant, M. (1978) Erythropoiesis: comparison of in vivo and in vitro amplification. *Blood Cells* **4**, 155-174

306. Astwood, E., and Vora, A. (2011) Erythroblastic islands. *Blood* **117**, 10

307. Chow, A., Huggins, M., Ahmed, J., Hashimoto, D., Lucas, D., Kunisaki, Y., Pinho, S., Leboeuf, M., Noizat, C., van Rooijen, N., Tanaka, M., Zhao, Z. J., Bergman, A., Merad, M., and Frenette, P. S. (2013) CD169(+) macrophages provide a niche promoting erythropoiesis under homeostasis and stress. *Nat Med* **19**, 429-436

308. Ramos, P., Casu, C., Gardenghi, S., Breda, L., Crielaard, B. J., Guy, E., Marongiu, M. F., Gupta, R., Levine, R. L., Abdel-Wahab, O., Ebert, B. L., Van Rooijen, N., Ghaffari, S., Grady, R. W., Giardina, P. J., and Rivella, S. (2013) Macrophages support pathological erythropoiesis in polycythemia vera and beta-thalassemia. *Nat Med* **19**, 437-445

309. Jacobsen, R. N., Forristal, C. E., Raggatt, L. J., Nowlan, B., Barbier, V., Kaur, S., van Rooijen, N., Winkler, I. G., Pettit, A. R., and Levesque, J. P. (2014) Mobilization with granulocyte colony-stimulating factor blocks medullar erythropoiesis by depleting F4/80(+)VCAM1(+)CD169(+)ER-HR3(+)Ly6G(+) erythroid island macrophages in the mouse. *Exp Hematol* **42**, 547-561 e544

310. Juarez, J. G., Harun, N., Thien, M., Welschinger, R., Baraz, R., Pena, A. D., Pitson, S. M., Rettig, M., DiPersio, J. F., Bradstock, K. F., and Bendall, L. J. (2012) Sphingosine-1-phosphate facilitates trafficking of hematopoietic stem cells and their mobilization by CXCR4 antagonists in mice. *Blood* **119**, 707-716

311. Seu, K. G., Papoin, J., Fessler, R., Hom, J., Huang, G., Mohandas, N., Blanc, L., and Kalfa, T. A. (2017) Unraveling Macrophage Heterogeneity in Erythroblastic Islands. *Front Immunol* **8**, 1140

312. Yeo, J. H., McAllan, B. M., and Fraser, S. T. (2016) Scanning Electron Microscopy Reveals Two Distinct Classes of Erythroblastic Island Isolated from Adult Mammalian Bone Marrow. *Microsc Microanal* **22**, 368-378

313. Spring, F. A., Griffiths, R. E., Mankelow, T. J., Agnew, C., Parsons, S. F., Chasis, J. A., and Anstee, D. J. (2013) Tetraspanins CD81 and CD82 facilitate alpha4beta1-mediated adhesion of human erythroblasts to vascular cell adhesion molecule-1. *PLoS One* **8**, e62654

314. Lee, G., Lo, A., Short, S. A., Mankelow, T. J., Spring, F., Parsons, S. F., Yazdanbakhsh, K., Mohandas, N., Anstee, D. J., and Chasis, J. A. (2006) Targeted gene deletion demonstrates that the cell adhesion molecule ICAM-4 is critical for erythroblastic island formation. *Blood* **108**, 2064-2071

315. Soni, S., Bala, S., Gwynn, B., Sahr, K. E., Peters, L. L., and Hanspal, M. (2006) Absence of erythroblast macrophage protein (Emp) leads to failure of erythroblast nuclear extrusion. *J Biol Chem* **281**, 20181-20189

316. Soni, S., Bala, S., and Hanspal, M. (2008) Requirement for erythroblast-macrophage protein (Emp) in definitive erythropoiesis. *Blood Cells Mol Dis* **41**, 141-147

317. Bartnikas, T. B. (2012) Known and potential roles of transferrin in iron biology. *Biometals* **25**, 677-686

318. Leimberg, M. J., Prus, E., Konijn, A. M., and Fibach, E. (2008) Macrophages function as a ferritin iron source for cultured human erythroid precursors. *J Cell Biochem* **103**, 1211-1218

319. Policard, A., and Bessis, M. (1962) Micropinocytosis and rhopheocytosis. *Nature* **194**, 110-111

320. Ganz, T., and Nemeth, E. (2012) Hepcidin and iron homeostasis. *Biochim Biophys Acta* **1823**, 1434-1443

321. Kautz, L., Jung, G., Valore, E. V., Rivella, S., Nemeth, E., and Ganz, T. (2014) Identification of erythroferrone as an erythroid regulator of iron metabolism. *Nat Genet* **46**, 678-684

322. Miyanishi, M., Tada, K., Koike, M., Uchiyama, Y., Kitamura, T., and Nagata, S. (2007) Identification of Tim4 as a phosphatidylserine receptor. *Nature* **450**, 435-439

323. Toda, S., Segawa, K., and Nagata, S. (2014) MerTK-mediated engulfment of pyrenocytes by central macrophages in erythroblastic islands. *Blood* **123**, 3963-3971

324. Isern, J., Fraser, S. T., He, Z., and Baron, M. H. (2008) The fetal liver is a niche for maturation of primitive erythroid cells. *Proc Natl Acad Sci U S A* **105**, 6662-6667

325. Fraser, S. T., Midwinter, R. G., Coupland, L. A., Kong, S., Berger, B. S., Yeo, J. H., Andrade, O. C., Cromer, D., Suarna, C., Lam, M., Maghzal, G. J., Chong, B. H., Parish, C. R., and Stocker, R. (2015) Heme oxygenase-1 deficiency alters erythroblastic island formation, steady-state erythropoiesis and red blood cell lifespan in mice. *Haematologica* **100**, 601-610

326. Campbell, M. R., Karaca, M., Adamski, K. N., Chorley, B. N., Wang, X., and Bell, D. A. (2013) Novel hematopoietic target genes in the NRF2-mediated transcriptional pathway. *Oxid Med Cell Longev* **2013**, 120305

327. Li, W., Wang, Y., Zhao, H., Zhang, H., Xu, Y., Wang, S., Guo, X., Huang, Y., Zhang, S., Han, Y., Wu, X., Rice, C. M., Huang, G., Gallagher, P. G., Mendelson, A., Yazdanbakhsh, K., Liu, J., Chen, L., and An, X. (2019) Identification and transcriptome analysis of erythroblastic island macrophages. *Blood* **134**, 480-491

328. Paulson, R. F. (2019) Epo receptor marks the spot. *Blood* **134**, 413-414

329. Sawada, K., Krantz, S. B., Dessypris, E. N., Koury, S. T., and Sawyer, S. T. (1989) Human colony-forming units-erythroid do not require accessory cells, but do require direct interaction with insulin-like growth factor I and/or insulin for erythroid development. *J Clin Invest* **83**, 1701-1709

330. Rubiolo, C., Piazzolla, D., Meissl, K., Beug, H., Huber, J. C., Kolbus, A., and Baccarini, M. (2006) A balance between Raf-1 and Fas expression sets the pace of erythroid differentiation. *Blood* **108**, 152-159

331. Weiss, G., Ganz, T., and Goodnough, L. T. (2019) Anemia of inflammation. *Blood* **133**, 40-50

332. Kassebaum, N. J., Jasrasaria, R., Naghavi, M., Wulf, S. K., Johns, N., Lozano, R., Regan, M., Weatherall, D., Chou, D. P., Eisele, T. P., Flaxman, S. R., Pullan, R. L., Brooker, S. J., and Murray, C. J. (2014) A systematic analysis of global anemia burden from 1990 to 2010. *Blood* **123**, 615-624

333. Fitzsimons, E. J., and Brock, J. H. (2001) The anaemia of chronic disease. *BMJ* **322**, 811-812

334. Weinberg, E. D. (1984) Iron withholding: a defense against infection and neoplasia. *Physiol Rev* **64**, 65-102

335. Cassat, J. E., and Skaar, E. P. (2013) Iron in infection and immunity. *Cell Host Microbe* **13**, 509-519

336. Gutteridge, J. M., and Halliwell, B. (2010) Antioxidants: Molecules, medicines, and myths. *Biochem Biophys Res Commun* **393**, 561-564

337. Vreugdenhil, G., and Swaak, A. J. (1990) Anaemia in rheumatoid arthritis: pathogenesis, diagnosis and treatment. *Rheumatol Int* **9**, 243-257

338. Tilg, H., Ulmer, H., Kaser, A., and Weiss, G. (2002) Role of IL-10 for induction of anemia during inflammation. *J Immunol* **169**, 2204-2209

339. Libregts, S. F., Gutierrez, L., de Bruin, A. M., Wensveen, F. M., Papadopoulos, P., van Ijcken, W., Ozgur, Z., Philipsen, S., and Nolte, M. A. (2011) Chronic IFN-gamma production in mice induces anemia by reducing erythrocyte life span and inhibiting erythropoiesis through an IRF-1/PU.1 axis. *Blood* **118**, 2578-2588

340. Kikkawa, I., Saito, S., Tominaga, K., Hoshino, Y., Ooi, Y., and Nakano, M. (1998) Lipopolysaccharide (LPS) stimulates the production of tumor necrosis factor (TNF)-alpha and expression of inducible nitric oxide synthase (iNOS) by osteoclasts (OCL) in murine bone marrow cell culture. *Microbiol Immunol* **42**, 591-598

341. Papadaki, H. A., Kritikos, H. D., Valatas, V., Boumpas, D. T., and Eliopoulos, G. D. (2002) Anemia of chronic disease in rheumatoid arthritis is associated with increased apoptosis of bone marrow erythroid cells: improvement following anti-tumor necrosis factor-alpha antibody therapy. *Blood* **100**, 474-482

342. Rusten, L. S., and Jacobsen, S. E. (1995) Tumor necrosis factor (TNF)-alpha directly inhibits human erythropoiesis in vitro: role of p55 and p75 TNF receptors. *Blood* **85**, 989-996

343. Heideveld, E., Masiello, F., Marra, M., Esteghamat, F., Yagci, N., von Lindern, M., Migliaccio, A. R., and van den Akker, E. (2015) CD14+ cells from peripheral blood positively regulate hematopoietic stem and progenitor cell survival resulting in increased erythroid yield. *Haematologica* **100**, 1396-1406

344. Imagawa, S., Nakano, Y., Obara, N., Suzuki, N., Doi, T., Kodama, T., Nagasawa, T., and Yamamoto, M. (2003) A GATA-specific inhibitor (K-7174) rescues anemia induced by IL-1beta, TNF-alpha, or L-NMMA. *FASEB J* **17**, 1742-1744

345. La Ferla, K., Reimann, C., Jelkmann, W., and Hellwig-Burgel, T. (2002) Inhibition of erythropoietin gene expression signaling involves the transcription factors GATA-2 and NF-kappaB. *FASEB J* **16**, 1811-1813

346. Jelkmann, W. (1998) Proinflammatory cytokines lowering erythropoietin production. *J Interferon Cytokine Res* **18**, 555-559

347. Dai, C. H., Price, J. O., Brunner, T., and Krantz, S. B. (1998) Fas ligand is present in human erythroid colony-forming cells and interacts with Fas induced by interferon gamma to produce erythroid cell apoptosis. *Blood* **91**, 1235-1242

348. Secchiero, P., Melloni, E., Heikinheimo, M., Mannisto, S., Di Pietro, R., Iacone, A., and Zauli, G. (2004) TRAIL regulates normal erythroid maturation through an ERK-dependent pathway. *Blood* **103**, 517-522

349. Dallalio, G., and Means, R. T., Jr. (2003) Effects of oxidative stress on human erythroid colony formation: Modulation by gamma-interferon. *J Lab Clin Med* **141**, 395-400

350. McCranor, B. J., Kim, M. J., Cruz, N. M., Xue, Q. L., Berger, A. E., Walston, J. D., Civin, C. I., and Roy, C. N. (2014) Interleukin-6 directly impairs the erythroid development of human TF-1 erythroleukemic cells. *Blood Cells Mol Dis* **52**, 126-133

351. Sassa, S., Wolpe, S., and Cerami, A. (1987) Inhibition of erythroid differentiation of mouse erythroleukemia cells by a macrophage product(s). *Blood Cells* **13**, 161-169

352. Nairz, M., Theurl, I., Swirski, F. K., and Weiss, G. (2017) "Pumping iron"-how macrophages handle iron at the systemic, microenvironmental, and cellular levels. *Pflugers Arch* **469**, 397-418

353. Nemeth, E., Rivera, S., Gabayan, V., Keller, C., Taudorf, S., Pedersen, B. K., and Ganz, T. (2004) IL-6 mediates hypoferremia of inflammation by inducing the synthesis of the iron regulatory hormone hepcidin. *J Clin Invest* **113**, 1271-1276

354. Masson, C. (2011) Rheumatoid anemia. *Joint Bone Spine* **78**, 131-137

355. Khalil, S., Delehanty, L., Grado, S., Holy, M., White, Z., 3rd, Freeman, K., Kurita, R., Nakamura, Y., Bullock, G., and Goldfarb, A. (2018) Iron modulation of erythropoiesis is associated with Scribble-mediated control of the erythropoietin receptor. *J Exp Med* **215**, 661-679

356. Moldawer, L. L., Marano, M. A., Wei, H., Fong, Y., Silen, M. L., Kuo, G., Manogue, K. R., Vlassara, H., Cohen, H., Cerami, A., and et al. (1989) Cachectin/tumor necrosis factor-alpha alters red blood cell kinetics and induces anemia in vivo. *FASEB J* **3**, 1637-1643

357. Sawyer, S. T., and Krantz, S. B. (1986) Transferrin receptor number, synthesis, and endocytosis during erythropoietin-induced maturation of Friend virus-infected erythroid cells. *J Biol Chem* **261**, 9187-9195

358. MacMicking, J., Xie, Q. W., and Nathan, C. (1997) Nitric oxide and macrophage function. *Annu Rev Immunol* **15**, 323-350

359. Weiss, G., Goossen, B., Doppler, W., Fuchs, D., Pantopoulos, K., Werner-Felmayer, G., Wachter, H., and Hentze, M. W. (1993) Translational regulation via iron-responsive elements by the nitric oxide/NO-synthase pathway. *EMBO J* **12**, 3651-3657

360. Wang, J., Chen, G., and Pantopoulos, K. (2005) Nitric oxide inhibits the degradation of IRP2. *Mol Cell Biol* **25**, 1347-1353

361. Rafferty, S. P., Domachowske, J. B., and Malech, H. L. (1996) Inhibition of hemoglobin expression by heterologous production of nitric oxide synthase in the K562 erythroleukemic cell line. *Blood* **88**, 1070-1078

362. Furukawa, T., Kohno, H., Tokunaga, R., and Taketani, S. (1995) Nitric oxide-mediated inactivation of mammalian ferrochelatase in vivo and in vitro: possible involvement of the iron-sulphur cluster of the enzyme. *Biochem J* **310 (Pt 2)**, 533-538

363. Kim, Y. M., Bergonia, H. A., Muller, C., Pitt, B. R., Watkins, W. D., and Lancaster, J. R., Jr. (1995) Loss and degradation of enzyme-bound heme induced by cellular nitric oxide synthesis. *J Biol Chem* **270**, 5710-5713

364. Pan, J., Burgher, K. L., Szczepanik, A. M., and Ringheim, G. E. (1996) Tyrosine phosphorylation of inducible nitric oxide synthase: implications for potential post-translational regulation. *Biochem J* **314 (Pt 3)**, 889-894

365. Brendt, P., Rehfeld, I., Kamphausen, A., Kreissig, C., and Peters, J. (2012) Lipopolysaccharide interference in erythropoiesis in mice. *Anaesthesia* **67**, 493-500

366. Brownlie, A., Donovan, A., Pratt, S. J., Paw, B. H., Oates, A. C., Brugnara, C., Witkowska, H. E., Sassa, S., and Zon, L. I. (1998) Positional cloning of the zebrafish sauternes gene: a model for congenital sideroblastic anaemia. *Nat Genet* **20**, 244-250

367. Nakajima, O., Takahashi, S., Harigae, H., Furuyama, K., Hayashi, N., Sassa, S., and Yamamoto, M. (1999) Heme deficiency in erythroid lineage causes differentiation arrest and cytoplasmic iron overload. *EMBO J* **18**, 6282-6289

368. Houston, T., Moore, M., Porter, D., Sturrock, R., and Fitzsimons, E. (1994) Abnormal haem biosynthesis in the chronic anaemia of rheumatoid arthritis. *Ann Rheum Dis* **53**, 167-170

369. Cavill, I., and Bentley, D. P. (1982) Erythropoiesis in the anaemia of rheumatoid arthritis. *Br J Haematol* **50**, 583-590

370. Fitzsimons, E. J., Houston, T., Munro, R., Sturrock, R. D., Speekenbrink, A. B., and Brock, J. H. (2002) Erythroblast iron metabolism and serum soluble transferrin receptor values in the anemia of rheumatoid arthritis. *Arthritis Rheum* **47**, 166-171

371. Sebastiani, G., Wilkinson, N., and Pantopoulos, K. (2016) Pharmacological Targeting of the Hepcidin/Ferroportin Axis. *Front Pharmacol* **7**, 160

372. Sugiyama, Y., Hiraiwa, Y., Hagiya, Y., Nakajima, M., Tanaka, T., and Ogura, S. I. (2018) 5-Aminolevulinic acid regulates the immune response in LPS-stimulated RAW 264.7 macrophages. *BMC Immunol* **19**, 41

373. Hua, Z., Gibson, S. L., Foster, T. H., and Hilf, R. (1995) Effectiveness of delta-aminolevulinic acid-induced protoporphyrin as a photosensitizer for photodynamic therapy in vivo. *Cancer Res* **55**, 1723-1731

374. Cordes, T., Michelucci, A., and Hiller, K. (2015) Itaconic Acid: The Surprising Role of an Industrial Compound as a Mammalian Antimicrobial Metabolite. *Annu Rev Nutr* **35**, 451-473

375. Kinoshita, K. (1932) Über die Produktion von Itaconsäure und Mannit durch einen neuen Schimmelpilz Aspergillus itaconicus. *Acta Phytochim* **5**, 271-287

376. Rittenhouse, J. W., and McFadden, B. A. (1974) Inhibition of isocitrate lyase from Pseudomonas indigofera by itaconate. *Arch Biochem Biophys* **163**, 79-86

377. Geilen, F. M., Engendahl, B., Harwardt, A., Marquardt, W., Klankermayer, J., and Leitner, W. (2010) Selective and flexible transformation of biomass-derived platform chemicals by a multifunctional catalytic system. *Angew Chem Int Ed Engl* **49**, 5510-5514

378. de Carvalho JC, M. A. J., Soccol CR. . (2018) Biobased itaconic acid market and research trends – is it really a promising chemical? *Chimico Oggi-Chem Today* **36**, 56-58

379. Okabe, M., Lies, D., Kanamasa, S., and Park, E. Y. (2009) Biotechnological production of itaconic acid and its biosynthesis in Aspergillus terreus. *Appl Microbiol Biotechnol* **84**, 597-606

380. Strelko, C. L., Lu, W., Dufort, F. J., Seyfried, T. N., Chiles, T. C., Rabinowitz, J. D., and Roberts, M. F. (2011) Itaconic acid is a mammalian metabolite induced during macrophage activation. *J Am Chem Soc* **133**, 16386-16389

381. Sugimoto, M., Sakagami, H., Yokote, Y., Onuma, H., Kaneko, M., Mori, M., Sakaguchi, Y., Soga, T., and Tomita, M. (2012) Non-targeted metabolite profiling in activated macrophage secretion. *Metabolomics* **8**, 624-633

382. Zaslona, Z., and O'Neill, L. A. J. (2020) Cytokine-like Roles for Metabolites in Immunity. *Mol Cell*

383. Kane J, F. A., Amann P (1945) Production of itaconic acid. USA

384. Larsen, H., and Eimhjellen, K. E. (1955) The mechanism of itaconic acid formation by Aspergillus terreus. 1. The effect of acidity. *Biochem J* **60**, 135-139

385. Willke, T., and Vorlop, K. D. (2001) Biotechnological production of itaconic acid. *Appl Microbiol Biotechnol* **56**, 289-295

386. Bentley, R., and Thiessen, C. P. (1957) Biosynthesis of itaconic acid in Aspergillus terreus. III. The properties and reaction mechanism of cis-aconitic acid decarboxylase. *J Biol Chem* **226**, 703-720

387. Jaklitsch WM, K. C., Scrutton MC. (1991) The subcellular organization of itaconate biosynthesis in *Aspergillus terreus*. *J. Gen. Microbiol.* **137**, 533-539

388. Eimhjellen, K. E., and Larsen, H. (1955) The mechanism of itaconic acid formation by Aspergillus terreus. 2. The effect of substrates and inhibitors. *Biochem J* **60**, 139-147

389. Kanamasa, S., Dwiarti, L., Okabe, M., and Park, E. Y. (2008) Cloning and functional characterization of the cis-aconitic acid decarboxylase (CAD) gene from Aspergillus terreus. *Appl Microbiol Biotechnol* **80**, 223-229

390. Yahiro, K. T. T. (1995) Breeding of *Aspergillus terreus* mutant TN-484 for itaconic acid production with high yield. *J. Ferment. Bioeng.* **79**, 506-508

391. McKinney, J. D., Honer zu Bentrup, K., Munoz-Elias, E. J., Miczak, A., Chen, B., Chan, W. T., Swenson, D., Sacchettini, J. C., Jacobs, W. R., Jr., and Russell, D. G. (2000) Persistence of Mycobacterium tuberculosis in macrophages and mice requires the glyoxylate shunt enzyme isocitrate lyase. *Nature* **406**, 735-738

392. Michelucci, A., Cordes, T., Ghelfi, J., Pailot, A., Reiling, N., Goldmann, O., Binz, T., Wegner, A., Tallam, A., Rausell, A., Buttini, M., Linster, C. L., Medina, E., Balling, R., and Hiller, K. (2013) Immune-responsive gene 1 protein links metabolism to immunity by catalyzing itaconic acid production. *Proc Natl Acad Sci U S A* **110**, 7820-7825

393. Fang, F. C., Libby, S. J., Castor, M. E., and Fung, A. M. (2005) Isocitrate lyase (AceA) is required for Salmonella persistence but not for acute lethal infection in mice. *Infect Immun* **73**, 2547-2549

394. McFadden, B. A., and Purohit, S. (1977) Itaconate, an isocitrate lyase-directed inhibitor in Pseudomonas indigofera. *J Bacteriol* **131**, 136-144

395. Dunn, M. F., Ramirez-Trujillo, J. A., and Hernandez-Lucas, I. (2009) Major roles of isocitrate lyase and malate synthase in bacterial and fungal pathogenesis. *Microbiology* **155**, 3166-3175

396. Berg, I. A., Filatova, L. V., and Ivanovsky, R. N. (2002) Inhibition of acetate and propionate assimilation by itaconate via propionyl-CoA carboxylase in isocitrate lyase-negative purple bacterium Rhodospirillum rubrum. *FEMS Microbiol Lett* **216**, 49-54

397. Upton, A. M., and McKinney, J. D. (2007) Role of the methylcitrate cycle in propionate metabolism and detoxification in Mycobacterium smegmatis. *Microbiology* **153**, 3973-3982

398. Shen, H., Campanello, G. C., Flicker, D., Grabarek, Z., Hu, J., Luo, C., Banerjee, R., and Mootha, V. K. (2017) The Human Knockout Gene CLYBL Connects Itaconate to Vitamin B12. *Cell* **171**, 771-782 e711

399. Ruetz, M., Campanello, G. C., Purchal, M., Shen, H., McDevitt, L., Gouda, H., Wakabayashi, S., Zhu, J., Rubin, E. J., Warncke, K., Mootha, V. K., Koutmos, M., and Banerjee, R. (2019) Itaconyl-CoA forms a stable biradical in methylmalonyl-CoA mutase and derails its activity and repair. *Science* **366**, 589-593

400. Gopinath, K., Venclovas, C., Ioerger, T. R., Sacchettini, J. C., McKinney, J. D., Mizrahi, V., and Warner, D. F. (2013) A vitamin B(1)(2) transporter in Mycobacterium tuberculosis. *Open Biol* **3**, 120175

401. Barron, M. (1933) Pernicious anemia and tuberculosis: is there an antagonism? *JAMA* **100**, 1590-1592

402. Sasikaran, J., Ziemski, M., Zadora, P. K., Fleig, A., and Berg, I. A. (2014) Bacterial itaconate degradation promotes pathogenicity. *Nat Chem Biol* **10**, 371-377

403. Cooper, R. A., and Kornberg, H. L. (1964) The utilization of itaconate by Pseudomonas sp. *Biochem J* **91**, 82-91

404. Adler, J., Wang, S. F., and Lardy, H. A. (1957) The metabolism of itaconic acid by liver mitochondria. *J Biol Chem* **229**, 865-879

405. Wang, S. F., Adler, J., and Lardy, H. A. (1961) The pathway of itaconate metabolism by liver mitochondria. *J Biol Chem* **236**, 26-30

406. Emmrich, R. (1939) Metabolism experiments with some methylised low molecular dicarbonic acids. *Z. Physiol. Chem.* **261**, 61-70

407. Finkelstein, M., Gold, H., and Paterno, C. A. (1947) Pharmacology of itaconic acid and its sodium, magnesium, and calcium salts. *J Am Pharm Assoc Am Pharm Assoc* **36**, 173-179

408. Ackermann, W. W., and Potter, V. R. (1949) Enzyme inhibition in relation to chemotherapy. *Proc Soc Exp Biol Med* **72**, 1-9

409. Booth, A. N., Taylor, J., Wilson, R. H., and Deeds, F. (1952) The inhibitory effects of itaconic acid in vitro and in vivo. *J Biol Chem* **195**, 697-702

410. Porpaczy, Z., Sumegi, B., and Alkonyi, I. (1983) Association between the alpha-ketoglutarate dehydrogenase complex and succinate thiokinase. *Biochim Biophys Acta* **749**, 172-179

411. Nakabayashi, K., Fernandez, B. A., Teshima, I., Shuman, C., Proud, V. K., Curry, C. J., Chitayat, D., Grebe, T., Ming, J., Oshimura, M., Meguro, M., Mitsuya, K., Deb-Rinker, P., Herbrick, J. A., Weksberg, R., and Scherer, S. W. (2002) Molecular genetic studies of human chromosome 7 in Russell-Silver syndrome. *Genomics* **79**, 186-196

412. Marlaire, S., Van Schaftingen, E., and Veiga-da-Cunha, M. (2014) C7orf10 encodes succinate-hydroxymethylglutarate CoA-transferase, the enzyme that converts glutarate to glutaryl-CoA. *J Inherit Metab Dis* **37**, 13-19

413. Shin, J. H., Yang, J. Y., Jeon, B. Y., Yoon, Y. J., Cho, S. N., Kang, Y. H., Ryu, D. H., and Hwang, G. S. (2011) (1)H NMR-based metabolomic profiling in mice infected with Mycobacterium tuberculosis. *J Proteome Res* **10**, 2238-2247

414. Mills, E., and O'Neill, L. A. (2014) Succinate: a metabolic signal in inflammation. *Trends Cell Biol* **24**, 313-320

415. Tannahill, G. M., Curtis, A. M., Adamik, J., Palsson-McDermott, E. M., McGettrick, A. F., Goel, G., Frezza, C., Bernard, N. J., Kelly, B., Foley, N. H., Zheng, L., Gardet, A., Tong, Z., Jany, S. S., Corr, S. C., Haneklaus, M., Caffrey, B. E., Pierce, K., Walmsley, S.,

Beasley, F. C., Cummins, E., Nizet, V., Whyte, M., Taylor, C. T., Lin, H., Masters, S. L., Gottlieb, E., Kelly, V. P., Clish, C., Auron, P. E., Xavier, R. J., and O'Neill, L. A. (2013) Succinate is an inflammatory signal that induces IL-1beta through HIF-1alpha. *Nature* **496**, 238-242

416. Mills, E. L., Kelly, B., Logan, A., Costa, A. S. H., Varma, M., Bryant, C. E., Tourlomousis, P., Dabritz, J. H. M., Gottlieb, E., Latorre, I., Corr, S. C., McManus, G., Ryan, D., Jacobs, H. T., Szibor, M., Xavier, R. J., Braun, T., Frezza, C., Murphy, M. P., and O'Neill, L. A. (2016) Succinate Dehydrogenase Supports Metabolic Repurposing of Mitochondria to Drive Inflammatory Macrophages. *Cell* **167**, 457-470 e413

417. Lampropoulou, V., Sergushichev, A., Bambouskova, M., Nair, S., Vincent, E. E., Loginicheva, E., Cervantes-Barragan, L., Ma, X., Huang, S. C., Griss, T., Weinheimer, C. J., Khader, S., Randolph, G. J., Pearce, E. J., Jones, R. G., Diwan, A., Diamond, M. S., and Artyomov, M. N. (2016) Itaconate Links Inhibition of Succinate Dehydrogenase with Macrophage Metabolic Remodeling and Regulation of Inflammation. *Cell Metab* **24**, 158-166

418. Nemeth, B., Doczi, J., Csete, D., Kacso, G., Ravasz, D., Adams, D., Kiss, G., Nagy, A. M., Horvath, G., Tretter, L., Mocsai, A., Csepanyi-Komi, R., Iordanov, I., Adam-Vizi, V., and Chinopoulos, C. (2016) Abolition of mitochondrial substrate-level phosphorylation by itaconic acid produced by LPS-induced Irg1 expression in cells of murine macrophage lineage. *FASEB J* **30**, 286-300

419. Chouchani, E. T., Pell, V. R., Gaude, E., Aksentijevic, D., Sundier, S. Y., Robb, E. L., Logan, A., Nadtochiy, S. M., Ord, E. N. J., Smith, A. C., Eyassu, F., Shirley, R., Hu, C. H., Dare, A. J., James, A. M., Rogatti, S., Hartley, R. C., Eaton, S., Costa, A. S. H., Brookes, P. S., Davidson, S. M., Duchen, M. R., Saeb-Parsy, K., Shattock, M. J., Robinson, A. J., Work, L. M., Frezza, C., Krieg, T., and Murphy, M. P. (2014) Ischaemic accumulation of succinate controls reperfusion injury through mitochondrial ROS. *Nature* **515**, 431-435

420. Michopoulos, F., Karagianni, N., Whalley, N. M., Firth, M. A., Nikolaou, C., Wilson, I. D., Critchlow, S. E., Kollias, G., and Theodoridis, G. A. (2016) Targeted Metabolic Profiling of the Tg197 Mouse Model Reveals Itaconic Acid as a Marker of Rheumatoid Arthritis. *J Proteome Res* **15**, 4579-4590

421. ElAzzouny, M., Tom, C. T., Evans, C. R., Olson, L. L., Tanga, M. J., Gallagher, K. A., Martin, B. R., and Burant, C. F. (2017) Dimethyl Itaconate Is Not Metabolized into Itaconate Intracellularly. *J Biol Chem* **292**, 4766-4769

422. Bambouskova, M., Gorvel, L., Lampropoulou, V., Sergushichev, A., Loginicheva, E., Johnson, K., Korenfeld, D., Mathyer, M. E., Kim, H., Huang, L. H., Duncan, D., Bregman, H., Keskin, A., Santeford, A., Apte, R. S., Sehgal, R., Johnson, B., Amarasinghe, G. K., Soares, M. P., Satoh, T., Akira, S., Hai, T., de Guzman Strong, C., Auclair, K., Roddy, T. P., Biller, S. A., Jovanovic, M., Klechevsky, E., Stewart, K. M.,

Randolph, G. J., and Artyomov, M. N. (2018) Electrophilic properties of itaconate and derivatives regulate the IkappaBzeta-ATF3 inflammatory axis. *Nature* **556**, 501-504

423. Mills, E. L., Ryan, D. G., Prag, H. A., Dikovskaya, D., Menon, D., Zaslona, Z., Jedrychowski, M. P., Costa, A. S. H., Higgins, M., Hams, E., Szpyt, J., Runtsch, M. C., King, M. S., McGouran, J. F., Fischer, R., Kessler, B. M., McGettrick, A. F., Hughes, M. M., Carroll, R. G., Booty, L. M., Knatko, E. V., Meakin, P. J., Ashford, M. L. J., Modis, L. K., Brunori, G., Sevin, D. C., Fallon, P. G., Caldwell, S. T., Kunji, E. R. S., Chouchani, E. T., Frezza, C., Dinkova-Kostova, A. T., Hartley, R. C., Murphy, M. P., and O'Neill, L. A. (2018) Itaconate is an anti-inflammatory metabolite that activates Nrf2 via alkylation of KEAP1. *Nature* **556**, 113-117

424. Yi, Z., Deng, M., Scott, M. J., Fu, G., Loughran, P. A., Lei, Z., Li, S., Sun, P., Yang, C., Li, W., Xu, H., Huang, F., and Billiar, T. R. (2020) IRG1/Itaconate Activates Nrf2 in Hepatocytes to Protect Against Liver Ischemia-Reperfusion Injury. *Hepatology*

425. Sakai, A., Kusumoto, A., Kiso, Y., and Furuya, E. (2004) Itaconate reduces visceral fat by inhibiting fructose 2,6-bisphosphate synthesis in rat liver. *Nutrition* **20**, 997-1002

426. Grant, C. M. (2008) Metabolic reconfiguration is a regulated response to oxidative stress. *J Biol* **7**, 1

427. Zimmermann, M., Aguilera, F. B., Castellucci, M., Rossato, M., Costa, S., Lunardi, C., Ostuni, R., Girolomoni, G., Natoli, G., Bazzoni, F., Tamassia, N., and Cassatella, M. A. (2015) Chromatin remodelling and autocrine TNFalpha are required for optimal interleukin-6 expression in activated human neutrophils. *Nat Commun* **6**, 6061

428. Cordes, T., Wallace, M., Michelucci, A., Divakaruni, A. S., Sapcariu, S. C., Sousa, C., Koseki, H., Cabrales, P., Murphy, A. N., Hiller, K., and Metallo, C. M. (2016) Immunoresponsive Gene 1 and Itaconate Inhibit Succinate Dehydrogenase to Modulate Intracellular Succinate Levels. *J Biol Chem* **291**, 14274-14284

429. Meiser, J., Kraemer, L., Jaeger, C., Madry, H., Link, A., Lepper, P. M., Hiller, K., and Schneider, J. G. (2018) Itaconic acid indicates cellular but not systemic immune system activation. *Oncotarget* **9**, 32098-32107

430. Puchalska, P., Huang, X., Martin, S. E., Han, X., Patti, G. J., and Crawford, P. A. (2018) Isotope Tracing Untargeted Metabolomics Reveals Macrophage Polarization-State-Specific Metabolic Coordination across Intracellular Compartments. *iScience* **9**, 298-313

431. Daly, R., Blackburn, G., Best, C., Goodyear, C. S., Mudaliar, M., Burgess, K., Stirling, A., Porter, D., McInnes, I. B., Barrett, M. P., and Dale, J. (2020) Changes in Plasma Itaconate Elevation in Early Rheumatoid Arthritis Patients Elucidates Disease Activity Associated Macrophage Activation. *Metabolites* **10**

432. Aliverdieva, D. A., and Mamaev, D. V. (2009) [Molecular characteristics of transporters of C4-dicarboxylates and mechanism of translocation]. *Zh Evol Biokhim Fiziol* **45**, 263-276

433. Trauelsen, M., Rexen Ulven, E., Hjorth, S. A., Brvar, M., Monaco, C., Frimurer, T. M., and Schwartz, T. W. (2017) Receptor structure-based discovery of non-metabolite agonists for the succinate receptor GPR91. *Mol Metab* **6**, 1585-1596

434. Littlewood-Evans, A., Sarret, S., Apfel, V., Loesle, P., Dawson, J., Zhang, J., Muller, A., Tigani, B., Kneuer, R., Patel, S., Valeaux, S., Gommermann, N., Rubic-Schneider, T., Junt, T., and Carballido, J. M. (2016) GPR91 senses extracellular succinate released from inflammatory macrophages and exacerbates rheumatoid arthritis. *J Exp Med* **213**, 1655-1662

435. Peruzzotti-Jametti, L., Bernstock, J. D., Vicario, N., Costa, A. S. H., Kwok, C. K., Leonardi, T., Booty, L. M., Bicci, I., Balzarotti, B., Volpe, G., Mallucci, G., Manferrari, G., Donega, M., Iraci, N., Braga, A., Hallenbeck, J. M., Murphy, M. P., Edenhofer, F., Frezza, C., and Pluchino, S. (2018) Macrophage-Derived Extracellular Succinate Licenses Neural Stem Cells to Suppress Chronic Neuroinflammation. *Cell Stem Cell* **22**, 355-368 e313

436. Kaur, S., Raggatt, L. J., Batoon, L., Hume, D. A., Levesque, J. P., and Pettit, A. R. (2017) Role of bone marrow macrophages in controlling homeostasis and repair in bone and bone marrow niches. *Semin Cell Dev Biol* **61**, 12-21

437. Hakak, Y., Lehmann-Bruinsma, K., Phillips, S., Le, T., Liaw, C., Connolly, D. T., and Behan, D. P. (2009) The role of the GPR91 ligand succinate in hematopoiesis. *J Leukoc Biol* **85**, 837-843

1.7 Figures and Tables

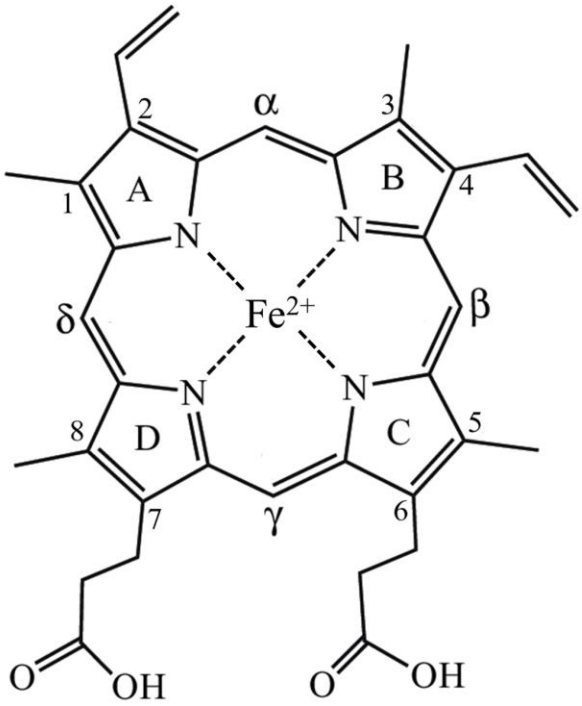

Figure 1. Heme *b* molecular structure. Pyrrole rings are labeled A, B, C, and D according to the Protein Data Bank (PDB) nomenclature and form the planar tetrapyrrole macrocycle via methene bridges a, b, g, and d in an unbound state. Pyrrole nitrogen atoms donate electrons to the central ferrous iron (coordination number of 6). Numbers 1-8 identify side chain substitution sites, where 1, 3, 5, and 8 are methane groups and 2, 4, 6, and 7 are propionate groups.

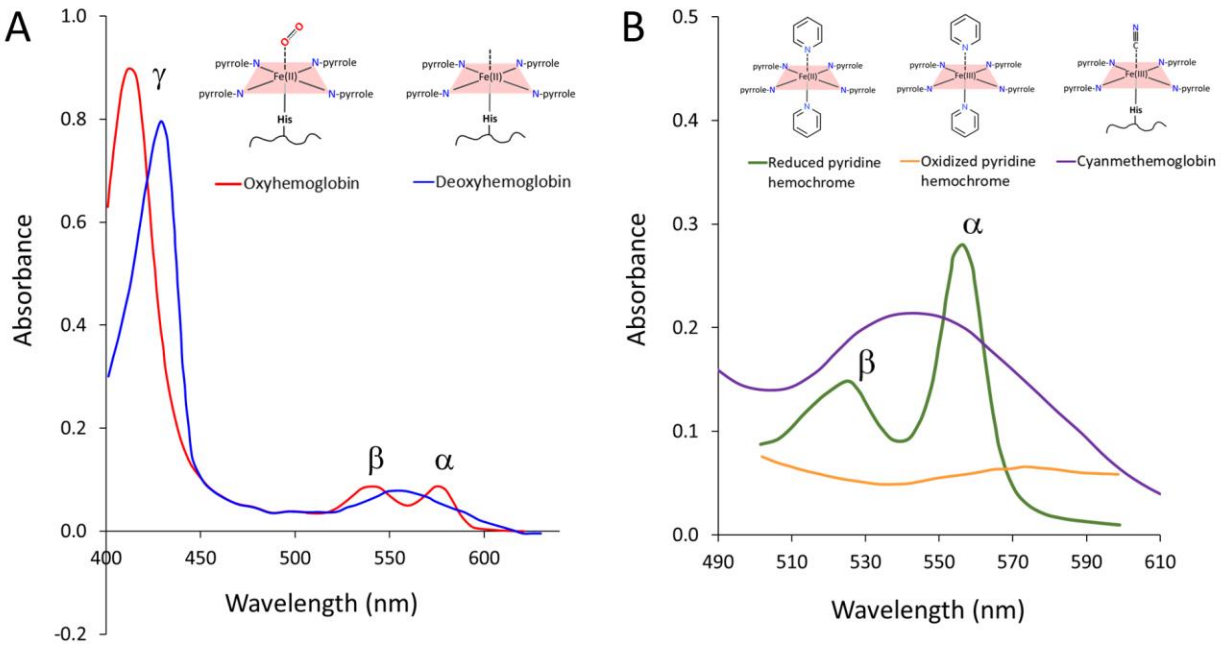

Figure 2. Absorbance spectra of heme species. (A) The oxyhemoglobin spectrum contains distinct α, β, and γ (Soret) peaks, whereas the a and b peaks are merged into a single, broader band in deoxyhemoglobin. (B) Pyridine hemochromes consist of pyridine molecules coordination to the two axial iron positions of heme and absorbances result in strong a and b peaks for reduced iron (Fe^{2+}) but no discernable peaks for oxidized iron (Fe^{3+}). Cyanmethemoglobin absorbs strongly in this region as manifested in a single, broad band centered at 540 nm.

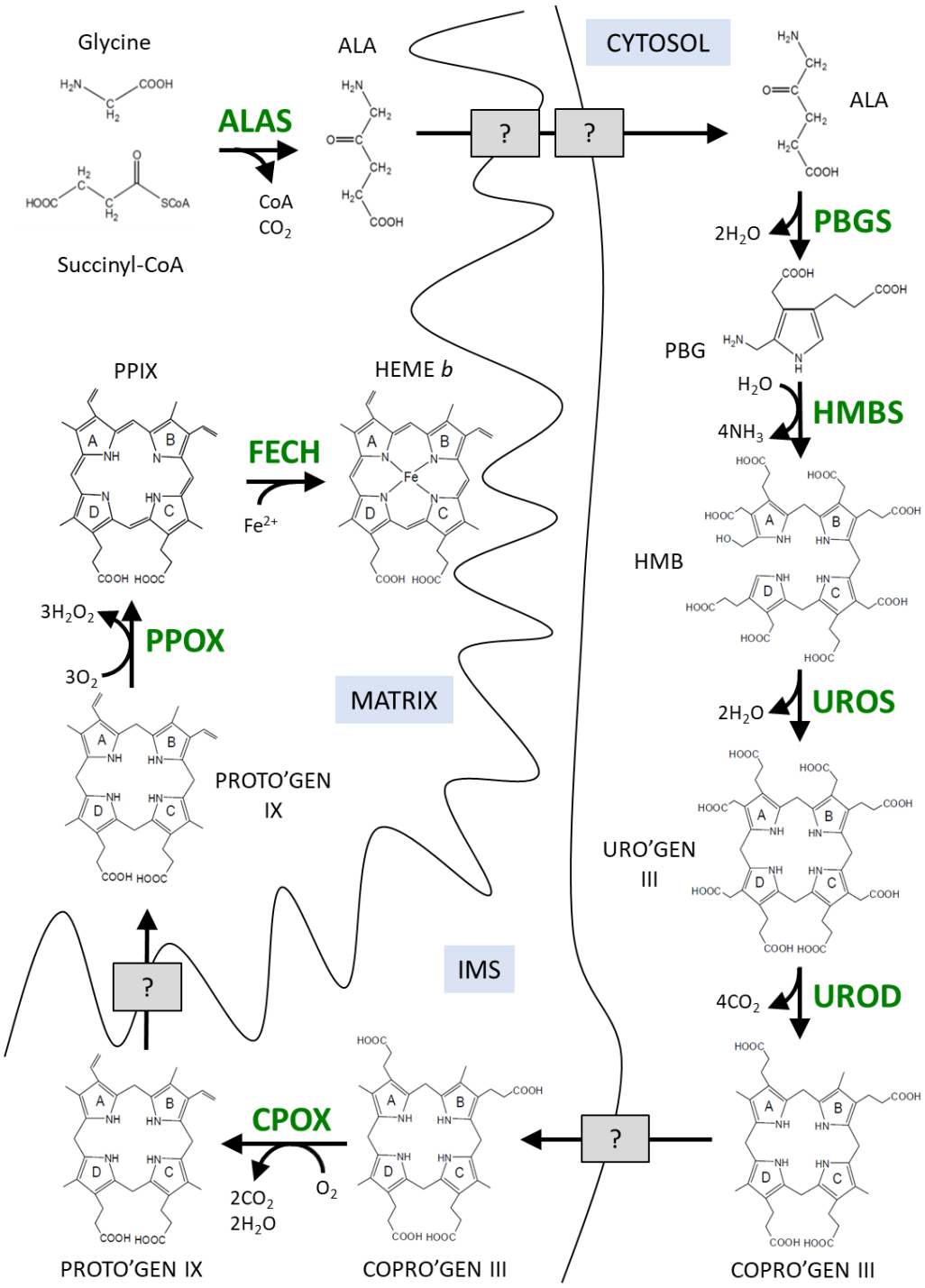

Figure 3. Mammalian heme biosynthesis pathway. Abbreviations are defined in the main text.

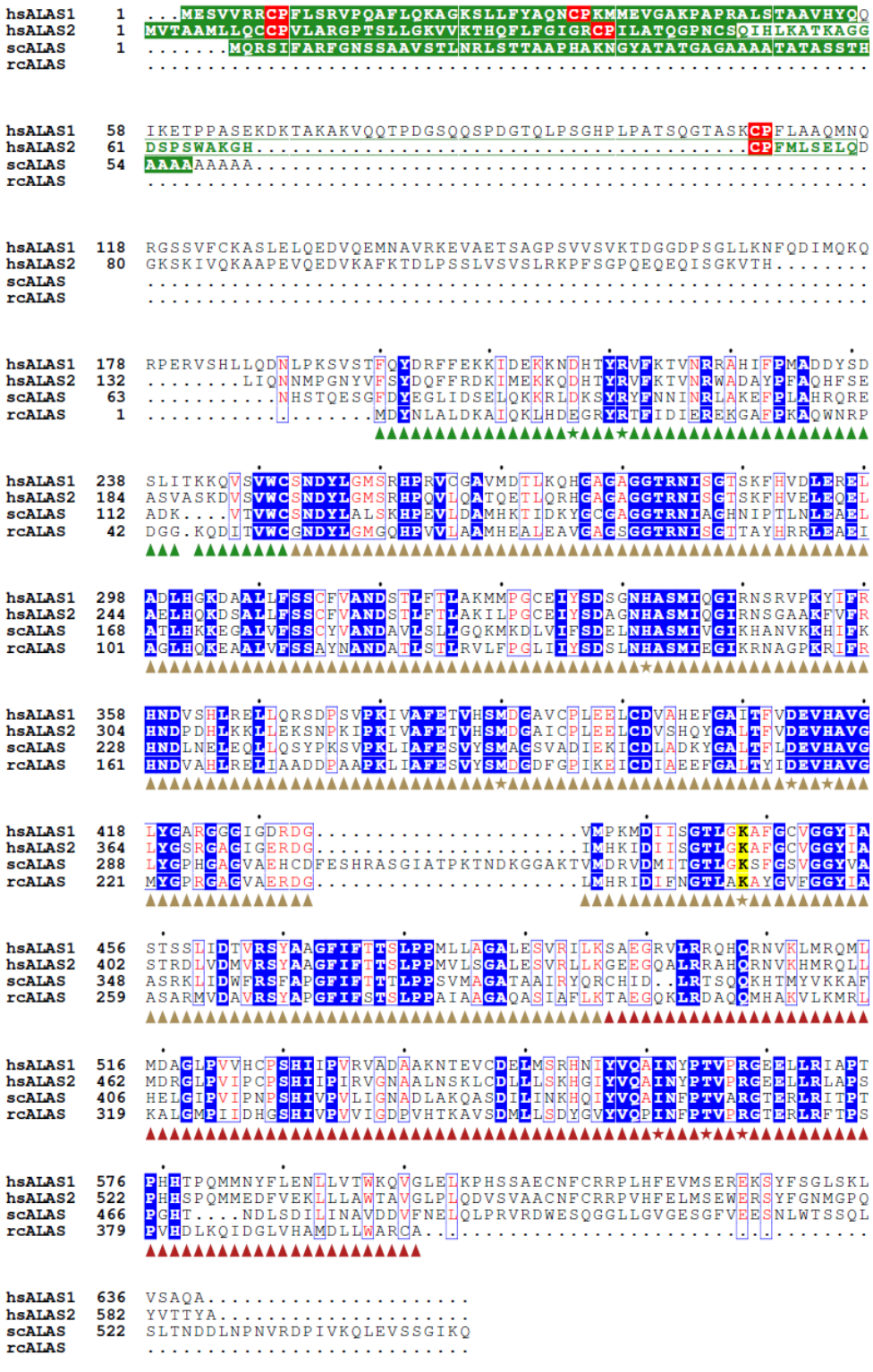

Figure 4. Protein alignments of human ALAS1 (hsALAS1) and ALAS2 (hsALAS2), *S. cerevisiae* ALAS (scALAS), and *R. capsulatus* ALAS (rcALAS). Green, sand, and red

triangles identify N-terminal, catalytic, and C-terminal domains of rcALAS. Starred residues are discussed further in the main text and Figures 5 and 6. The conserved catalytic lysine is highlighted in yellow. Identical residues across all aligned sequences are highlighted in blue, while positions with 75% consensus contain red letter symbols boxed in blue. Mitochondrial targeting sequences (MTSs) and heme-regulatory CP motifs are highlighted in green and red, respectively. Residues 50-78 of hsALAS2 are disputedly part of the MTS (see main text) and is distinguished from the first 49 AAs with a green font and green outline.

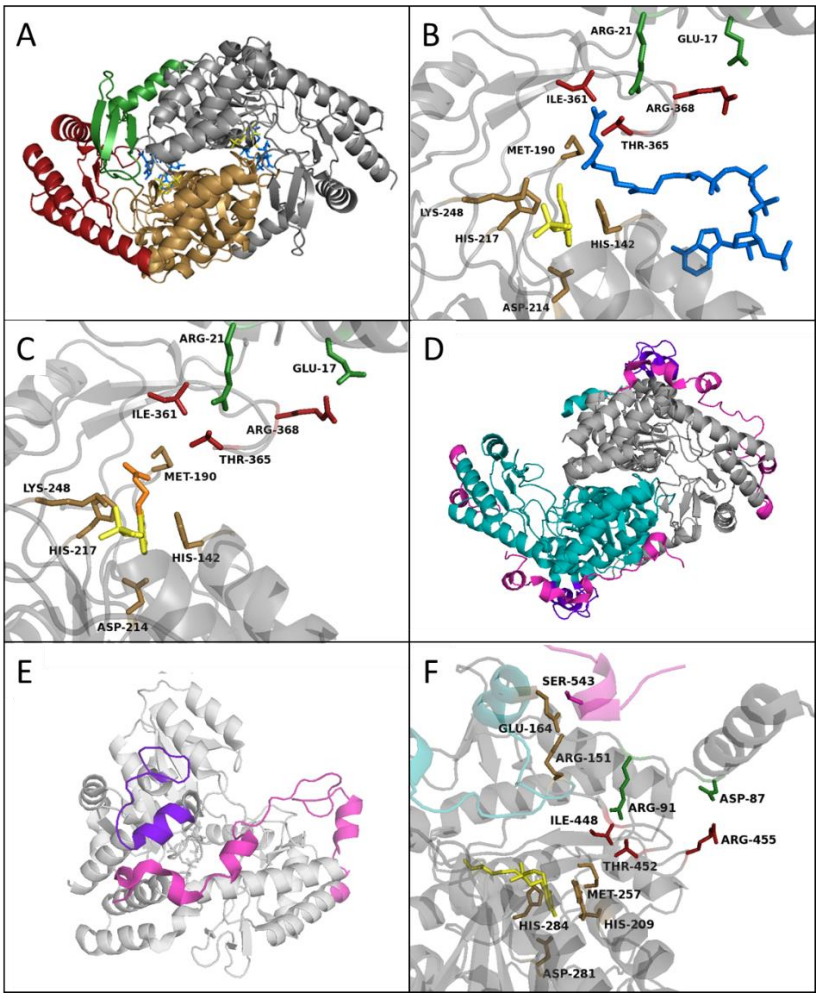

Figure 5. Structural highlights from published rcALAS and scALAS structures. (A) rcALAS dimer (closed conformation) with N-terminal, catalytic, and C-terminal domains are colored green, sand, and red, respectively. PLP = yellow, succinyl-CoA = blue. (B) rcALAS active site, closed conformation; same color scheme as (A); (C) rcALAS active site, open conformation; same color scheme as (A). (D) scALAS dimer (open conformation) with aligned rcALAS residues colored cyan and gray on separate monomers; eukaryotic-specific C-terminal residues (Ct-extension) = magenta, yeast-specific 22-residue catalytic domain insertion = purple. (E) Top view of (D). (F) scALAS active site with conserved rcALAS residues colored as in (A) and Ct-extension and 22AA insertion colored as in (E). Glycine-PLP external aldimine = yellow.

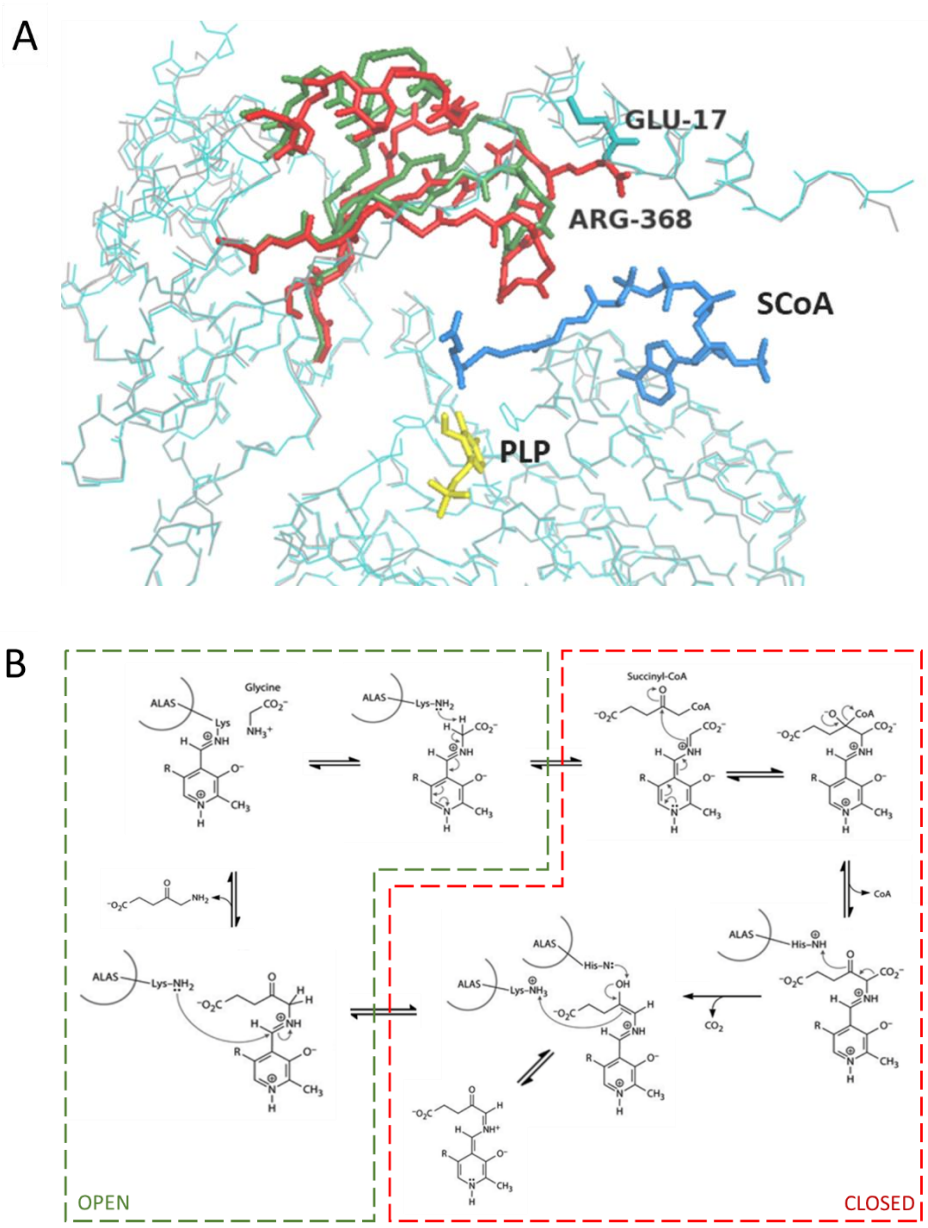

Figure. 6. Open and closed conformations and associated kinetic cycle of rcALAS. (A) Alignment of monomer in open conformation (gray with green C-terminal segments) and opposing monomer in closed conformation (teal with red C-terminal segments). (B) Kinetic cycle of ALAS with corresponding open and closed enzyme conformations as described in the main text.

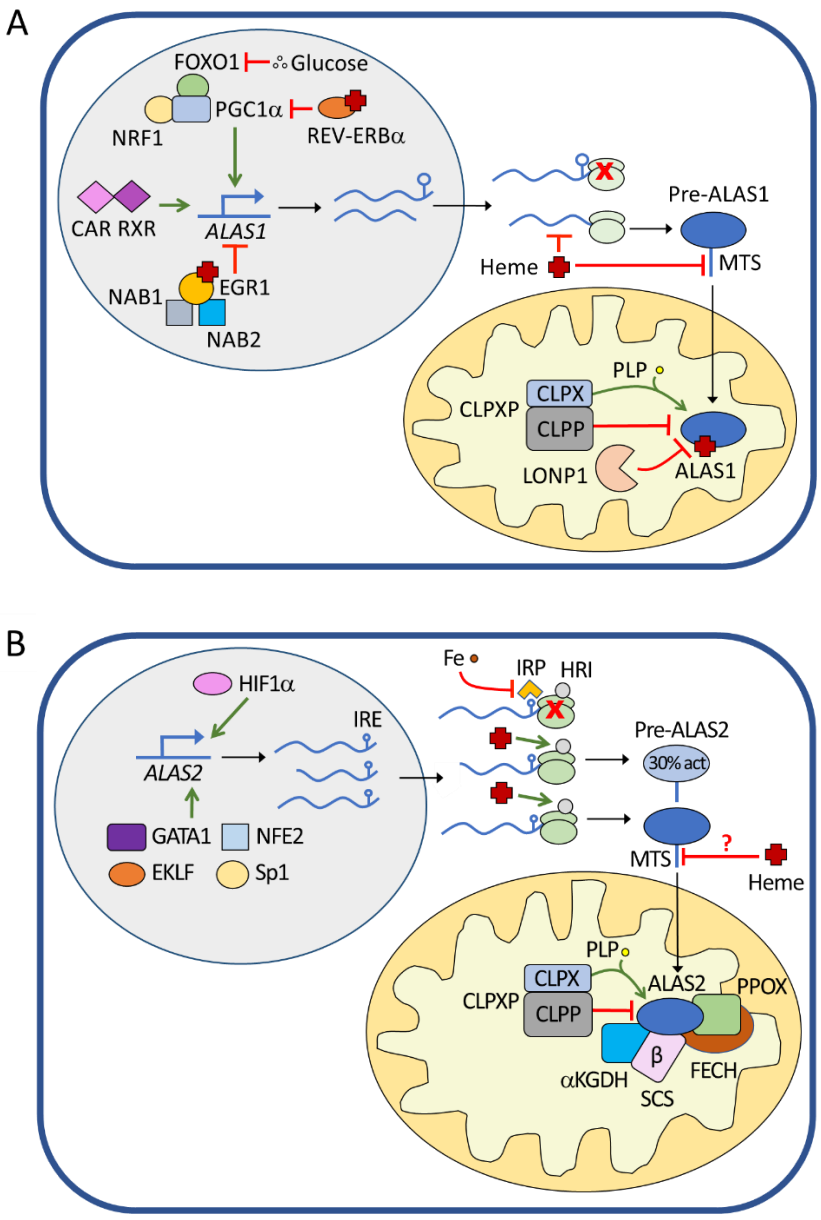

Figure 7. Key regulatory features of mammalian ALAS synthesis, stability and activity.

(A) ALAS1 regulation in a nonerythroid cell and (B) ALAS2 regulation in an erythroid-specific cell, as described in detail in the main text.

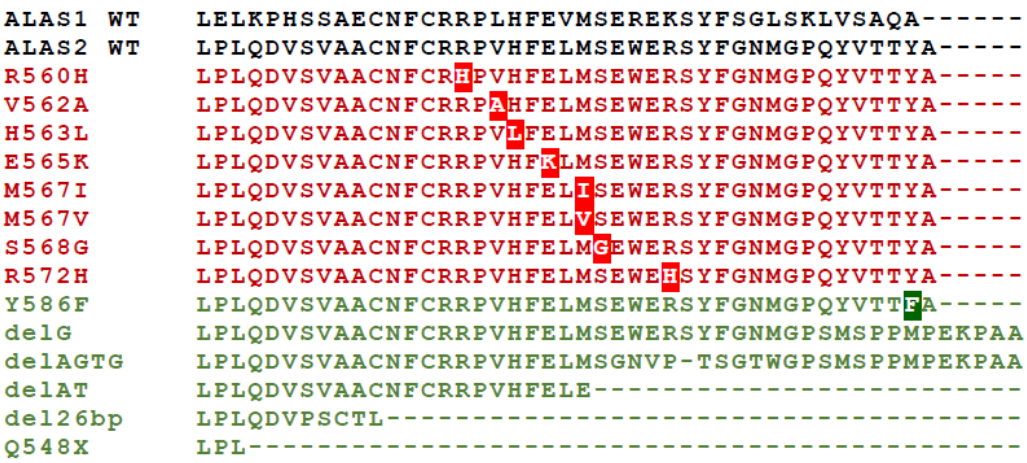

Figure 8. Human ALAS Ct-extension alignment. Wild-type, XLSA, and XLP sequences are colored in black, red, and green, respectively. Missense mutations are highlighted in the corresponding font colors.

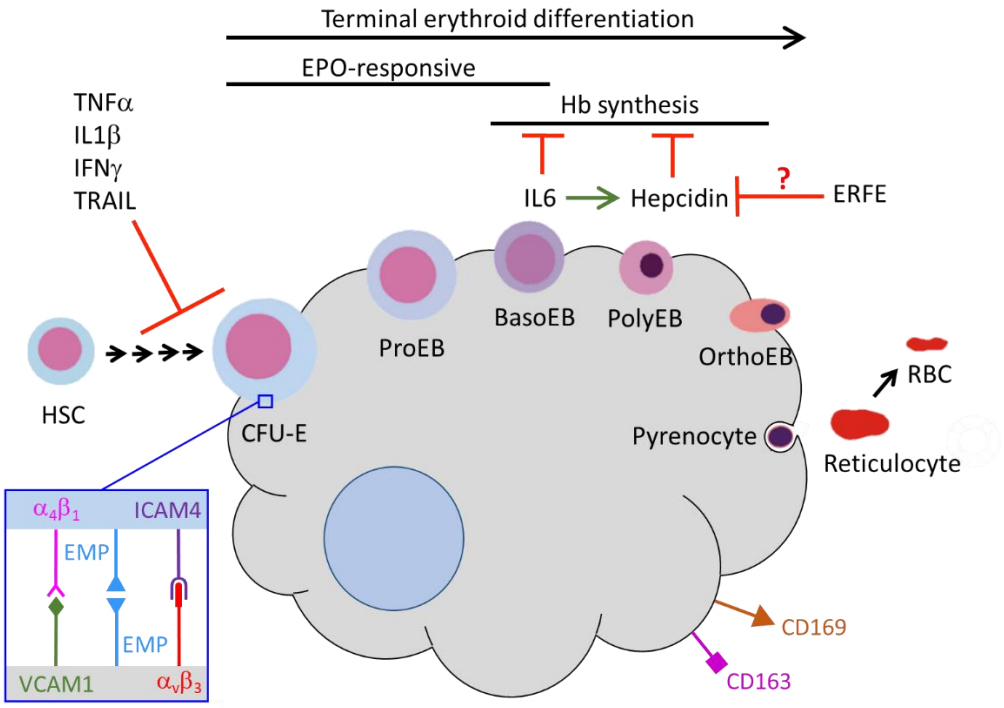

Figure 9. Erythroid differentiation in the context of the erythroblastic island niche.

Diagram includes inflammatory factors found to impact terminal erythropoiesis during infection as described in the main text. Abbreviations are also defined in the main text.

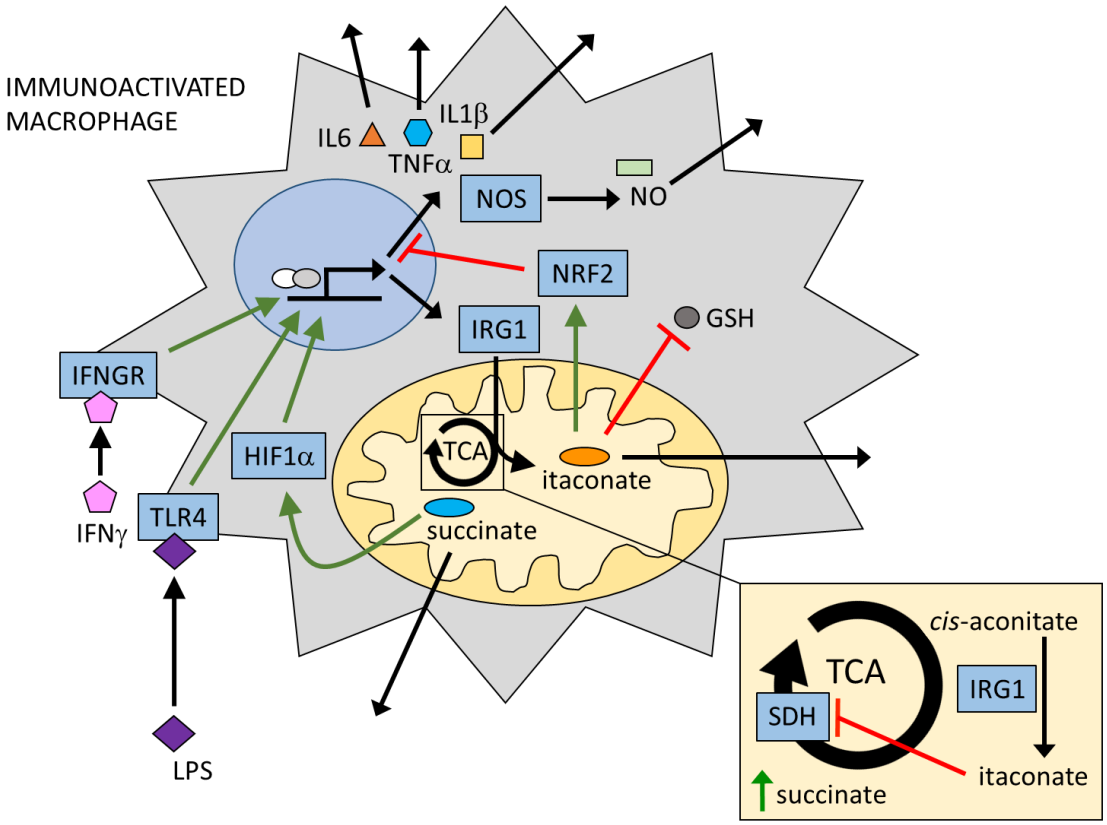

Figure 10. The proinflammatory (M1) macrophage and role of cytokines and itaconate in the immune response. Abbreviations are defined in the main text.

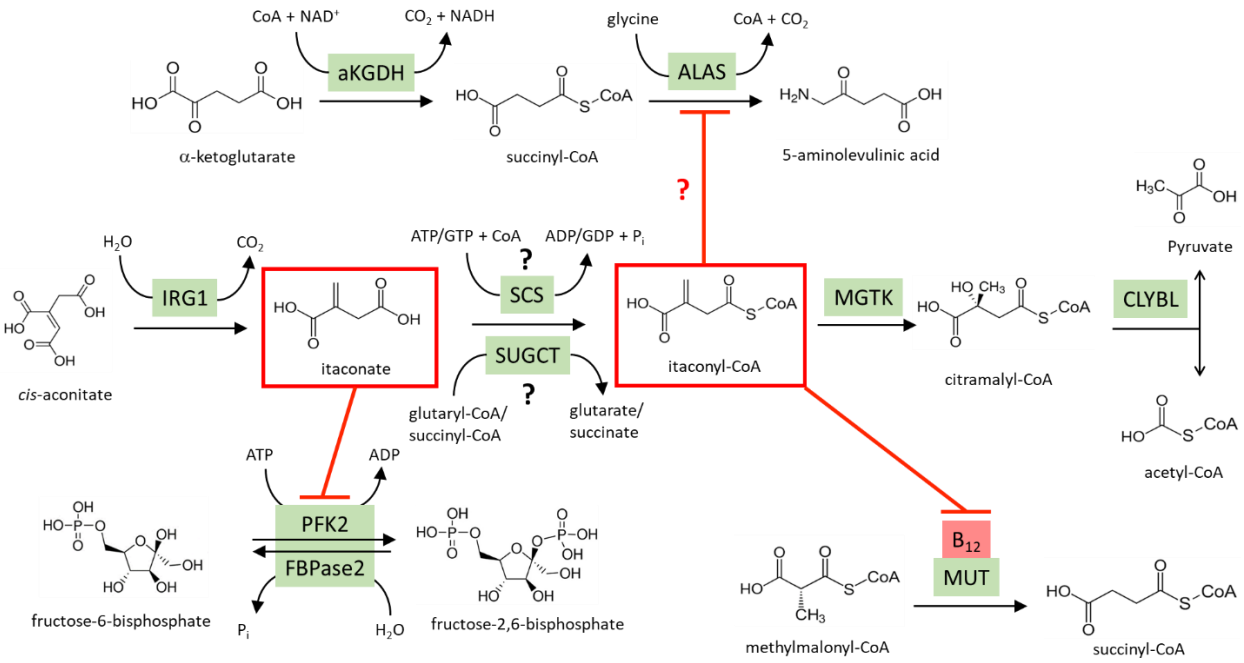

Figure 11. Itaconate metabolism in mammals. Abbreviations are defined in the main text.

Table 1. Human disease states associated with aberrant heme synthesis.

Enzyme	Mutation	Inheritance	Affected Tissue	Accumulated Metabolites	Phenotype	Disease
ALAS2	LOF	X	Erythroid	Fe	Anemia	X-linked sideroblastic anemia
	GOF	X	Erythroid	PPIX, ZnPPIX	NB Photo	X-linked protoporphyria
PBGS	LOF	AR	Hepatic	ALA, Copro III, ZnPPIX	Neuro	ALA deficiency porphyria
HMBS	LOF	AD	Hepatic	ALA, PBG, Uro III	Neuro	Acute intermittent porphyria
UROS	LOF	AR	Erythroid	Uro I, Copro I	B Photo, Anemia	Congenital erythropoietic porphyria
UROD	LOF	AD	Hepatic	Uro III, Hepta, Isocopro	B Photo	Porphyria cutanea tarda
	LOF	AR	Erythroid, Hepatic	Uro III, Hepta, Isocopro, ZnPPIX	Anemia, B Photo	Hepatoerythropoietic porphyria
CPOX	LOF	AD	Hepatic	ALA, PBG, Copro III	Neuro, B Photo	Hereditary coproporphyria
	LOF	AD	Erythroid, Hepatic	ALA, PBG, Copro III, Hardero	Anemia, Neuro, B Photo	Harderoporphyria
PPOX	LOF	AD	Hepatic	ALA, PBG, Copro III, PPIX	Neuro, B Photo	Variegate porphyria
FECH	LOF	AR	Erythroid	PPIX	NB Photo	Erythropoietic protoporphyria

GOF = gain of function, LOF = loss of function; X = X-linked, AR = autosomal recessive, AD = autosomal dominant; ALA = aminolevulinic acid, PBG = porphobilinogen, Uro = uroporphyrin, Copro = coproporphyrin, Hepta = heptacarboxyl porphyrin, Isocopro = isocoproporphyrin, Hardero = harderoporphyrin, PP = protoporphyrin; I, III, IX = isomers; B Photo = blistering photosensitivity, NB Photo = nonblistering photosensitivity, Neuro = neurovisceral.

Table 2. Proinflammatory cytokines and their impacts on erythropoiesis and RBC survival. Abbreviations are defined in the main text.

Process Inhibited	Cytokine(s)	Direct/Indirect Effect(s) (Mediator)
Early erythropoiesis (HSC to BFU-E)	TNFα TRAIL IFNγ IL1β	Direct
Terminal erythropoiesis/EBI (CFU-E to reticulocyte)	TNFα, IL1β	Indirect (↓ EPO supply, ↓ Fe supply)
	IFNγ	Indirect (↑ EPOR synthesis, ↑ FAS synthesis)
	IL6	Direct and indirect (↑ hepcidin/↓ Fe supply)
Erythrophagocytosis	TNFα	Direct

CHAPTER 2

RAPID AND SENSITIVE QUANTITATION OF HEME IN HEMOGLOBINIZED CELLS

Marcero, J. R., et al. (2016) *Biotechniques*. **61**, 83-91.

2.1 Abstract

Rapid and accurate heme quantitation in the research lab has become more desirable as the crucial role that intracellular hemoproteins play in metabolism continues to emerge. Here the time-honored approaches of pyridine hemochromogen and fluorescence heme assays are compared to direct absorbance-based technologies using the CLARiTY spectrophotometer (Olis, Inc.). All samples tested with these methods were rich in hemoglobin-associated heme, including buffered hemoglobin standards, whole blood from mice, and murine erythroleukemia (MEL) and K562 cells. While the pyridine hemochromogen assay demonstrated the greatest linear range of heme detection, the three methods demonstrated similar analytical sensitivities and normalized limits of quantitation of approximately 1 μM. Surprisingly, the fluorescence assay was only shown to be distinct in its ability to quantitate extremely small samples. Using the CLARiTY system in combination with pyridine hemochromogen and cell count data, a common hemoglobin extinction coefficient for blood and differentiating MEL and K562 cells of 0.46 μM^{-1} cm^{-1} was derived. This value was applied to supplemental experiments designed to measure MEL cell hemoglobinization in response to the addition or removal of factors previously shown to affect heme biosynthesis (e.g., L-glutamine, iron).

2.2 Introduction

Heme is an essential and central component in diverse biological processes ranging from gas metabolism, one-electron chemistry, and bacterial pathogenesis (1-3) to its more recently recognized roles in circadian rhythm and small RNA processing (4,5). From a clinical standpoint, the level of hemoglobin-associated heme in blood and body fluid samples can be diagnostic of many pathological conditions. Here we have focused on the quantitation of heme in

standard hemoglobin solutions, erythroid model cell lines, and blood samples as a benchmark for comparison of currently available technologies.

Traditional strategies for measuring hemoglobin include but are not limited to Drabkin's (cyanmethemoglobin) method (6), pyridine hemochromogen assay (7), fluorescence heme assay (8), and reverse-phase HPLC (9). With the exception of the cyanmethemoglobin assay, these approaches infer hemoglobin concentrations from measurements of heme. More recently, chemiluminescent-based methods based on horseradish peroxidase biochemistry have also been developed to quantitate total cellular heme (10) and regulatory heme (11). We have previously relied on the pyridine hemochromogen and fluorescence assays to determine cellular heme and hemoglobin concentrations as described elsewhere (12,13). Fluorescence analysis is a more sensitive technique per se, yet signal emission is complicated by multiple environmental factors and therefore does not permit application of the Beer-Lambert law (14). Like the chemiluminescence method, both pyridine hemochromogen and fluorescence assays involve laborious sample preparations that require the handling and disposal of hazardous chemicals.

As an alternative, the CLARiTY 1000 spectrophotometer by Olis, Inc. (Bogart, GA) has made it possible to measure hemoglobinization in turbid whole-cell suspensions quickly and without sample derivatization. This technology has been implemented in situ elsewhere (15-18), and here we demonstrate use of the CLARiTY system (Fig. 1A) to quantitate heme in buffered blood and cell culture resuspensions. The key component of the CLARiTY is a novel integrating cavity absorption meter (ICAM) that contains a quartz cuvette surrounded by a highly reflective coating. UV/visible light bracketing the heme Soret band is generated by a rapid-scanning monochromator (RSM) and directed into the cuvette to produce isotropic, fully diffused light that is subsequently altered only by sample absorption. The light is trapped within the reflective

confines of the cuvette until it encounters the output port, and thus its effective pathlength is increased significantly. The enhanced pathlength is inversely related to the detected (apparent) sample absorbance, and this non-linear effect is corrected by converting the apparent absorbance to absorbance per centimeter with the Fry equation (19). The resulting sensitivity of the CLARiTY to light absorption in turbid samples is overwhelmingly superior to that of traditional transmission spectrophotometers (Fig. 1B).

In the present study, we assess and validate our protocol for hemoglobin quantitation using the CLARiTY system in a side-by-side comparison to pyridine hemochromogen and fluorescence heme assays on standard hemoglobin solutions and blood samples. Pyridine hemochromogen and CLARiTY assays are further employed to analyze hemoglobinization in cultures of differentiating MEL and K562 cells. Specifically, we demonstrate the use of heme concentrations from pyridine hemochromogen spectra to calculate red cell indices for mouse blood and cell culture samples, a heme proportionality constant for the fluorescence assay, and a micromolar hemoglobin extinction coefficient for the CLARiTY. Additional tests of the CLARiTY verify the ability of our system to determine the effects of oxygen, glutamine, iron, aminolevulinic acid (ALA), and succinylacetone (SA) on hemoglobin levels in MEL cells. In general, we expect the protocol described here to be useful for heme quantitation in many non-erythroid cell types as well. One exception is plant cells, in which the absorbance signatures of chlorophylls and carotenoids significantly overlap the heme Soret peak.

2.3 Materials and Methods

Hemoglobin standards and mouse blood

Lyophilized hemoglobin from bovine blood (Sigma, St. Louis, MO) was dissolved in phosphate buffered saline (1XPBS) to 20 μM concentration and diluted for use as standards. Whole mouse blood samples were generously provided by L. Wang (University of Georgia, Athens, GA). Samples were collected in K_2EDTA tubes from adult wild-type C57BL/6 mice (one female and one male) and subsequently diluted between 1:250 and 1:100,000 in 1XPBS and kept on ice.

Cell culture

Cells from the MEL strain DS19 (20) and K562 line ATCC CCL-243, originally established by Lozzio and Lozzio (21), were maintained at 37°C and 5% CO_2 in complete media consisting of DMEM with 25 mM glucose and 1 mM sodium pyruvate (Cellgro, Corning, NY) supplemented with 2 mM L-glutamine, 9% (v/v) FBS (Atlanta Biologicals, Atlanta, GA), and 1X Pen/Strep (Cellgro). K562 cells were seeded at 1×10^5 cells/mL and induced to differentiate in complete media containing 1 mM sodium butyrate (Sigma). MEL cultures were seeded at 2.5×10^5 cells/mL and induced in media with 1.5% (v/v) DMSO (Sigma). Multiday induction courses of MEL and K562 cells were carried out in triplicate. In addition, MEL cells were induced for 72 or 96 hours under each of the following sets of conditions: 1) 0-4 mM L-glutamine (Cellgro), 2) 5% and 20% oxygen, 3) 100 μM iron as iron dextran (Fisons, UK) and/or 100 μM ALA (Sigma), and 4) 500 μM SA (Sigma). Hypoxic cultures were grown in a sealed incubator flushed with 5% O_2/5% CO_2/balance N_2 at 37°C.

Cell counting

Mouse red cells (1:500 dilution in 1XPBS) were counted on a hemocytometer. MEL and K562 cells were washed and diluted in 1XPBS before cell counts were made with a Scepter handheld cell counter (Millipore, Billerica, MA) as previously described (22). MEL and K562 cell proliferation values were obtained by dividing the ratio of live cells at the end of each time course to the number of cells seeded at the beginning by the same ratio for untreated cultures.

Spectrophotometric hemoglobin quantitation using the CLARiTY

Absorbances for hemoglobin standards and whole-cell suspensions were measured in the Olis CLARiTY 1000A spectrophotometer with an integrated RSM-ICAM containing a 1 mL cuvette. A total of 10 scans from 280-520 nm were collected per sample. Apparent absorbance values for 1 mL samples were recorded relative to a 1XPBS baseline at the heme Soret peaks of 400 nm for the standard solutions (which contained methemoglobin) and 410 nm for cell samples. Fry correction (19) was carried out to normalize enhanced pathlength values to 1 cm using SpectralWorks software (Olis, Inc.). The Soret peak baseline was then determined for the corrected spectra by linear interpolation. Heme concentrations were obtained from pyridine hemochromogen assays and combined with Fry-corrected absorbance values from the CLARiTY to define a hemoglobin extinction coefficient for mouse blood and MEL and K562 cell cultures. The assumptions that all cellular heme in these samples is bound to hemoglobin and that each hemoglobin tetramer contains four heme molecules were made. The mean corpuscular hemoglobin (MCH) was then calculated in picograms per cell according to the following form of the Beer-Lambert law,

$$\mathrm{MCH} = \frac{\mathrm{M_{Hb}A_{Fry}}}{\varepsilon_{\mathrm{Hb}}\,\mathrm{N}} \quad \text{(Eq. 1)}$$

where M_{Hb} = molecular weight of hemoglobin (64.5 kDa), A_{Fry} = Fry-corrected absorbance (absorbance/cm) at 410 nm, ε_{Hb} = hemoglobin extinction coefficient, and N = absolute number of cells.

Pyridine hemochromogen assay

Samples of mouse blood and cell culture resuspensions were kept on ice and disrupted by sonication. An equal volume of 50% (v/v) pyridine:0.2 N NaOH solution was added to the hemoglobin standards or homogenized cell samples to prepare the pyridine hemochrome derivative. Heme content was measured from reduced minus oxidized difference spectra as described by Berry and Trumpower (23) and based on the original work of Paul et al (7). Scans were carried out on a Cary 1G UV-visible spectrophotometer, whose settings were controlled using Cary WinUV software (Agilent, Santa Clara, CA). The absorbance difference between the reduced peak at 556 nm and oxidized trough at 540 nm (Fig. S1A) was converted to heme concentrations using the extinction coefficient 23.98 μM^{-1} cm^{-1} (23).

Fluorescence heme assay

Fluorescence assays were carried out as previously published (8,13) with minor modifications. Briefly, aliquots of hemoglobin standards or sonicated cell samples were diluted 40-fold in separate solutions of concentrated oxalic acid and split. One sample was boiled at 99°C for 30 minutes in a Robocycler PCR machine (Stratagene, La Jolla, CA). The other solution was treated in the same way except maintained at room temperature throughout to control for the presence of endogenous porphyrins. Samples were then analyzed on a CLARIOstar microplate reader (BMG LABTECH, Offenburg, Germany) at excitation and emission wavelengths of 400 nm and 662 nm, respectively.

Sensitivity and limits of detection and quantitation

Calibration data for hemoglobin standards were pooled to derive a limit of detection (LOD) for the CLARiTY, pyridine hemochromogen, and fluorescence heme assays using the 'limit of blanks' approach summarized elsewhere (24). Limits of quantitation (LOQ) and upper limits of linearity (LOL) were also determined. The LOQ was defined as the lowest concentration at which the calibration curve is linear and the coefficient of variance (CV) of replicate samples is less than 20%. The LOL was identified as the highest concentration of standard that remained in linear range of the curve. Limits were established for raw sample concentrations (e.g., LOQ_R) and normalized to original, pre-derivatized concentrations (e.g., LOQ_N). Finally, analytical sensitivity was defined as the slope of the linear region of the curve divided by the standard deviation of the response variable.

Statistics

Extinction coefficients and red cell indices for mouse blood and cell culture samples were determined as means ± one standard deviation. Statistical significance between slope values was evaluated with GraphPad Prism 6 (GraphPad Software, LaJolla, CA). Significance between two sets of cell culture conditions was established with the two-tailed Student's t-test. Multiple treatments were analyzed with one-way ANOVA followed by Tukey's post-hoc analyses using freeware from Statistica (Statsoft).

2.4 Results and Discussion

Detection parameters in pyridine hemochromogen, CLARiTY, and fluorescence assays of hemoglobin standards

Hemoglobin standards were used to derive calibration curves and to compare the detection parameters for pyridine hemochromogen, CLARiTY, and fluorescence assays,

including LOD, LOQ, LOL, and analytical sensitivity. The pyridine hemochromogen assays served a dual purpose in that the results were also used to check the heme content of the commercially available hemoglobin, which was not expected to contain four bound heme molecules per hemoglobin tetramer due to impurities, the unknown impact of oxidation (i.e., conversion to methemoglobin), and molecular structure deformities inherent to the lyophilization process. Based on a comparison of slope values from pooled plots of reduced minus oxidized absorbances against both hemoglobin and heme concentrations (Fig. 2A), it was found that the lyophilized hemoglobin contained 2.13 heme groups per hemoglobin tetramer. The detection parameters listed in Table 1 were defined in terms of heme concentrations using this value.

Corrected CLARiTY absorbances for the hemoglobin standards at 400 nm (Fig. 2B, S1B) were pooled and yielded a heme extinction coefficient (slope) of 0.266 ± 0.004 μM^{-1} cm^{-1}. The CLARiTY calibration curve was sigmoidal in shape, and the linear range of response was determined by maximizing R^2 values between visually identified bend points in the curve (Table 1). Although the LOD_R for the CLARiTY was approximately one-third the LOD_R for pyridine hemochromogen assays, the LOQ_R for the CLARiTY was more than twice the LOQ_R for pyridine hemochromogen. Because the CV dropped below 20% at 0.11 μM heme, we defined LOQ_R for the CLARiTY system by the lowest heme concentration in the linear region of the curve. This two-fold difference in LOQ_R was mirrored closely by the analytical sensitivities of the two methods.

Fluorescence heme assays also generated nonlinear calibration data across the range of standard concentrations (Fig. 2C). However, unlike the CLARiTY, two of the three series maintained linearity through the origin. The slope of the line (505 ± 8 μM^{-1}) is referred to as K_{heme}, a proportionality constant in the expression,

$$I_F = K_{heme}c_{heme} \quad \text{(Eq. 2)}$$

where I_F = fluorescence intensity and c_{heme} = heme concentration. The K_{heme} constant is a complex term that is directly proportional to the excitation beam intensity, quantum yield, heme extinction coefficient (ε_{heme}), and pathlength (14). This relationship holds at absorbances below 0.05, which can be assumed with the 40-fold dilution of the standard solutions prior to analysis. The analytical sensitivity of the fluorescence assay was unexpectedly close to the sensitivity of the CLARiTY and less than half the sensitivity of the pyridine hemochromogen assay (Table 1). Analytical sensitivity is dependent on statistical variance and is thus indicative of changes in fluorescence signal with environmental conditions. Surprisingly, the CLARiTY demonstrated a lower normalized LOD (LOD_N) than the fluorescence assay. That is, given at least 1 mL of sample, the CLARiTY and pyridine hemochromogen assays are superior to the fluorescence assay at low concentrations. At higher concentrations, the greater linear range and analytical sensitivity of the pyridine hemochromogen assay identify it as the preferred approach. Indeed, the fluorescence assay protocol employed here is only unmatched in its ability to quantitate extremely small samples.

Heme and hemoglobinization in mouse blood

As with the hemoglobin standards, the pyridine hemochromogen assay was used to determine heme levels in mouse blood dilutions (Fig. 3A). Blood was collected from one male and one female C57BL/6 mouse on separate days and analyzed (Table 2). With the exception of the female MCH (17.2 pg/cell), HGB and MCH values for both mice fell well within the normal ranges for these indices (25,26). Considering established inaccuracies in the hemocytometer relative to automated means (27), the elevated female MCH was likely due to an erroneously low cell count.

Plots of fluorescence (Fig. 3B) and corrected CLARiTY absorbance at 410 nm (Fig. 3C, S1C) against heme concentration generated slope values equivalent to K_{heme} and ε_{heme}, respectively (Table 2). While we expected ε_{heme} values for the CLARiTY to be the same for both mice, the lower value for the female mouse could also be explained by a lower than actual cell count. Regardless of the deviation, assuming that hemoglobin is saturated with heme and that it is the only hemoprotein present in the cells allows us to calculate ε_{Hb} as $4\varepsilon_{heme}$ and directly convert absorbance/cm (Beer-Lambert law) or fluorescence intensity (Eq. 2) to hemoglobin concentration. In this way, the ε_{Hb} for the CLARiTY was found to be $0.46 \pm 0.01\ \mu M^{-1}\ cm^{-1}$. Of further note, visually identified LOQ_R values for the CLARiTY and fluorescence calibration curves were similar to the values for hemoglobin standards. LOL_R values, however, were significantly higher than the hemoglobin standards for both methods, suggesting that detection parameters are analyte specific.

Hemoglobin quantitation in differentiating K562 and MEL cells

K562 cells are known to differentiate irreversibly along the erythroid lineage, expressing markers such as glycophorin A and synthesizing unusually large quantities of embryonic and fetal globins when treated with inducing agents such as sodium butyrate (28). MEL cells induced to differentiate by DMSO also exhibit erythroid-specific membrane antigens (29), an increase in globin mRNA (30), as well as a decrease in cell size (31) not observed in K562 cells.

Applying the same approach used to analyze mouse blood, pyridine hemochromogen assays on MEL and K562 cells that were induced to differentiate with DMSO (five days) and sodium butyrate (seven days), respectively, or left untreated (uninduced) were used to determine heme concentrations for each culture. Corrected absorbances from the CLARiTY plotted against the heme concentrations for MEL and K562 cells generated slope values that were not

significantly different between the two cell types (Fig. 4A). All samples were thus pooled to derive a single value for ε_{Hb} of 0.462 ± 0.004 μM^{-1} cm^{-1} (Table 3), which is equivalent to ε_{Hb} for pooled mouse blood (Table 2) to two decimal places. Incidentally, we decided to include data points that fell outside of the defined linear range (LOQ_R to LOL_R) for the hemoglobin standards. We felt this was justified for two reasons: 1) no sigmoidal trend was observed in the cell culture analysis, and 2) the CV for the standards was less than 20% at 0.11 μM heme, well below the minimum observed sample concentration.

Substitution of 0.462 μM^{-1} cm^{-1} and cell count numbers into Eq. 1 yielded MCH values. The seven-day K562 induction time course (Fig. 4B) produced a mean maximum MCH value of 7.31 pg/cell in induced samples and only 0.983 pg/cell in the uninduced controls (day 7). The induced value is significantly lower than the normal red cell level of 27-33 pg/cell (32), which has only been approached previously in K562 cells with glutamine starvation combined with hemin treatment (33). The five-day MEL induction time course (Fig. 4C) resulted in a mean maximum MCH of 4.47 pg/cell in induced cultures and 0.583 pg/cell in uninduced cultures (day 5). These values indicate that cellular hemoglobin levels are much lower in MEL cells than K562 cells. However, this is not unexpected as the average volume of a K562 cell is more than three times that of an MEL cell.

The results of additional studies that validate the ability of the CLARiTY system to quantitate hemoglobin in MEL cells under various conditions can be found in the Supplemental Material. Specifically, the effects of hypoxia (Fig. S2), glutamine starvation (Fig. S3), iron and ALA supplementation (Fig. S4A), and SA treatment (Fig. S4B) on heme production and cell proliferation are described.

In summary, CLARiTY, pyridine hemochromogen, and fluorescence methods have unique strengths and weaknesses for the measurement of hemoproteins. The pyridine hemochromogen assay has the largest linear range of operation and the highest analytical sensitivity, but it is also the most labor-intensive of the three approaches. The ability of the fluorescence assay to detect extremely low concentrations of heme is well known, yet the processes of derivatization and associated dilution considerably offset this attribute. Additionally, fluorescence requires calibration on a day-to-day basis due to variables such as temperature and lamp intensity. In contrast, the consistency of the CLARiTY between sample types was clearly established here in defining equivalent ε_{Hb} values for whole-cell resuspensions of mouse blood and differentiating MEL and K562 cells. The CLARiTY also maintained normalized limits of detection and quantitation that were comparable, if not superior, to the other assays. Although the linear range of the CLARity is smaller than the other methods, this parameter appears to be sample dependent and is significantly larger for whole-cell samples than standard solutions of hemoglobin. Perhaps most importantly, the CLARiTY system is able to quantitate protein-associated heme in situ quickly and without sample derivatization or destruction, permitting downstream applications and/or analysis.

2.5 References

1. Ponka, P. (1999) Cell biology of heme. *Am J Med Sci* **318**, 241-256

2. Tsiftsoglou, A. S., Tsamadou, A. I., and Papadopoulou, L. C. (2006) Heme as key regulator of major mammalian cellular functions: molecular, cellular, and pharmacological aspects. *Pharmacol Ther* **111**, 327-345

3. Weinberg, E. D. (1978) Iron and infection. *Microbiol Rev* **42**, 45-66

4. Dioum, E. M., Rutter, J., Tuckerman, J. R., Gonzalez, G., Gilles-Gonzalez, M. A., and McKnight, S. L. (2002) NPAS2: a gas-responsive transcription factor. *Science* **298**, 2385-2387

5. Faller, M., Matsunaga, M., Yin, S., Loo, J. A., and Guo, F. (2007) Heme is involved in microRNA processing. *Nature structural & molecular biology* **14**, 23-29

6. Drabkin, D. L. a. A., J.H. . (1935) Spectrophotometric Studies II. Preparations from washed blood cells; nitric oxide hemoglobin and sulfhemoglobin. *Journal of Biological Chemistry* **112**, 51-65

7. Paul, K. G., Theorell, H., and Akeson, A. (1953) The molar light absorption of pyridine ferroprotoporphyrin (pyridine hemochromogen). *Acta Chemica Scandinavica* **7**, 1284-1287

8. Morrison, G. R. (1965) Fluorometric Microdetermination of Heme Protein. *Anal Chem* **37**, 1124-1126

9. Bonkovsky, H. L., Wood, S. G., Howell, S. K., Sinclair, P. R., Lincoln, B., Healey, J. F., and Sinclair, J. F. (1986) High-performance liquid chromatographic separation and quantitation of tetrapyrroles from biological materials. *Anal Biochem* **155**, 56-64

10. Masuda, T., and Takahashi, S. (2006) Chemiluminescent-based method for heme determination by reconstitution with horseradish peroxidase apo-enzyme. *Anal Biochem* **355**, 307-309

11. Atamna, H., Brahmbhatt, M., Atamna, W., Shanower, G. A., and Dhahbi, J. M. (2015) ApoHRP-based assay to measure intracellular regulatory heme. *Metallomics* **7**, 309-321

12. Furhop, J. H. a. S., K.M. (1975) *Laboratory methods in porphyrin and metalloporphyrin research*, Elsevier Scientific Publishing, Amsterdam

13. Sassa, S. (1976) Sequential induction of heme pathway enzymes during erythroid differentiation of mouse Friend leukemia virus-infected cells. *J Exp Med* **143**, 305-315

14. Harris, D. A. a. B., C.L. (Eds). (1987) *Spectrophotometry and spectrofluorimetry - a practical approach*, IRL press, Oxford

15. Blake, R. C., 2nd, and Griff, M. N. (2012) In situ Spectroscopy on Intact Leptospirillum ferrooxidans Reveals that Reduced Cytochrome 579 is an Obligatory Intermediate in the Aerobic Iron Respiratory Chain. *Front Microbiol* **3**, 136

16. Zorz, J. K., Allanach, J. R., Murphy, C. D., Roodvoets, M. S., Campbell, D. A., and Cockshutt, A. M. (2015) The RUBISCO to Photosystem II Ratio Limits the Maximum Photosynthetic Rate in Picocyanobacteria. *Life (Basel)* **5**, 403-417

17. Li, T. F., Painter, R. G., Ban, B., and Blake, R. C., 2nd. (2015) The Multicenter Aerobic Iron Respiratory Chain of Acidithiobacillus ferrooxidans Functions as an Ensemble with a Single Macroscopic Rate Constant. *J Biol Chem* **290**, 18293-18303

18. Rana, N., McLean, S., Mann, B. E., and Poole, R. K. (2014) Interaction of the carbon monoxide-releasing molecule Ru(CO)3Cl(glycinate) (CORM-3) with Salmonella enterica serovar Typhimurium: in situ measurements of carbon monoxide binding by integrating cavity dual-beam spectrophotometry. *Microbiology* **160**, 2771-2779

19. Fry, E. S., Kattawar, G. W., Strycker, B. D., and Zhai, P. W. (2010) Equivalent path lengths in an integrating cavity: comment. *Appl Opt* **49**, 575-577

20. Ohta, Y., Tanaka, M., Terada, M., Miller, O. J., Bank, A., Marks, P., and Rifkind, R. A. (1976) Erythroid cell differentiation: murine erythroleukemia cell variant with unique pattern of induction by polar compounds. *Proc Natl Acad Sci U S A* **73**, 1232-1236

21. Lozzio, C. B., and Lozzio, B. B. (1975) Human chronic myelogenous leukemia cell-line with positive Philadelphia chromosome. *Blood* **45**, 321-334

22. Ongena, K., Das, C., Smith, J. L., Gil, S., and Johnston, G. (2010) Determining cell number during cell culture using the Scepter cell counter. *J Vis Exp*

23. Berry, E. A., and Trumpower, B. L. (1987) Simultaneous determination of hemes a, b, and c from pyridine hemochrome spectra. *Anal Biochem* **161**, 1-15

24. Shrivastava, A. a. G., V.B. (2011) Methods for the determination of limit detection and limit of quantitation of the analytical methods. *Chronicles of Young Scientists* **2**, 21-25

25. Hedrich, H. J. (2012) *The laboratory mouse*, Second edition / ed., AP, Elsevier, Amsterdam

26. (C57BL/6 Mouse Biochemistry (North American Colonies) [pdf]) 2012. Charles River Laboratories International, Inc., Wilmington, MA

27. Stone, L. R., Gray, D.R., Remple, K., and Beaudet, M.P. (2009) Accuracy and precision comparison of the hemocytometer and automated cell counting methods. *FASEB J.* Meeting abstract 827.2

28. Andersson, L. C., Jokinen, M., and Gahmberg, C. G. (1979) Induction of erythroid differentiation in the human leukaemia cell line K562. *Nature* **278**, 364-365

29. Furusawa, M., and Takahashi, K. P. (1972) Erythrocyte membrane-specific antigens common to several species of rodentia. *Nat New Biol* **235**, 242

30. Ross, J., Ikawa, Y., and Leder, P. (1972) Globin messenger-RNA induction during erythroid differentiation of cultured leukemia cells. *Proc Natl Acad Sci U S A* **69**, 3620-3623

31. Friend, C., Scher, W., Holland, J. G., and Sato, T. (1971) Hemoglobin synthesis in murine virus-induced leukemic cells in vitro: stimulation of erythroid differentiation by dimethyl sulfoxide. *Proc Natl Acad Sci U S A* **68**, 378-382

32. Vajpayee, N., Graham, S.S., Bem, S. (2011) Basic examination of blood and bone marrow. in *Henry's Clinical Diagnosis and Management by Laboratory Methods* (McPherson, R. A. a. P., M.R. ed.), 22 Ed., Saunders Elsevier, Philadelphia, PA. pp 509-535

33. Erard, F., Dean, A., and Schechter, A. N. (1981) Inhibitors of cell division reversibly modify hemoglobin concentration in human erythroleukemia K562 cells. *Blood* **58**, 1236-1239

34. Canh Hiep, N., Kinohira, S., Furuyama, K., and Taketani, S. (2012) Depletion of glutamine enhances sodium butyrate-induced erythroid differentiation of K562 cells. *J Biochem* **152**, 509-519

35. Mates, J. M., Segura, J. A., Alonso, F. J., and Marquez, J. (2006) Pathways from glutamine to apoptosis. *Front Biosci* **11**, 3164-3180

36. Parmar, K., Mauch, P., Vergilio, J. A., Sackstein, R., and Down, J. D. (2007) Distribution of hematopoietic stem cells in the bone marrow according to regional hypoxia. *Proc Natl Acad Sci U S A* **104**, 5431-5436

37. Hofer, T., Wenger, R. H., Kramer, M. F., Ferreira, G. C., and Gassmann, M. (2003) Hypoxic up-regulation of erythroid 5-aminolevulinate synthase. *Blood* **101**, 348-350

38. Zhang, F. L., Shen, G. M., Liu, X. L., Wang, F., Zhao, Y. Z., and Zhang, J. W. (2012) Hypoxia-inducible factor 1-mediated human GATA1 induction promotes erythroid differentiation under hypoxic conditions. *J Cell Mol Med* **16**, 1889-1899

39. Abu-Farha, M., Niles, J., and Willmore, W. G. (2005) Erythroid-specific 5-aminolevulinate synthase protein is stabilized by low oxygen and proteasomal inhibition. *Biochemistry and cell biology = Biochimie et biologie cellulaire* **83**, 620-630

40. Kawasaki, N., Morimoto, K., Tanimoto, T., and Hayakawa, T. (1996) Control of hemoglobin synthesis in erythroid differentiating K562 cells. I. Role of iron in erythroid cell heme synthesis. *Arch Biochem Biophys* **328**, 289-294

41. Sassa, S., and Kappas, A. (1983) Hereditary tyrosinemia and the heme biosynthetic pathway. Profound inhibition of delta-aminolevulinic acid dehydratase activity by succinylacetone. *J Clin Invest* **71**, 625-634

42. Grandchamp, B., Beaumont, C., de Verneuil, H., and Nordmann, Y. (1985) Accumulation of porphobilinogen deaminase, uroporphyrinogen decarboxylase, and alpha- and beta-globin mRNAs during differentiation of mouse erythroleukemic cells. Effects of succinylacetone. *J Biol Chem* **260**, 9630-9635

2.6 Figures and Tables

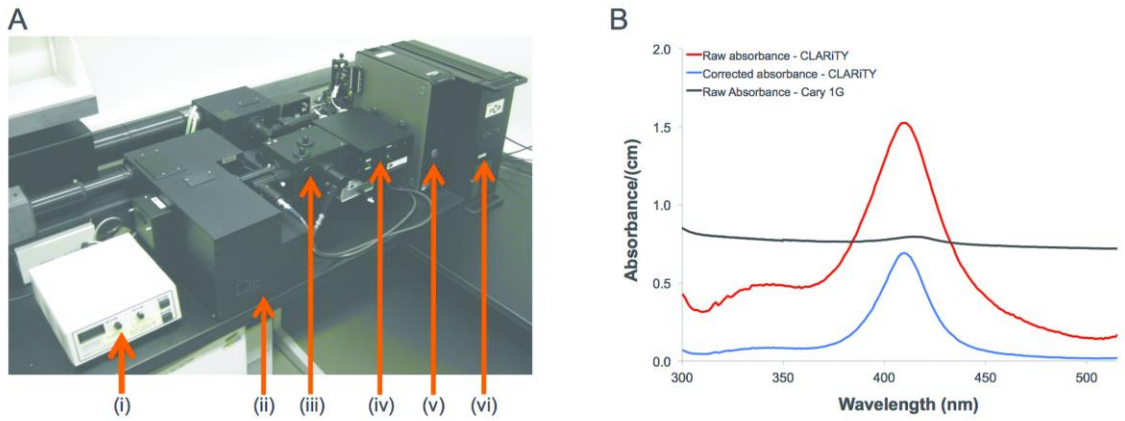

Figure 1. The Olis CLARiTY spectrophotometer diffuses light from a rapid scanning monochromator (RSM) to obtain absorbance readings for hemoglobin in turbid whole-cell solutions. (A) Major components of the CLARiTY system include: (i) xenon arc lamp with igniter, (ii) RSM, (iii) CLARiTY module with 1-and 10-mL cuvettes adjoined to separate photomultiplier tubes, (24) control box to switch scan settings between RSM and CLARiTY, (v) computer hard drive, and (vi) electronic box. (B) Overlay of absorbance spectra for MEL cells washed and resuspended in 1XPBS following a 72-hour induction in regular media containing 1.5% DMSO. The apparent absorbance scan of a 1 mL cell sample on the RSM-CLARiTY is decreased upon Fry correction (19) for the increased pathlength within the cuvette. A traditional transmission spectrophotometer (Cary 1G by Varian) was used to scan a 1:10 dilution of the same cell resuspension analyzed on the CLARiTY.

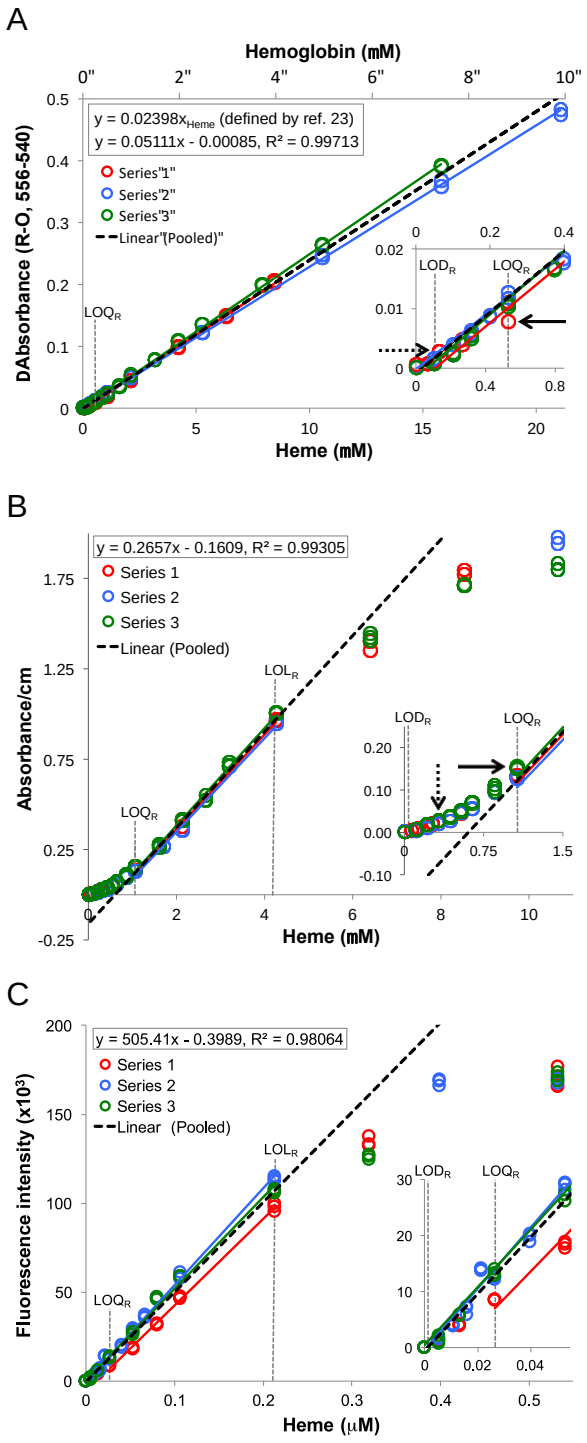

Figure 2. Determination of detection parameters for pyridine hemochromogen, CLARiTY, and fluorescence assays of standard hemoglobin dilutions. (A) Pyridine hemochromogen and (B) CLARiTY calibration curves. Scans for select points (see arrows) in the LOD_R-LOQ_R range

can be found in the Supplementary Material (Fig. S1A, S1B). (C) Fluorescence calibration line. Inset plots magnify the region near the origin. Each method was carried out on three separate days (Series 1, 2, and 3) with two or three repeat measurements per day. Slopes of the linear regions of pyridine hemochromogen and CLARiTY curves represent micromolar extinction coefficients for pooled data in each type of analysis. Abbreviations: LOD = limit of detection, LOQ = limit of quantitation, LOL = limit of linearity, subscript *R* = value in terms of the raw sample concentration.

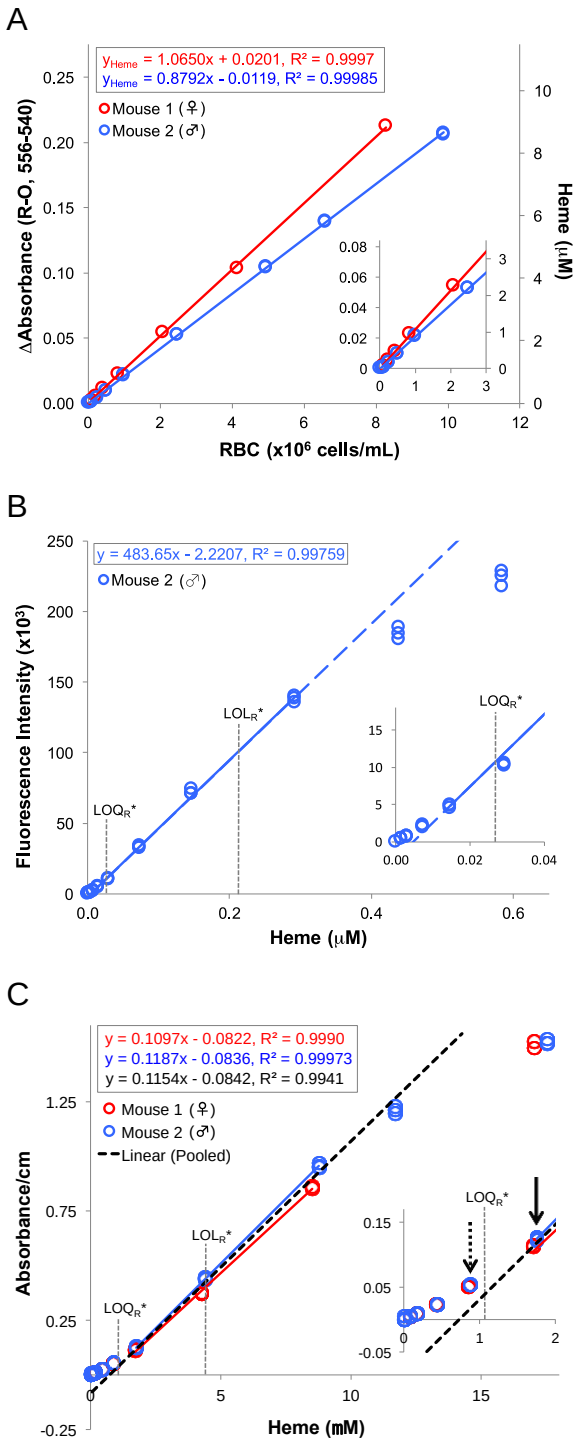

Figure 3. Pyridine hemochromogen, CLARiTY, and fluorescence assays of whole mouse blood. Dilutions of clot-free blood between 1:250 and 1:150,000 were prepared in 1XPBS and analyzed for each mouse (Mouse 1 = female, Mouse 2 = male). (A) Pyridine hemochromogen

absorbance differences were measured twice for each mouse and corresponding heme concentrations were plotted against the number of red cells counted on a hemocytometer. The slope values are equivalent to heme content in fmol/cell. Scans maintained the same profile illustrated in Fig. S1A. (B) Fluorescence assays were carried out on three repeat samples for each dilution of Mouse 2 blood. (C) CLARiTY analysis produced two statistically different extinction coefficients for heme in Mouse 1 and Mouse 2. Individual data points bracketing the LOQ_R reveal a Soret peak shift from 400 nm in the hemoglobin standards (Fig. S1B) to 410 nm in blood (Fig. S1C). This 10 nm difference was not unexpected, as the lyophilized hemoglobin solid used in the standards contained a significant amount of methemoglobin. Inset plots magnify the region near the origin. The asterisk mark (*) indicates a limit parameter established for purified hemoglobin standards (Fig. 2), shown for comparison.

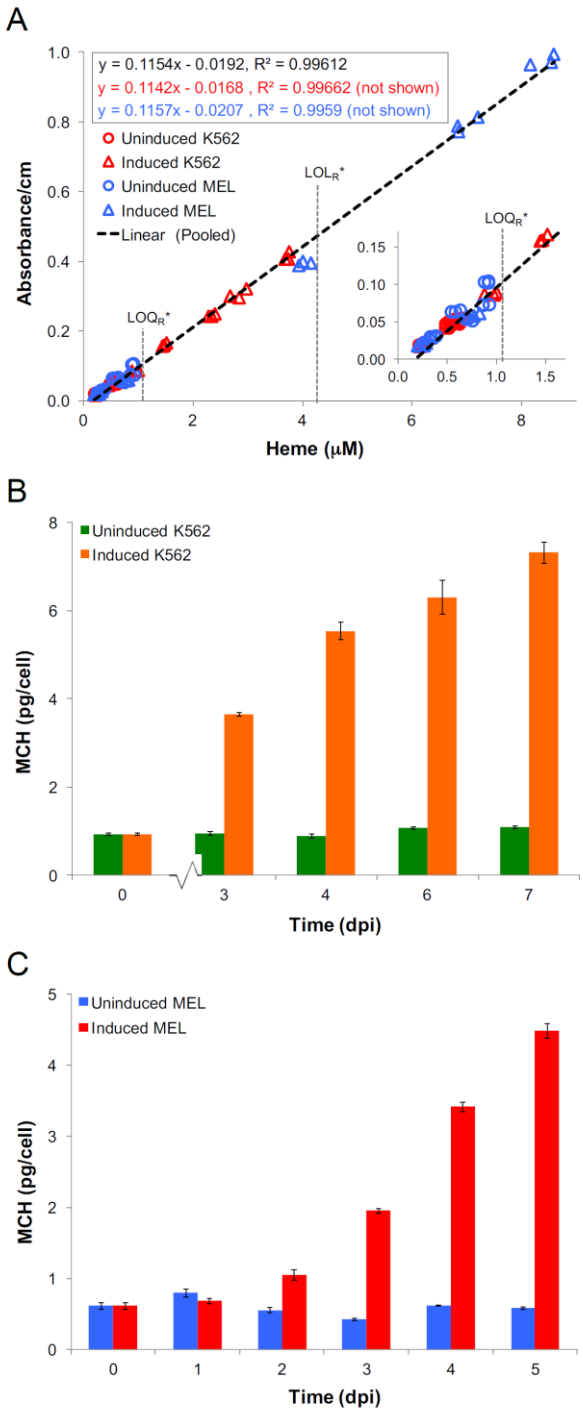

Figure 4. Determination and application of a micromolar extinction coefficient for whole-cell K562 and MEL suspensions. Data from CLARiTY and pyridine hemochromogen assays were used in combination (A) to derive MCH values for induced and uninduced K562 (B) and MEL (C) cultures over seven- and five-day time courses, respectively. The regression line for

pooled absorbance/cm values (CLARiTY) and heme concentrations (pyridine hemochromogen assays) (A) was used to a derive single heme extinction coefficient because individual K562 and MEL slopes (lines not shown for clarity) were not significantly different ($p = 0.115$). Note that points that fell outside the linear range determined for hemoglobin standards (LOQ_R*-LOL_R*) were included in the regression analysis, as explained in the main text. Error bars indicate ± one standard deviation from the mean.

Table 1. Detection parameters and assay information for hemoglobin standard solutions.

Method	LOD_R, LOD_N (μM)	LOQ_R, LOQ_N (μM)	LOL_R, LOL_N (μM)	Analytical sensitivity (μM^{-1})	Sample volume (mL)	Requires sample derivatization?	Approximate time for 1, 96 cell assay(s)
Pyridine hemochromogen	0.0959, 0.194	0.533, 1.08	≥ 10, ≥ 20	72.3	1	Yes	10 min, 6 h
Fluorescence	0.00143, 0.0572	0.0266, 1.06	0.213, 8.52	28.5	0.012	Yes	1 h, 2.5 h
CLARiTY	0.0362, 0.0362	1.07, 1.07	4.26, 4.26	30.8	1	No	1 min, 1.5 h

All micromolar units reflect heme concentrations. LOD = limit of detection, LOQ = limit of quantitation, LOL = (upper) limit of linearity; *R* subscript indicates the limits in terms of the raw, analyzed sample concentration (as shown in Fig. 2); *N* subscript indicates limit normalization to the underivatized and undiluted sample concentration.

Table 2. Mouse whole blood indices and spectroscopic constants.

Sample	Density (10^9 cells/mL)	Pyridine hemochromogen		Fluorescence	CLARiTY	
		HGB (g/dL)	MCH (pg/cell)	K_{heme} (μM^{-1})	ε_{heme} (μM^{-1} cm^{-1})	ε_{Hb} (μM^{-1} cm^{-1})
Mouse 1 (♀)	8.35	14.7 ± 0.6	17.2 ± 0.1	NE	0.110 ± 0.002	0.439 ± 0.007
Mouse 2 (♂)	9.97	14.1 ± 0.4	14.2 ± 0.1	0.484 ± 0.007	0.119 ± 0.001	0.475 ± 0.003
Pooled	–	–	–	–	0.115 ± 0.002	0.46 ± 0.01

Pyridine hemochromogen assay results are based on an extinction coefficient of 23.98 μM^{-1} cm^{-1} (21). Cellular heme, K_{heme}, and ε_{heme} are equivalent to slope values reported in Fig. 2. Reference 25 reports normal HGB and MCH ranges of 13-18 g/dL and 13-17 pg/cell, respectively. Reference 26 provides clinical lab data for normal HGB (10.9-18.1 g/dL for female mice and 10.8-19.2 g/dL for males) and MCH (13.0-16.8 pg/cell for female mice and 11.7-16.3 pg/cell for males).

Table 3. Cell culture heme and hemoglobin properties.

Sample	Pyridine hemochromogen (induced cells)		CLARiTY (all cells)	
	Cellular heme (fmol/cell)	MCH (pg Hb/cell)	ε_{heme} (μM^{-1} cm^{-1})	ε_{Hb} (μM^{-1} cm^{-1})
K562 cells	0.477 ± 0.005	7.32 ± 0.24	0.114 ± 0.001	0.457 ± 0.005
MEL cells	0.216 ± 0.001	4.48 ± 0.10	0.116 ± 0.001	0.463 ± 0.005
Pooled	–	–	0.115 ± 0.001	0.462 ± 0.004

Pyridine hemochromogen assay results were obtained for K562 and MEL cells harvested at seven and five days post induction, respectively. CLARiTY ε_{heme} and ε_{Hb} values were taken from the linear regression data in Fig. 4A.

2.7 Supplementary Information

Supplemental Figures

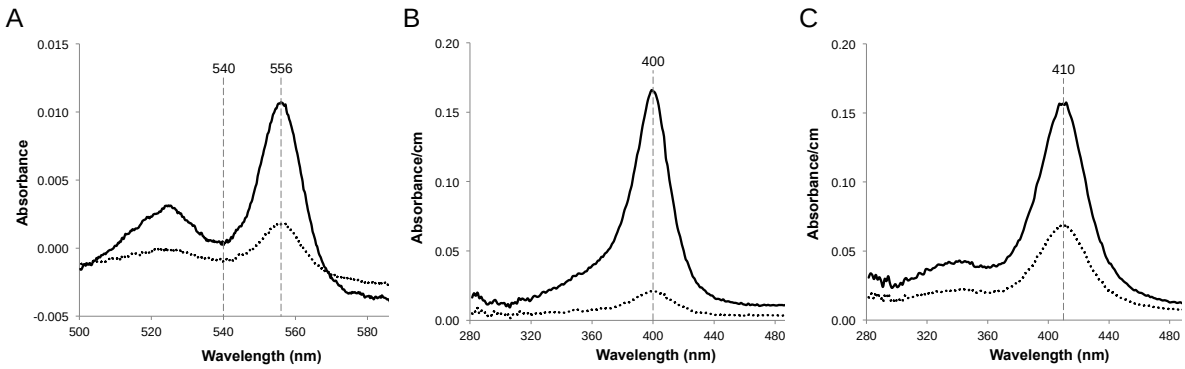

Figure S1. Individual scans of hemoglobin standards and mouse blood. Reduced-minus-oxidized spectra (A) and Fry-corrected CLARiTY scans (B) for hemoglobin standards in the LOD_R-LOQ_R range, as indicated by arrows in Fig. 2A and 2B, respectively. Corrected CLARiTY scans for select mouse blood dilutions (see arrows in Fig. 3C) bracketing the LOQ_R from the hemoglobin standards analysis. Note the shift in the Soret peak from 400 nm (B) to 410 nm (C).

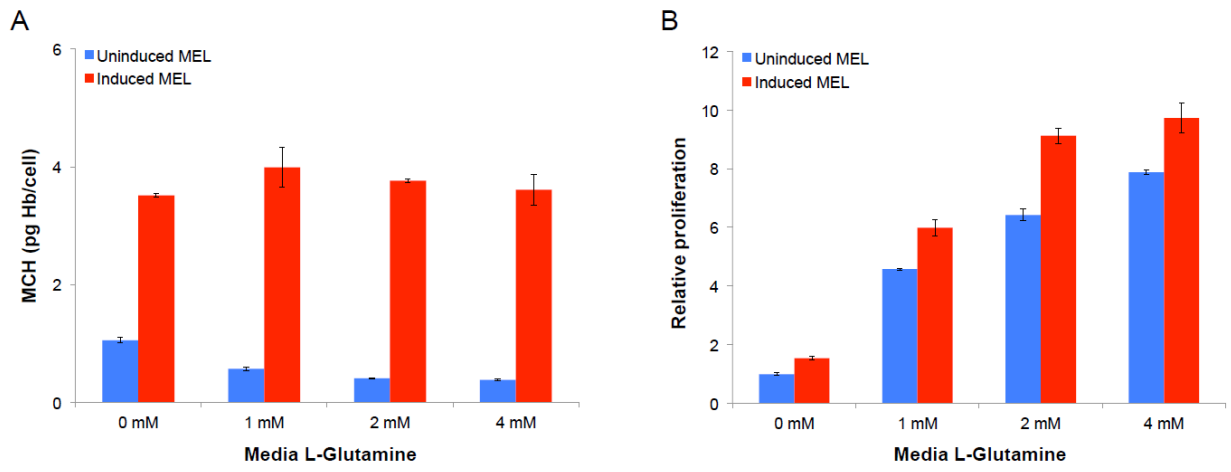

Figure S2. MEL cells incubated for 96 hours in media containing 0-4 mM L-glutamine. Glutamine starvation in K562 cells has been shown to significantly increase hemoglobinization, putatively stemming from a decrease in intracellular glutathione and the associated increase in oxidative stress (34). Hence we used the CLARiTY to test whether MEL cells respond in a similar way to glutamine deficiency (A). However, we did not detect a statistically significant difference in the hemoglobinization of induced MEL cells across all glutamine concentrations ($p = 0.1050$) nor uninduced cells incubated in 2 mM and 4 mM glutamine ($p = 0.705$). On the other hand, cell proliferation levels changed markedly with glutamine levels in the media (B). Specifically, cell growth increased among uninduced cells with each increase in glutamine concentration ($p \leq 0.01$). The same held true for induced cells ($p \leq 0.01$) except between 2 mM and 4 mM cultures ($p = 0.175$). These data are not surprising, as glutamine is known to be both a nutrient and signal molecule in apoptotic pathways (35). Note that each concentration was determined in triplicate, and error bars indicate ± one standard deviation from the mean.

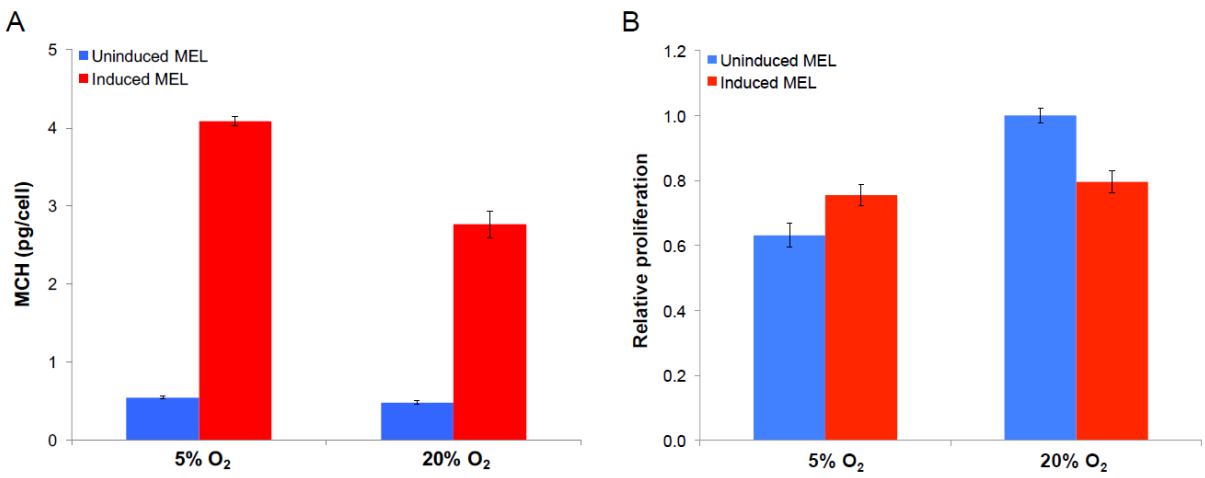

Figure S3. MEL cells incubated for 72 hours under hypoxic (5% O_2) and normoxic (20% O_2) conditions. It has previously been shown that an oxygen gradient controls hematopoietic stem cell function in bone marrow, where the most primitive cells concentrate in nearly anoxic (and radical-free) regions of the marrow (36). Because hypoxia directly upregulates heme biosynthesis at transcriptional (37, 38) and post-translational levels (39), we have used the CLARiTY system to verify that hypoxia (5% O_2) over a 72-hour induction (A) causes significantly greater hemoglobinization in induced MEL cells ($p \leq 0.01$). Regarding proliferation (B), induced MEL cells grew at a greater rate than uninduced cells at 5% O_2 ($p = 0.0123$). The opposite was true under normoxic conditions ($p = 0.0009$), as is commonly observed. Unlike uninduced MEL cells, no change in relative proliferation was observed for induced cells ($p = 0.6455$) between 5% O_2 and 20% O_2. These data thus support the proposed suitability of erythroid precursors to hypoxic environments.

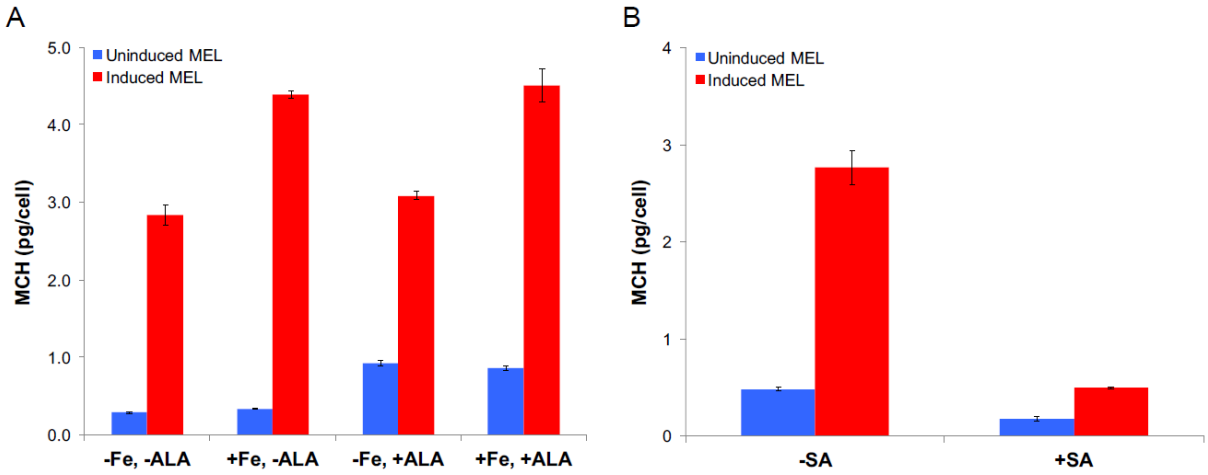

Figure S4. Induction of MEL cells treated with iron, ALA, and SA. A previous report by Kawasaki et al (40) has established the limiting factors of iron and ALA synthesis and their synergistic effects on hemoglobinization in K562 cells. Using combinations of 100 μM iron dextran and 100 μM ALA over a 96-hour induction period (A), we used the CLARiTY system to show that iron increases MCH values independent of ALA in induced cells. Conversely, ALA increases hemoglobinization independent of iron in uninduced cells. Thus we conclude that iron is rate limiting for hemoglobinization in induced MEL cells, while ALA synthesis is limiting in uninduced cells. Unlike in K562 cells, there is no apparent synergy between iron and ALA treatments in MEL cells. Note that differences in cell growth among induced or uninduced samples were marginal (data not shown). Regarding SA supplementation, Sassa et al (41) were the first to demonstrate the inhibition of the heme biosynthesis enzyme aminolevulinic acid dehydratase by the compound. Our results for a 72-hour induction experiment confirm the significant effects of SA on hemoglobinization in both induced and uninduced MEL cells (B). We also observed no significant changes in cell proliferation in induced or uninduced cells (data not shown), consistent with data published elsewhere (42).

Main Text References for Supplemental Figures

Figure S2. (34,35), Figure S3. (36-39), Figure S4. (40-42)

CHAPTER 3

HUMAN AMINOLEVULINATE SYNTHASE STRUCTURE REVEALS A EUKARYOTIC-SPECIFIC AUTOINHIBITORY LOOP REGULATING SUBSTRATE BINDING AND PRODUCT RELEASE

Marcero, J. R.[*], Bailey H. J.[*], Bezerra, G. A.[*], Padhi, S.[*], et al. (2020) *Nat Commun* **11**(1), 1-12

[*]These authors contributed equally.

3.1 Abstract

5’-aminolevulinate synthase (ALAS) catalyzes the first step in heme biosynthesis, generating 5’-aminolevulinate from glycine and succinyl-CoA. Inherited frameshift indel mutations of human erythroid-specific isozyme ALAS2, within a C-terminal (Ct-)extension of its catalytic core that is only present in higher eukaryotes, lead to gain-of-function X-linked protoporphyria (XLP). Here we report the human ALAS2 crystal structure, revealing that its Ct-extension folds onto the catalytic core, sits atop the active site, and precludes binding of substrate succinyl-CoA. The Ct-extension is therefore an autoinhibitory element which must reorient during catalysis, as supported by molecular dynamics simulations. Our data explain how Ct deletions in XLP alleviate autoinhibition and increase enzyme activity. Crystallography-based fragment screening reveals a binding hotspot around the Ct-extension, where fragments interfere with the Ct conformational dynamics and inhibit ALAS2 activity. These fragments represent a starting point to develop ALAS2 inhibitors as substrate reduction therapy for porphyria disorders that accumulate toxic heme intermediates.

3.2 Introduction

The tetrapyrrole cofactor heme is essential for various cellular processes across lifeforms. In metazoans, heme synthesis occurs via a conserved eight-reaction pathway that requires iron, glycine and succinyl-CoA. The first and rate-limiting step is carried out by 5’-aminolevulinate synthase (ALAS; EC 2.3.1.37) in the mitochondria (1,2). ALAS catalyzes the pyridoxal 5’-phosphate (PLP)-dependent condensation of succinyl-CoA and glycine to form aminolevulinic acid (ALA), with CoA and CO_2 as by-products. The product ALA is then transported into the cytoplasm for the subsequent biosynthetic steps that eventually lead back into the mitochondria,

where ferrochelatase (FECH) ultimately inserts iron into protoporphyrin IX (PPIX) to produce heme(3,4). Vertebrates have evolved two nuclear-encoded ALAS isozymes (5,6) that share ~60% amino acid sequence identity. ALAS1 (gene location 3p21.2) is the housekeeping enzyme providing a basal level of heme in non-erythroid cell types for cytochromes and other hemoproteins. ALAS2 (gene location Xp11.21) is predominantly expressed in erythroid progenitor cells and synthesizes 85-90% of total body heme specifically for hemoglobin production during erythropoiesis. Mutations in the heme biosynthetic genes, resulting in an accumulation of toxic porphyrin intermediates, are associated with a group of inherited disorders called porphyrias (3,7).

The ALAS catalytic mechanism, involving Schiff-base formation between the aldehyde carbonyl of the PLP cofactor and ε-amino group of a conserved lysine residue, has been well characterized (8-11). Without substrates, PLP is covalently attached to the active site lysine (Lys391 in human ALAS2 (hsALAS2)) as an internal aldimine adduct. The reaction begins with the glycine substrate replacing lysine in the Schiff-base linkage to form an external aldimine. Next, deprotonation of glycine forms a transient quinonoid intermediate that is competent for nucleophilic attack on the co-substrate, succinyl-CoA, resulting in a condensation reaction releasing the CoA moiety, followed by a decarboxylation assisted by the active site histidine (His285 in hsALAS2). Subsequent protonation regenerates the internal aldimine, and allows release of the product, ALA. A number of kinetic studies have suggested that the ALAS rate-determining step is product (ALA) release (8,9). The structure of *R. capsulatus* ALAS (rcALAS) was the first reported for the enzyme (12), revealing an induced-fit mechanism upon substrate binding, via an open-to-close transition of a mobile active site loop. Conformational mobility of this loop has also been proposed to be a kinetic barrier for product release (8,11,13).

Eukaryotic ALAS enzymes have evolved extensions appending to both N- and C-termini of the highly conserved catalytic core (Fig. 1a) (14). The N-terminal extensions, harboring the mitochondrial targeting sequence (14-17), are poorly conserved between higher and lower eukaryotic ALAS enzymes, as well as between metazoan ALAS1 and ALAS2 (Supplementary Fig. 1). Metazoan enzymes further encode three Cys-Pro motifs (18), two of which are within the targeting sequence. The third Cys-Pro motif, together with an invariant Gln-Glu-Asp-Val motif, are found within a 70-90 aa region of poor sequence conservation and unknown function. In both ALAS1 and ALAS2, the Cys-Pro motifs have been shown to be responsible for heme-dependent inhibition of mitochondrial translocation of the enzyme precursor (19,20).

The eukaryotic extension at the C-terminus (Ct-extension) ranges from 35 to 60 aa in length. Metazoan ALAS1 and ALAS2 share about 53% sequence identity in their Ct-extensions (their major differences are found in the last 9 amino acids), while *S. cerevisiae* encodes an entirely different Ct-extension from metazoans, and also from *S. pombe* (Supplementary Fig. 1). Frameshift indel mutations in exon 11 of the human *ALAS2* gene (on chromosome Xp11.21) that result in deletion, replacement, or elongation of its Ct-extension are the molecular cause of X-linked protoporphyria (XLP, MIM 300752), an inherited disorder that presents with painful phototoxicity and an increased risk for liver dysfunction and failure (21,22), due to high levels of the toxic heme intermediate PPIX. At the protein level, these genetic lesions cause enhanced enzyme activity, lending to XLP being referred to as a gain-of-function (GOF) disorder (23-25). Recently, a GOF XLP phenotype was reported for mutations of the mitochondrial ATP-dependent Clp protease ClpX, an AAA+ (ATPases associated with diverse cellular activities) unfoldase shown to activate ALAS dimers through partial unfolding of the enzyme to enhance loading of the PLP cofactor into the active site (26,27). XLP contrasts with another ALAS2-

associated blood disorder, X-linked sideroblastic anemia (XLSA, MIM 300751), which results in loss of enzyme function and is characterized by heme-deficient and iron-overloaded red blood cells (ringed sideroblasts) (28-31). XLSA is attributable to mutations within exons 5-11 (including a few in the Ct-extension; from Human Gene Mutation Database (32)) that are predominantly missense in nature.

While the dichotomous genotype-phenotype correlation of XLSA and XLP is now widely recognized, it remains unknown how the GOF phenotypes in XLP are brought about by various mutations in the ALAS2 Ct-extension, although a self-inhibitory role has been proposed for this region (33). The recently published ALAS2 structure from *S. cerevisiae* (scALAS) showed its Ct-extension wrapping around the surface of the ALAS homodimer, albeit distant from the enzyme active site (34). This sequence, furthermore, bears no homology with other eukaryotic counterparts and is likely to be evolutionarily distinct from the mammalian ALAS2 Ct-extension. Importantly, deletion of the scALAS extension does not increase its enzyme activity (34), contrary to the XLP-causing mutations in hsALAS2. Here, we have determined the crystal structure of hsALAS2 which, in combination with molecular dynamics simulations and enzyme kinetics, reveals salient features of the Ct-extension that explain its role in enzyme regulation and in causing XLP.

3.3 Methods

Protein expression and purification

DNA fragments encoding hsALAS2 harboring different N- and C-terminal boundaries (Supplementary Fig. 2) were cloned into the pFB-LIC-Bse vector in-frame with a tobacco etch virus protease cleavable N-terminal His_6-tag and expressed in baculovirus-infected insect cells in

Sf9 media. Site directed mutagenesis (R511E) was carried out on hsALAS2$_{\Delta N142}$ and hsALAS2$_{\Delta N142\Delta C545}$ cloned into pNIC28-Bsa4 vector using the QuikChange method and confirmed by sequencing. In addition, hsALAS2$_{\Delta N78}$ containing NheI and BamHI restriction sites was cloned into the pET28a vector in-frame with the N-terminal His$_6$-tag. Variants of the hsALAS2$_{\Delta N78}$:pET28a plasmid were prepared via Quikchange mutagenesis, including R511E, E569Q, and XLP mutants delAT, delAGTG, delG, and Q548X. All pET28a fusion proteins were transformed into BL21(DE3) competent cells and single-colony inoculations were induced at an OD_{600} of 0.5-0.7 with 0.1 mM IPTG for 16-18 h at 12°C. Cultures were then centrifuged, and cell pellets were stored at -80°C.

Proteins expressed in pFB-LIC-Bse and pNIC28-Bsa4 were lysed by sonication and centrifuged at 35,000 x *g*. The clarified cell extract was incubated with 2.5 mL of Ni-NTA resin pre-equilibrated with lysis buffer (50 mM HEPES pH 7.5, 500 mM NaCl, 10 mM imidazole, 5% Glycerol, 0.5 mM TCEP). The column was washed with 100 mL Binding Buffer (50 mM HEPES pH 7.5, 500 mM NaCl, 5% glycerol, 10 mM imidazole, 0.5 mM TCEP), 50 mL Wash Buffer (50 mM HEPES pH 7.5, 500 mM NaCl, 5% glycerol, 40 mM imidazole, 0.5 mM TCEP) and eluted with 15 mL of Elution Buffer (50 mM HEPES pH 7.5, 500 mM NaCl, 5% glycerol, 250 mM imidazole, 0.5 mM TCEP). The eluant fractions were concentrated to 5 mL and applied to a Superdex 200 16/60 column pre-equilibrated in GF Buffer (50 mM HEPES pH 7.5, 500 mM NaCl, 0.5 mM TCEP, 5% glycerol). Eluted protein fractions were pooled and concentrated to 10-17 mg mL^{-1}. Where applicable, His$_6$-tag removal was carried out by overnight treatment with TEV protease, followed by purification over Ni-NTA resin.

The hsALAS2 variants expressed in pET28a were similarly purified. Specifically, each protein was captured on a HisPur Cobalt Resin (Thermo Scientific) in solubilization buffer

consisting of 50 mM Tris-HCl, pH 8.0, 20 μM PLP, 100 mM KCl, 10% glycerol, and 0.2% Tween-20. The resin was washed with solubilization buffer containing 15 mM imidazole. PMSF was also added at 0.5 mM during sonication, binding and washing steps. Elutions in 250 mM imidazole were buffer exchanged over Sephadex G-25 spin columns and quantitated with the Pierce BCA Protein Assay Kit (Thermo Scientific). Purified protein samples (1 μg for SDS-PAGE and 100 ng for western blots) were run out on Mini-PROTEAN Stain-Free polyacrylamide gels (Bio-Rad) and bands detected using the ChemiDoc MP imaging system (Bio-Rad) and ImageLab software (version 5.1, Bio-Rad). Multiplex western blotting was carried out by transferring gel bands to low-fluorescence PVDF membrane, followed by blocking the membrane in 2% BSA at room temperature for one hour and incubation overnight at 4°C in 1:10,000 rabbit whole-serum polyclonal hsALAS2 (custom-made, purified antibody from Invitrogen available through Thermo Scientific, catalog number 21553) and 1:5,000 mouse monoclonal anti-6xHis (Proteintech, catalog number 66005-1-lg) primary antibodies in 1% BSA. After washing extensively in TBST, the membrane was incubated in 1:50,000 dilutions of Invitrogen fluorescent donkey anti-rabbit IgG (DyLight 550, catalog number SA5-10039) and goat anti-mouse IgG (DyLight 650, catalog number SA5-10041) secondary antibodies (Thermo Scientific) before washing again and imaging on the ChemiDoc system. Uncropped and unprocessed scans of blots and gels are provided in the Source Data file.

Crystallization and structure determination

Crystals were grown by the vapor diffusion method. To crystallize hsALAS2$_{\Delta N142}$, protein was pre-incubated with 5 mM hydroxylamine for 30 minutes on ice to convert PLP into the non-covalent form. Sitting drops containing 75 nL protein (17 mg mL^{-1}) and 75 nL well solution containing 25% (w/v) PEG 3350, 0.1 M Bis-Tris pH 6.7 and 0.3 M $MgCl_2$ were

equilibrated at 20°C. To crystallize hsALAS2$_{\Delta N78}$, sitting drops containing 200 nL protein (11 mg mL^{-1}), 133 nL well solution containing 20% (w/v) PEG3350 and 0.2 M NH_4Cl, and 67 nL seed solution derived from previously obtained micro crystals. Crystals were cryo-protected using 25% (v/v) ethylene glycol and flash-cooled in liquid nitrogen. Diffraction data were collected at the DLS beamline i04 and i24.

HsALAS2$_{\Delta N142}$ was crystallized in the monoclinic space group C2 with two molecules in the asymmetric unit. The data was processed using the Xia2 autoprocessing dials pipeline. hsALAS2$_{\Delta N78}$ was crystallized in the monoclinic space group $P2_1$ with four molecules in the asymmetric unit. The data were processed using non-ellipsoidal anisotropy truncations by the STARANISO server, based on a lower limit of 1.2 for the local I/sigI producing resolution cutoff of 2.65 Å in the best direction and 3.55 Å in worst. The human structures were solved by molecular replacement using the program PHASER from CCP4 (49) and the rcALAS structure (PDB code 2BWN) (12) as the search model. The final model was produced by iterative cycles of restrained refinement and model building using COOT (50), REFMAC5 from CCP4 (51) and Phenix.refine (52).

The final model consists of Phe143-Met578 of chains A and B. In both chains the last 9 residues, aa 579-587, and a loop between Ser182 and Ser188 were not visible in the electron density map indicating that this region was largely unstructured. Additionally, chain-to-chain variation in electron density quality and loop orientation were found between residues Asp549 and Cys558, likely reflective of differing crystal packing restraints and an intrinsic tendency for conformational heterogeneity within these regions. Coordinates and structure factors for hsALAS2$_{\Delta N142}$ were deposited in the PDB with the accession code 6HRH. Statistics for data collection and refinement are summarized in Table 1.

Crystallography-based fragment screening

To grow crystals for the fragment screening campaign, 10 mg mL^{-1} of $hsALAS2_{\Delta N142}$ was pre-incubated with 5 mM hydroxylamine for 30 minutes on ice to convert PLP into the homogenous, non-covalent form. Crystals were grown by vapor diffusion in 400 nL sitting drops in the presence of seeds at 20°C equilibrated against well solutions of 0.1 M Bis-Tris pH 7.0, 0.3 M magnesium chloride and 23% PEG3350. For soaking, 50 nL of each fragment compound (final concentration of 125 mM) was added to a crystallization drop using an ECHO acoustic liquid handler dispenser at the Diamond light source XChem facility. Crystals were soaked for two hours with fragments from the DSi-Poised Library (Diamond Light Source Ltd) before being harvested using XChem SHIFTER technology, cryo-cooled in liquid nitrogen, and data sets collected at the beamline I04-1 in "automated unattended" mode. The XChemXplorer pipeline (53) was used for structure solution with parallel molecular replacement with DIMPLE from CCP4 (54), followed by map averaging and statistical modeling to identify weak electron densities generated from low occupancy fragments using PANDDA software (55). Coordinates and structure factors for data sets with the 9 bound fragments have been deposited in the PDB (Supplementary Table 3), and refinement statistics are found in Supplementary Data 1.

SAXS

SAXS experiments for the $hsALAS2_{\Delta N142}$ and $hsALAS2_{\Delta N142\Delta C545}$ were performed at 0.99 Å wavelength on the Diamond Light Source beamline B21 coupled to the Shodex KW403-4F size exclusion column (Harwell, UK) and equipped with Pilatus 2M two-dimensional detector at 4.014 m distance from the sample, $0.005 < q < 0.4$ Å-1 ($q = 4\pi \sin \theta/\lambda$, 2θ is the scattering angle). The samples were prepared in a buffer containing 300 mM NaCl, 25 mM HEPES 7.5, 1 mM TCEP, 2 % glycerol, 1% sucrose and the measurements were performed at 20℃. The data

were processed and analyzed with Scatter (56) and the ATSAS program package (57). Scatter was used to calculate the radius of gyration Rg and forward scattering I(0) via Guinier approximation, and to derive the maximum particle dimension Dmax and P(r) function. The *ab initio* model was derived using DAMMIF (57). Ten individual models were created, then overlaid and averaged using DAMAVER (57).

Activity assays and kinetics

To measure enzyme activity of hsALAS2$_{\Delta N78}$ and hsALAS2$_{\Delta N142}$ proteins, discontinuous colorimetric activity assays were conducted per Shoolingin-Jordan *et al* (58) with modifications. Reaction mixtures consisted of 50 mM potassium phosphate buffer, pH 7.4, 50 μM PLP, 1 mM DTT, 10 mM $MgCl_2$, various concentrations of glycine and succinyl-CoA (Sigma), and 1-4 μg mL^{-1} freshly purified hsALAS2 enzyme (175 μL total). After incubation at 37°C for 15 minutes (previously checked for linear ALA formation with each enzyme concentration), reactions were terminated with 100 μL trichloroacetic acid and centrifuged at 13,000 x *g* for 5 min to remove protein. Supernatants (240 μL) were added to freshly prepared mixtures of 240 μL of 1 M sodium acetate, pH 4.7, and 20 μL acetylacetone (500 μL total) and boiled for 10 min to derivatize the ALA product. Samples were cooled and three 150 μL aliquots per reaction (two or three technical replicates) were further derivatized with 150 μL modified Ehrlich's reagent and monitored at 554 nm every 60 s in a CLARIOstar microplate reader (BMG Labtech). Assays containing small-molecule fragments were scaled down to 140 μL reaction mixtures (two technical replicates) and included 5% v/v (7 μL) of fragment stock solutions or DMSO diluent. Absorbance values collected after 5 minutes were converted to molar quantities of ALA using an extinction coefficient of 60.4 mM^{-1} cm^{-1}. For kinetic studies, apparent V_{max}, K_m, and k_{cat} values were determined by titrating 2.5-50 mM glycine in the presence of 100 μM succinyl-CoA and 5-

100 μM succinyl-CoA in the presence of 50 mM glycine. Michaelis-Menten nonlinear regression analysis was subsequently carried out on data for two or three separate protein preparations (two or three biological replicates) with Prism software (GraphPad 8.0). As control, we confirmed that the His_6-tag on the recombinant protein did not influence hsALAS2 activity, as shown for WT and R511E variant of $hsALAS2_{\Delta N142}$ (Fig. 3d,e and Table 2).

Differential scanning fluorimetry

$HsALAS2_{\Delta N142}$ was assayed for shifts in melting temperature caused by titration of PLP and succinyl-CoA in a 96-well PCR plate using an Mx3005p RT-PCR machine (Stratagene). Each reaction well (20 μL) consisted of protein (20 μM in a buffer containing 50 mM HEPES, pH 7.5, 500 mM NaCl), SYPRO-Orange (Invitrogen) diluted 1,000×. Fluorescence intensities were measured from 25 °C to 96 °C with a ramp rate of 1 °C min^{-1}, as described(59). The temperature shifts, $\Delta T_{m,\,obs}$, for each ligand were determined. The experiment was repeated three times and an error was calculated based on the standard deviation.

Fluorescence intensity

$HsALAS2_{\Delta N142}$ was assayed for shifts in fluorescence intensity caused by titration of PLP. Each well (10 μL) consisted of protein (20 μM in a buffer containing 50 mM HEPES, pH 7.5, 500 mM NaCl) and varying concentrations of PLP. Schiff base formation was monitored via excitation at 440 nm and emission at 520 nm using an Omega plate reader. The experiment was repeated three times and an error was calculated based on the standard deviation.

Modelling hsALAS2 for MD simulation

The crystal structure of hsALAS2 (this study) was used for all MD simulation studies. Missing residues were modelled into the crystal structure based on a homology model of hsALAS2 constructed with the scALAS crystal structure (PDB ID: 5TXT) as a template using the MODELLER program(60). The homology model was first structurally aligned with the

hsALAS2 crystal structure, and the coordinates of the missing residues were then taken from the homology model and incorporated into the crystal structure. The structure generated, after an energy minimization step, thereby included residues 137-578 from both monomeric units. Three different systems were modelled: (i) hsALAS2 apo form (without PLP), (ii) hsALAS2 holo form with PLP covalently attached to Lys391 (but without substrates), and (iii) hsALAS2 holo form with substrates glycine-PLP and succinyl-CoA.

In order to model system (iii), the starting structure for the protein was chosen from the simulation on system (ii) by clustering all conformations sampled in the trajectory and then choosing the structure at the center of the largest cluster as the representative structure. PLP was then removed from Lys391 in the representative structure. The substrates glycine-PLP and succinyl-CoA were modelled into this structure by using the substrate-bound *Rhodobacter capsulatus* ALAS (rcALAS) structure as a reference template. The structure with PDB ID 2BWP (rcALAS with glycine PLP) was first aligned with the representative hsALAS2 structure, and the resulting orientation of glycine-PLP was modelled into the representative hsALAS2 structure. In a similar manner, the structure with PDB ID 2BWO (rcALAS with succinyl-CoA) was used for modelling succinyl-CoA into the representative hsALAS2 structure. Both the monomeric units of the representative structure included the two substrates. In order to remove possible bad contacts between the substrates and the protein, minimization and equilibration of the system was performed in the presence of restraints on the heavy atoms of the protein (a restraining force with force constant 1000 kJ mol^{-1} nm^{-2} was used).

All MD simulations were performed in the NPT ensemble (constant number of particles (N), constant pressure (P) and constant temperature (T)) for 50 ns using the GROMACS program with the CHARMM36 all-atom force field(61,62) and the TIP3P water model(63)

(Supplementary Software 1). A time-step of 2 fs was used, and all covalent bonds involving hydrogen atoms were constrained using the LINCS algorithm(64). A cut-off of 12 Å was used for short-range non-bonded interactions, and the particle mesh Ewald method was employed for long-range electrostatics(65). Force field parameters for PLP-lysine, PLP-glycine, and succinyl-CoA were obtained from the Paramchem server(66,67). Details of the simulation box for all systems are shown in Supplementary Table 5. Two sets of simulations were performed for all the systems.

To study the conformational dynamics of ALAS2 R511E variant, the crystal structure of hsALAS2$_{\Delta N142}$ was used to perform the R511E substitution using the CHARMM-GUI server(68). The simulation protocol was the same as that followed for wild-type ALAS2.

3.4 Results

hsALAS2 without presequence is sufficient for catalysis

We expressed in *E. coli*, as soluble proteins, several constructs of hsALAS2 with different truncations within the N-terminal extension, while keeping their Ct-extensions intact (Supplementary Fig. 2). The isolated as-purified proteins showed varying degrees of proteolysis (see below), as observed previously (24), which we attributed to cleavage of the 40-aa Ct-extension. For crystallography experiments, we next employed baculovirus-infected insect Sf9 cells to express hsALAS2 aa 79-587 (hsALAS2$_{\Delta N78}$) and aa 143-587 (hsALAS2$_{\Delta N142}$) resulting in soluble proteins with no signs of proteolytic degradation. The majority of the as-purified hsALAS2$_{\Delta N78}$ and hsALAS2$_{\Delta N142}$ proteins from insect cells contain the PLP cofactor, with their Schiff base predominantly in the deprotonated enolimine tautomer (Supplementary Fig. 3) (35). Insect cell-expressed hsALAS2 is active with K_m values (31±4 μM for succinyl-CoA, 11.8±1.0

μM for glycine) close to those reported by others using a similar assay (24) (Supplementary Fig. 4a,b). This form of the enzyme is also capable of forming an interaction with the previously reported partner, beta subunit (SUCLA2) of the succinyl-CoA synthetase complex SUCLG1-SUCLA2 (36,37), as revealed by cross-linking using disuccinimidyl glutarate (Supplementary Fig. 4c).

Overall structure of hsALAS2 & conserved features

We first crystallized the hsALAS2$_{\Delta N78}$ protein and determined its crystal structure at 2.7 Å resolution by molecular replacement, using the rcALAS structure as a search model. Unexpectedly, the N-terminal residues 79-142 of our construct were not visible in the electron density. Intact mass spectrometry of purified hsALAS2$_{\Delta N78}$ nonetheless indicates that aa 79-142 are present (Supplementary Fig. 5a), suggesting this region remains intact in the crystal, albeit disordered. This is further revealed by crystal packing analysis of ALAS2 protomers in the crystal lattice, leaving space for the N-terminal region (Supplementary Fig. 5b). Subsequently, the shorter hsALAS2$_{\Delta N142}$ protein was crystallized, and its higher resolution structure at 2.3 Å resolution was determined (Table 1) and will be referred to hereafter in the manuscript.

The crystal asymmetric unit contains an hsALAS2 homodimer (Fig. 1b), as shown in solution by size exclusion chromatography and small angle X-ray scattering (SAXS) (Supplementary Fig. 6, Supplementary Table 1). The two monomers (rmsd 0.167 Å) are tightly interlocked in the structure, burying a total of 4850 Å^2 accessible surface per monomer. The dimer interface is largely derived from the catalytic domain and highly conserved with the rcALAS structure (Supplementary Fig. 1), although the Ct-extension contributes three aromatic residues that mediate inter-monomer interactions (see next section). This said, an hsALAS2

construct encoding the catalytic domain alone (aa 143-545, hsALAS2$_{\Delta N142 \Delta C545}$) is sufficient to homodimerize in solution (Supplementary Fig. 6b,e).

The catalytic core of hsALAS2 is highly similar to rcALAS (sequence identity 50%, rmsd 1.1 Å) and to scALAS (45%, 1.5 Å) (Fig. 1c). Together they are part of the superfamily of type I PLP-dependent enzymes, in which the catalytic core can be dissected into three sub-domains. In hsALAS2 (Fig. 1d), they correspond to: subdomain 1 (aa 143-195) forming an α-helix and a three-stranded, antiparallel β-sheet; the large central subdomain 2 (aa 196-439) forming a seven-stranded β-sheet enclosed by nine α-helices in repeated β/α motifs; and the last subdomain 3 (aa 440-544) including a three-stranded antiparallel β-sheet, three α-helices and a fourth β-strand that contributes to the sub-domain 1 β-sheet.

Like its orthologs, hsALAS2 is an obligate homodimer in that each active site is formed from both monomeric subunits, with one PLP molecule bound per active site. Prior to crystallization, the protein was treated with hydroxylamine to convert the covalently-bound PLP (in equilibrium between two tautomers; Supplementary Fig. 3) into the non-covalent form that is more homogenous (Supplementary Fig. 7). As expected from the sequence alignment (Supplementary Fig. 1), hsALAS2 employs a highly conserved set of interactions with PLP, involving mainly the central sub-domain of the catalytic core (Fig. 1e). In short, the pyridinium ring fits snugly through hydrophobic interactions with His285 and Val359, as well as hydrogen bonds with His360 and Asp357. The PLP phosphate is neutralized by four hydrogen bonds from its own subunit (Ser257 and Thr388 side-chains, Cys258 and Phe259 main-chains), as well as three hydrogen bonds contributed from the opposing monomer (Thr420 and Thr421 side-chains, Thr421 main-chain).

hsALAS2 C-terminus is a self-inhibitory loop

The largest structural difference between hsALAS2 and homologs resides in the C-terminus following the catalytic core. The 40-residue hsALAS2 Ct-extension (Fig. 1b and Supplementary Fig. 8) begins with a poorly structured segment (aa 544-557) which stretches outward to the protein exterior. There is no clear electron density for part of this segment (aa 549-555, Supplementary Fig. 8a), suggesting its mobility. The next segment of the Ct-extension (aa 560-568, Supplementary Fig. 8b) threads across the interface of sub-domains 2 and 3 as a linear polypeptide, with several main-chain amides and carbonyls shielded by hydrogen-bonding with catalytic core residues (Arg479 and Glu513, which are not present in scALAS or rcALAS). A two-turn helix (α15; Ser568-Phe575) then ensues, forming a lid atop the PLP-bound active site, before being directed to the protein exterior (Phe575-Met578). Close examination of helix α15 (Fig. 2a) reveals that its two Glu residues, Glu569 and Glu571, form charged interactions respectively with Arg511 from subdomain 3 and Lys299/Arg293 from subdomain 2. This helix also contributes three aromatic residues Trp570, Tyr574 and Phe575 which stack among themselves through π-π interactions and anchor the dimerization interface through hydrophobic interactions with Phe267, Thr268 and Ala415 of the opposite dimer subunit. Additional hydrogen bonds were contributed from Phe575 and Gly576 (main chain), with Lys271 on the opposing subunit and Arg293, respectively. The last 9 residues of the hsALAS2 Ct-extension (aa 579-587) were not modelled in the structure, likely due to high disorder as they are surface-exposed. These residues also represent one of the largest sequence divergences between ALAS1 and ALAS2 (Supplementary Fig. 1).

The succinyl-CoA-bound rcALAS structure (PDB 2BWO)(12) revealed residues involved in substrate succinyl-CoA binding, which are nearly invariant across the phyla (based

on sequence alignment in Supplementary Fig. 1), suggesting that hsALAS2 has evolved the same binding site. However, when superimposing hsALAS2 and succinyl-CoA-bound rcALAS structures, we observed to our surprise that the hsALAS2 succinyl-CoA site is blocked by helix α15 and the C-terminus (Fig. 2b), which would sterically overlap with the ADP-diphosphate moiety of a modelled succinyl-CoA molecule. Our hsALAS2 structure therefore represents a conformation of the Ct-extension that precludes binding of succinyl-CoA to the active site. The steric blockade is mediated by several interactions between helix α15 and the catalytic core (Fig. 2a). These include (i) salt bridges of Glu571 with both Lys299 and Arg293, blocking the expected position of the succinyl-CoA ADP adenine group, (ii) the hydrogen bond between Gly576 (main-chain) and Arg293 that blocks the 3'-phosphoadenosine moiety, and (iii) the salt bridge between Glu569 and Arg511. It is of note that Arg511, a residue from the mobile active site loop (aa 505-514), also forms a salt bridge with Asp159 from helix α1. In rcALAS, the equivalent Arg511:Asp159 interaction plays a role in succinyl-CoA-induced conformational change during catalysis(12) (*cf.* Fig. 3a).

The observed direct interaction between the Ct-extension and the active site loop in our hsALAS2 structure, through Arg511, implies that the mobility of the active site loop is driven by a conformational change of the Ct-extension, and suggests that these two regions act in concert to drive the ALAS2 catalytic cycle of substrate binding and product release. We explored further the role of R511 by site-directed mutagenesis on the crystallized construct, hsALAS2$_{\Delta N142}$, to generate the R511E variant which abolishes charged interactions with Glu569 (Ct-extension) and Asp159 (active site loop). Compared to wild-type (WT), the R511E variant is more prone to proteolysis at the Ct-extension as shown by SDS-PAGE (Fig. 3b) and intact mass spectrometry (Supplementary Fig. 5c,d), suggesting that the interaction of the Ct-extension with the catalytic

domain active site loop has been significantly disrupted. Consistent with this, the R511E variant is >2 ^{o}C more thermolabile than WT protein, with melting temperature similar to the hsALAS2$_{\Delta N142 \Delta C545}$ (WT or R511E) protein with Ct-extension omitted from the construct (Fig. 3c). Furthermore, we showed by steady-state kinetics that the proteolysis-prone R511E variant has 2-fold higher enzyme activity than WT, as indicated by V_{max} and k_{cat} values (Fig. 3d,e and Table 2). Of additional note, the R511E variant demonstrates a lower specificity (k_{cat}/K_m) for glycine than WT protein, while the opposite was observed for succinyl-CoA (Table 2). Altogether, our data suggest that the salt bridge network of Glu569:Arg511:Asp159 plays important roles in regulating the Ct-extension during catalysis.

Comparison of our hsALAS2 structure with that of scALAS (34) shows that their Ct-extensions not only differ in sequence (Supplementary Fig. 1) but also in structural locations and conformations (Fig. 2c,d). The point of structural divergence occurs after the last helix (α14) in the catalytic domain, at position Leu545 of hsALAS2 (Leu489 of scALAS). The hsALAS2 extension threads across the subdomain interface and shields the substrate binding site from the exterior (Fig. 2c, left). In scALAS, by contrast, a two-turn helix directs its Ct-extension back along the periphery of sub-domain 3, packs against a unique 22-aa insertion in sub-domain 2 (aa 302-323, scALAS numbering) not present in hsALAS2 (Fig. 2c, right), and continues to wrap around the homodimer surface reaching as far as the N-terminal sub-domain 1 of the opposing monomer. Unlike hsALAS2, the Ct-extension in scALAS did not interact with the substrate binding site, leaving it exposed as in the rcALAS structure (Fig. 2d).

Simulations of the ALAS2 C-terminal dynamics

We next employed molecular dynamics (MD) simulations to understand the mobility of the hsALAS2 Ct-extension. Based on the experimental structure, we modelled hsALAS2 in the

apo form, the *holo* form with PLP covalently-bound to Lys391, and the ternary complex with glycine-PLP and succinyl-CoA. In the substrate-free *apo* and *holo* forms, the Glu569:Arg511 and Glu571:Arg293/Lys299 salt bridges, serving to stabilize the Ct-extension over the active site, remain intact for most of the duration of the simulations (Fig. 4a, left and Supplementary Figs. 9-11). In order for succinyl-CoA to bind and orientate in the active site, we reason that the Ct-extension must change its conformation. Indeed, simulation of the substrate-bound ternary complex shows complete breakage of the salt bridges (Fig. 4a, right and Supplementary Figs. 9-11), resulting in an open conformation that is structurally poised to bind the substrate succinyl-CoA (Fig. 4b and Supplementary Movies 1-2). We also carried out MD simulations on a hsALAS2 R511E model in which the salt bridge with Glu569 would not be formed, to support our experimental observations that Arg511 is important for the integrity of Ct-extension (see previous section and Fig. 3). Indeed, the accessibility of the Ct-extension in the R511E model is higher than WT, in that the R511E Ct-extension has moved away from the catalytic core over the course of the simulation, and this movement leads to an increase in the solvent accessible surface area (Supplementary Fig. 12).

During MD simulations, dimeric hsALAS2 exhibits asymmetry between the two subunits, a feature previously reported for murine ALAS2 (38). This asymmetry is particularly observed in the dynamics of salt bridges from the two subunits of the ternary complex (Supplementary Figs. 10-11, compare bottom left and right panels). Asymmetry is also observed at the secondary structure level. Analysis of dynamic cross correlation maps (DCCM), which quantify correlations in motions between different regions of a protein (39), shows that covalent attachment of PLP to the active site leads to an increased anti-correlation between subdomain 2 (containing active site residues) of one subunit and subdomain 3 (containing the Ct-extension) of

the other subunit (Supplementary Fig. 13a). The anti-correlation across the two subunits is facilitated by interaction of PLP from one subunit with Thr420 and Thr421 from the other subunit (Supplementary Fig. 13b). Altogether, the simulations data indicate the mobility of the hsALAS2 Ct-extension between different conformations during catalysis.

Revised understanding of disease-causing mutations

The hsALAS2 crystal structure provides a template to understand the molecular basis of disease-causing mutations for XLSA and XLP. To date, over 82 missense mutations affecting 69 different residues of hsALAS2 have been identified as causing XLSA (Supplementary Table 2 and Supplementary Fig. 14). These mutations are largely concentrated in the catalytic core and many have been previously mapped onto the rcALAS structure (12), allowing the categorization of their putative molecular defects including disruption of the dimerization interface, direct disruption of catalytic regions, or a global destabilization of the enzymatic fold.

The hsALAS2 Ct-extension sheds insights on some previously characterized mutations in the catalytic core, namely D159N and D159Y. The rcALAS open and closed structures (PDB 2BWN) show that formation and disruption of a salt bridge between Glu17 (Asp159 in hsALAS2) and Arg368 (Arg511 in hsALAS2) is key to transitioning between open and closed states (Fig. 3a). Aforementioned in our hsALAS2 structure, Arg511 forms a salt bridge to Glu569 of the Ct-extension, and to Asp159 in helix α1 of catalytic core (Fig. 3a). Results from our DSF, activity assay and MD simulations (Fig. 3b-e and Supplementary Fig. 12) altogether demonstrate the importance of the Arg511:Glu569 interaction towards the structural integrity of the Ct-extension. By contrast, disruption of the Asp159:Arg511 interaction, the likely culprit for the disease-causing D159N and D159Y variants, may reduce the ability of ALAS2 to adopt the catalytically active closed conformation, and stabilize the interaction of Arg511 with Glu569.

Gain-of-function XLP mutations all locate to exon 11 encoding the hsALAS2 Ct-extension. Three reported indel mutations (Q548X, delAT and delAGTG) completely delete the two-turn α15 helical region that blocks the ALAS2 active site. A fourth known indel mutation (delG) leaves the Ct-extension helix intact, though it results in a frameshift and an additional 12-aa sequence downstream of that region (24) (Supplementary Fig. 2). Not surprisingly, the elongated C-terminus of recombinant delAGTG is subject to proteolysis during protein preparation, while the same region of the delG variant is not (Supplementary Fig. 15a). Disruption of the α15 helix would alleviate the restriction of conformational change imposed by the interaction of the Ct-extension with the active site loop, providing an explanation for the increased rates of product release as detailed previously in stopped-flow experiments (9). Our steady-state kinetic analysis of intact recombinant hsALAS2 wild-type and XLP variants (Supplementary Fig.15b,c) reveals that the k_{cat} and V_{max} values for delAT and Q548X are 3- to 6-fold greater than wild-type and delG proteins (Table 3), in agreement with those reported in the literature (9,24) (delAGTG was not assayed due to C-terminal proteolysis and the putative formation of heterodimers). The association of the delG mutation with XLP has been hypothesized to be the result of increased *in vivo* enzyme stability relative to that of the wild-type (24). We show here that delG has the same 2- to 3-fold wild-type efficiency (k_{cat}/K_m) with respect to succinyl-CoA as delAT and Q548X (Table 3). Interestingly, this appears to be due in part to the lower K_m of delG for succinyl-CoA compared to delAT, Q548X, and wild-type forms, suggesting that delG has a greater affinity for succinyl-CoA and this may contribute to its hyperactivity.

Crystallography-based fragment screening

We performed crystallography-based fragment screening to identify chemical ligands that serve as a starting point for development of small molecule therapy towards inherited defects of erythroid heme biosynthesis situated downstream of the ALAS2 reaction step, via a substrate reduction approach. Through solving 295 X-ray data sets (1.44-1.93 Å resolution) from hsALAS2$_{\Delta N142}$ crystals, each soaked with a different compound from a diverse fragment library, we identified 9 co-crystal structures each with a fragment bound to a hotspot region surrounding the Ct-extension (Fig. 5a and Supplementary Table 3 and Supplementary Data 1).

Fragments **1-8** (Fig. 5b) are accommodated in a pocket between helix α15 of one subunit and its interacting regions (helix α4) in the opposite subunit (Fig. 5c). This pocket is mainly hydrophobic in nature, contributed by Tyr574 from helix α15 and residues Phe267, Thr268, Lys271, Ile272, Tyr413 from the opposite chain. Five of the fragments (**1**-**5**) extend into a subsite (referred to as '*Ia*' in Fig. 5c) packing against Glu155 and Lys152 from the first helix (α1) of the catalytic core. As described above, helix α1 stabilizes the active site mobile loop and C-terminal helix α15, with contributions from Asp159 that forms the network of charged interactions among Asp159:Arg511:Glu569. The aromatic side-chain of Tyr574 (helix α15) adopts an alternate conformation when bound to fragments **2-4** (Supplementary Fig. 16). Three other fragments (**6-8**) occupy another subsite ('*Ib*' in Fig. 5c) in direct proximity to the last turn of helix α15 (e.g. Phe575 and Gly576).

A ninth fragment (**9**, Fig. 5b) was found at the opposite side of C-terminal helix α15 with respect to the above 8 fragments (Fig. 5c). This site is situated along the 2-fold axis of the hsALAS2 homodimer. One side of the fragment contacts a hydrophobic surface (Asn294, Ser295, Gly296 and Lys271) from its own subunit; its nitrile group captures hydrogen bonds

with the main chain carbonyl of Phe575 (in C-terminal helix α15) and guanidinium side-chain from Arg293. The opposite face of the fragment forms van der Waals contact with the same fragment bound to the dimeric subunit (**9'**).

We next interrogated the effects of the nine fragments in solution using our colorimetric activity assay. Activity of hsALAS2 was moderately inhibited by nearly 15% in the presence of 1 mM fragments **1** or **8** (Supplementary Fig. 17a), an effect that was not due to fragments alone interfering with the assay signal, and was also dependent on fragment concentration, reaching 28% and 22% inhibition with 5 mM fragments 1 and 8, respectively (Supplementary Table 4). MD simulations of *holo* hsALAS2 in the presence of fragment ***1*** further showed that the fragment remained bound to one protomer of the homodimer throughout the 50 ns interval and led to enhanced stabilization of R293-E571 salt bridge (Supplementary Fig. 17b), compared to fragment-free hsALAS2. Our data therefore suggest that hsALAS2 catalytic activity can be potentially modulated by small molecules that target the region close to the Ct-extension.

3.5 Discussion

ALAS2 represents one of a handful of metabolic enzymes, where different mutations within the same protein can lead to distinct disorders associated with loss-of-function (enzyme deficiency) or gain-of-function (enzyme superactivity) disorders (40). In particular, this study uncovers an autoinhibitory mechanism of ALAS2 mediated by its Ct-extension, providing the framework to explain how frameshift indel mutations in the ALAS2 C-terminus lead to the gain-of-function disorder XLP.

Previously, a conserved mobile loop in the rcALAS active site, undergoing conformational change to bind succinyl-CoA, was proposed as a regulatory feature that

committed the enzyme to catalysis through an open-to-close active site transition (12). Here, the hsALAS2 Ct-extension imposes additional conformational restriction on this active site loop (through the salt bridge network Glu569:Arg511:Asp159), preventing transition to the open conformation. To overcome these restraints, displacement of the Ct-extension from the conformation depicted in our structure, as supported by our MD simulations, is hence essential for both substrate binding and product release. Our data therefore add to the described complexity of regulatory mechanisms known to exist to modulate ALAS2 activity (41), underlining the importance of its tight regulation to maintain metabolic flux during erythropoiesis.

It is of note that others have shown that the Ct-extension of hsALAS2 most significantly impacts ALA release after succinyl-CoA binding (9), suggesting why product release is the rate determining step. Previous studies (24) have highlighted that truncation of the Ct-extension does not significantly affect the K_m for either substrate. Our data here, however, indicate that a lower K_m for the delG XLP variant may contribute to its elevated catalytic efficiency. Transient kinetics monitoring the formation and decay of the intermediate quinoid species pointed to an increase in the rate of product release in the truncated forms of ALAS2 (9). Our structure also provides insight into the role of engineered mutations of the active site loop from previous studies (33). Specifically, engineered mutations directed to the active site loop of murine ALAS2 also lead to a similar hyperactivity as the clinical mutations causing XLP. This observation can be easily reconciled with the hsALAS2 structure, as it would likely abolish interactions with the Ct-extension helix α15 and relieve the autoinhibition.

We speculate that the C-terminal regulatory feature, observed here for ALAS2, will also be present with a similar role in the more ubiquitous ALAS1 isozyme, considering their

sequence conservation within this region (e.g. helix α15). However, beyond helix α15 at the far C-terminus, ALAS1 and ALAS2 have evolved very diverse amino acid sequences. Being surface-exposed, these residues may endow the two isoforms with different protein interaction functions. For example, the hsALAS2 Ct-extension is implicated from *in vitro* pull-down studies (24,36,37), as the binding site for the beta subunit SUCLA2 of the succinyl-CoA synthetase (SCS) complex in the TCA cycle (42). It has been suggested that during erythropoiesis, the ALAS2-SUCLA2 interaction may play a role in directing the cellular pool of succinyl-CoA towards heme biosynthesis, away from its conversion to succinate in the TCA cycle (43). Additionally, ALAS2 has been shown to be part of a larger heme synthesis metabolon whose role is currently undefined, but may involve coordinated regulation of ALAS2 and FECH, the last enzyme in the multi-step heme biosynthesis pathway (44). Future studies may determine if and how these protein-protein interactions mediate the ALAS2 Ct-extension to regulate catalysis, most likely through the autoinhibitory mechanism shown in this study, but potentially also through facilitating the PLP loading process of the enzyme, shown to involve the AAA+ protease ClpX(26).

Finally, our structural data provide a starting point for small molecule drug discovery. Three porphyria disorders can be classified as erythroid-specific, associated with loss of enzyme function in the heme biosynthetic pathway downstream of the ALAS2 step (Supplementary Fig. 18). These porphyrias result in the accumulation of toxic heme intermediates and point to the inhibition of ALAS2 as a potential therapeutic target via the substrate reduction approach that has precedence in other inherited metabolic disorders(45). This is supported by the recent siRNA knockdown of the *ALAS1* mRNA showing effective prevention of adverse effects from acute hepatic porphyrias(46,47), pointing to a similar therapeutic benefit of ALAS2 inhibition for

porphyrias in the erythropoietic pathway. Small molecule inhibitors that target the ALAS2 active site such as the itaconic acid derivative itaconyl-CoA(48), or take advantage of the enzyme's autoinhibitory mechanism mediated by the Ct-extension, are potential avenues for drug discovery. Relevant to this, fragments identified from our crystallography-based screening campaign have the potential for chemistry optimization into lead inhibitors in the future, aimed at increasing residence time at the Ct-extension region to prevent substrate access and product release during catalysis.

3.6 References

1. Gibson, K. D., Laver, W. G., and Neuberger, A. (1958) Initial stages in the biosynthesis of porphyrins. 2. The formation of delta-aminolaevulic acid from glycine and succinyl-coenzyme A by particles from chicken erythrocytes. *Biochem J* **70**, 71-81

2. Akhtar, M., Abboud, M. M., Barnard, G., Jordan, P., and Zaman, Z. (1976) Mechanism and stereochemistry of enzymic reactions involved in porphyrin biosynthesis. *Philos Trans R Soc Lond B Biol Sci* **273**, 117-136

3. Dailey, H. A., and Meissner, P. N. (2013) Erythroid heme biosynthesis and its disorders. *Cold Spring Harb Perspect Med* **3**, a011676

4. Dailey, H. A., and Dailey, T. A. (2003) Ferrochelatase. in *The porphyrin handbook* (Kadish, K. M., Smith, K. M., and Guilard, R. eds.), Academic Press, San Diego. pp 93-122

5. Bishop, D. F., Henderson, A. S., and Astrin, K. H. (1990) Human delta-aminolevulinate synthase: assignment of the housekeeping gene to 3p21 and the erythroid-specific gene to the X chromosome. *Genomics* **7**, 207-214

6. Riddle, R. D., Yamamoto, M., and Engel, J. D. (1989) Expression of delta-aminolevulinate synthase in avian cells: separate genes encode erythroid-specific and nonspecific isozymes. *Proc Natl Acad Sci U S A* **86**, 792-796

7. Besur, S., Hou, W., Schmeltzer, P., and Bonkovsky, H. L. (2014) Clinically important features of porphyrin and heme metabolism and the porphyrias. *Metabolites* **4**, 977-1006

8. Hunter, G. A., Zhang, J., and Ferreira, G. C. (2007) Transient kinetic studies support refinements to the chemical and kinetic mechanisms of aminolevulinate synthase. *J Biol Chem* **282**, 23025-23035

9. Fratz, E. J., Clayton, J., Hunter, G. A., Ducamp, S., Breydo, L., Uversky, V. N., Deybach, J. C., Gouya, L., Puy, H., and Ferreira, G. C. (2015) Human Erythroid 5-Aminolevulinate Synthase Mutations Associated with X-Linked Protoporphyria Disrupt the Conformational Equilibrium and Enhance Product Release. *Biochemistry* **54**, 5617-5631

10. Stojanovski, B. M., Hunter, G. A., Jahn, M., Jahn, D., and Ferreira, G. C. (2014) Unstable reaction intermediates and hysteresis during the catalytic cycle of 5-aminolevulinate synthase: implications from using pseudo and alternate substrates and a promiscuous enzyme variant. *J Biol Chem* **289**, 22915-22925

11. Hunter, G. A., and Ferreira, G. C. (1999) Pre-steady-state reaction of 5-aminolevulinate synthase. Evidence for a rate-determining product release. *J Biol Chem* **274**, 12222-12228

12. Astner, I., Schulze, J. O., van den Heuvel, J., Jahn, D., Schubert, W. D., and Heinz, D. W. (2005) Crystal structure of 5-aminolevulinate synthase, the first enzyme of heme biosynthesis, and its link to XLSA in humans. *EMBO J* **24**, 3166-3177

13. Lendrihas, T., Hunter, G. A., and Ferreira, G. C. (2010) Targeting the active site gate to yield hyperactive variants of 5-aminolevulinate synthase. *J Biol Chem* **285**, 13704-13711

14. Munakata, H., Yamagami, T., Nagai, T., Yamamoto, M., and Hayashi, N. (1993) Purification and structure of rat erythroid-specific delta-aminolevulinate synthase. *J Biochem* **114**, 103-111

15. Srivastava, G., Borthwick, I. A., Maguire, D. J., Elferink, C. J., Bawden, M. J., Mercer, J. F., and May, B. K. (1988) Regulation of 5-aminolevulinate synthase mRNA in different rat tissues. *J Biol Chem* **263**, 5202-5209

16. Schoenhaut, D. S., and Curtis, P. J. (1986) Nucleotide sequence of mouse 5-aminolevulinic acid synthase cDNA and expression of its gene in hepatic and erythroid tissues. *Gene* **48**, 55-63

17. Cox, T. C., Sadlon, T. J., Schwarz, Q. P., Matthews, C. S., Wise, P. D., Cox, L. L., Bottomley, S. S., and May, B. K. (2004) The major splice variant of human 5-aminolevulinate synthase-2 contributes significantly to erythroid heme biosynthesis. *Int J Biochem Cell Biol* **36**, 281-295

18. Dailey, T. A., Woodruff, J. H., and Dailey, H. A. (2005) Examination of mitochondrial protein targeting of haem synthetic enzymes: in vivo identification of three functional haem-responsive motifs in 5-aminolaevulinate synthase. *Biochem J* **386**, 381-386

19. Lathrop, J. T., and Timko, M. P. (1993) Regulation by heme of mitochondrial protein transport through a conserved amino acid motif. *Science* **259**, 522-525

20. Munakata, H., Sun, J. Y., Yoshida, K., Nakatani, T., Honda, E., Hayakawa, S., Furuyama, K., and Hayashi, N. (2004) Role of the heme regulatory motif in the heme-mediated inhibition of mitochondrial import of 5-aminolevulinate synthase. *J Biochem* **136**, 233-238

21. Whatley, S. D., Ducamp, S., Gouya, L., Grandchamp, B., Beaumont, C., Badminton, M. N., Elder, G. H., Holme, S. A., Anstey, A. V., Parker, M., Corrigall, A. V., Meissner, P. N., Hift, R. J., Marsden, J. T., Ma, Y., Mieli-Vergani, G., Deybach, J. C., and Puy, H. (2008) C-terminal deletions in the ALAS2 gene lead to gain of function and cause X-linked dominant protoporphyria without anemia or iron overload. *Am J Hum Genet* **83**, 408-414

22. Ducamp, S., Schneider-Yin, X., de Rooij, F., Clayton, J., Fratz, E. J., Rudd, A., Ostapowicz, G., Varigos, G., Lefebvre, T., Deybach, J. C., Gouya, L., Wilson, P., Ferreira, G. C., Minder, E. I., and Puy, H. (2013) Molecular and functional analysis of the C-terminal region of human erythroid-specific 5-aminolevulinic synthase associated with X-linked dominant protoporphyria (XLDPP). *Hum Mol Genet* **22**, 1280-1288

23. Balwani, M., Doheny, D., Bishop, D. F., Nazarenko, I., Yasuda, M., Dailey, H. A., Anderson, K. E., Bissell, D. M., Bloomer, J., Bonkovsky, H. L., Phillips, J. D., Liu, L., Desnick, R. J., and Porphyrias Consortium of the National Institutes of Health Rare Diseases Clinical Research, N. (2013) Loss-of-function ferrochelatase and gain-of-function erythroid-specific 5-aminolevulinate synthase mutations causing erythropoietic protoporphyria and x-

linked protoporphyria in North American patients reveal novel mutations and a high prevalence of X-linked protoporphyria. *Mol Med* **19**, 26-35

24. Bishop, D. F., Tchaikovskii, V., Nazarenko, I., and Desnick, R. J. (2013) Molecular expression and characterization of erythroid-specific 5-aminolevulinate synthase gain-of-function mutations causing X-linked protoporphyria. *Mol Med* **19**, 18-25

25. Tchaikovskii, V., Desnick, R. J., and Bishop, D. F. (2019) Molecular expression, characterization and mechanism of ALAS2 gain-of-function mutants. *Mol Med* **25**, 4

26. Kardon, J. R., Yien, Y. Y., Huston, N. C., Branco, D. S., Hildick-Smith, G. J., Rhee, K. Y., Paw, B. H., and Baker, T. A. (2015) Mitochondrial ClpX Activates a Key Enzyme for Heme Biosynthesis and Erythropoiesis. *Cell* **161**, 858-867

27. Yien, Y. Y., Ducamp, S., van der Vorm, L. N., Kardon, J. R., Manceau, H., Kannengiesser, C., Bergonia, H. A., Kafina, M. D., Karim, Z., Gouya, L., Baker, T. A., Puy, H., Phillips, J. D., Nicolas, G., and Paw, B. H. (2017) Mutation in human CLPX elevates levels of delta-aminolevulinate synthase and protoporphyrin IX to promote erythropoietic protoporphyria. *Proc Natl Acad Sci U S A* **114**, E8045-E8052

28. Harigae, H., and Furuyama, K. (2010) Hereditary sideroblastic anemia: pathophysiology and gene mutations. *Int J Hematol* **92**, 425-431

29. Ducamp, S., Kannengiesser, C., Touati, M., Garcon, L., Guerci-Bresler, A., Guichard, J. F., Vermylen, C., Dochir, J., Poirel, H. A., Fouyssac, F., Mansuy, L., Leroux, G., Tertian, G., Girot, R., Heimpel, H., Matthes, T., Talbi, N., Deybach, J. C., Beaumont, C., Puy, H., and Grandchamp, B. (2011) Sideroblastic anemia: molecular analysis of the ALAS2 gene in a series of 29 probands and functional studies of 10 missense mutations. *Hum Mutat* **32**, 590-597

30. Bottomley, S. S., May, B. K., Cox, T. C., Cotter, P. D., and Bishop, D. F. (1995) Molecular defects of erythroid 5-aminolevulinate synthase in X-linked sideroblastic anemia. *J Bioenerg Biomembr* **27**, 161-168

31. Cotter, P. D., Baumann, M., and Bishop, D. F. (1992) Enzymatic defect in "X-linked" sideroblastic anemia: molecular evidence for erythroid delta-aminolevulinate synthase deficiency. *Proc Natl Acad Sci U S A* **89**, 4028-4032

32. Stenson, P. D., Mort, M., Ball, E. V., Evans, K., Hayden, M., Heywood, S., Hussain, M., Phillips, A. D., and Cooper, D. N. (2017) The Human Gene Mutation Database: towards a comprehensive repository of inherited mutation data for medical research, genetic diagnosis and next-generation sequencing studies. *Hum Genet* **136**, 665-677

33. Kadirvel, S., Furuyama, K., Harigae, H., Kaneko, K., Tamai, Y., Ishida, Y., and Shibahara, S. (2012) The carboxyl-terminal region of erythroid-specific 5-aminolevulinate synthase acts as an intrinsic modifier for its catalytic activity and protein stability. *Exp Hematol* **40**, 477-486 e471

34. Brown, B. L., Kardon, J. R., Sauer, R. T., and Baker, T. A. (2018) Structure of the Mitochondrial Aminolevulinic Acid Synthase, a Key Heme Biosynthetic Enzyme. *Structure* **26**, 580-589 e584

35. Yadav, P. K., Xie, P., and Banerjee, R. (2012) Allosteric communication between the pyridoxal 5'-phosphate (PLP) and heme sites in the H2S generator human cystathionine beta-synthase. *J Biol Chem* **287**, 37611-37620

36. Bishop, D. F., Tchaikovskii, V., Hoffbrand, A. V., Fraser, M. E., and Margolis, S. (2012) X-linked sideroblastic anemia due to carboxyl-terminal ALAS2 mutations that cause loss of binding to the beta-subunit of succinyl-CoA synthetase (SUCLA2). *J Biol Chem* **287**, 28943-28955

37. Furuyama, K., and Sassa, S. (2000) Interaction between succinyl CoA synthetase and the heme-biosynthetic enzyme ALAS-E is disrupted in sideroblastic anemia. *J Clin Invest* **105**, 757-764

38. Na, I., Catena, D., Kong, M. J., Ferreira, G. C., and Uversky, V. N. (2018) Anti-Correlation between the Dynamics of the Active Site Loop and C-Terminal Tail in Relation to the Homodimer Asymmetry of the Mouse Erythroid 5-Aminolevulinate Synthase. *Int J Mol Sci* **19**

39. Swaminathan, S., Harte, W. E., and Beveridge, D. L. (1991) Investigation of domain structure in proteins via molecular dynamics simulation: application to HIV-1 protease dimer. *Journal of the American Chemical Society* **113**, 2717-2721

40. Ferreira, C. R., van Karnebeek, C. D. M., Vockley, J., and Blau, N. (2018) A proposed nosology of inborn errors of metabolism. *Genet Med*

41. Peoc'h, K., Nicolas, G., Schmitt, C., Mirmiran, A., Daher, R., Lefebvre, T., Gouya, L., Karim, Z., and Puy, H. (2019) Regulation and tissue-specific expression of delta-aminolevulinic acid synthases in non-syndromic sideroblastic anemias and porphyrias. *Mol Genet Metab*

42. Lambeth, D. O., Tews, K. N., Adkins, S., Frohlich, D., and Milavetz, B. I. (2004) Expression of two succinyl-CoA synthetases with different nucleotide specificities in mammalian tissues. *J Biol Chem* **279**, 36621-36624

43. Burch, J. S., Marcero, J. R., Maschek, J. A., Cox, J. E., Jackson, L. K., Medlock, A. E., Phillips, J. D., and Dailey, H. A., Jr. (2018) Glutamine via alpha-ketoglutarate dehydrogenase provides succinyl-CoA for heme synthesis during erythropoiesis. *Blood* **132**, 987-998

44. Medlock, A. E., Shiferaw, M. T., Marcero, J. R., Vashisht, A. A., Wohlschlegel, J. A., Phillips, J. D., and Dailey, H. A. (2015) Identification of the Mitochondrial Heme Metabolism Complex. *PLoS One* **10**, e0135896

45. Yue, W. W., Mackinnon, S., and Bezerra, G. A. (2019) Substrate reduction therapy for inborn errors of metabolism. *Emerging Topics in Life Sciences*, ETLS20180058

46. Sardh, E., Harper, P., Balwani, M., Stein, P., Rees, D., Bissell, D. M., Desnick, R., Parker, C., Phillips, J., Bonkovsky, H. L., Vassiliou, D., Penz, C., Chan-Daniels, A., He, Q., Querbes, W., Fitzgerald, K., Kim, J. B., Garg, P., Vaishnaw, A., Simon, A. R., and Anderson, K. E. (2019) Phase 1 Trial of an RNA Interference Therapy for Acute Intermittent Porphyria. *N Engl J Med* **380**, 549-558

47. Yasuda, M., Gan, L., Chen, B., Kadirvel, S., Yu, C., Phillips, J. D., New, M. I., Liebow, A., Fitzgerald, K., Querbes, W., and Desnick, R. J. (2014) RNAi-mediated silencing of hepatic Alas1 effectively prevents and treats the induced acute attacks in acute intermittent porphyria mice. *Proc Natl Acad Sci U S A* **111**, 7777-7782

48. Marcero, J. R., Burch, J. S., Phillips, J. D., Cox, J. E., Jackson, L. K., and Dailey, H. A. (2017) The Role of TCA Cycle Compounds in Erythroid Heme Synthesis and Its Regulation During an Inflammatory Response. *Blood* **130**, 3473-3473

49. McCoy, A. J., Grosse-Kunstleve, R. W., Storoni, L. C., and Read, R. J. (2005) Likelihood-enhanced fast translation functions. *Acta Crystallogr D Biol Crystallogr* **61**, 458-464

50. Emsley, P., and Cowtan, K. (2004) Coot: model-building tools for molecular graphics. *Acta Crystallogr D Biol Crystallogr* **60**, 2126-2132

51. Murshudov, G. N., Vagin, A. A., and Dodson, E. J. (1997) Refinement of macromolecular structures by the maximum-likelihood method. *Acta Crystallogr D Biol Crystallogr* **53**, 240-255

52. Afonine, P. V., Grosse-Kunstleve, R. W., Echols, N., Headd, J. J., Moriarty, N. W., Mustyakimov, M., Terwilliger, T. C., Urzhumtsev, A., Zwart, P. H., and Adams, P. D. (2012) Towards automated crystallographic structure refinement with phenix.refine. *Acta Crystallogr D Biol Crystallogr* **68**, 352-367

53. Krojer, T., Talon, R., Pearce, N., Collins, P., Douangamath, A., Brandao-Neto, J., Dias, A., Marsden, B., and von Delft, F. (2017) The XChemExplorer graphical workflow tool for routine or large-scale protein-ligand structure determination. *Acta Crystallogr D Struct Biol* **73**, 267-278

54. Winn, M. D., Ballard, C. C., Cowtan, K. D., Dodson, E. J., Emsley, P., Evans, P. R., Keegan, R. M., Krissinel, E. B., Leslie, A. G., McCoy, A., McNicholas, S. J., Murshudov, G. N., Pannu, N. S., Potterton, E. A., Powell, H. R., Read, R. J., Vagin, A., and Wilson, K. S. (2011) Overview of the CCP4 suite and current developments. *Acta Crystallogr D Biol Crystallogr* **67**, 235-242

55. Pearce, N. M., Krojer, T., Bradley, A. R., Collins, P., Nowak, R. P., Talon, R., Marsden, B. D., Kelm, S., Shi, J., Deane, C. M., and von Delft, F. (2017) A multi-crystal method for extracting obscured crystallographic states from conventionally uninterpretable electron density. *Nat Commun* **8**, 15123

56. Förster, S., Apostol, L., and Bras, W. (2010) Scatter: software for the analysis of nano- and mesoscale small-angle scattering. *Journal of Applied Crystallography* **43**, 639-646

57. Petoukhov, M. V., Franke, D., Shkumatov, A. V., Tria, G., Kikhney, A. G., Gajda, M., Gorba, C., Mertens, H. D., Konarev, P. V., and Svergun, D. I. (2012) New developments in the ATSAS program package for small-angle scattering data analysis. *J Appl Crystallogr* **45**, 342-350

58. Shoolingin-Jordan, P. M., LeLean, J. E., and Lloyd, A. J. (1997) Continuous coupled assay for 5-aminolevulinate synthase. *Methods Enzymol* **281**, 309-316

59. Niesen, F. H., Berglund, H., and Vedadi, M. (2007) The use of differential scanning fluorimetry to detect ligand interactions that promote protein stability. *Nat Protoc* **2**, 2212-2221

60. Sali, A., and Blundell, T. L. (1993) Comparative protein modelling by satisfaction of spatial restraints. *J Mol Biol* **234**, 779-815

61. Best, R. B., Zhu, X., Shim, J., Lopes, P. E., Mittal, J., Feig, M., and Mackerell, A. D., Jr. (2012) Optimization of the additive CHARMM all-atom protein force field targeting improved sampling of the backbone phi, psi and side-chain chi(1) and chi(2) dihedral angles. *J Chem Theory Comput* **8**, 3257-3273

62. Abraham, M. J., Murtola, T., Schulz, R., Páll, S., Smith, J. C., Hess, B., and Lindahl, E. (2015) GROMACS: High performance molecular simulations through multi-level parallelism from laptops to supercomputers. *SoftwareX* **1-2**, 19-25

63. Jorgensen, W. L., Chandrasekhar, J., Madura, J. D., Impey, R. W., and Klein, M. L. (1983) Comparison of simple potential functions for simulating liquid water. *J Chem Phys* **79**, 926-935

64. Hess, B., Bekker, H., Berendsen, H. J. C., and Fraaije, J. G. E. M. (1997) LINCS: A linear constraint solver for molecular simulations. *Journal of Computational Chemistry* **18**, 1463-1472

65. Essmann, U., Perera, L., Berkowitz, M. L., Darden, T., Lee, H., and Pedersen, L. G. (1995) A smooth particle mesh Ewald method. *The Journal of Chemical Physics* **103**, 8577-8593

66. Vanommeslaeghe, K., and MacKerell, A. D., Jr. (2012) Automation of the CHARMM General Force Field (CGenFF) I: bond perception and atom typing. *J Chem Inf Model* **52**, 3144-3154

67. Vanommeslaeghe, K., Raman, E. P., and MacKerell, A. D., Jr. (2012) Automation of the CHARMM General Force Field (CGenFF) II: assignment of bonded parameters and partial atomic charges. *J Chem Inf Model* **52**, 3155-3168

68. Jo, S., Kim, T., Iyer, V. G., and Im, W. (2008) CHARMM-GUI: a web-based graphical user interface for CHARMM. *J Comput Chem* **29**, 1859-1865

3.7 Figures and Tables

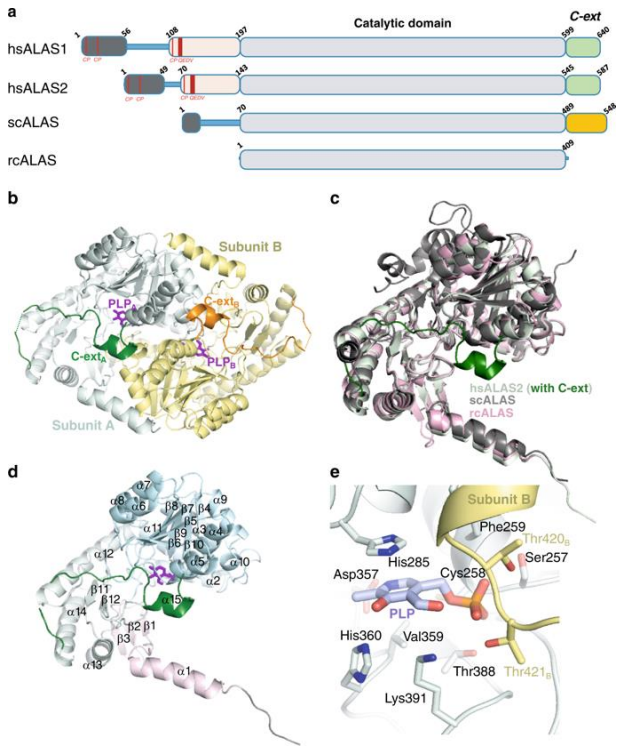

Fig. 1 Domain organization and structure of hsALAS2. (**a**) Domain architecture of hsALAS1, hsALAS2, scALAS and rcALAS, highlighting the catalytic core (grey box) flanked by N-terminal (black, pink boxes) and C-terminal extension (green in higher eukaryotes, orange in lower eukaryotes). (**b**) hsALAS2 homodimer (this study) composed of monomer A (catalytic domain in grey, Ct-extension in dark green) and the opposite monomer B (catalytic domain in yellow, Ct-extension in orange. PLP is shown in purple sticks. (**c**) Structure superimposition of protomer from hsALAS2 (this study), scALAS (PDB 5TXR) and rcALAS (PDB 2BWN). (**d**) Domain organization and secondary structure assignment for hsALAS2. Subdomain 1 is shown in pink, subdomain 2 in grey, subdomain 3 in cyan, and the Ct-extension in dark green. (**e**) PLP binding site of hsALAS2. PLP-interacting residues from monomer A are shown in grey and from opposing monomer B in yellow. PLP is shown in mauve (carbon color).

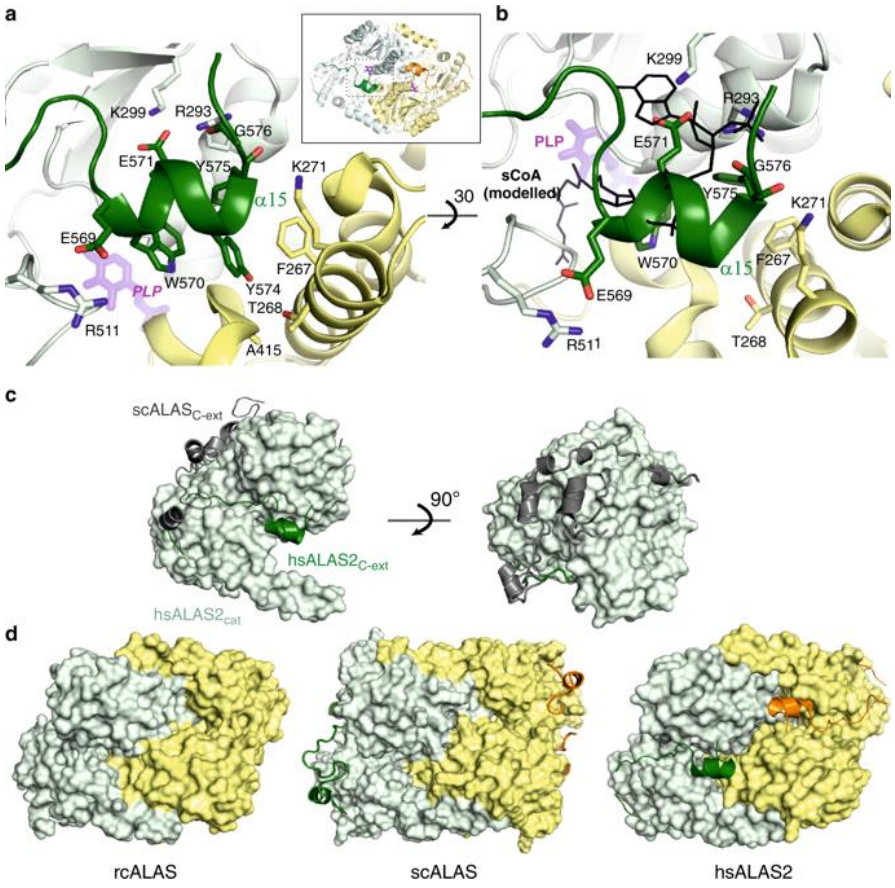

Fig. 2 hsALAS2 C-terminal extension is mobile and interferes directly with active site. (**a**) Interactions of helix α15 from the Ct-extension (dark green) with the catalytic core of monomer A shown in light green and the opposing monomer B shown in yellow. (**b**) Similar view as panel A, related by 30^{o} rotation along the horizontal axis. The succinyl-CoA (sCoA) ligand, modelled into hsALAS2 from rcALAS (PDB 2BWO), is shown in black lines to highlight steric clashes with helix α15. (**c**) hsALAS2 monomer with catalytic domain in surface representation (light green) and Ct-extension in cartoon representation (dark green). The scALAS Ct-extension is also superimposed in cartoon representation (grey). (**d**) rcALAS (PDB 2BWN), scALAS (PDB 5TXR) and hsALAS2 (this study) homodimers. Catalytic domains are shown in surface representation (monomer A light green, monomer B yellow). Ct-extensions are shown in cartoon representation for scALAS and rcALAS (dark green for monomer A, orange for monomer B).

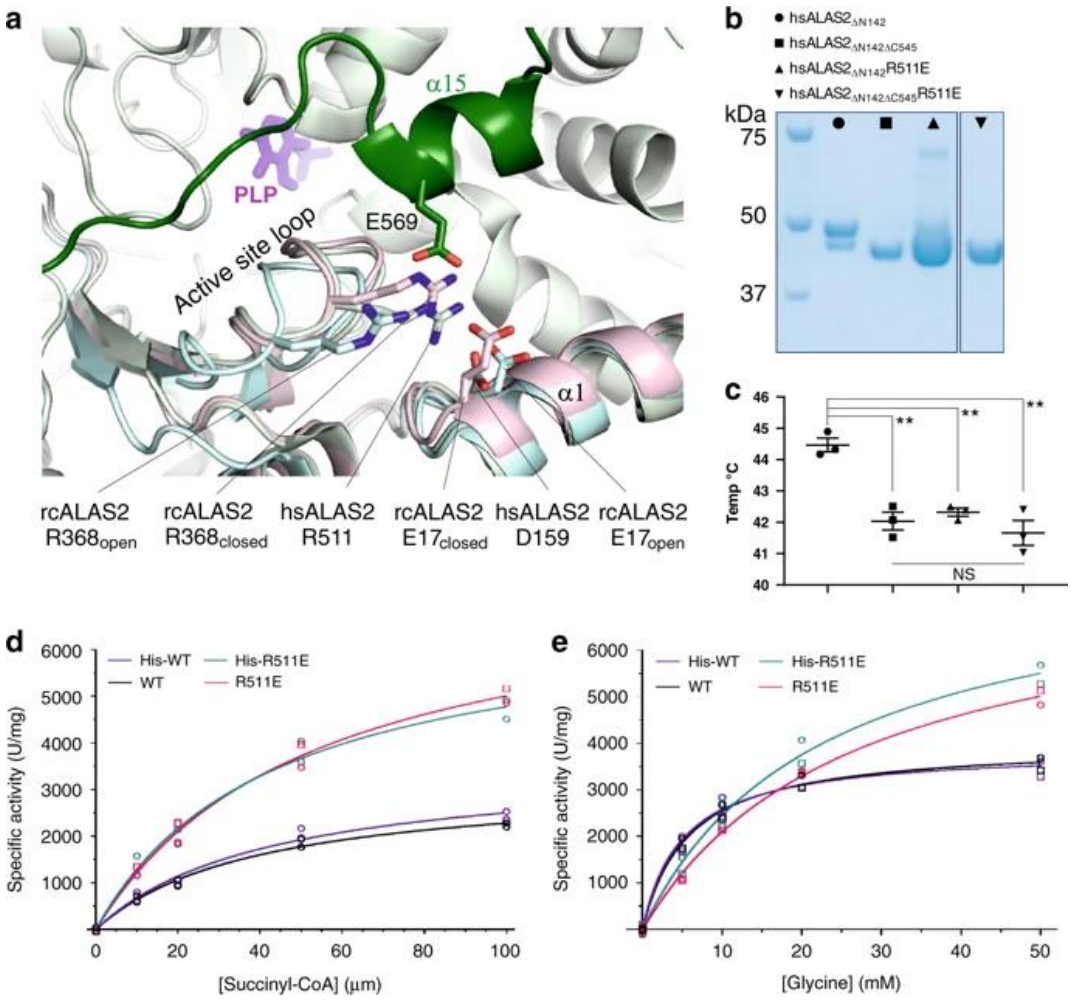

Fig. 3 Role of C-terminal extension in structural and functional integrity. (**a**) View of the hsALAS2 active site loop conformation within one monomer (catalytic domain light green, Ct-extension dark green). The active site loop from the open and closed forms of rcALAS (2BWN) are overlayed onto hsALAS2. (**b**) SDS-PAGE of the purified samples from hsALAS2$_{\Delta N142}$ WT (square) and R511E variant (up triangle), as well as hsALAS2$_{\Delta N142\Delta C545}$ WT (circle) and R511E variant (down triangle). (**c**) Midpoint melting temperatures, determined by differential scanning fluorimetry, of the four samples in panel b. Error bars represent mean values +/- SEM from n=3 technical replicates. **: *p*-values determined by two sample t-test; p= 0.0026, 0.0011 and 0.0002 from left to right. (**d, e**) Progression curves for recombinant hsALAS2$_{\Delta N142}$ WT and R511E

variant, for both His-tagged and untagged proteins. Specific activity is equivalent to the initial velocity normalized to protein in each assay. Succinyl-CoA and glycine titrations contained 50 mM glycine and 100 mM succinyl-CoA, respectively. Each nonlinear regression line was fitted to data from two biological replicates (n=2), with the data for each replicate (average of two technical replicates) plotted as distinct symbols (circle and square). Source data for Fig. 3b-e are provided as a Source Data file.

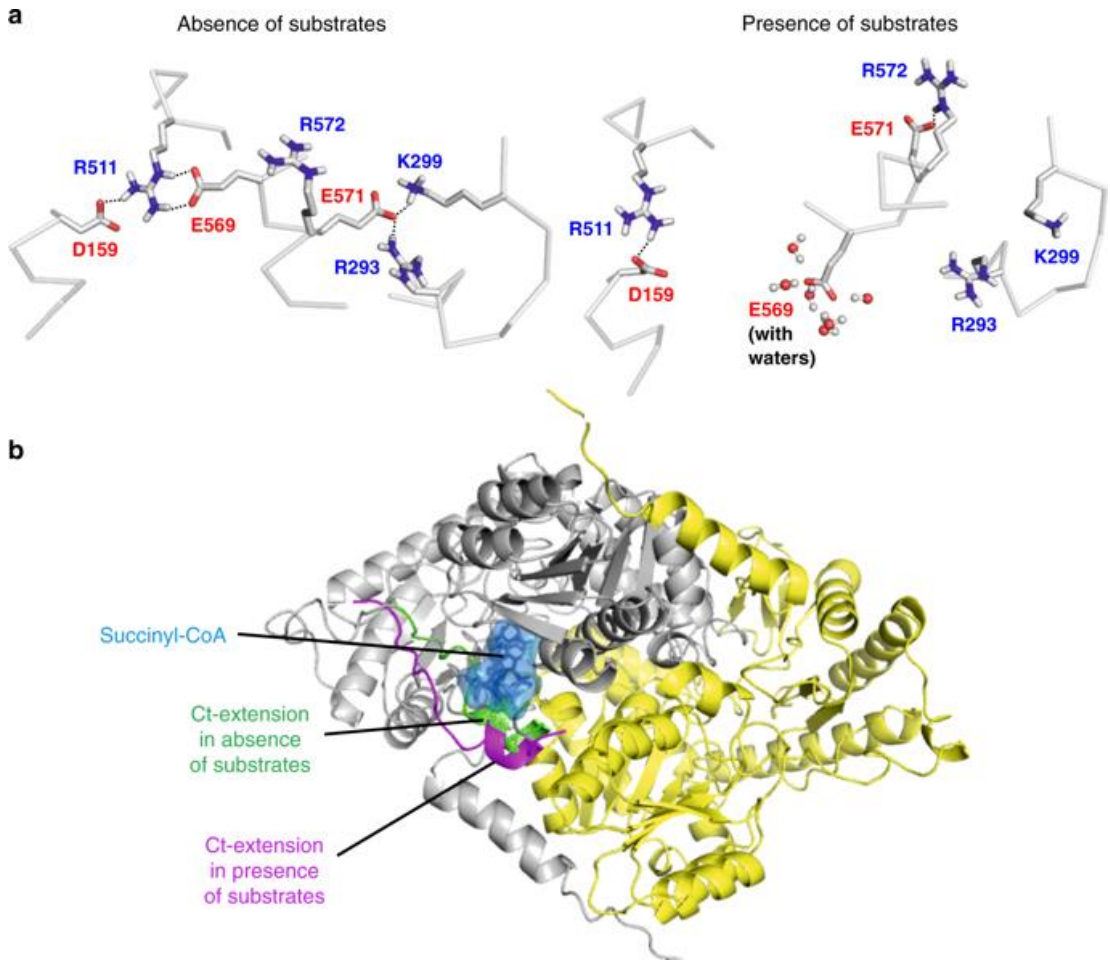

Fig. 4 Dynamics of the Ct-extension revealed by MD simulations. (**a**) Salt bridges in the absence (*left*) and presence (*right*) of substrates. The structure depicted on the left is the crystal structure subjected to energy minimization, and the structure depicted on the right is a representative snapshot taken from the simulation performed in the presence of substrates. Salt bridges are indicated by dashed lines. Water molecules stabililizing the E569 residue are shown in ball and stick representation. (**b**) The orientation of the Ct-extension in the absence and presence of substrates (shown in green and magenta, respectively). The space occupied by succinyl-CoA in the simulated structure is shown in blue.

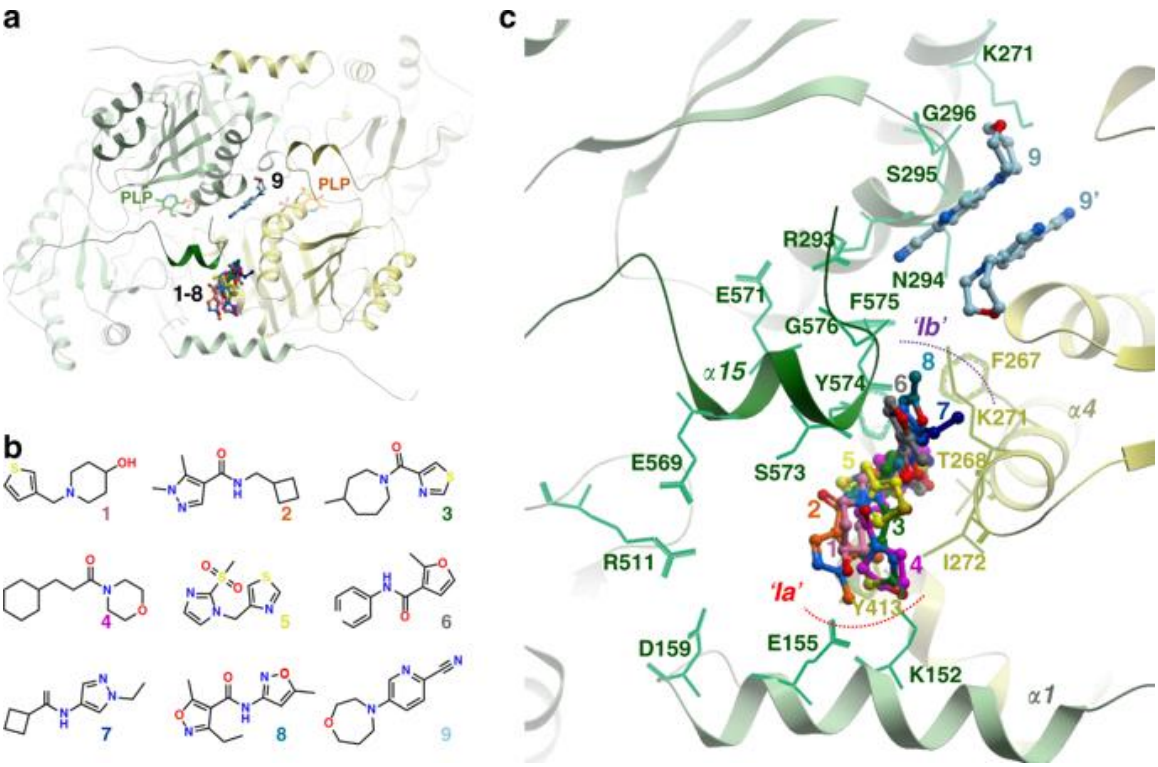

Fig. 5 Crystallography-based fragment screening of hsALAS2 (**a**) ALAS2-bound fragments are clustered into distinct regions of the protein. The two subunits of an ALAS2 homodimer are colored green and yellow. (**b**) Chemical structures of the fragments **1-9**, which are bound in proximity to the hsALAS2 Ct-extension. (**c**) Close-up view of the Ct-extension region of one subunit (green) and its neighboring subunit (yellow), showing the binding modes of fragments **1-9**. For fragment **9**, the second molecule (**9'**) bound to the yellow dimeric subunit is also shown.

Table 1 Data collection and refinement statistics for hsALAS2$_{\Delta N142}$ and hsALAS2$_{\Delta N78}$ crystal structures.

Dataset	hsALAS2$_{\Delta N142}$	hsALAS2$_{\Delta N78}$
Beamline	Diamond Beamline I04	Diamond Beamline I24
Wavelength (Å)	0.9795	0.9795
Unit cell parameters (a,b,c)	125.77 Å, 107.7 Å, 75.71Å	78.21 Å, 155.62 Å, 86.24 Å
(α, β, γ)	90.0°, 109.0°, 90.0°	90.0°, 98.45°, 90.0°
Space group	*C* 1 2 1	*P* 1 21 1
Resolution range (Å)	71.53 – 2.30	85.32 – 2.65*
Unique reflections	40141	58818
Rsym (%)	0.09 (0.71)	0.21 (0.76)
I/sig(I)	5.8 (1.0)	4.9 (1.5)
Completeness (%)	94.8 (95.0)	72.6 (19.3)*
Multiplicity	2.3 (2.3)	3.4 (3.0)
R_{cryst} (%)	0.21	0.21
R_{free} (%)	0.23	0.26
Wilson *B* factor (Å^2)	43.16	26.8
Average total *B* factor (Å^2)		
R.m.s.d. bond length (Å^2)	0.003	0.004
R.m.s.d. bond angle (°)	0.69	0.68
Clashscore	6.7	5.78
Ramachadran favoured (%)	95.6	95.6
Ramachandran disallowed (%)	0	0
Rotamer outliers (%)	0	0.15

*Anisotropic data truncated in STARANISO using local I/sigI cut off at 1.2 results in the inclusion of data to 2.65 with low isotropic completeness.

Data from highest resolution shell shown in parenthesis.

Table 2 Steady-state kinetics of recombinant hsALAS2 to study effect of His-tag and variants.

Enzyme (His_6-tagged or tag-free)	k_{cat} (min^{-1})	V_{max},SCoA (U mg^{-1})	K_m,SCoA (μM)	k_{cat}/K_m,SCoA (min^{-1} μM^{-1})	V_{max},Gly (U mg^{-1})	K_m,Gly (mM)	k_{cat}/K_m,Gly (min^{-1} mM^{-1})
WT	3.0 ± 0.2	3200 ± 200	39 ± 6	0.075 ± 0.012	4000 ± 130	5.7 ± 0.7	0.52 ± 0.07
His-WT	3.2 ± 0.3	3600 ± 300	42 ± 8	0.076 ± 0.015	3900 ± 180	5.0 ± 0.9	0.64 ± 0.12
R511E	6.3 ± 0.5	7700 ± 500	53 ± 7	0.120 ± 0.019	7700 ± 300	26 ± 2	0.24 ± 0.03
His-R511E	6.4 ± 0.7	6800 ± 500	43 ± 8	0.15 ± 0.03	8000 ± 500	22 ± 3	0.29 ± 0.05

Kinetic parameters for recombinant N-terminal His_6-tagged and tag-free $hsALAS2_{\Delta N142}$ WT and R511E proteins. Reported parameters are best-fit values ± SE for progression curves (Fig. 3d,e) derived from the Prism software (GraphPad 8.0).

Table 3 Steady-state kinetics of recombinant hsALAS2 XLP variants.

Enzyme (His_6-tagged)	k_{cat} (min^{-1})	V_{max},SCoA (U mg^{-1})	K_m,SCoA (μM)	k_{cat}/K_m,SCoA (min^{-1} μM^{-1})	V_{max},Gly (U mg^{-1})	K_m,Gly (mM)	k_{cat}/K_m,Gly (min^{-1} mM^{-1})
WT	3.5 ± 0.2	3600 ± 200	32 ± 4	0.110 ± 0.014	3440 ± 90	8.5 ± 0.8	0.41 ± 0.04
delAT	15.4 ± 0.8	17500 ± 800	56 ± 5	0.28 ± 0.03	16100 ± 310	10.3 ± 0.6	1.50 ± 0.12
Q548X	17.3 ± 1.1	19900 ± 1000	55 ± 5	0.31 ± 0.04	17700 ± 330	12.4 ± 0.6	1.40 ± 0.11
delG	4.5 ± 0.2	4000 ± 180	20 ± 3	0.23 ± 0.03	4960 ± 140	6.7 ± 0.7	0.66 ± 0.08

Kinetic parameters for recombinant His_6-tagged $hsALAS2_{\Delta N78}$ WT and XLP variant proteins expressed in *E. coli*. Reported parameters are best-fit values ± SE for progression curves (Supplementary Fig. 15) derived from the Prism software (GraphPad 8.0).

3.8 Supplementary Information

Supplemental Tables and Figures

Supplementary Table 1 Data collection and sample parameters for SAXS experiments.

Sample	hsALAS2$_{\Delta N142}$	hsALAS2$_{\Delta N142\Delta C545}$
Structural Parameters		
Guinier		
I(0) (cm^3)	0.06	0.07
Rg (Å)	33.33	31.61
P(r)		
I(0) (cm^3)	0.06	0.07
Rg (Å)	33.37	31.64
Dmax (Å)	122	121
Shape model-fitting results		
DAMMIF	default parameters, 13 calculations	default parameters, 13 calculations
q range for fitting	8.15E-03 - 2.46E-01	1.13E-02 - 2.57E-01
Symmetry, anisotropy assumptions	P2, none	P2, none
χ^2 range	1.351 – 1.641	1.134 – 1.379

hsALAS2$_{\Delta N142}$ and hsALAS2$_{\Delta N142\Delta C545}$ constructs are referred to in Supplementary Fig. 2.

Supplementary Table 2 Missense mutations reported to cause XLSA

No.	Exon	DNA change	Amino acid change	# Unrelated pedigrees	Supplementary References
1	5	c.462G>A	p.Met154Ile	1	(1)
2	5	c.466A>G	p.Lys156Glu	2	(2,3)
3	5	c.475G>A	p.Asp159Asn	1	(4)
4	5	c.475G>T	p.Asp159Tyr	1	(5)
5	5	c.481A>G	p.Thr161Ala	1	(6)
6	5	c.485A>G	p.Tyr162Cys	1	(7)
7	5	c.488G>A	p.Arg163His	2	(8)
8	5	c.495C>A	p.Phe165Leu	2	(9,10)
9	5	c.508C>A	p.Arg170Ser	2	(11,12)
10	5	c.508C>T	p.Arg170Cys	6	(10,13,14)
11	5	c.509G>T	p.Arg170Leu	4	(15,16)
12	5	c.509G>A	p.Arg170His	5	(7,14,15)
13	5	c.514G>A	p.Ala172Thr	2	(17)
14	5	c.569A>T	p.Asp190Val	1	(18)
15	5	c.577G>T	p.Val193Phe	1	(19)
16	5	c.595T>C	p.Tyr199His	1	(20)
17	5	c.606G>A	p.Met202Ile	4	(7,19)
18	5	c.611G>A	p.Arg204Gln	2	(21,22)
19	5	c.622G>T	p.Val208Phe	1	(23)
20	6	c.653G>A	p.Arg218His	1	(16)
21	6	c.670G>C	p.Gly224Arg	1	Bishop-unpublished
22	6	c.679C>T	p.Arg227Cys	3	(24,25)
23	6	c.724G>A	p.Glu242Lys	2	(16,25)
24	6	c.751T>C	p.Ser251Pro	1	(26)
25	6	c.776T>G	p.Phe259Cys	1	(19)
26	6	c.787G>A	p.Asp263Asn	3	(16,27)
27	6	c.791C>A	p.Ser264Tyr	1	(28)
28	6	c.800T>C	p.Phe267Ser	1	(19)
29	7	c.824G>A	p.Gly275Glu	1	(29)
30	7	c.828C>G	p.Cys276Trp	1	(30)
31	7	c.866T>C	p.Ile289Thr	1	(31)
32	7	c.871G>A	p.Gly291Ser	2	(19,32)
33	7	c.895A>C	p.Lys299Gln	1	(17)
34	7	c.897G>C	p.Lys299Asn	1	(19)
35	7	c.902T>C	p.Val301Ala	2	(10,33)
36	7	c.919C>A	p.Pro307Thr	1	(19)
37	7	c.946A>G	p.Lys316Glu	1	(19)
38	7	c.971T>C	p.Ile324Thr	2	(7,34)
39	7	c.984G>?	p.Glu328Asp	1	(34)
40	8	c.1016C>T	p.Pro339Leu	1	(16)
41	8	c.1051G>A	p.Gly351Arg	1	(35)
42	8	c.1054G>A	p.Ala352Thr	1	Bishop-unpublished

43	8	c.1070A>T	p.Asp357Val	1	(19)
44	8	c.1094A>G	p.Tyr365Cys	1	(36)
45	8	c.1093T>C	p.Tyr365His	1	(7)
46	8	c.1102C>T	p.Arg368Trp	1	(34)
47	8	c.1123C>T	p.Arg375Cys	1	(16)
48	8	c.1163C>G	p.Thr388Ser	1	(19)
49	8	c.1162A>C	p.Thr388Pro	1	(37)
50	9	c.1184G>A	p.Cys395Tyr	1	(38)
51	9	c.1193G>A	p.Gly398Asp	1	(30)
52	9	c.1218G>T	p.Leu406Phe	1	(39)
53	9	c.1231C>T	p.Arg411Cys	7	(10,14,16,20,40)
54	9	c.1232G>A	p.Arg411His	4	(16,41)
55	9	c.1247G>A	p.Gly416Asp	1	(42)
56	9	c.1253T>G	p.Ile418Ser	1	(43)
57	9	c.1276A>G	p.Met426Val	1	(18)
58	9	c.1306C>T	p.Arg436Trp	1	(44)
59	9	c.1315A>G	p.Lys439Glu	1	(45)
60	9	c.1343G>A	p.Arg448Gln	5	(13,20,42,46)
61	9	c.1349A>T	p.His450Leu	1	(19)
62	9	c.1354C>A	p.Arg452Ser	6	(42,47-49)
63	9	c.1354C>T	p.Arg452Gly	1	(16)
64	9	c.1354C>T	p.Arg452Cys	15	(2,13,14,16,19,20,42,50)
65	9	c.1355G>A	p.Arg452His	26	(2,10,13,14,42,50-54)
66	9	c.1373G>A	p.Arg458His	1	(55)
67	9	c.1412G>A	p.Cys471Tyr	2	(53,56)
68	9	c.1427T>A	p.Ile476Asn	1	(57)
69	9	c.1436G>A	p.Arg479Gln	1	(58)
70	10	c.1499A>G	p.Tyr500Cys	2	(22,25)
71	10	c.1508C>T	p.Ala503Val	2	(59,60)
72	10	c.1522A>T	p.Thr508Ser	1	(30)
73	10	c.1549C>T	p.Arg517Cys	1	(30)
74	10	c.1549C>T	p.Arg517Gly	1	(10)
75	10	c.1559C>T	p.Pro520Leu	5	(10,16,61)
76	10	c.1570C>G	p.His524Asp	2	(62)
77	11	c.1634T>A	p.Leu545Gln	1	(19)
78	11	c.1676G>A	p.Arg559His	1	(55)
79	11	c.1679G>A	p.Arg560His	1	(63)
80	11	c.1685T>C	p.Val562Ala	1	(14)
81	11	c.1688A>T	p.His563Leu	1	(19)
82	11	c.1693G>A	p.Glu565Lys	1	(19)
83	11	c.1699A>G	p.Met567Val	1	(64)
84	11	c.1701G>C	p.Met567Ile	1	(14)
85	11	c.1702A>G	p.Ser568Gly	4	(65)
86	11	c.1715G>A	p.Arg572His	2	(16)

Supplementary Table 3 Fragment-bound hsALAS2 structures from crystallography-based screening

PDB ID	Fragment-bound structure	Resolution (Å)	Chemical structure
5QQY	Structure of hsALAS2 bound with PLP and fragment ***1*** (F9000350): (1-(thiophen-3-ylmethyl)piperidin-4-ol)	1.49	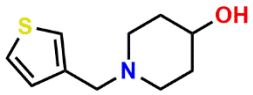
5QR1	Structure of hsALAS2 bound with PLP and fragment ***2*** (F9000534): *N*-(cyclobutylmethyl)-1,5-dimethyl-1*H*-pyrazole-4-carboxamide	1.44	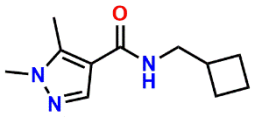
5QRA	Structure of hsALAS2 bound with PLP and fragment ***3*** (F9000413): (4-methylazepan-1-yl)(thiazol-4-yl)methanone	1.73	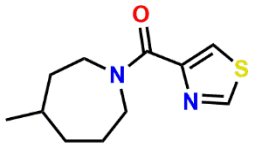
5QRC	Structure of hsALAS2 bound with PLP and fragment ***4*** (FM010110): 3-cyclohexyl-1-morpholinopropan-1-one	1.83	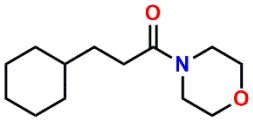
5QRD	Structure of hsALAS2 bound with PLP and fragment ***5*** (F9000430): 4-((2-(methylsulfonyl)-1*H*-imidazol-1-yl)methyl)thiazole	1.76	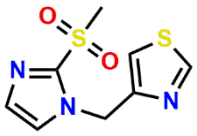
5QQW	Structure of hsALAS2 bound with PLP and fragment ***6*** (XS179878): 2-methyl-N-(pyridin-4-yl)furan-3-carboxamide	1.56	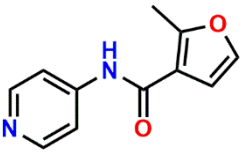
5QQX	Structure of hsALAS2 bound with PLP and fragment ***7*** (F9000532): N-(1-ethyl-1H-pyrazol-4-yl)cyclobutanecarboxamide	1.51	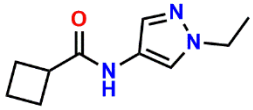
5QRE	Structure of hsALAS2 bound with PLP and fragment ***8*** (Z117233350): 3-ethyl-5-methyl-N-(5-methylisoxazol-3-yl)isoxazole-4-carboxamide	1.68	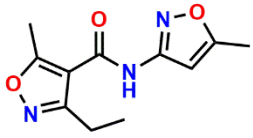
5QQU	Structure of hsALAS2 bound with PLP and fragment ***9*** (F9000370): 5-(1,4-oxazepan-4-yl)picolinonitrile	1.55	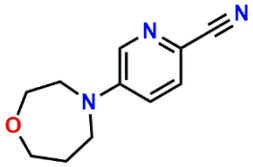

Data collection and refinement statistics can be found in Supplementary Data 1.

Supplementary Table 4 Relative enzyme activities of recombinant hsALAS2 WT (0.025 μM) in the presence of small-molecule fragments 1 and 8.

Additive	Concentration	WT Activity	% WT Activity
DMSO	–	1.00 ± 0.06	100 ± 6
Fragment **1**	1 mM	0.84 ± 0.03	84 ± 3
	5 mM	0.72 ± 0.02	72 ± 2
Fragment **8**	1 mM	0.85 ± 0.04	85 ± 4
	5 mM	0.78 ± 0.03	78 ± 3

Activity values represent the mean of three biological replicates ± SD (each biological replicate is the average of two technical replicates) and have been normalized to WT enzyme treated with DMSO (diluent). Source data are provided as a Source Data file.

Supplementary Table 5 Simulation box details

System	Number of atoms (including water)	Box dimensions (in Å)
No PLP	168,426	119.1 × 119.1 × 119.1
With PLP	168,478	119.1 × 119.1 × 119.1
With substrates	170,469	119.6 × 119.6 × 119.6

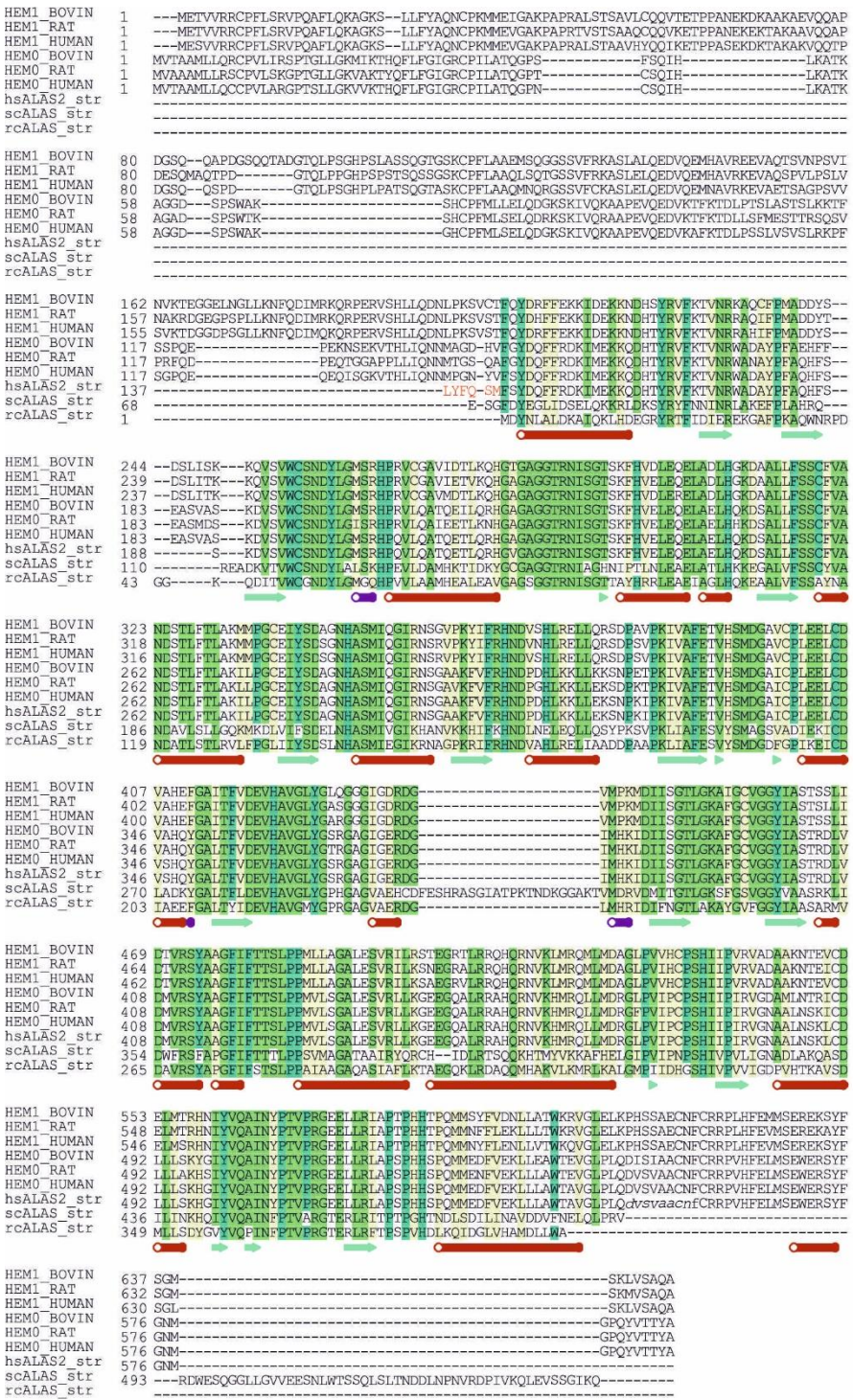

Supplementary Fig. 1 Structure-based sequence alignment of ALAS orthologues. Sequences of the crystallized constructs used in the structure determination of hsALAS2 (hsALAS2_str), *S. cerevisiae* ALAS (scALAS_str), and *R. capsulatus* ALAS (rcALAS_str) are aligned, on the basis

of Cα-superposition of their structures. Additionally, full-length sequences of ALAS1 from bovine (HEM1_BOVIN), rat (HEM1_RAT) and human (HEM1_HUMAN), as well as full-length sequences of ALAS2 from bovine (HEM0_BOVIN), rat (HEM0_RAT) and human (HEM0_HUMAN) are appended to the alignment. For the hsALAS2_str sequence, vector-encoded residues at the beginning of the construct are denoted in red letters, and secondary structure assignment is shown at the bottom of the alignment (α-helix, red; 3_{10} helix, purple; β-strand, green).

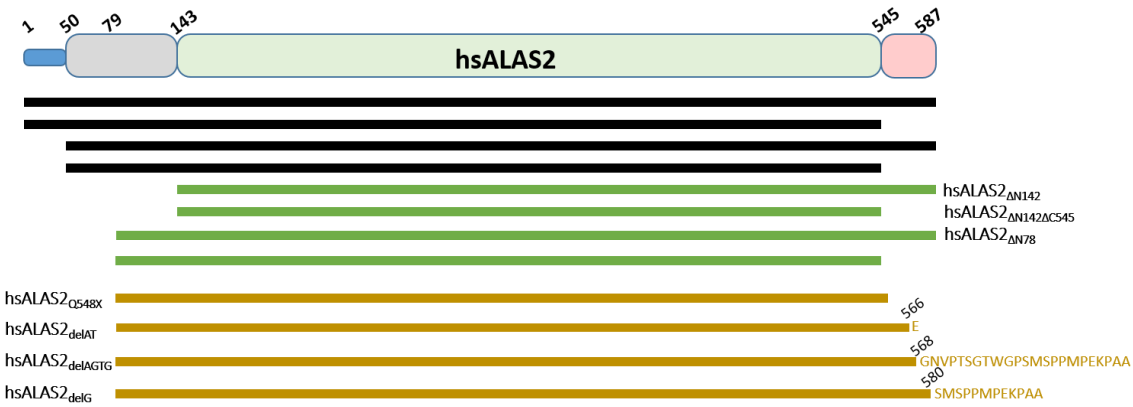

Supplementary Fig. 2 Domain architecture of hsALAS2. hsALAS2 is a 587-aa polypeptide (top) containing a mitochondrial targeting sequence (blue), an unstructured domain of unknown function (grey), a conserved catalytic domain (light green) and a C-terminal extension unique to eukaryotes (pink). Bottom*:* Black bars denote attempted constructs that were insoluble during expression tests, green bars represent soluble wild-type constructs in this study, and orange bars indicate constructs of disease-associated variants in this study.

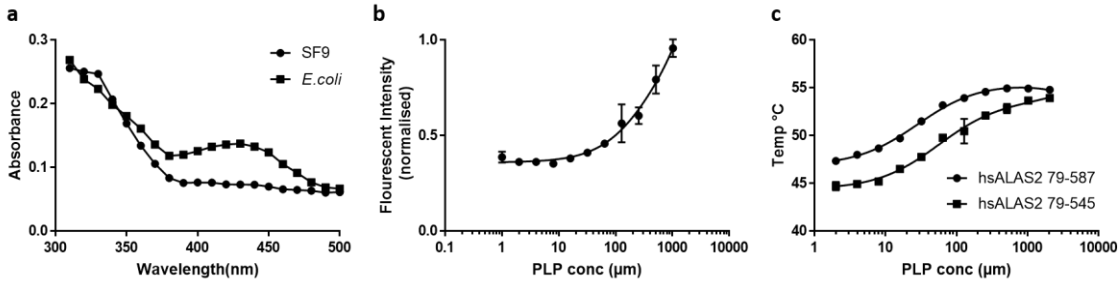

Supplementary Fig. 3 PLP loading of recombinant hsALAS2. (**a**) UV-Vis spectrum of hsALAS2$_{\Delta N142}$ comparing different ratios of the PLP tautomeric states of holoenzyme when isolated from insect cell (Sf9) or *E. coli* cell expression systems. *E.coli*-expressed hsALAS2 produces holoenzyme in the protonated ketoenamine tautomer (shown by absorption maximum at 420 nm), whereas insect cell-expressed hsALAS2 likely yields holoenzyme in the deprotonated enolimine tautomer (shown by absorption maximum at 335 nm and lack of absorbance at 420 nm). Raw data points plotted from one experiment. (**b**) A plot of fluorescence intensity increase with excitation at 440nm and emission at 520nm. Titration of excess PLP to insect cell-expressed hsALAS2$_{\Delta N78}$ shifts the equilibrium towards the protonated ketoenamine form, shown by increased fluorescence of the internal aldimine. Data are presented as mean values +/- SEM from three technical replicates (n=3). (**c**) Midpoint melting temperatures, determined by differential scanning fluorimetry, of insect cell-expressed hsALAS2$_{\Delta N78}$ and hsALAS2$_{\Delta N78\Delta C545}$. The ketoenamine form resulting from titration of PLP to both proteins is thermally more stable. Data are presented as mean values +/- SEM, from n=3 technical replicates. Source data are provided as a Source Data file.

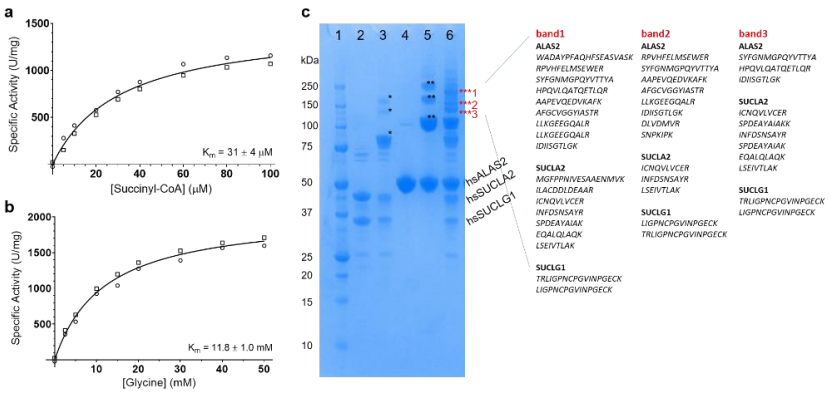

Supplementary Fig. 4 Functional integrity of recombinant hsALAS2$_{\Delta N78}$ and hsALAS2$_{\Delta N142}$ proteins. (**a, b**) Kinetic progress curves for recombinant hsALAS2$_{\Delta N142}$ protein overexpressed in Sf9 insect cells. Specific activity represents initial reaction velocity normalized to protein in each assay (4 μg mL^{-1}), where succinyl-CoA and glycine were titrated in the presence of 50 mM glycine and 100 μM succinyl-CoA, respectively. One unit of activity (U) is the amount of enzyme needed to catalyze the formation of 1 nmol ALA per hour. Each regression line was fitted to data from two biological replicates (n=2), with the data for each replicate plotted as distinct symbols (circles and squares). (**c**) Crosslinking SDS-PAGE of interactions between hsALAS2$_{\Delta N78}$ and succinyl-CoA ligase. Results shown are representative of three independent experiments. Lane 1, molecular weight markers in kDa; Lane 2, purified succinyl-CoA ligase (SUCLG1-SUCLA2); Lane 3, SUCLG1-SUCLA2 after incubation with di(N-succinimidyl) glutarate crosslinker (DSG), showing crosslinked oligomeric species of SUCLG1-SUCLA2 (*); Lane 4, purified hsALAS2$_{\Delta N78}$; Lane 5, hsALAS2$_{\Delta N78}$ incubated with DSG, showing crosslinked oligomeric species of hsALAS2 (**); Lane 6, mixture of SUCLG1-SUCLA2 and hsALAS2$_{\Delta N78}$ incubated with DSG, showing crosslinked species representing the complex between SUCLG1-SUCLA2 and hsALAS2$_{\Delta N78}$ (***). Protein identity of all asterisked bands (1-3) were confirmed by tryptic digest MS/MS, in which mapped peptides corresponding to each of the three component proteins are shown in the inset figure. Source data are provided as a Source Data file.

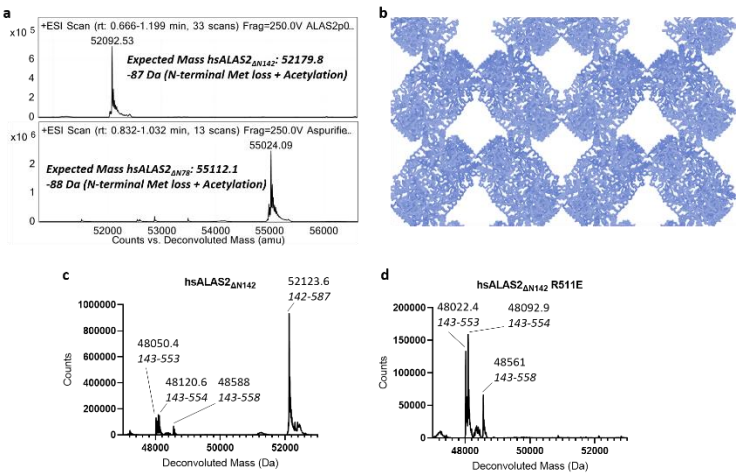

Supplementary Fig. 5 N- and C-termini of our recombinant hsALAS2 proteins. (**a**) Deconvoluted mass spectrum of both purified hsALAS2$_{\Delta N142}$ and hsALAS2$_{\Delta N78}$ proteins expressed in SF9 cells and used in structural studies are shown to have a fully intact N-terminus and C-terminus, after expression and purification. (**b**) Intermolecular packing of hsALAS2$_{\Delta N78}$ crystals, showing space between dimers (blue ribbons) that could account for the disordered N-terminus. (**c**) Deconvoluted mass spectrum of *E.coli* expressed hsALAS2ΔN142 shows predominantly intact protein (expected MW 52122.7 Da, measured MW 52123.6 Da) with three additional degradation peaks at low relative abundance to intact protein. Peak at 48588 Da corresponds to hsALAS2 143-558, peak at 48120.6 Da corresponds to hsALAS2 143-554 and peak at 48050.4 corresponds to hsALAS2 143-553 (**d**) Deconvoluted mass spectrum of *E.coli* expressed R511E variant of hsALAS2ΔN142 shows no signal for intact protein (expected MW 52095.49 Da) and high abundance of the three degradation peaks seen in WT. Peak at 48561 Da corresponds to R511E hsALAS2 143-558, peak at 48092.9 Da corresponds to R511E hsALAS2 143-554 and peak at 48022.4 corresponds to R511E hsALAS2 143-553. Source data for Supplementary Fig. 5a, c and d are provided as a Source Data file.

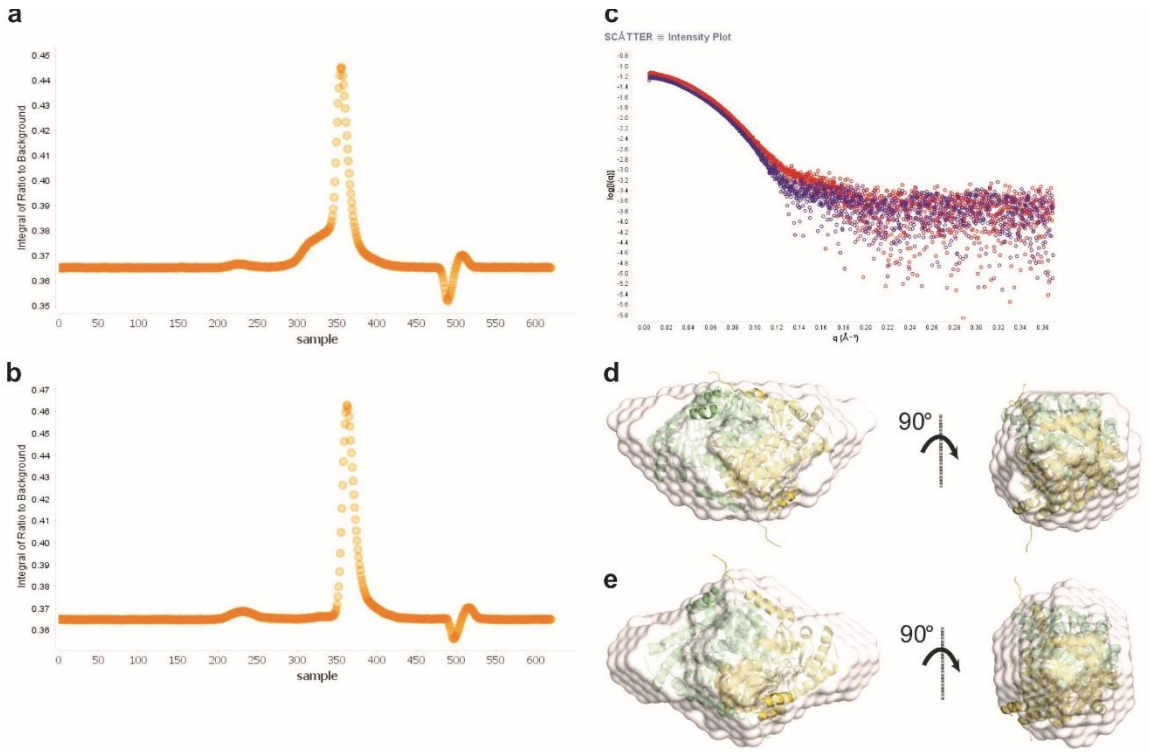

Supplementary Fig. 6 Small angle X-ray scattering studies of hsALAS2$_{\Delta N142}$ and hsALAS2$_{\Delta N142\Delta C545}$. (**a**) SEC-SAXS signal plot of hsALAS2$_{\Delta N142}$, with each data point (orange circle) representing the integrated area of the ratio of the sample SAXS curve to the estimated background. (**b**) SEC-SAXS signal plot of hsALAS2$_{\Delta N142\Delta C545}$, construct that contains only the catalytic domain without the C-terminal extension. (**c**) Log10 intensity plot of subtracted and merged SAXS frames. Red circles represent scattering data points from hsALAS2$_{\Delta N142\Delta C545}$, and blue circles represent scattering data points from hsALAS2$_{\Delta N142.}$ (**d**) Orthogonal views of the *ab initio* envelopes calculated from SAXS data for hsALAS2$_{\Delta N142.}$ (**e**) Orthogonal views of the *ab initio* envelopes calculated from SAXS data for hsALAS2$_{\Delta N142\Delta C545.}$ Source data are provided as a Source Data file.

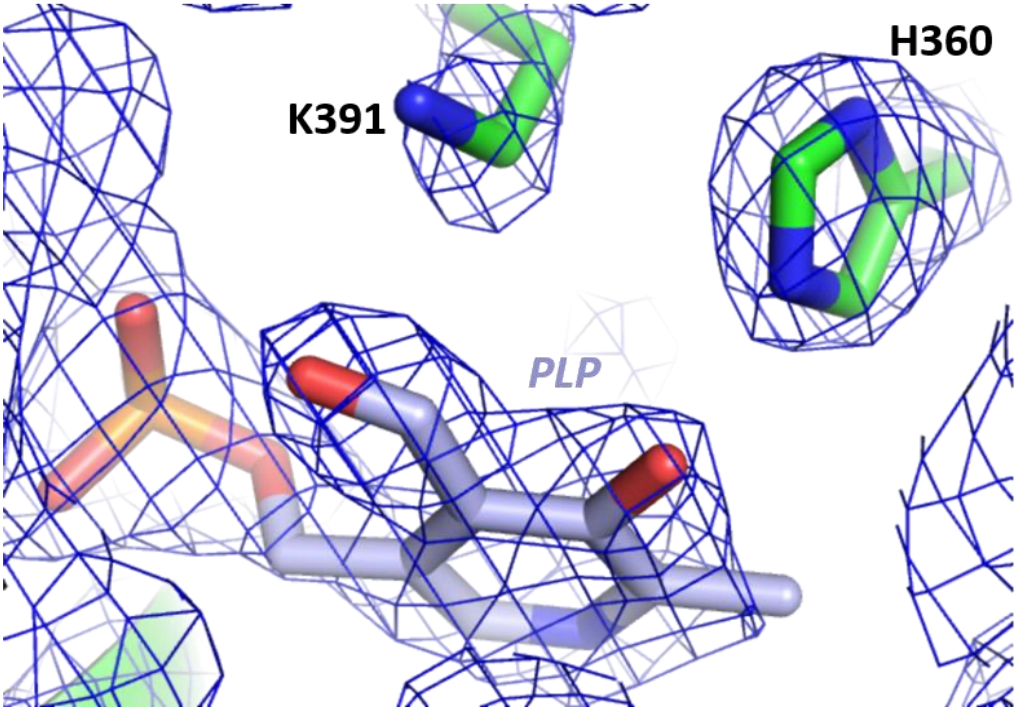

Supplementary Fig. 7 PLP binding site. 2*Fo* − *Fc* electron density map of the active site region, contoured at 1σ, revealing residues of hsALAS2 that interact with PLP. As expected, no covalent linkage was observed between PLP and its Schiff base Lys391 in the crystal.

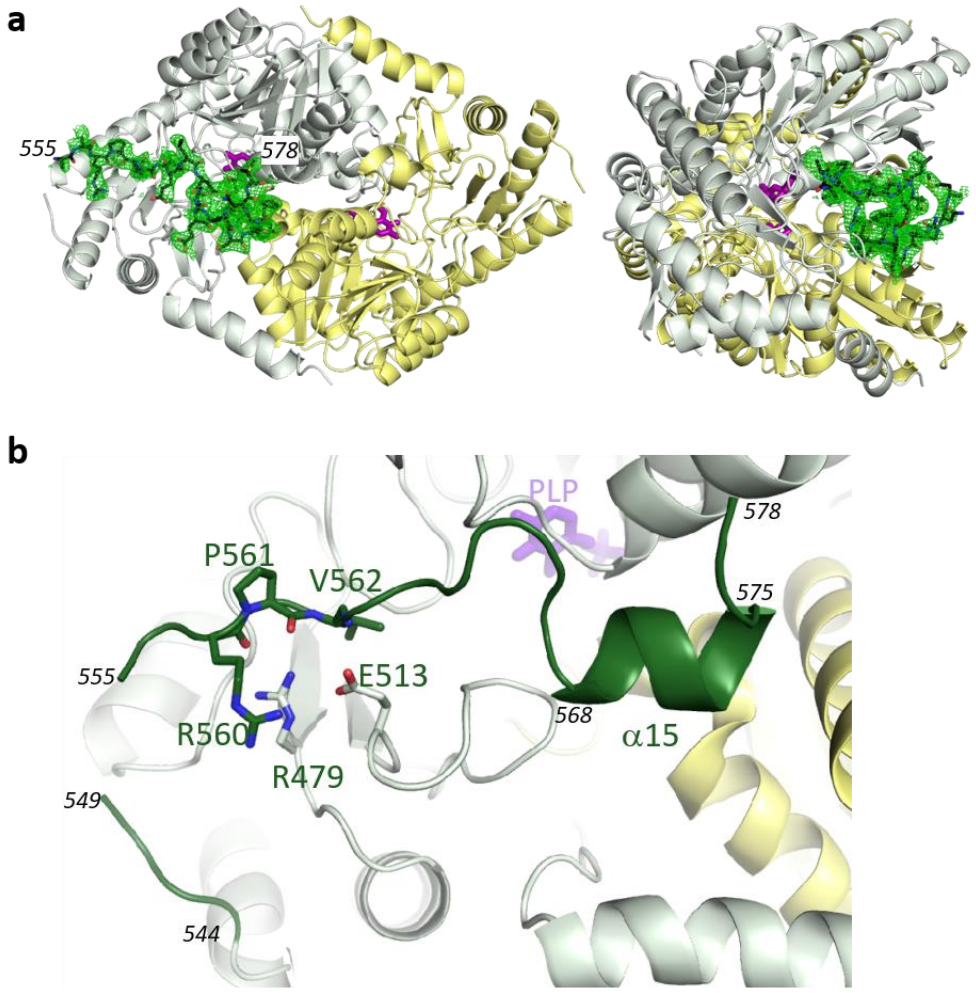

Supplementary Fig. 8 The hsALAS2 C-terminal extension. (**a**) Composite 2mFo-DFc omit map (by Phenix software) of the hsALAS2 Ct-extension, contoured at 1σ , shown for one subunit of the homodimer. Black lines represent Ct-extension residues 555-578 built onto the density. (**b**) Topology of an hsALAS2 Ct-extension (dark green), packing against the catalytic core of its own protomer (light green) and of the opposing protomer in the homodimer (yellow). PLP is shown as purple sticks. Interacting residues of the catalytic core and the unstructured portion of the Ct-extension are displayed. Residues 550-554 are disordered in the structure and hence not modeled.

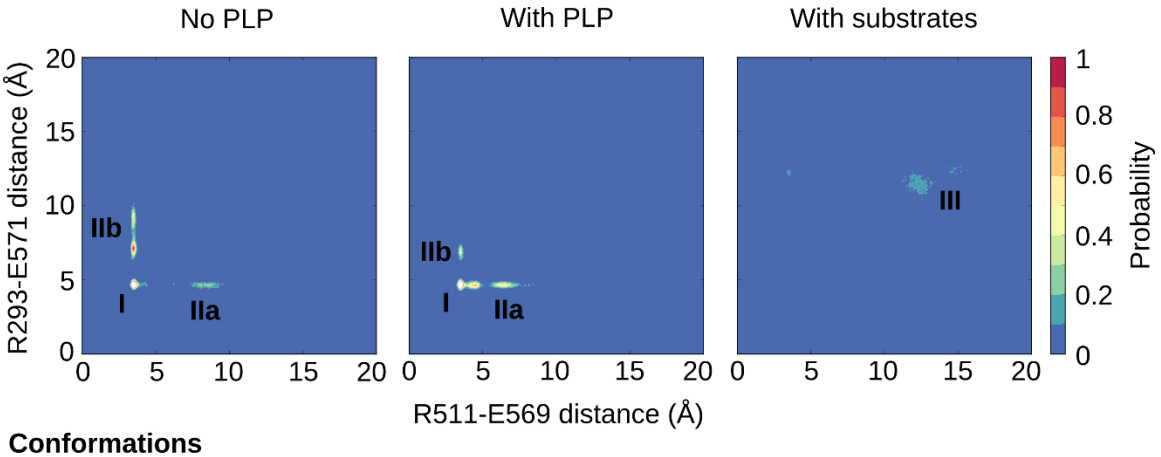

Conformations

I: Both R511-569 and R293-E571 intact
IIa: R511-569 broken, R293-E571 intact
IIb: R511-569 intact, R293-E571 broken
III: Both R511-569 and R293-E571 broken

Supplementary Fig. 9 Conformational landscape of the Ct-extension in terms of salt bridge dynamics. The figure shows probabilities as a function of R511-E569 distance and R293-E571 distance. To calculate the distance between two residues, the distance between the centers of the guanidium group of arginine and the carboxylate group of glutamate was calculated. Distance values were calculated separately for the two subunits. The data for the two subunits was merged while computing the probabilities. A total of 50 ns of simulation was performed for each of the three systems shown above. Distinct conformations of the Ct-extension have been marked in the figure as “I”, “IIa”, “IIb” and “III”. These conformations have been defined below the probability plots. Source data are provided as a Source Data file.

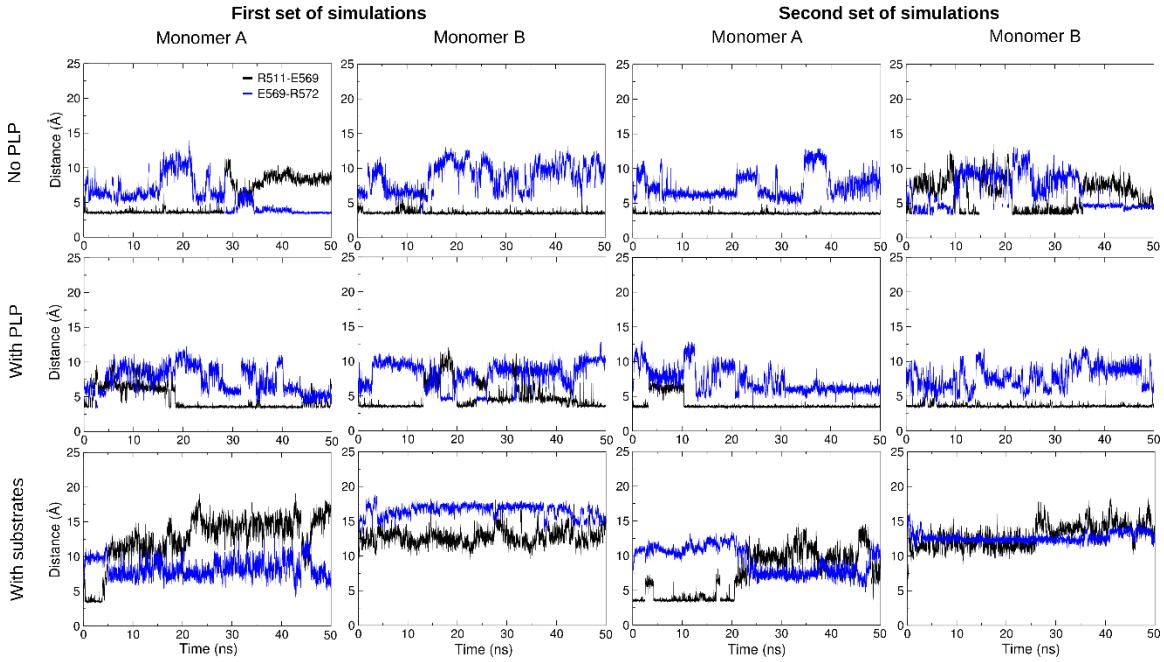

Supplementary Fig. 10 Dynamics of salt bridges involving E569. The variation of the distance between the residues participating in salt bridges is shown as a function of simulation time. To calculate the distance between two residues, the center of a given residue was defined as the center of mass of the side-chain guanidinium/amine/carboxylate group, depending on the amino acid type. The distance between the residue centers was then calculated. The salt bridge R511-E569 is stable in the apo form but broken in order to accommodate substrates. E569-R572 is a non-native salt bridge that is observed when R511-E569 is broken. Two sets of simulation were performed and both data are shown here. Source data are provided as a Source Data file.

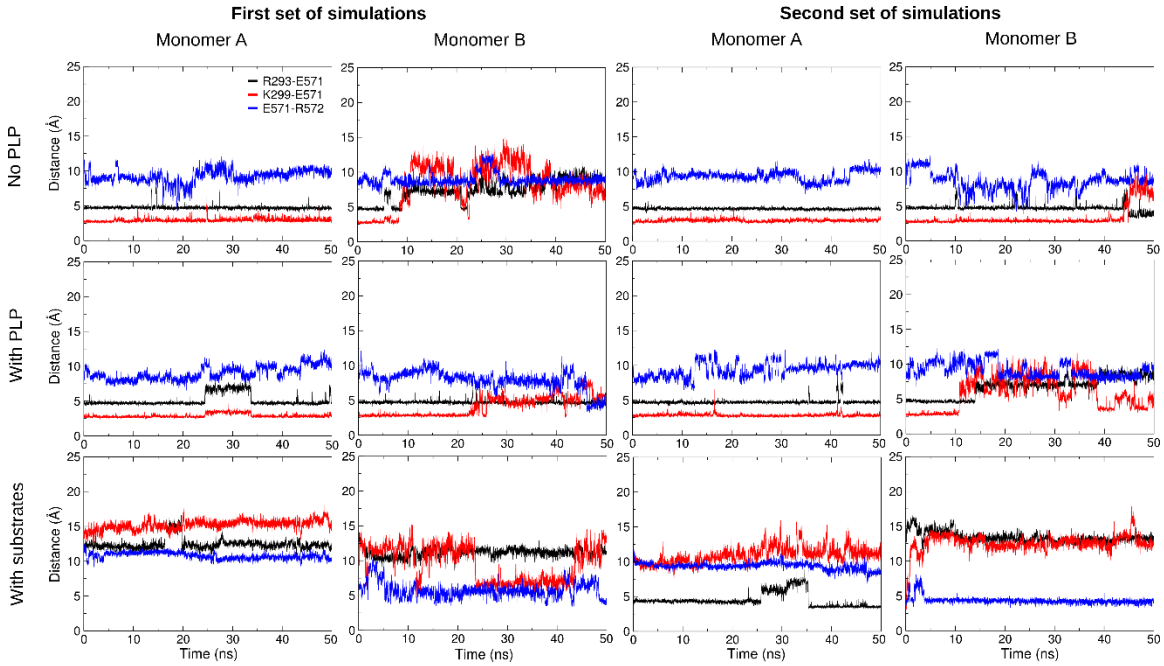

Supplementary Fig. 11 Dynamics of salt bridges involving E571. The variation of the distance between the residues participating in salt bridges is shown as a function of simulation time. To calculate the distance between two residues, the center of a given residue was defined as the center of mass of the side-chain guanidinium/amine/carboxylate group, depending on the amino acid type. The distance between residue centers was then calculated. The salt bridges R293-E571 and K299-E571 are broken in order to accommodate substrates. E571-R572 is a non-native salt bridge that is observed when R293-E571 and K299-E571 are broken. Two sets of simulation were performed and both data are shown here. Source data are provided as a Source Data file.

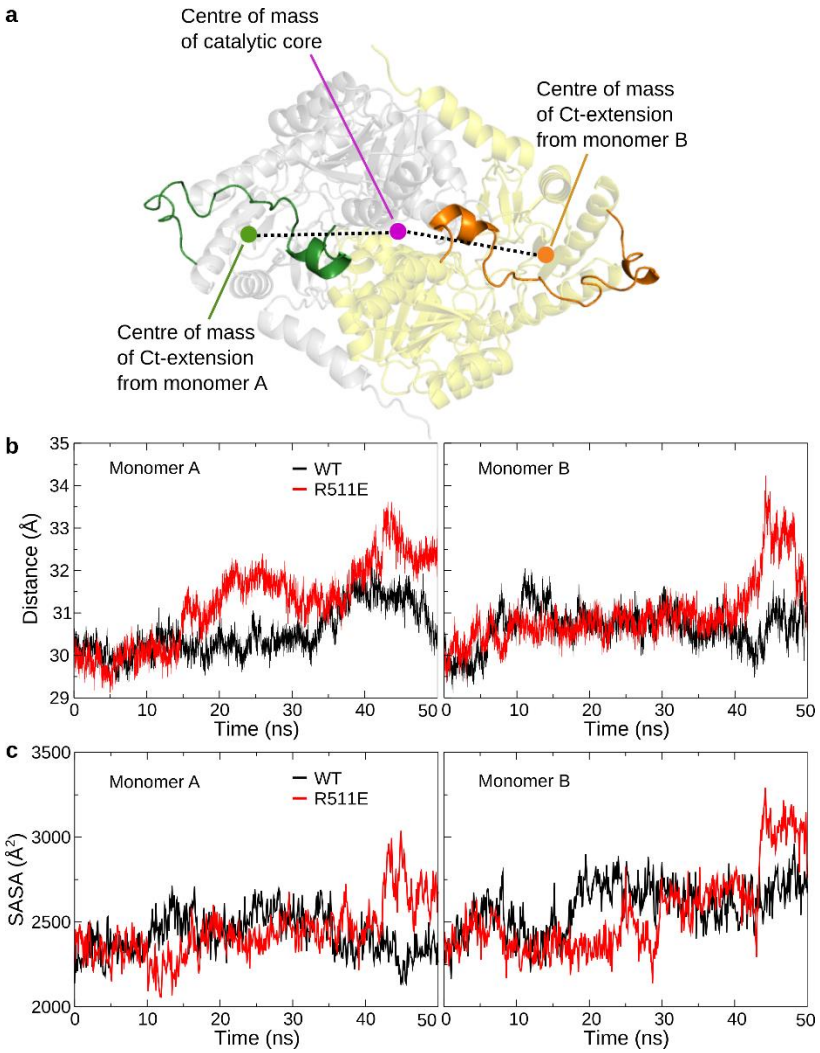

Supplementary Fig. 12 Accessibility of the Ct-extension. (a) In the current MD simulations, the distance between the center of mass of the catalytic core of the homodimer (purple dot) and the center of mass of Ct-extensions from each of the two monomers (orange and green dots) is being measured. These distances are marked by two dotted lines. **(b)** Variation of the distance defined in (a). The R511E model exists in conformations in which the Ct-extension has moved away from the catalytic core, especially in the last 10 ns. **(c)** Variation of solvent accessible surface area (SASA) of the Ct-extension over the course of the simulation. The R511E mutant exists in conformations in which the Ct-extension has moved away from the catalytic core, and therefore has a higher SASA. Source data are provided as a Source Data file.

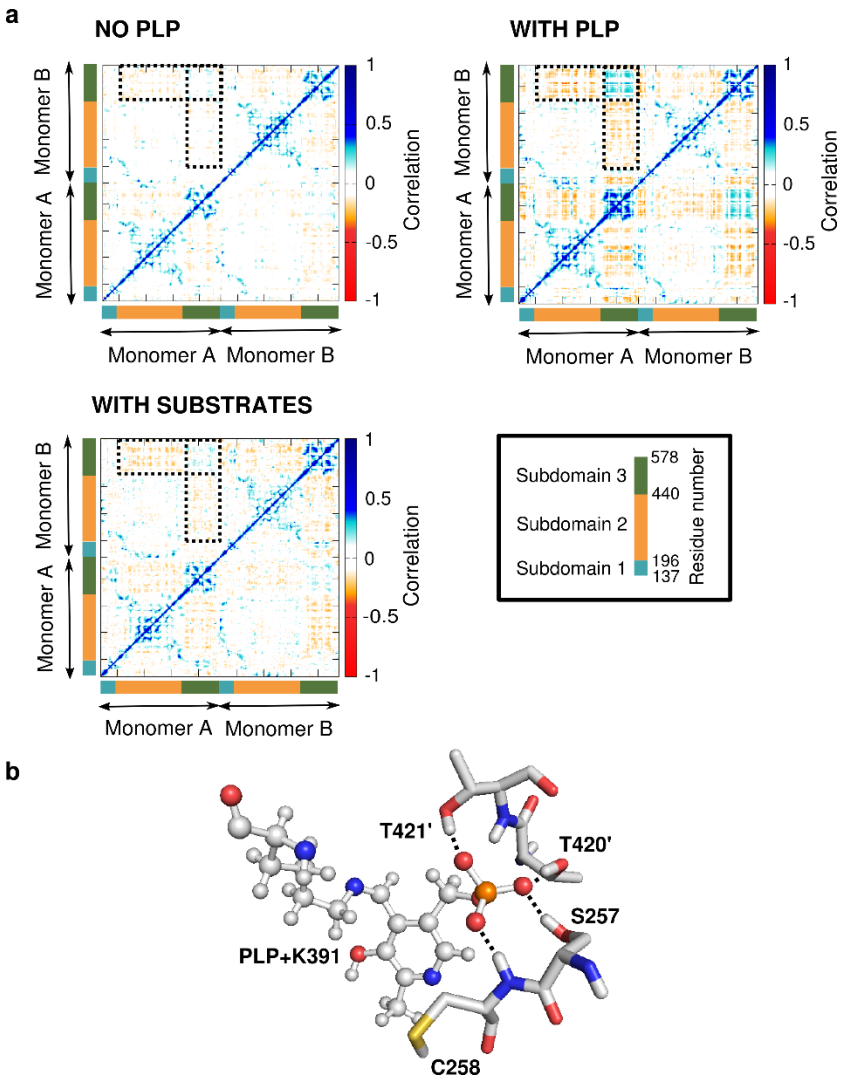

Supplementary Fig. 13 Dynamic cross correlation maps (DCCM). (**a**) The correlation in the dynamics of different regions of the protein is shown here. The last 10 ns of the trajectories were considered in the analysis. The dotted rectangles on the plots indicate regions that show increased correlation upon covalent attachment of PLP to the active site. (**b**) Interactions between the phosphate moiety on PLP and surrounding residues. Dotted lines indicate hydrogen bonds. S257 and C258 belong to the same subunit as PLP, and T420' and T421' belong to the opposite subunit. Source data for Supplementary Fig. 13a are provided as a Source Data file.

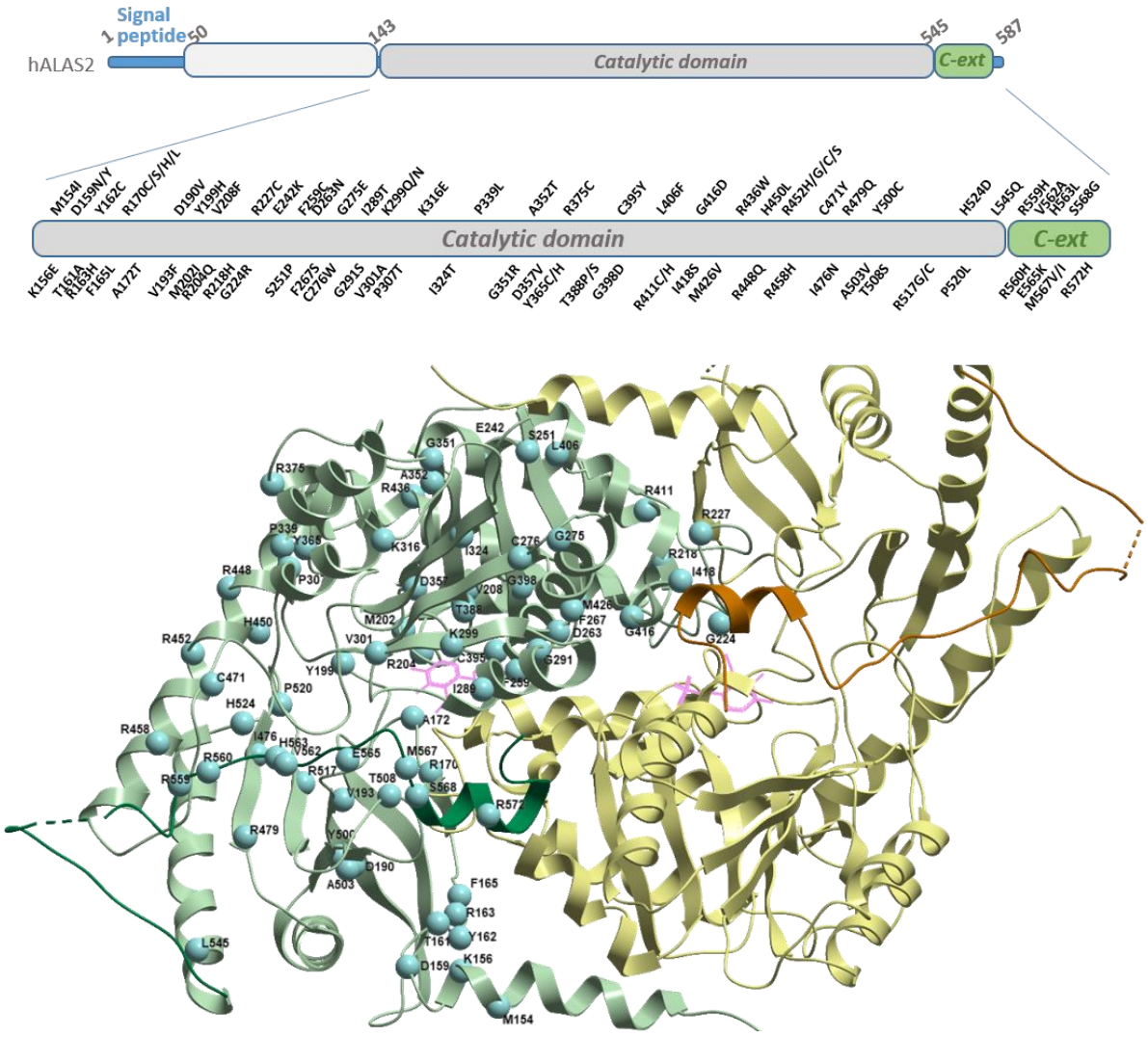

Supplementary Fig. 14 Mapping of disease-causing missense mutations onto hsALAS2 structure. Sites of missense mutations that lead to the XLSA disorder (spheres) are mapped onto a domain organization schematic (*top*) and the hsALAS2 structure shown as a homodimer (green and yellow subunits)(*bottom*).

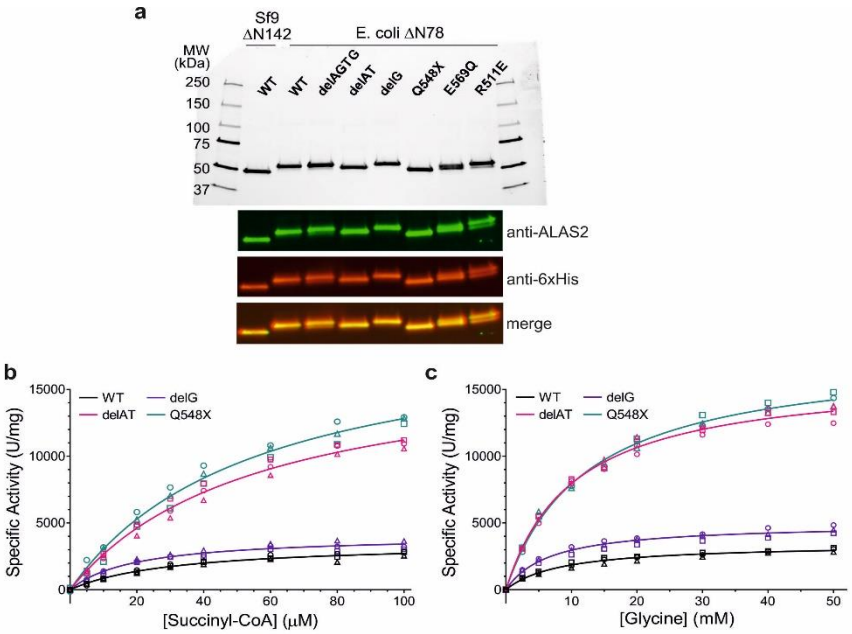

Supplementary Fig. 15 XLP causing variants of hsALAS2. (**a**) SDS-PAGE (top) and multiplex western blot (bottom) of recombinant His_6-tagged hsALAS2 proteins (1 µg/lane and 100 µg/lane, respectively; purity > 90%), expressed in either Sf9 ($hsALAS2_{\Delta N142}$) or *E. coli* BL21(DE3) ($hsALAS2_{\Delta N78}$) cells as indicated. Results are representative of two independent experiments. Lanes 1 and 10 are molecular weight standards; lane 2 is WT $hsALAS2_{\Delta N142}$; lane 3 is WT $hsALAS2_{\Delta N78}$; lanes 4-7 are XLP variants reconstructed on $hsALAS2_{\Delta N78}$, lanes 8 and 9 are the experimental variants E569Q and R511E reconstructed on $hsALAS2_{\Delta N78}$. (**b**,**c**) Michaelis-Menten curves for purified, *E.* coli-expressed $hsALAS2_{\Delta N78}$ WT and XLP variants with titration of succinyl-CoA (b) and glycine (c). Regression lines represent the mean of three biological replicates (n=3), with the data for each replicate plotted as distinct symbols (circles, squares and triangles). Specific activity represents initial velocity normalized to protein in each assay (1-4 µg mL^{-1}), where succinyl-CoA and glycine titrations were conducted in the presence of 50 mM glycine and 100 µM succinyl-CoA, respectively. Data with statistics are presented in Table 3. Source data are provided as a Source Data file.

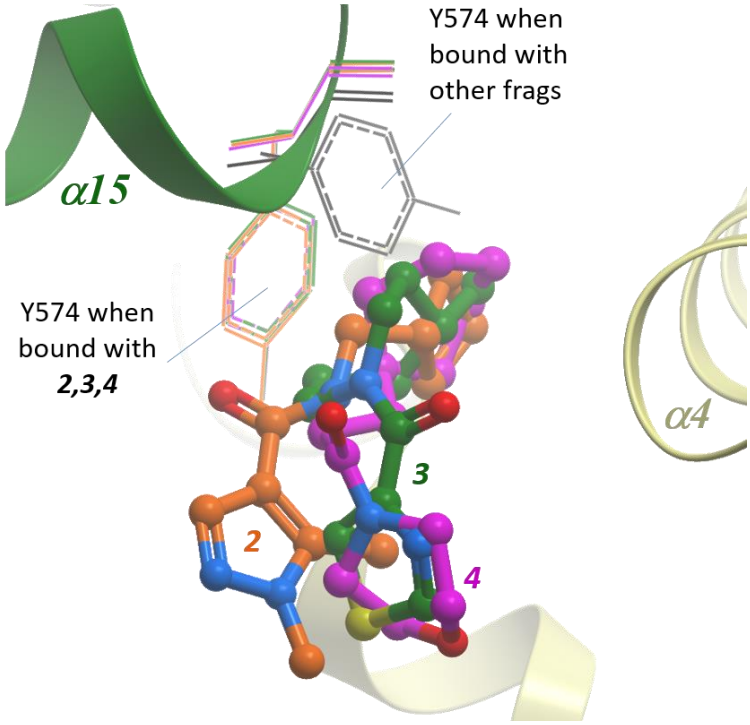

Supplementary Fig. 16 Alternative conformation of Tyr574. In structures bound with fragments **2-4** (colored sticks), the Tyr574 side-chain (colored lines) adopts a different rotamer conformation from other structures (black line).

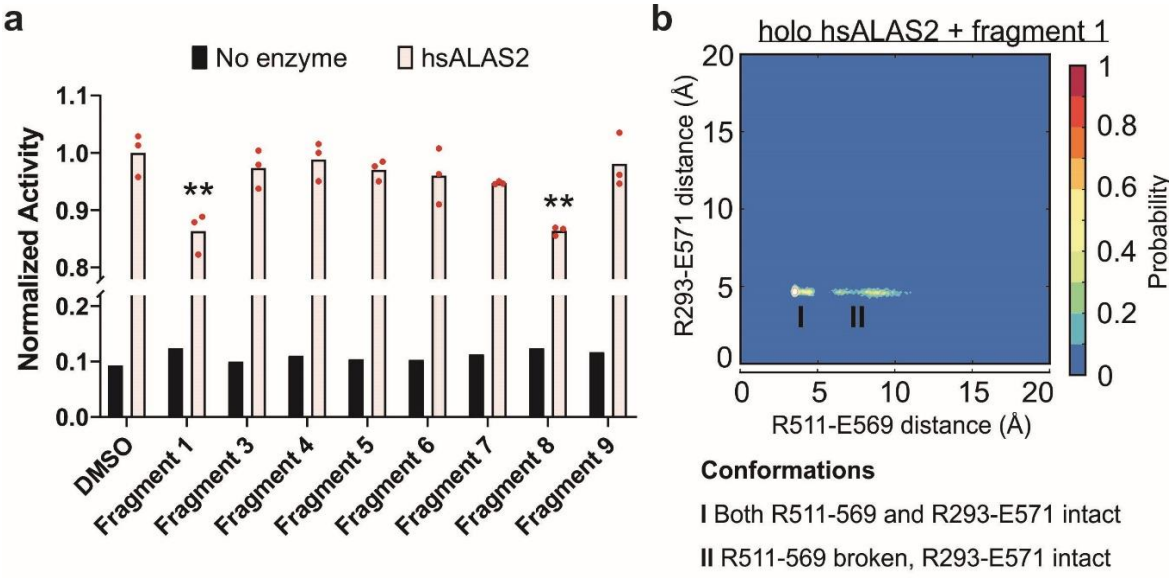

Supplementary Fig. 17 Impacts of fragment binding on hsALAS2. (**a**) Enzyme activity of hsALAS2$_{\Delta N78}$ expressed in *E. coli* and pretreated with fragments. Purified hsALAS2$_{\Delta N78}$ (4 μg mL^{-1}) or buffer (no enzyme) was preincubated with fragments **1** and **3-9** at 1 mM concentrations or DMSO (diluent for fragments) at 37°C for 15 min prior to the initiation of reactions as detailed in the Methods. Assays with protein were run using three separate hsALAS2$_{\Delta N78}$ preps (each with n=3 technical replicates). Each plotted activity value (biological replicate) was normalized to protein pretreated with DMSO, and each bar represents the mean of three biological replicates. No-enzyme assays were run in n=3 technical replicates (bars represent the only biological replicate). Statistical significance relative to assays with protein and DMSO was established using one-way ANOVA (p = 0.0003) followed by Tukey's post-hoc analysis (** indicates $p < 0.01$ vs. DMSO control: fragment 1, p = 0.0022; fragment 3, p = 0.98; fragment 4, $p > 0.99$; fragment 5, p = 0.97; fragment 6, p = 0.85; fragment 7, p = 0.60; fragment 8, p = 0.0023; fragment 9, $p > 0.99$). (**b**) Conformational landscape of the Ct-extension in terms of salt bridge dynamics, from MD simulations of *holo* hsALAS2 in the presence of fragment **1**. The figure shows probabilities as a function of R511-E569 distance and R293-E571 distance. The

distances have been calculated in a manner similar to that described for fragment-free ALAS2 (Supplementary Fig. 9). Two distinct conformations (I and II) are observed. Only monomer B of the homodimer was included in the analysis because fragments have dissociated from monomer A during the 50 ns run. Source data are provided as a Source Data file.

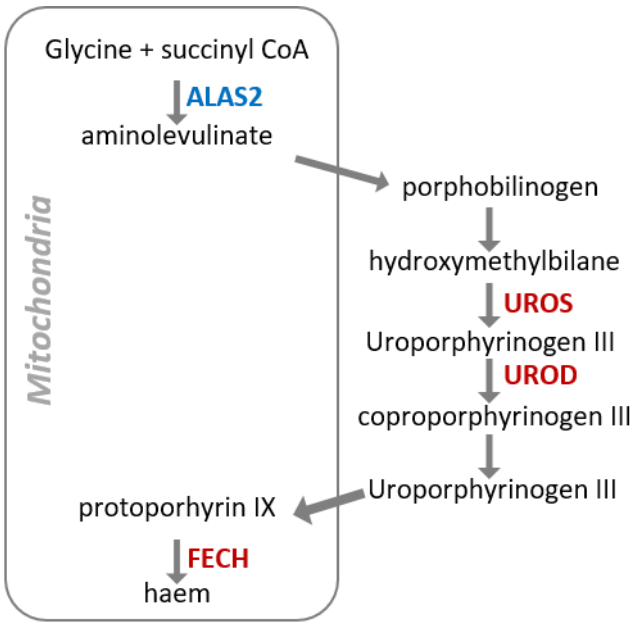

Supplementary Fig. 18 Pathway of haem biosynthesis in developing erythrocytes. Enzymes associated with erythropoietic porphyria are labelled in red, and the proposed therapeutic target via the substrate reduction approach, ALAS2, in blue.

Supplemental References

1. Astner, I., Schulze, J. O., van den Heuvel, J., Jahn, D., Schubert, W. D., and Heinz, D. W. (2005) Crystal structure of 5-aminolevulinate synthase, the first enzyme of heme biosynthesis, and its link to XLSA in humans. *EMBO J* **24**, 3166-3177

2. Kucerova, J., Horvathova, M., Mojzikova, R., Belohlavkova, P., Cermak, J., and Divoky, V. (2011) New mutation in erythroid-specific delta-aminolevulinate synthase as the cause of X-linked sideroblastic anemia responsive to pyridoxine. *Acta Haematol* **125**, 193-197

3. Cui, R., Xu, Z., Qin, T., Zhang, Y., and Xiao, Z. (2014) [Congenital sideroblastic anemia-a new family with identification of K156E mutation of ALAS2 gene and literature review]. *Zhonghua Xue Ye Xue Za Zhi* **35**, 142-146

4. Furuyama, K., Harigae, H., Kinoshita, C., Shimada, T., Miyaoka, K., Kanda, C., Maruyama, Y., Shibahara, S., and Sassa, S. (2003) Late-onset X-linked sideroblastic anemia following hemodialysis. *Blood* **101**, 4623-4624

5. Hurford, M. T., Marshall-Taylor, C., Vicki, S. L., Zhou, J. Z., Silverman, L. M., Rezuke, W. N., Altman, A., and Tsongalis, G. J. (2002) A novel mutation in exon 5 of the ALAS2 gene results in X-linked sideroblastic anemia. *Clin Chim Acta* **321**, 49-53

6. Zhu, P., and Bu, D. (2000) [A novel mutation of the ALAS2 gene in a family with X-linked sideroblastic anemia]. *Zhonghua Xue Ye Xue Za Zhi* **21**, 478-481

7. Moreno-Carralero, M. I., Arrizabalaga-Amuchastegui, B., Sanchez-Calero-Guilarte, J., Morado-Arias, M., Velasco-Valdazo, A. E., de-la-Iglesia-Inigo, S., Mendez, M., and Moran-Jimenez, M. J. (2019) Missense variants in ALAS2 gene in five patients. *Int J Lab Hematol* **41**, e5-e9

8. Fujiwara, T., Fukuhara, N., Ichikawa, S., Kobayashi, M., Okitsu, Y., Onishi, Y., Furuyama, K., and Harigae, H. (2017) A novel heterozygous ALAS2 mutation in a female with macrocytic sideroblastic anemia resembling myelodysplastic syndrome with ring sideroblasts: a case report and literature review. *Ann Hematol* **96**, 1955-1957

9. Cotter, P. D., Rucknagel, D. L., and Bishop, D. F. (1994) X-linked sideroblastic anemia: identification of the mutation in the erythroid-specific delta-aminolevulinate synthase gene (ALAS2) in the original family described by Cooley. *Blood* **84**, 3915-3924

10. Bergmann, A. K., Campagna, D. R., McLoughlin, E. M., Agarwal, S., Fleming, M. D., Bottomley, S. S., and Neufeld, E. J. (2010) Systematic molecular genetic analysis of congenital sideroblastic anemia: evidence for genetic heterogeneity and identification of novel mutations. *Pediatr Blood Cancer* **54**, 273-278

11. May, A., and Bishop, D. F. (1998) The molecular biology and pyridoxine responsiveness of X-linked sideroblastic anaemia. *Haematologica* **83**, 56-70

12. Yu, H. J., Lee, Y. J., Shim, J. W., Kim, D. S., Shim, J. Y., Park, M. S., Woo, H. Y., Park, H., Jung, H. L., and Kwon, M. J. (2018) Mutation Analysis of X-linked Sideroblastic Anemia in a 12-Month-Old Boy by Massively Parallel Sequencing. *Ann Lab Med* **38**, 389-392

13. Furuyama, K., and Sassa, S. (2002) Multiple mechanisms for hereditary sideroblastic anemia. *Cell Mol Biol (Noisy-le-grand)* **48**, 5-10

14. Harigae, H., and Furuyama, K. (2010) Hereditary sideroblastic anemia: pathophysiology and gene mutations. *Int J Hematol* **92**, 425-431

15. Edgar, A. J., Vidyatilake, H. M., and Wickramasinghe, S. N. (1998) X-linked sideroblastic anaemia due to a mutation in the erythroid 5-aminolaevulinate synthase gene leading to an arginine170 to leucine substitution. *Eur J Haematol* **61**, 55-58

16. Ducamp, S., Kannengiesser, C., Touati, M., Garcon, L., Guerci-Bresler, A., Guichard, J. F., Vermylen, C., Dochir, J., Poirel, H. A., Fouyssac, F., Mansuy, L., Leroux, G., Tertian, G., Girot, R., Heimpel, H., Matthes, T., Talbi, N., Deybach, J. C., Beaumont, C., Puy, H., and Grandchamp, B. (2011) Sideroblastic anemia: molecular analysis of the ALAS2 gene in a series of 29 probands and functional studies of 10 missense mutations. *Hum Mutat* **32**, 590-597

17. Cotter, P. D., May, A., Fitzsimons, E. J., Houston, T., Woodcock, B. E., al-Sabah, A. I., Wong, L., and Bishop, D. F. (1995) Late-onset X-linked sideroblastic anemia. Missense mutations in the erythroid delta-aminolevulinate synthase (ALAS2) gene in two pyridoxine-responsive patients initially diagnosed with acquired refractory anemia and ringed sideroblasts. *J Clin Invest* **96**, 2090-2096

18. Furuyama, K., Fujita, H., Nagai, T., Yomogida, K., Munakata, H., Kondo, M., Kimura, A., Kuramoto, A., Hayashi, N., and Yamamoto, M. (1997) Pyridoxine refractory X-linked sideroblastic anemia caused by a point mutation in the erythroid 5-aminolevulinate synthase gene. *Blood* **90**, 822-830

19. Liu, G., Guo, S., Kang, H., Zhang, F., Hu, Y., Wang, L., Li, M., Ru, Y., Camaschella, C., Han, B., and Nie, G. (2013) Mutation spectrum in Chinese patients affected by congenital sideroblastic anemia and a search for a genotype-phenotype relationship. *Haematologica* **98**, e158-160

20. Cotter, P. D., May, A., Li, L., Al-Sabah, A. I., Fitzsimons, E. J., Cazzola, M., and Bishop, D. F. (1999) Four new mutations in the erythroid-specific 5-aminolevulinate synthase (ALAS2) gene causing X-linked sideroblastic anemia: increased pyridoxine responsiveness after removal of iron overload by phlebotomy and coinheritance of hereditary hemochromatosis. *Blood* **93**, 1757-1769

21. Harigae, H., Furuyama, K., Kudo, K., Hayashi, N., Yamamoto, M., Sassa, S., and Sasaki, T. (1999) A novel mutation of the erythroid-specific gamma-Aminolevulinate synthase gene in a patient with non-inherited pyridoxine-responsive sideroblastic anemia. *Am J Hematol* **62**, 112-114

22. Mendez, M., Moreno-Carralero, M. I., Morado-Arias, M., Fernandez-Jimenez, M. C., de la Iglesia Inigo, S., and Moran-Jimenez, M. J. (2016) Sideroblastic anemia: functional study of two novel missense mutations in ALAS2. *Mol Genet Genomic Med* **4**, 273-282

23. Rose, C., Callebaut, I., Pascal, L., Oudin, C., Fournier, M., Gouya, L., Lambilliotte, A., and Kannengiesser, C. (2017) Lethal ALAS2 mutation in males X-linked sideroblastic anaemia. *Br J Haematol* **178**, 648-651

24. Katsurada, T., Kawabata, H., Kawabata, D., Kawahara, M., Nakabo, Y., Takaori-Kondo, A., and Yoshida, Y. (2016) A Japanese family with X-linked sideroblastic anemia affecting females and manifesting as macrocytic anemia. *Int J Hematol* **103**, 713-717

25. Le Rouzic, M. A., Fouquet, C., Leblanc, T., Touati, M., Fouyssac, F., Vermylen, C., Jakel, N., Guichard, J. F., Maloum, K., Toutain, F., Lutz, P., Perel, Y., Manceau, H., Kannengiesser, C., and Vannier, J. P. (2017) Non syndromic childhood onset congenital sideroblastic anemia: A report of 13 patients identified with an ALAS2 or SLC25A38 mutation. *Blood Cells Mol Dis* **66**, 11-18

26. Rivera, C. E., and Heath, A. P. (1999) Identification of a new mutation in erythroid-specific delta-aminolevulinate synthase in a patient with congential sideroblastic anemia. *Blood* **94(Suppl)**, 19b

27. Garcon, L., and Kannengiesser, C. (2014) A double red cells population in a woman with a microcytic anemia. *Blood* **123**, 808

28. Creasey, T., Biss, T., Lambert, J., Smith, F., Clark, B., and Carey, P. (2018) Pyridoxine-sensitive X-linked 'sideroblastic' anaemia in the absence of ring sideroblasts - molecular diagnosis. *Br J Haematol* **180**, 10

29. Bluteau, O., Sebert, M., Leblanc, T., Peffault de Latour, R., Quentin, S., Lainey, E., Hernandez, L., Dalle, J. H., Sicre de Fontbrune, F., Lengline, E., Itzykson, R., Clappier, E., Boissel, N., Vasquez, N., Da Costa, M., Masliah-Planchon, J., Cuccuini, W., Raimbault, A., De Jaegere, L., Ades, L., Fenaux, P., Maury, S., Schmitt, C., Muller, M., Domenech, C., Blin, N., Bruno, B., Pellier, I., Hunault, M., Blanche, S., Petit, A., Leverger, G., Michel, G., Bertrand, Y., Baruchel, A., Socie, G., and Soulier, J. (2018) A landscape of germ line mutations in a cohort of inherited bone marrow failure patients. *Blood* **131**, 717-732

30. Bottomley, S. S., Wise, P. D., Wasson, E. G., and Carpenter, N. J. (1998) X-linked sideroblastic anemia in 10 female probands due to ALAS2 mutations and skewed X chromosome inactivation. *Am J Hum Genet* **63 (Suppl)**, A352

31. Percy, M. J., Cuthbert, R. J., May, A., and McMullin, M. F. (2006) A novel mutation, Ile289Thr, in the ALAS2 gene in a family with pyridoxine responsive sideroblastic anaemia. *J Clin Pathol* **59**, 1002

32. Prades, E., Chambon, C., Dailey, T. A., Dailey, H. A., Briere, J., and Grandchamp, B. (1995) A new mutation of the ALAS2 gene in a large family with X-linked sideroblastic anemia. *Hum Genet* **95**, 424-428

33. Chen, C., Ding, Q., Lu, Y., Dai, J., Wang, X., Xi, X., and Wang, H. (2016) [Genetic diagnosis of a Chinese pedigree with X-Linked sideroblastic anemia: a case report and literature review]. *Zhonghua Xue Ye Xue Za Zhi* **37**, 154-156

34. May, A., Kerr, B. C., Whatley, S. D., and Woolf, J. (2006) The differential diagnosis of inherited sideroblastic anaemia *Haematologica* **91 (s1)**, 24

35. Bottomley, S. S. (2009) Sideroblastic anemias. in *Wintrobe's Clinical Hematology* (Greer, J. P., Foerster, J., Rogers, G. M., Paraskevas, F., Glader, B., Arber, D. A., and Means, R. T. eds.), 12th Ed., Lippincott Williams & Wilkins, Inc, Philadelphia, PA. pp 835-856

36. Sankaran, V. G., Ulirsch, J. C., Tchaikovskii, V., Ludwig, L. S., Wakabayashi, A., Kadirvel, S., Lindsley, R. C., Bejar, R., Shi, J., Lovitch, S. B., Bishop, D. F., and Steensma, D. P. (2015) X-linked macrocytic dyserythropoietic anemia in females with an ALAS2 mutation. *J Clin Invest* **125**, 1665-1669

37. Cox, T. C., Bottomley, S. S., Wiley, J. S., Bawden, M. J., Matthews, C. S., and May, B. K. (1994) X-linked pyridoxine-responsive sideroblastic anemia due to a Thr388-to-Ser substitution in erythroid 5-aminolevulinate synthase. *N Engl J Med* **330**, 675-679

38. Cazzola, M., May, A., Bergamaschi, G., Cerani, P., Rosti, V., and Bishop, D. F. (2000) Familial-skewed X-chromosome inactivation as a predisposing factor for late-onset X-linked sideroblastic anemia in carrier females. *Blood* **96**, 4363-4365

39. Rollon, N., Fernandez-Jimenez, M. C., Moreno-Carralero, M. I., Murga-Fernandez, M. J., and Moran-Jimenez, M. J. (2015) Microcytic anemia in a pregnant woman: beyond iron deficiency. *Int J Hematol* **101**, 514-519

40. Furuyama, K., Uno, R., Urabe, A., Hayashi, N., Fujita, H., Kondo, M., Sassa, S., and Yamamoto, M. (1998) R411C mutation of the ALAS2 gene encodes a pyridoxine-responsive enzyme with low activity. *Br J Haematol* **103**, 839-841

41. Goncalves, P., Pereira, J. C., and Ribeiro, M. L. (2004) Gene symbol: ALAS2. Disease: sideroblastic anaemia. *Hum Genet* **115**, 532

42. Bottomley, S. S., May, B. K., Cox, T. C., Cotter, P. D., and Bishop, D. F. (1995) Molecular defects of erythroid 5-aminolevulinate synthase in X-linked sideroblastic anemia. *J Bioenerg Biomembr* **27**, 161-168

43. Moon, S. Y., Jun, I. J., Kim, J. E., Lee, S. J., Kim, H. K., and Yoon, S. S. (2014) A novel hemizygous I418S mutation in the ALAS2 gene in a young Korean man with X-linked sideroblastic anemia. *Ann Lab Med* **34**, 159-162

44. Aivado, M., Gattermann, N., Rong, A., Giagounidis, A. A., Prall, W. C., Czibere, A., Hildebrandt, B., Haas, R., and Bottomley, S. S. (2006) X-linked sideroblastic anemia associated with a novel ALAS2 mutation and unfortunate skewed X-chromosome inactivation patterns. *Blood Cells Mol Dis* **37**, 40-45

45. Lee, J. S., Gu, J., Yoo, H. J., Koh, Y., and Kim, H. K. (2017) A Novel ALAS2 Mutation Resulting in Variable Phenotypes and Pyridoxine Response in a Family with X-linked Sideroblastic Anemia. *Ann Clin Lab Sci* **47**, 319-322

46. May, A., and Fitzsimons, E. (1994) Sideroblastic anaemia. *Baillieres Clin Haematol* **7**, 851-879

47. Sussman, N. L., Lee, P. L., Dries, A. M., Schwartz, M. R., and Barton, J. C. (2008) Multi-organ iron overload in an African-American man with ALAS2 R452S and SLC40A1 R561G. *Acta Haematol* **120**, 168-173

48. Collins, T. S., and Arcasoy, M. O. (2004) Iron overload due to X-linked sideroblastic anemia in an African American man. *Am J Med* **116**, 501-502

49. Lee, P. L., Reid, T. J., 3rd, Bottomley, S. S., and Barton, J. C. (2011) Sideroblastic anemia, iron overload, and ALAS2 R452S in African-American males: phenotype and genotype features of five unrelated patients. *Am J Hematol* **86**, 787-789

50. Furuyama, K., Harigae, H., Heller, T., Hamel, B. C., Minder, E. I., Shimizu, T., Kuribara, T., Blijlevens, N., Shibahara, S., and Sassa, S. (2006) Arg452 substitution of the erythroid-specific 5-aminolaevulinate synthase, a hot spot mutation in X-linked sideroblastic anaemia, does not itself affect enzyme activity. *Eur J Haematol* **76**, 33-41

51. Barton, J. C., and Lee, P. L. (2006) Disparate phenotypic expression of ALAS2 R452H (nt 1407 G --> A) in two brothers, one with severe sideroblastic anemia and iron overload, hepatic cirrhosis, and hepatocellular carcinoma. *Blood Cells Mol Dis* **36**, 342-346

52. Edgar, A. J., Losowsky, M. S., Noble, J. S., and Wickramasinghe, S. N. (1997) Identification of an arginine452 to histidine substitution in the erythroid 5-aminolaevulinate synthetase gene in a large pedigree with X-linked hereditary sideroblastic anaemia. *Eur J Haematol* **58**, 1-4

53. Donker, A. E., Raymakers, R. A., Nieuwenhuis, H. K., Coenen, M. J., Janssen, M. C., MacKenzie, M. A., Brons, P. P., and Swinkels, D. W. (2014) X-linked sideroblastic anaemia due to ALAS(2) mutations in the Netherlands: a disease in disguise. *Neth J Med* **72**, 210-217

54. Kawakami, T., Nakazawa, H., Kawakami, F., Matsuzawa, S., Sudo, Y., Sakai, H., Nishina, S., Senoo, N., Senoo, Y., Komatsu, M., Umemura, T., Yamaguchi, T., Kosho, T., Fujiwara, T., Harigae, H., and Ishida, F. (2018) [Successful treatment of X-linked sideroblastic anemia with ALAS2 R452H mutation using vitamin B6]. *Rinsho Ketsueki* **59**, 401-406

55. Pereira, J. C., Gutierrez, E. O., and Ribeiro, M. L. (2004) Gene symbol: ALAS2. Disease: sideroblastic anaemia. *Hum Genet* **115**, 533

56. An, W., Zhang, J., Chang, L., Zhang, Y., Wan, Y., Ren, Y., Niu, D., Wu, J., Zhu, X., and Guo, Y. (2015) Mutation analysis of Chinese sporadic congenital sideroblastic anemia by targeted capture sequencing. *J Hematol Oncol* **8**, 55

57. Cotter, P. D., Baumann, M., and Bishop, D. F. (1992) Enzymatic defect in "X-linked" sideroblastic anemia: molecular evidence for erythroid delta-aminolevulinate synthase deficiency. *Proc Natl Acad Sci U S A* **89**, 4028-4032

58. Doshi, B. S., Abramowsky, C., Briones, M., and Bunting, S. T. (2014) Concomitant a novel ALAS2 mutation and GATA1 mutation in a newborn: a case report and review of the literature. *Am J Blood Res* **4**, 41-45

59. Pereira, J. C., Barbot, J., and Ribeiro, M. L. (2009) Novel human pathological mutations. Gene symbol: ALAS2. Disease: sideroblastic anaemia. *Hum Genet* **126**, 333

60. Aguiar, E., Freitas, M. I., and Barbot, J. (2014) Different haematological picture of congenital sideroblastic anaemia in a hemizygote and a heterozygote. *Br J Haematol* **166**, 469

61. Lee, P. L., Barton, J. C., Rao, S. V., Acton, R. T., Adler, B. K., and Beutler, E. (2006) Three kinships with ALAS2 P520L (c. 1559 C --> T) mutation, two in association with severe iron overload, and one with sideroblastic anemia and severe iron overload. *Blood Cells Mol Dis* **36**, 292-297

62. Edgar, A. J., and Wickramasinghe, S. N. (1998) Hereditary sideroblastic anaemia due to a mutation in exon 10 of the erythroid 5-aminolaevulinate synthase gene. *Br J Haematol* **100**, 389-392

63. Cazzola, M., May, A., Bergamaschi, G., Cerani, P., Ferrillo, S., and Bishop, D. F. (2002) Absent phenotypic expression of X-linked sideroblastic anemia in one of 2 brothers with a novel ALAS2 mutation. *Blood* **100**, 4236-4238

64. Bishop, D. F., Tchaikovskii, V., Hoffbrand, A. V., Fraser, M. E., and Margolis, S. (2012) X-linked sideroblastic anemia due to carboxyl-terminal ALAS2 mutations that cause loss of binding to the beta-subunit of succinyl-CoA synthetase (SUCLA2). *J Biol Chem* **287**, 28943-28955

65. Harigae, H., Furuyama, K., Kimura, A., Neriishi, K., Tahara, N., Kondo, M., Hayashi, N., Yamamoto, M., Sassa, S., and Sasaki, T. (1999) A novel mutation of the erythroid-specific delta-aminolaevulinate synthase gene in a patient with X-linked sideroblastic anaemia. *Br J Haematol* **106**, 175-177

CHAPTER 4

THE IMMUNOMETABOLITE ITACONIC ACID INHIBITS ERYTHROID HEME SYNTHESIS AND DIFFERENTIATION AT THE POINT OF AMINOLEVULINATE SYNTHESIS IN STATES OF INFLAMMATORY ANEMIA

4.1 Introduction

Induction of heme biosynthesis is a critical process in differentiating red cell precursors and is ultimately responsible for the production of over 400 billion hemoglobin molecules per second in adult human bone marrow (1). In metazoans, heme production in the erythroid compartment is a committed pathway that consists of eight catalyzed steps, beginning with 5-aminolevulinic acid (ALA) production via the rate-limiting and pyridoxal 5'-phosphate (PLP)-dependent enzyme ALA synthase 2 (ALAS2) and concluding with the insertion of ferrous iron into protoporphyrin IX (PPIX) by the iron-sulfur protein ferrochelatase (FECH) (2) (Figure 1). *ALAS2* is massively upregulated by erythroid-specific factors such as GATA binding factor 1 (GATA1), nuclear factor, erythroid 2 (NFE2), and erythroid Krüppel-like factor (EKLF) (3,4) in the proerythroblast and basophilic stages of development in mice and humans, respectively (5), and subsequently promotes the remaining steps of erythroid differentiation (6-8). Notably, *ALAS2* induction occurs after intimate contacts between a red cell progenitor and central macrophage (CM) are established in an erythroblastic island (EBI) (Figure 1) (9-11). The CM reportedly assists in erythroblast development by inhibiting apoptosis (12), facilitating iron delivery (13-15), and enhancing enucleation by pyrenocytosis (11,16). By affecting iron supply,

the CM indirectly controls porphyrin synthesis in the developing red cells via the iron-responsive element (IRE) present in the *ALAS2* 5'-UTR (17-19). Low cellular iron status has been shown to enhance the binding of iron-responsive protein 1 (IRP1) (20) or IRP2 (21) to the *ALAS2* IRE and inhibit translation.

Several congenital and acquired disorders have been linked to aberrant ALAS2 activity. For example, missense mutations throughout *ALAS2* result in X-linked sideroblastic anemia (XLSA) with associated microcytosis and mitochondrial iron overload due to enzyme loss of function (22,23). Some XLSA mutations occur in the C-terminal domain of eukaryotes and have been linked to disruption of the ALAS2-specific interaction with the succinyl-CoA synthetase (SCS) ATP beta subunit (SUCLA2) (24). In contrast, frameshift mutations in the same region are responsible for PPIX accumulation and photosensitivity caused by gain-of-function ALAS2 in X-linked protoporphyria (XLP) (25-27). A missense substitution of the penultimate residue of ALAS2 has also been found to increase intermediate porphyrin levels during heme synthesis and exacerbate congenital erythropoietic porphyria (CEP), a disease caused by loss-of-function uroporphyrinogen synthase (28).

Most relevant to our work here, microcytosis and loss of ALAS2 activity have been observed in the bone marrow of patients suffering from anemia of chronic disease (ACD) and underlying rheumatoid arthritis (RA) (29). Systemic iron loss resulting from interleukin-6 (IL6) induction of the iron-regulating serum peptide hepcidin during infection (30,31) may serve to restrict iron availability to invading pathogens and could control ALAS2 synthesis and heme iron levels via the inhibitory action of apo-IRPs (21,32). However, ferrokinetic studies in RA patients do not indicate reduced iron supply to bone marrow erythroblasts (33,34), and FECH activity in RA patients is normal (29). This contrasts with what is found in iron-deficiency

anemia (IDA) (35), IRP2 knockout mice with decreased transferrin receptor expression (21), and low cellular iron conditions in general (36), where FECH is thought to be limited by decreased iron-sulfur cofactor assembly. In addition, ALA synthesis is reduced to a far greater magnitude in RA samples of whole bone marrow than in purified erythroblasts (29), suggesting that resident immunoactivated leukocytes contribute to the loss of ALAS2 activity and the corresponding anemia.

In the last decade, multiple studies have revealed that macrophages synthesize itaconic acid (Figure 2A), an α,β-unsaturated carboxylic acid and close analog of succinic acid (Figure 2B) (methylenesuccinic acid), at the outset of an inflammatory response (37-42). Itaconate is generated in millimolar quantities from the TCA cycle intermediate *cis*-aconitate via immune-response gene 1 (IRG1) protein, which highly upregulated by proinflammatory factors such as lipopolysaccharide (LPS) and interferon-gamma (IFNγ) in bone-marrow derived macrophages (BMDMs) (39,41). Importantly, itaconate is secreted by macrophages (38,40,42), including bone marrow-derived macrophages (BMDMs), and has been identified in local tissues during sepsis (40) and in the blood plasma of RA patients (43). Thus it is believed that itaconate has cytokine-like character and impacts mammalian metabolism via autocrine, paracrine, and endocrine processes (44). Such effects could be pro- and/or anti-inflammatory in nature, as described in detail elsewhere (42,43,45-48). For example, itaconate has been shown to consume glutathione on one hand (46) but stimulate the nuclear factor erythroid 2–related factor 2 (NRF2) antioxidant pathway on the other (47), both via Michael addition-like alkylations of sulfur moieties (46,47). Itaconate inhibits SDH activity (41,42,49) and has been associated with succinate-driven stabilization of HIF1α stabilization and proinflammatory interleukin 1-beta (IL1β) production (50). It has also attenuates liver phosphofructokinase 2 (PFK2) activity in

glycolysis (51) and further disrupts the TCA cycle by blocking substrate-level phosphorylation (52). Older publications proposed that itaconate is converted to itaconyl-CoA (Figure 2C) by reverse SCS activity (53,54) with ATP or GTP supplementation, though direct evidence for this was lacking. Itaconyl-CoA has recently demonstrated antimicrobial activity by inactivation of vitamin B_{12} (55). B_{12} can be scavenged by microbes in their host organisms (56), and the suicide inhibition of the B_{12}-dependent methylmalonic acid mutase (MUT) by itaconyl-CoA leads to the accumulation of toxic proprionyl-CoA and may curtail cholesterol-dependent growth of *Mycobacterium tuberculosis* (55,57).

Here we further expand on our previous work showing that itaconate inhibits erythroblast hemoglobin synthesis in an ALA-responsive manner (58). Specifically, we hypothesize that the itaconic acid produced and secreted by bone marrow macrophages during an inflammatory response is converted to itaconyl-CoA in neighboring erythrocyte precursors and controls porphyrin synthesis at the point of ALAS2 catalysis. Moreover, we provide evidence that itaconyl-CoA is produced by a CoA transferase and not SCS in red cell progenitors. We believe this mechanism as a whole is important during chronic conditions of anemia when itaconate has been shown to accumulate.

4.2 Materials and Methods

Reagents

All reagents were obtained from Sigma unless otherwise noted. $^{13}C_5$-itaconic acid was synthesized by the Metabolite Standards Synthesis Core at SRI International, arranged through the NIH Common Funds Metabolomics initiative (59). The biologically active isomer of itaconyl-CoA (3-methylenesuccinyl-CoA) was prepared from recombinant human succinyl-

CoA:glutarate-CoA transferase (SUGCT) using itaconate and succinyl-CoA as substrates. The synthesis reaction was conducted in MOPS-KOH buffer at pH 7.0 and 37ºC for 10 min using 250 μg/mL SUGCT before quenching with formic acid. The resulting mixture containing the itaconyl-CoA product was clarified by centrifugation, and supernatant aliquots were loaded onto a Bridged Ethylene Hybrid (BEH) C18 column in a Waters Acquity UPLC system. Separations were run using a linear mobile phase gradient of ammonium formate and acetonitrile as reported elsewhere (60), and eluting itaconyl-CoA peaks were collected and pooled over multiple injections before spectrophotometric quantitation (260 nm, 16.4 $mM^{-1}cm^{-1}$ extinction coefficient) and freeze-drying.

Cell culture

DS19 murine erythroleukemia (MEL) cells (61,62) were used as erythroblast models and propagated in DMEM/F12 media (Corning) containing 25 mM glucose and 1 mM sodium pyruvate supplemented with 2 mM glutamine, 10% FBS, and 1% penicillin-streptomycin (pen/strep) under a humidified 5% CO_2 atmosphere. Erythroid differentiation of these cells was induced with 1.5% v/v dimethyl sulfoxide (DMSO). Uninduced cells were passaged at 2 x 10^4 cells/mL every 48 h while induced cells were seeded at 5-10 x 10^4 cells/mL and cultured in DMSO media for 72 h. Select differentiating cultures were treated with 1 mM $^{13}C_5$-labeled itaconate or 2.5 mM unlabeled itaconate as indicated.

A stable DS19 MEL cell line overexpressing human ALAS2 (DS19-ALAS2) was created and used to test the effects of 2.5 mM itaconate on the elevated levels of porphyrins produced by these cells. Human ALAS2 was subcloned from pMAL-c2AE2 (gift of David Bishop) into the pEF1a vector (gift of Alan Cantor) as previously described (63) to generate a construct with an amino terminal FLAG tag after the ALAS2 mitochondrial targeting sequence (MTS).

Heme and porphyrin analysis

MEL cells treated with or without 2.5 mM unlabeled itaconate and 1.5% DMSO were analyzed in quadruplicate (n=4 biological replicates) for heme and porphyrins by HPLC as reported previously (64). Briefly, 50-200 million cells from each replicate were washed in PBS and pelleted before snap freezing and storage at -80°C. Thawed 100 μL samples were sonicated and extracted with either 3 M HCl for 1 h at 37ºC (for porphyrin intermediates) or a 1:4 volume ratio of glacial acetic acid and ethyl acetate mixture (for heme and PPIX) and then centrifuged. Intermediate porphyrins were measured by HPLC analysis of the supernatant in the clarified HCl mixture. Heme and PPIX levels were quantitated from the upper (organic layer) of the acetic acid-ethyl acetate mixture. Molar quantities were normalized to protein in all samples.

Fluorescence scans of 200 μL media samples from uninduced DS19-hsALAS2 cells treated with 2.5 mM itaconate over 72 h were conducted in triplicate (n=3 biological replicates) on a microplate reader and subsequently quantitated at 405/10 nm excitation and 630/40 nm emission. Media were harvested and clarified of cells by centrifugation and filtration. Raw relative fluorescence units (RFUs) were corrected by background subtraction (same media incubated without cells) and normalization to cell counts (Scepter 2.0 from EMD Millipore).

Metabolomics

LC- and GC-MS were implemented as described in previous work (58) in a targeted metabolomic analysis of intra- and extracellular compounds from MEL cell cultures under various conditions as indicated (n=4 biological replicates). Collected output signals represent Area Under the Curve (AUC) values normalized to both total signal and cell counts. LC-MS was employed to trace 1 mM $^{13}C_5$-itaconate metabolism and primarily determine the impact of itaconate on levels of associated CoA derivatives in DMSO-induced MEL cells. GC-MS data

were gathered for cell pellet and culture media samples and were used to assess small-molecule effects of 2.5 mM itaconate on differentiating MEL cell metabolism. Specifically, metabolites associated with glycolysis, the TCA cycle, amino acid metabolism, and odd-chain fatty acid oxidation were targeted.

Bioinformatics

UniProtKB (65) and the National Center for Biotechnology Information (NCBI) were used to blast the amino acid sequence of the *Pseudomonas aeruginosa* itaconyl-CoA transferase (PaIct) to search for a human CoA transferase homolog. BLASTp from NCBI was configured for pairwise amino acid alignment to quantitate sequence homology. The alignment figure was prepared using T-Coffee freeware (66).

Expression and purification of recombinant enzymes

The cDNA encoding mitochondrial human ALAS2 (AA79-587) and SUGCT (AA39-445) were subcloned into the pET28a vector (Novagen) downstream of an in-frame N-terminal His_6-tag using NheI and BamHI sites for the ALAS2 (pET-A79) plasmid and NheI and HindIII sites for SUGCT (pET-SUGCT). The pET-A79 and pET-SUGCT plasmids were transformed into BL21(DE3) competent cells (New England Biologicals), and single-colony inoculations were induced at an OD_{600} of 0.5-0.7 with 0.1 mM IPTG for 16-18 h at 12°C and 18°C, respectively. Culture pellets were stored at -80°C until purification. After thawing, protein was resuspended in ice-cold solubilization buffer consisting of 50 mM Tris-HCl, pH 8.0, 20 μM PLP, 100 mM KCl, 10% glycerol, and 0.2% Tween-20. Mixtures were then sonicated in the presence of 0.5 mM phenylmethylsulfonyl fluoride (PMSF) to minimize proteolysis during cell lysis. Proteins in the lysate were subsequently batch purified on HisPur Cobalt Resin (Thermo Scientific) and washed with solubilization buffer containing 0.5 mM PMSF and 15 mM

imidazole at 4ºC. Elutions in 250 mM imidazole were buffer exchanged over Sephadex G-25 spin columns at 4ºC to > 90% purity (SDS-PAGE). Final protein concentrations were determined with the Pierce BCA Assay Kit (Thermo Scientific).

Human SCS-A was prepared by subcloning mature SUCLA2 and SUCGL1 cDNA (DNASU) into pET14b NdeI and BamHI sites and pET28a NheI and BamHI sites, respectively, followed by cotransformation of the two constructs (pET14b-SUCLA2) and pET28a-SUCGL1) into BL21(DE3) cells. Single-colony inoculations were induced as was done for pET-A79 and pET-SUGCT plasmids, except that cultures were grown overnight at 22°C before harvest and freezing of cell pellets. Thawed pellets were solubilized in 50 mM Tris-HCl, pH 8.0, 300 mM KCl, 10% glycerol, 0.2% Tween-20, and 1 mM PMSF, with sonication and SCS-A protein was isolated by batch affinity purification on HisPur Cobalt Resin. The resin was washed with solubilization buffer including 2 mM Mg-ATP to eliminate DnaK contamination. After elution in 250 mM imidazole, protein was concentrated with buffer exchange (to solubilization buffer alone) using an Amicon 30K Centrifugal Filter (EMD Millipore). Protein concentrations were determined by BCA analysis.

Spectrophotometric assays and kinetics

Discontinuous colorimetric ALAS activity assays were conducted with derivatized ALA detection via Ehrlich's modified reagent as previously described (67), except with microscale modifications. Reaction mixtures were 175 μL in volume and consisted of 50 mM potassium phosphate buffer, pH 7.4, 50 μM PLP, 1 mM DTT, 10 mM $MgCl_2$, 50 mM glycine, various concentrations of succinyl-CoA, and 2-4 μg/mL purified human ALAS2 (hsALAS2) enzyme. After incubation at 37°C for 15 minutes (checked for linear ALA formation with applied enzyme

concentrations), reactions were terminated with 100 μL of 15% w/v trichloroacetic acid (TCA) and then centrifuged at 13,000 x g for 5 min to remove protein. Supernatant volumes of 240 μL were added to 260 μL of freshly prepared 1:12 v/v mixtures of acetylacetone:1 M sodium acetate, pH 4.7, and boiled for 10 min to derivatize the ALA product. Samples were cooled and 150 μL aliquots per reaction were combined with 150 μL modified Ehrlich's reagent (300 μL total) and monitored at 554 nm every 60 s in a CLARIOstar microplate reader (BMG Labtech). Absorbance values collected after 5-10 minutes were converted to molar quantities of ALA using an extinction coefficient of 60.4 mM^{-1} cm^{-1}. For inhibition studies, K_i and mode of inhibition were determined by titrating 10-200 μM succinyl-CoA in the presence of 50 mM glycine substrate and 0, 200, and 1000 μM itaconyl-CoA. Michaelis-Menten nonlinear regression analysis was subsequently carried out on data for three separate protein preparations (three biological replicates) with Prism software (GraphPad 8.4).

Pig heart SCS-G (Sigma) and recombinant SCS-A were assayed for reverse activity (GTP or ATP consumption as appropriate) with succinate and/or itaconate as substrates using a direct spectrophotometric assay for CoA ester bond formation at 225-235 nm (68). Reaction mixtures included 10-50 mM neutralized succinate and/or variable itaconate concentrations with 0.1 mM CoA, 0.1 mM GTP or ATP, 1 mM $MgCl_2$, and 2.5 μg/mL SCS-G or SCS-A at room temperature in potassium phosphate or Tris buffer, pH 7.4, respectively. Reactions were monitored in 1-mL volumes on a Cary 1G UV-Vis spectrophotometer (Varian) or in 300-μL volumes on the microplate reader. Assays were conducted in duplicate or triplicate.

HPLC assays of CoA transferase activity

SUGCT activity was determined as reported in the literature (69) with minor changes. Briefly, 400 μL reaction mixtures were prepared containing 2 mM itaconate, 0.2 mM succinyl-

CoA, and 2 μM purified enzyme in 50 mM Na-HEPES buffer, pH 7.2, at 30ºC. After 3 min, 150 μL reaction aliquots were quenched with 15 μL of 20% formic acid and diluted further with 150 μL H_2O. Mixtures were clarified at 20,000xg for 15 min before 20 μL aliquots were injected into an Agilent 1220 Infinity LC HPLC equipped with a 100 mm x 4.6 mm Poroshell 120 EC-C18 column (2.7 μm particle size) at 30ºC. Itaconyl-CoA, succinyl-CoA, and CoA peaks were detected at 260 nm upon elution and identified against standards loaded in the same background without enzyme. Experiments were conducted in duplicate (n=2 biological replicates).

Immunoblotting

Mitochondria from MEL cells treated with and without DMSO and 2.5 mM itaconate for 72 h were isolated using the reagent-based protocol from the Pierce Mitochondrial Isolation Kit (Thermo Scientific). Two biological replicates (n=2) were prepared for each condition. Protein levels were quantitated with the Pierce BCA Protein Assay Kit (Thermo Scientific), and 20 μg samples boiled in Laemmli buffer were loaded into wells on Mini-PROTEAN Stain-Free polyacrylamide gels (Bio-Rad). Protein bands were detected using the ChemiDoc MP imaging system (Bio-Rad) and ImageLab software (version 5.1, Bio-Rad). Immunoblotting was carried out by transferring gel bands to low-fluorescence PVDF membrane (Bio-Rad), followed by blocking the membrane in 2% BSA at room temperature for 1 h. Membranes were incubated in 1:2,000 rabbit polyclonal hsALAS2 (custom-made), 1:5,000 rabbit polyclonal hsFECH (custom-made) and 1:1,000 rabbit polyclonal SUGCT (Novus Biologicals) primary antibodies in 1% BSA overnight at 4ºC. After extensive washing in TBST, membranes were placed in dilutions of 1:50,000 Pierce fluorescent donkey anti-rabbit IgG (Dylight 650) secondary antibody (Thermo Scientific) before washing again and imaging on the ChemiDoc system.

Statistics

Statistical significance was determined for experiments with n > 2 biological replicates based on $\alpha = 0.05$ unless otherwise noted. Regression analysis of kinetic ALAS2 data were carried out on the Prism software (GraphPad 8.4). One- or two-way ANOVA analysis or Student's t-tests were conducted with Bonferroni correction for multiple comparisons (to control for Type I errors) for LC-MS and other data as indicated. GC-MS metabolomic data for MEL samples (n=4) were analyzed using MetaboAnalystR (70) and included partial least squares discriminant analysis (PLS-DA) based on PCA analysis, volcano plotting (α=0.01 and fold-change > 2.0), and heat mapping of the 25 most discriminatory metabolites (t-test on groups treated with or without itaconate).

4.3 Results

Itaconate decreases heme and porphyrin synthesis in erythroid precursors

We have previously shown that the inflammatory metabolite itaconic acid attenuates hemoglobin production in an ALA-responsive fashion in MEL cells (58). Here we demonstrate that heme, PPIX, and intermediate porphyrin levels are significantly decreased during MEL cell differentiation in the presence of itaconate (Figures 3A-D), indicating that inhibition occurs upstream of uroporphyrinogen decarboxylase (UROD) catalysis in the heme synthesis pathway (Figure 1). We have also examined the effects of itaconate on transgenic MEL cells overexpressing hsALAS2. These cells normally will exhibit porphyrin-based fluorescence resulting from the excess production of ALA. However this fluorescence is reduced (Figure 3E) by itaconate treatment. In agreement with the literature (71), we verified that medium from itaconate-producing RAW264.7 macrophage cultures decreases heme levels in MEL cells (Figure S1A).

In agreement with our MEL cell data (58), hemoglobin production in EPO-induced human TF1 cells is diminished with itaconate and can be rescued by ALA (Figure S1B). Additionally, we noticed a significant increase in cell proliferation with itaconate. TF1 cells express the succinate cognate G-protein coupled receptor 91 (GPR91, or SUCNR1) (72), which is not expressed in MEL cells (73) or erythroid-differentiated $CD34^+$ cells (74). Because SUCNR1 is sensitive to itaconate (75) and known to stimulate ERK signaling, we added combinations of itaconate and the SUCNR1 antagonist compound 4c (gift of Xin Li) or MEK inhibitor U0126 to differentiating TF1 cultures to interrogate the impact of the SUCNR1-MAPK/ERK pathway on differentiation. The inhibitors independently rescued hemoglobin levels and proliferation rates measured in control cells, suggesting that the observed decrease in hemoglobinization is at least partially due to nonspecific itaconate binding to SUCNR1 and the associated increase in TF1 cell proliferation via the SUCNR1-ERK signaling axis (72) (Figure S2A, S2B).

Itaconate is imported by erythroid precursors and converted to itaconyl-CoA

Metabolomic tracing of uniformly-labeled ($^{13}C_5$)-itaconate in DMSO-induced MEL cultures resulted in the intracellular accumulation of the same species (Figures 4A, 5A, S3A, S4A). Mitochondrial itaconate transporters including SLC25A10 (succinate) and SLC25A1 (citrate) have been identified *in vitro* (47). While these proteins are expressed at significant levels in erythroid-differentiating MEL (73) and $CD34^+$ cells (74), their plasmalemmal counterparts are not. To date a cell-surface itaconate transporter has not been identified in any mammalian cell type (76). Interestingly, differentiating MEL cells treated with $^{13}C_5$-itaconate accumulated $^{13}C_5$-itaconyl-CoA as well (Figure 4B), demonstrating that these cells have the capacity to convert itaconate directly to itaconyl-CoA.

Itaconyl-CoA is produced from itaconate via SUGCT but not SCS

Indirect evidence from approximately half a century ago suggested that itaconate is converted to itaconyl-CoA by SCS (53,54) and in the absence of definitive data it has been assumed by others to occur in this fashion (52,60). We examined this question experimentally and found that neither ATP- nor GTP-specific SCS is able to utilize itaconate under the same conditions as succinate *in vitro* (Figures 6A, 6B, S5A, S5B) and that SCS activity is inhibited by itaconate in a dose-dependent manner (Figure 6C).

Pseudomonas aeruginosa itaconyl-CoA transferase (PaIct) is a protein that has been shown to be capable of generating itaconyl-CoA from itaconate without nucleotides. Using a bioinformatics approach, we found that mammalian succinyl-CoA:glutarate-CoA transferase (SUGCT) (encoded by the *C7ORF10* gene) is a homolog of PaIct with ~30% sequence identity and ~50% similarity (Figure 7A). Others have demonstrated SUGCT activity with the canonical substrate glutaryl-CoA (69). We cloned, expressed, and isolated recombinant SUGCT and determined that it effectively catalyzes the production of itaconyl-CoA using succinyl-CoA as well (Figure 7B). In agreement with transcript data in MEL cells (73), immunoblotting showed that SUGCT protein is present at similar levels in mitochondria isolated from DMSO-induced and -uninduced MEL cells (Figure 7C).

Itaconate impacts flux through the erythroblast TCA cycle and glycolytic shunts

Chromatographic MS analysis of differentiating MEL cells treated with 1 mM $^{13}C_5$-itaconate or 2.5 mM unlabeled itaconate indicated that TCA-cycle metabolite levels deviated significantly from untreated controls. Specifically, succinate (Figures 4C, 5A, 5B, S3A, S4A, S4B) and succinyl-CoA (Figure 4D) were elevated in itaconate-treated cultures. Neither was labeled by $^{13}C_5$-itaconate. Succinate was particularly high, which is not surprising given the

established direct inhibitory action of itaconate on SDH in other cell types (41,42). Fumarate increased as well with itaconate (Figure 5A) despite putative SDH inhibition. The α-ketoglutarate derivative 2-hydroxyglutarate (Figures 5A, S3A, S4A, S4B) also accumulated, and increased glutamic acid was found in the media (Figure S4B). Both of these observations may be due to product inhibition of α-ketoglutarate dehydrogenase (αKGDH) by succinyl-CoA (77).

Our results also suggest that glycolysis is disrupted by itaconate during terminal erythropoiesis. Intermediates of glycolytic shunts such as the pentose phosphate and serine-glycine synthesis pathways increased compared to controls, including AMP (Figure 4E), adenosine and thymine (Figure 5A), serine (Figures 5A, 5B, S3A, S3B, S4A, S4B) and glycine (Figure S4A). Glutathione levels were also elevated (Figures 5B, S4B), which was unexpected since itaconate has been reported to directly alkylate glutathione in LPS-activated macrophages (46). Myoinositol (Figures 5A, S3A, S4A) and inositol (Figure 4F), products of glucose-6-phosphate metabolism, increased with itaconate as well. Allosteric inhibition of the glycolysis-activating phosphofructokinase 2 (PFK2) by itaconate, a phosphoenolpyruvate (PEP) analog, has been described in the liver (51) could also explain these observations in our differentiating erythroid progenitors.

Itaconate impairs metabolism of amino acids and fatty acid oxidation compounds

It is well established that aliphatic amino acids and odd-chain fatty acids are ultimately catabolized to propionyl-CoA and then methylmalonyl-CoA by propionyl-CoA carboxylase (PCC) and B_{12}-dependent methylmalonyl-CoA mutase (MUT), respectively. Further metabolomic data gathered here indicate that flux through these pathways is attenuated in differentiating erythroblast cultures treated with itaconate, likely via itaconyl-CoA and its ability to inactivate B_{12} and MUT activity as previously discussed in adipocytes (55) and macrophages

(57). We found increased levels of propionyl-CoA (Figure 4G), propionyl-carnitine (Figure 4H), and methylmalonic acid (Figures 5A, 5B, S3A, S3B, S4A, S4B) with itaconate treatment. Upstream of propionyl-CoA, we measured elevations in the odd-chain fatty acids heptadecanoic acid (Figures 5A, S4A) and nonanoic acid (Figure S4B), as well as the aliphatic amino acids threonine, valine, methionine, and isoleucine (Figures S4A, S4B). Notably, itaconyl-CoA accumulations may also explain increased pyruvate and glyoxylate levels (Figures 5B, S3B, S4B). Itaconyl-CoA is an alternative substrate of methylglutaconase (MGTK) and is converted by this enzyme to citramalyl-CoA (54,55). It is therefore reasonable to believe that citramalyl-CoA lyase (CLYBL) catalyzes the cleavage of citramalyl-CoA to pyruvate and acetyl-CoA (54) in lieu of metabolizing glyoxylate (78).

Itaconyl-CoA inhibits ALAS2

Itaconyl-CoA (Figure 2C) is a close analog of succinyl-CoA (Figure 2D) and therefore may impact ALAS2 enzyme activity and contribute to the increase in succinyl-CoA in induced MEL cells (Figure 4D). To investigate this, we carried out a comprehensive steady-state kinetic analysis of recombinant hsALAS2 using a modified discontinuous colorimetric assay protocol (67). Assay data revealed itaconyl-CoA to be a competitive inhibitor of recombinant hsALAS2 with a K_i of 100 ± 20 μM (Figures 8A, 8B). The measured K_m of succinyl-CoA of 10 ± 2 μM for the uninhibited enzyme agrees with the literature for the mammalian enzyme (24,27,67,79,80). We further showed that itaconate is not an inhibitor of ALAS2 (Figure S6A). Continuous coupled ALAS assays were also carried out because ALA derivatives synthesized from alternative acyl-CoA substrates have unpredictable stability in the α-aminoketone formed via reaction with acetylacetone in the discontinuous assay protocol (67). Results of the coupled

assays indicate that itaconyl-CoA is not an alternative ALAS2 substrate even at millimolar concentrations (Figure S6B).

4.4 Discussion

Itaconate is an antimicrobial compound whose impact on mammalian liver metabolism was first explored in the 1940s (53,81,82). Itaconate has recently been identified as a product of IRG1 catalysis in immunoactivated macrophages (39-42) that manifests cytokine-like properties once secreted (44). Importantly, measurable quantities of itaconate have been found in bronchial lavages of patients with severe lung infections (40) and in blood plasma of RA patients (43). Experiments examining the impact of RA on the erythroid compartment have shown diminished ALAS2 activity in microcytic red cell precursors, most significantly in the context of whole bone marrow samples containing immunoactivated leukocytes such as BMDMs (29). We provide evidence here that itaconate has a significant impact on the erythroid compartment (Figures 8, S7).

Based upon the results of this study, we propose that itaconate negatively alters heme biosynthesis and erythroid differentiation at the point of ALAS2 catalysis in the context of an inflammatory EBI. Specifically, we have determined that heme, PPIX, and intermediate porphyrin levels are decreased in MEL cells differentiated in the presence of itaconate or media from immunoactivated, itaconate-generating macrophages. Addition of ALA to itaconate-treated cultures rescues hemoglobinization as described previously (58). Carbon-13 tracing data show that itaconate is imported by differentiating MEL cells and is subsequently metabolized to itaconyl-CoA. Levels of succinyl-CoA are also increased in these cells with itaconate supplementation, suggesting that ALAS2 is directly affected. Indeed, our kinetic assays

demonstrated that itaconyl-CoA is a competitive inhibitor of ALAS2 without acting as an alternative substrate.

An alternative explanation for decreased ALAS2 activity in inflammatory states such as ACD is that systemic iron is sequestered via hepcidin (30,31) and could thus downregulate ALAS2 synthesis via the IRE-IRP system. However, the effects of hepcidin on systemic iron levels may lag behind the induction of *IRG1* and itaconate synthesis that occurs at the beginning of an inflammatory response. Additionally, erythroblast iron delivery during terminal erythropoiesis bypasses the cytosolic iron pool for IRPs, and IRP numbers in general appear to be overwhelmed late in erythroid differentiation when heme synthesis is massively upregulated (83). A more recent study has verified low levels of IRP1 and IRP2 relative to ALAS2 at the basophilic erythroblast stage in mice and has provided evidence that heme-regulated eukaryotic initiation factor 2 alpha (eIF2α) kinase (HRI) predominantly controls hemoglobin synthesis in both iron-replete and -deficient conditions in these cells (84). Perhaps most significantly, ferrokinetic data from RA patients do not indicate reduced iron supply to marrow erythroblasts (33,34) and suggest that iron may not significantly regulate ALAS2 in this disease state. Iron-dependent FECH activity is also unaffected in these cells (29). We therefore postulate that itaconate plays a significant role in ACD by inhibiting ALAS2 catalysis in the bone marrow during an inflammatory response.

Additional data also support many of the previously substantiated effects of itaconate on glycolysis (51), B_{12} metabolism (55,57), and the TCA cycle (39,41,42) in other tissues (Figure S7). For example, we see increases in compounds such as inositol as well as products of the pentose phosphate and serine-glycine synthesis pathways, possibly due to allosteric inhibition of PFK2 (51). Elevated levels of aliphatic amino acids (e.g., valine), odd-chain fatty acids (e.g.,

heptadecanoic acid), and propionyl-CoA metabolites suggest that itaconyl-CoA compromises B_{12} constitution in erythroblasts and irreversibly inhibits the MUT enzyme as seen in adipocytes and immunoactivated macrophages (55,57). In addition to succinyl-CoA, elevations in succinate and fumarate were also observed with itaconate treatment. It is tempting to postulate that succinate accumulation is caused by itaconate-driven inhibition of SDH and accounts for succinyl-CoA production via the reverse SCS reaction. However, this does not justify the increase in fumarate. We also demonstrated *in vitro* that itaconate inhibits reverse SCS activity and is not converted to itaconyl-CoA by SCS as proposed by others (52-54). Instead, bioinformatic and immunoblotting data suggest that exogenous itaconate is derivatized to itaconyl-CoA by SUGCT in red cell progenitors. Additionally, we now know that succinate contributes very little to the supply of heme carbon during erythroid differentiation and that succinyl-CoA used for heme synthesis is supplied primarily through a separate pool of αKGDH acting outside of the TCA cycle (58). ALAS2 inhibition thus provides a valid explanation for both increased succinyl-CoA and decreased porphyrin synthesis when erythroid precursors are exposed to itaconate.

Despite the many findings of this study, additional questions regarding the impacts of itaconate *in vivo* remain. For instance, erythroblast and macrophage studies here were limited to immortalized cell lines. While investigation of itaconate effects in immune-stimulated EBI cultures would be ideal, colonization of these cells while maintaining their *in vivo* integrity is not straightforward (85,86). The differentiation of murine $Ter119^+$ or human $CD34^+$ erythroid precursors in co-cultures with LPS-stimulated BMDMs or $CD14^+$-derived M2c-like cells (87), respectively, would be a logical next step to improve our understanding of itaconate in this complex system. Current knowledge of itaconate transport is limited to mitochondrial succinate, α-ketoglutarate, and citrate carriers from the SLC25 family (47). The corresponding plasma-

membrane SLC13 transporters are not expressed in MEL cells (73) or EPO-induced $CD34^+$ cells (74), and so additional means of itaconate cell entry necessitate exploration. As our data from EPO-induced TF1 cell experiments indicate, the cell-surface succinate receptor SUCNR1 previously investigated during hematopoiesis (72) also merits further attention. Additionally, the contributions of SCS, SUGCT, or other CoA transferases such as malonyl-CoA synthetase (88) to the synthesis of itaconyl-CoA in developing red cells are unknown. Protein complexes in the TCA cycle (89), glycolysis (90), fatty acid oxidation (91), and heme synthesis (63), may also be involved in itaconate metabolism and should be explored, including the well-established ALAS2-SUCLA2 interaction (24,92).

Finally, the precise mechanism of ALAS2 enzyme modulation by itaconate and the therapeutic benefits of this immunometabolite are yet to be elucidated. We have recently crystallized hsALAS2 and have proposed an autoinhibitory mechanism for the eukaryotic-specific C-terminal extension (27) that may be impacted by itaconyl-CoA. Surface plasmon resonance (SPR) and bilayer interferometry (BLI) experiments are currently under way to precisely characterize the binding of itaconyl-CoA to ALAS2. Itaconate cysteine residue alkylation (i.e., itaconylation) has been demonstrated in macrophages (47) and should thus be examined in ALAS2 and its associated protein complexes. Importantly, ALAS2 is a valuable drug target under conditions where cytotoxic porphyrins accumulate. Tissue-specific delivery of itaconate to the erythroid compartment could potentially serve to mitigate porphyrin synthesis in diseases such as XLP or cancer patients prescribed kinase inhibitors known to inhibit FECH and elicit porphyria symptoms (93).

4.5 References

1. Harris, J. W. (1994) X-linked, pyridoxine-responsive sideroblastic anemia. *N Engl J Med* **330**, 709-711

2. Phillips, J. D. (2019) Heme biosynthesis and the porphyrias. *Mol Genet Metab* **128**, 164-177

3. Ferreira, G. C., Andrew, T. L., Karr, S. W., and Dailey, H. A. (1988) Organization of the terminal two enzymes of the heme biosynthetic pathway. Orientation of protoporphyrinogen oxidase and evidence for a membrane complex. *J Biol Chem* **263**, 3835-3839

4. Kramer, M. F., Gunaratne, P., and Ferreira, G. C. (2000) Transcriptional regulation of the murine erythroid-specific 5-aminolevulinate synthase gene. *Gene* **247**, 153-166

5. An, X., Schulz, V. P., Li, J., Wu, K., Liu, J., Xue, F., Hu, J., Mohandas, N., and Gallagher, P. G. (2014) Global transcriptome analyses of human and murine terminal erythroid differentiation. *Blood* **123**, 3466-3477

6. Lake-Bullock, H., and Dailey, H. A. (1993) Biphasic ordered induction of heme synthesis in differentiating murine erythroleukemia cells: role of erythroid 5-aminolevulinate synthase. *Mol Cell Biol* **13**, 7122-7132

7. Nakajima, O., Takahashi, S., Harigae, H., Furuyama, K., Hayashi, N., Sassa, S., and Yamamoto, M. (1999) Heme deficiency in erythroid lineage causes differentiation arrest and cytoplasmic iron overload. *EMBO J* **18**, 6282-6289

8. Brownlie, A., Donovan, A., Pratt, S. J., Paw, B. H., Oates, A. C., Brugnara, C., Witkowska, H. E., Sassa, S., and Zon, L. I. (1998) Positional cloning of the zebrafish sauternes gene: a model for congenital sideroblastic anaemia. *Nat Genet* **20**, 244-250

9. Chasis, J. A., and Mohandas, N. (2008) Erythroblastic islands: niches for erythropoiesis. *Blood* **112**, 470-478

10. Astwood, E., and Vora, A. (2011) Erythroblastic islands. *Blood* **117**, 10

11. Yeo, J. H., Lam, Y. W., and Fraser, S. T. (2019) Cellular dynamics of mammalian red blood cell production in the erythroblastic island niche. *Biophys Rev* **11**, 873-894

12. Rhodes, M. M., Kopsombut, P., Bondurant, M. C., Price, J. O., and Koury, M. J. (2008) Adherence to macrophages in erythroblastic islands enhances erythroblast proliferation and increases erythrocyte production by a different mechanism than erythropoietin. *Blood* **111**, 1700-1708

13. Iacopetta, B. J., and Morgan, E. H. (1983) The kinetics of transferrin endocytosis and iron uptake from transferrin in rabbit reticulocytes. *J Biol Chem* **258**, 9108-9115

14. Sheftel, A. D., Zhang, A. S., Brown, C., Shirihai, O. S., and Ponka, P. (2007) Direct interorganellar transfer of iron from endosome to mitochondrion. *Blood* **110**, 125-132

15. Kafina, M. D., and Paw, B. H. (2017) Intracellular iron and heme trafficking and metabolism in developing erythroblasts. *Metallomics* **9**, 1193-1203

16. Yoshida, H., Kawane, K., Koike, M., Mori, Y., Uchiyama, Y., and Nagata, S. (2005) Phosphatidylserine-dependent engulfment by macrophages of nuclei from erythroid precursor cells. *Nature* **437**, 754-758

17. Cox, T. C., Bawden, M. J., Martin, A., and May, B. K. (1991) Human erythroid 5-aminolevulinate synthase: promoter analysis and identification of an iron-responsive element in the mRNA. *EMBO J* **10**, 1891-1902

18. Dandekar, T., Stripecke, R., Gray, N. K., Goossen, B., Constable, A., Johansson, H. E., and Hentze, M. W. (1991) Identification of a novel iron-responsive element in murine and human erythroid delta-aminolevulinic acid synthase mRNA. *EMBO J* **10**, 1903-1909

19. Melefors, O., Goossen, B., Johansson, H. E., Stripecke, R., Gray, N. K., and Hentze, M. W. (1993) Translational control of 5-aminolevulinate synthase mRNA by iron-responsive elements in erythroid cells. *J Biol Chem* **268**, 5974-5978

20. Wang, Y., Langer, N. B., Shaw, G. C., Yang, G., Li, L., Kaplan, J., Paw, B. H., and Bloomer, J. R. (2011) Abnormal mitoferrin-1 expression in patients with erythropoietic protoporphyria. *Exp Hematol* **39**, 784-794

21. Cooperman, S. S., Meyron-Holtz, E. G., Olivierre-Wilson, H., Ghosh, M. C., McConnell, J. P., and Rouault, T. A. (2005) Microcytic anemia, erythropoietic protoporphyria, and neurodegeneration in mice with targeted deletion of iron-regulatory protein 2. *Blood* **106**, 1084-1091

22. Cotter, P. D., Baumann, M., and Bishop, D. F. (1992) Enzymatic defect in "X-linked" sideroblastic anemia: molecular evidence for erythroid delta-aminolevulinate synthase deficiency. *Proc Natl Acad Sci U S A* **89**, 4028-4032

23. Bottomley, S. S., May, B. K., Cox, T. C., Cotter, P. D., and Bishop, D. F. (1995) Molecular defects of erythroid 5-aminolevulinate synthase in X-linked sideroblastic anemia. *J Bioenerg Biomembr* **27**, 161-168

24. Bishop, D. F., Tchaikovskii, V., Hoffbrand, A. V., Fraser, M. E., and Margolis, S. (2012) X-linked sideroblastic anemia due to carboxyl-terminal ALAS2 mutations that cause loss of binding to the beta-subunit of succinyl-CoA synthetase (SUCLA2). *J Biol Chem* **287**, 28943-28955

25. Whatley, S. D., Ducamp, S., Gouya, L., Grandchamp, B., Beaumont, C., Badminton, M. N., Elder, G. H., Holme, S. A., Anstey, A. V., Parker, M., Corrigall, A. V., Meissner, P. N., Hift, R. J., Marsden, J. T., Ma, Y., Mieli-Vergani, G., Deybach, J. C., and Puy, H. (2008) C-terminal deletions in the ALAS2 gene lead to gain of function and cause X-

linked dominant protoporphyria without anemia or iron overload. *Am J Hum Genet* **83**, 408-414

26. Balwani, M. (2019) Erythropoietic Protoporphyria and X-Linked Protoporphyria: pathophysiology, genetics, clinical manifestations, and management. *Mol Genet Metab* **128**, 298-303

27. Bailey, H. J., Bezerra, G. A., Marcero, J. R., Padhi, S., Foster, W. R., Rembeza, E., Roy, A., Bishop, D. F., Desnick, R. J., Bulusu, G., Dailey, H. A., Jr., and Yue, W. W. (2020) Human aminolevulinate synthase structure reveals a eukaryotic-specific autoinhibitory loop regulating substrate binding and product release. *Nat Commun* **11**, 2813

28. To-Figueras, J., Ducamp, S., Clayton, J., Badenas, C., Delaby, C., Ged, C., Lyoumi, S., Gouya, L., de Verneuil, H., Beaumont, C., Ferreira, G. C., Deybach, J. C., Herrero, C., and Puy, H. (2011) ALAS2 acts as a modifier gene in patients with congenital erythropoietic porphyria. *Blood* **118**, 1443-1451

29. Houston, T., Moore, M., Porter, D., Sturrock, R., and Fitzsimons, E. (1994) Abnormal haem biosynthesis in the chronic anaemia of rheumatoid arthritis. *Ann Rheum Dis* **53**, 167-170

30. Ganz, T., and Nemeth, E. (2012) Hepcidin and iron homeostasis. *Biochim Biophys Acta* **1823**, 1434-1443

31. Masson, C. (2011) Rheumatoid anemia. *Joint Bone Spine* **78**, 131-137

32. Chung, J., Anderson, S. A., Gwynn, B., Deck, K. M., Chen, M. J., Langer, N. B., Shaw, G. C., Huston, N. C., Boyer, L. F., Datta, S., Paradkar, P. N., Li, L., Wei, Z., Lambert, A. J., Sahr, K., Wittig, J. G., Chen, W., Lu, W., Galy, B., Schlaeger, T. M., Hentze, M. W., Ward, D. M., Kaplan, J., Eisenstein, R. S., Peters, L. L., and Paw, B. H. (2014) Iron regulatory protein-1 protects against mitoferrin-1-deficient porphyria. *J Biol Chem* **289**, 7835-7843

33. Cavill, I., and Bentley, D. P. (1982) Erythropoiesis in the anaemia of rheumatoid arthritis. *Br J Haematol* **50**, 583-590

34. Fitzsimons, E. J., Houston, T., Munro, R., Sturrock, R. D., Speekenbrink, A. B., and Brock, J. H. (2002) Erythroblast iron metabolism and serum soluble transferrin receptor values in the anemia of rheumatoid arthritis. *Arthritis Rheum* **47**, 166-171

35. Sharma, D. C., and Mathur, R. (2000) Some biochemical changes in heme synthesis in iron deficiency. *Indian J Physiol Pharmacol* **44**, 491-494

36. Crooks, D. R., Ghosh, M. C., Haller, R. G., Tong, W. H., and Rouault, T. A. (2010) Posttranslational stability of the heme biosynthetic enzyme ferrochelatase is dependent on iron availability and intact iron-sulfur cluster assembly machinery. *Blood* **115**, 860-869

37. Strelko, C. L., Lu, W., Dufort, F. J., Seyfried, T. N., Chiles, T. C., Rabinowitz, J. D., and Roberts, M. F. (2011) Itaconic acid is a mammalian metabolite induced during macrophage activation. *J Am Chem Soc* **133**, 16386-16389

38. Sugimoto, M., Sakagami, H., Yokote, Y., Onuma, H., Kaneko, M., Mori, M., Sakaguchi, Y., Soga, T., and Tomita, M. (2012) Non-targeted metabolite profiling in activated macrophage secretion. *Metabolomics* **8**, 624-633

39. Michelucci, A., Cordes, T., Ghelfi, J., Pailot, A., Reiling, N., Goldmann, O., Binz, T., Wegner, A., Tallam, A., Rausell, A., Buttini, M., Linster, C. L., Medina, E., Balling, R., and Hiller, K. (2013) Immune-responsive gene 1 protein links metabolism to immunity by catalyzing itaconic acid production. *Proc Natl Acad Sci U S A* **110**, 7820-7825

40. Meiser, J., Kraemer, L., Jaeger, C., Madry, H., Link, A., Lepper, P. M., Hiller, K., and Schneider, J. G. (2018) Itaconic acid indicates cellular but not systemic immune system activation. *Oncotarget* **9**, 32098-32107

41. Cordes, T., Wallace, M., Michelucci, A., Divakaruni, A. S., Sapcariu, S. C., Sousa, C., Koseki, H., Cabrales, P., Murphy, A. N., Hiller, K., and Metallo, C. M. (2016) Immunoresponsive Gene 1 and Itaconate Inhibit Succinate Dehydrogenase to Modulate Intracellular Succinate Levels. *J Biol Chem* **291**, 14274-14284

42. Lampropoulou, V., Sergushichev, A., Bambouskova, M., Nair, S., Vincent, E. E., Loginicheva, E., Cervantes-Barragan, L., Ma, X., Huang, S. C., Griss, T., Weinheimer, C. J., Khader, S., Randolph, G. J., Pearce, E. J., Jones, R. G., Diwan, A., Diamond, M. S., and Artyomov, M. N. (2016) Itaconate Links Inhibition of Succinate Dehydrogenase with Macrophage Metabolic Remodeling and Regulation of Inflammation. *Cell Metab* **24**, 158-166

43. Daly, R., Blackburn, G., Best, C., Goodyear, C. S., Mudaliar, M., Burgess, K., Stirling, A., Porter, D., McInnes, I. B., Barrett, M. P., and Dale, J. (2020) Changes in Plasma Itaconate Elevation in Early Rheumatoid Arthritis Patients Elucidates Disease Activity Associated Macrophage Activation. *Metabolites* **10**

44. Zaslona, Z., and O'Neill, L. A. J. (2020) Cytokine-like Roles for Metabolites in Immunity. *Mol Cell*

45. Michopoulos, F., Karagianni, N., Whalley, N. M., Firth, M. A., Nikolaou, C., Wilson, I. D., Critchlow, S. E., Kollias, G., and Theodoridis, G. A. (2016) Targeted Metabolic Profiling of the Tg197 Mouse Model Reveals Itaconic Acid as a Marker of Rheumatoid Arthritis. *J Proteome Res* **15**, 4579-4590

46. Bambouskova, M., Gorvel, L., Lampropoulou, V., Sergushichev, A., Loginicheva, E., Johnson, K., Korenfeld, D., Mathyer, M. E., Kim, H., Huang, L. H., Duncan, D., Bregman, H., Keskin, A., Santeford, A., Apte, R. S., Sehgal, R., Johnson, B., Amarasinghe, G. K., Soares, M. P., Satoh, T., Akira, S., Hai, T., de Guzman Strong, C., Auclair, K., Roddy, T. P., Biller, S. A., Jovanovic, M., Klechevsky, E., Stewart, K. M.,

Randolph, G. J., and Artyomov, M. N. (2018) Electrophilic properties of itaconate and derivatives regulate the IkappaBzeta-ATF3 inflammatory axis. *Nature* **556**, 501-504

47. Mills, E. L., Ryan, D. G., Prag, H. A., Dikovskaya, D., Menon, D., Zaslona, Z., Jedrychowski, M. P., Costa, A. S. H., Higgins, M., Hams, E., Szpyt, J., Runtsch, M. C., King, M. S., McGouran, J. F., Fischer, R., Kessler, B. M., McGettrick, A. F., Hughes, M. M., Carroll, R. G., Booty, L. M., Knatko, E. V., Meakin, P. J., Ashford, M. L. J., Modis, L. K., Brunori, G., Sevin, D. C., Fallon, P. G., Caldwell, S. T., Kunji, E. R. S., Chouchani, E. T., Frezza, C., Dinkova-Kostova, A. T., Hartley, R. C., Murphy, M. P., and O'Neill, L. A. (2018) Itaconate is an anti-inflammatory metabolite that activates Nrf2 via alkylation of KEAP1. *Nature* **556**, 113-117

48. Cordes, T., Michelucci, A., and Hiller, K. (2015) Itaconic Acid: The Surprising Role of an Industrial Compound as a Mammalian Antimicrobial Metabolite. *Annu Rev Nutr* **35**, 451-473

49. Ackermann, W. W., and Potter, V. R. (1949) Enzyme inhibition in relation to chemotherapy. *Proc Soc Exp Biol Med* **72**, 1-9

50. Tannahill, G. M., Curtis, A. M., Adamik, J., Palsson-McDermott, E. M., McGettrick, A. F., Goel, G., Frezza, C., Bernard, N. J., Kelly, B., Foley, N. H., Zheng, L., Gardet, A., Tong, Z., Jany, S. S., Corr, S. C., Haneklaus, M., Caffrey, B. E., Pierce, K., Walmsley, S., Beasley, F. C., Cummins, E., Nizet, V., Whyte, M., Taylor, C. T., Lin, H., Masters, S. L., Gottlieb, E., Kelly, V. P., Clish, C., Auron, P. E., Xavier, R. J., and O'Neill, L. A. (2013) Succinate is an inflammatory signal that induces IL-1beta through HIF-1alpha. *Nature* **496**, 238-242

51. Sakai, A., Kusumoto, A., Kiso, Y., and Furuya, E. (2004) Itaconate reduces visceral fat by inhibiting fructose 2,6-bisphosphate synthesis in rat liver. *Nutrition* **20**, 997-1002

52. Nemeth, B., Doczi, J., Csete, D., Kacso, G., Ravasz, D., Adams, D., Kiss, G., Nagy, A. M., Horvath, G., Tretter, L., Mocsai, A., Csepanyi-Komi, R., Iordanov, I., Adam-Vizi, V., and Chinopoulos, C. (2016) Abolition of mitochondrial substrate-level phosphorylation by itaconic acid produced by LPS-induced Irg1 expression in cells of murine macrophage lineage. *FASEB J* **30**, 286-300

53. Adler, J., Wang, S. F., and Lardy, H. A. (1957) The metabolism of itaconic acid by liver mitochondria. *J Biol Chem* **229**, 865-879

54. Wang, S. F., Adler, J., and Lardy, H. A. (1961) The pathway of itaconate metabolism by liver mitochondria. *J Biol Chem* **236**, 26-30

55. Shen, H., Campanello, G. C., Flicker, D., Grabarek, Z., Hu, J., Luo, C., Banerjee, R., and Mootha, V. K. (2017) The Human Knockout Gene CLYBL Connects Itaconate to Vitamin B12. *Cell* **171**, 771-782 e711

56. Gopinath, K., Venclovas, C., Ioerger, T. R., Sacchettini, J. C., McKinney, J. D., Mizrahi, V., and Warner, D. F. (2013) A vitamin B(1)(2) transporter in Mycobacterium tuberculosis. *Open Biol* **3**, 120175

57. Ruetz, M., Campanello, G. C., Purchal, M., Shen, H., McDevitt, L., Gouda, H., Wakabayashi, S., Zhu, J., Rubin, E. J., Warncke, K., Mootha, V. K., Koutmos, M., and Banerjee, R. (2019) Itaconyl-CoA forms a stable biradical in methylmalonyl-CoA mutase and derails its activity and repair. *Science* **366**, 589-593

58. Burch, J. S., Marcero, J. R., Maschek, J. A., Cox, J. E., Jackson, L. K., Medlock, A. E., Phillips, J. D., and Dailey, H. A., Jr. (2018) Glutamine via alpha-ketoglutarate dehydrogenase provides succinyl-CoA for heme synthesis during erythropoiesis. *Blood* **132**, 987-998

59. Sud, M., Fahy, E., Cotter, D., Azam, K., Vadivelu, I., Burant, C., Edison, A., Fiehn, O., Higashi, R., Nair, K. S., Sumner, S., and Subramaniam, S. (2016) Metabolomics Workbench: An international repository for metabolomics data and metadata, metabolite standards, protocols, tutorials and training, and analysis tools. *Nucleic Acids Res* **44**, D463-470

60. Sasikaran, J., Ziemski, M., Zadora, P. K., Fleig, A., and Berg, I. A. (2014) Bacterial itaconate degradation promotes pathogenicity. *Nat Chem Biol* **10**, 371-377

61. Ohta, Y., Tanaka, M., Terada, M., Miller, O. J., Bank, A., Marks, P., and Rifkind, R. A. (1976) Erythroid cell differentiation: murine erythroleukemia cell variant with unique pattern of induction by polar compounds. *Proc Natl Acad Sci U S A* **73**, 1232-1236

62. Singer, D., Cooper, M., Maniatis, G. M., Marks, P. A., and Rifkind, R. A. (1974) Erythropoietic differentiation in colonies of cells transformed by Friend virus. *Proc Natl Acad Sci U S A* **71**, 2668-2670

63. Medlock, A. E., Shiferaw, M. T., Marcero, J. R., Vashisht, A. A., Wohlschlegel, J. A., Phillips, J. D., and Dailey, H. A. (2015) Identification of the Mitochondrial Heme Metabolism Complex. *PLoS One* **10**, e0135896

64. Yien, Y. Y., Robledo, R. F., Schultz, I. J., Takahashi-Makise, N., Gwynn, B., Bauer, D. E., Dass, A., Yi, G., Li, L., Hildick-Smith, G. J., Cooney, J. D., Pierce, E. L., Mohler, K., Dailey, T. A., Miyata, N., Kingsley, P. D., Garone, C., Hattangadi, S. M., Huang, H., Chen, W., Keenan, E. M., Shah, D. I., Schlaeger, T. M., DiMauro, S., Orkin, S. H., Cantor, A. B., Palis, J., Koehler, C. M., Lodish, H. F., Kaplan, J., Ward, D. M., Dailey, H. A., Phillips, J. D., Peters, L. L., and Paw, B. H. (2014) TMEM14C is required for erythroid mitochondrial heme metabolism. *J Clin Invest* **124**, 4294-4304

65. UniProt, C. (2019) UniProt: a worldwide hub of protein knowledge. *Nucleic Acids Res* **47**, D506-D515

66. Notredame, C., Higgins, D. G., and Heringa, J. (2000) T-Coffee: A novel method for fast and accurate multiple sequence alignment. *J Mol Biol* **302**, 205-217

67. Shoolingin-Jordan, P. M., LeLean, J. E., and Lloyd, A. J. (1997) Continuous coupled assay for 5-aminolevulinate synthase. *Methods Enzymol* **281**, 309-316

68. Cha, S., and Parks, R. E. (1964) Succinic Thiokinase: I. Purification of the enzyme from pig heart. *Journal of Biological Chemistry* **239**, 1961-1967

69. Marlaire, S., Van Schaftingen, E., and Veiga-da-Cunha, M. (2014) C7orf10 encodes succinate-hydroxymethylglutarate CoA-transferase, the enzyme that converts glutarate to glutaryl-CoA. *J Inherit Metab Dis* **37**, 13-19

70. Chong, J., and Xia, J. (2018) MetaboAnalystR: an R package for flexible and reproducible analysis of metabolomics data. *Bioinformatics* **34**, 4313-4314

71. Sassa, S., Wolpe, S., and Cerami, A. (1987) Inhibition of erythroid differentiation of mouse erythroleukemia cells by a macrophage product(s). *Blood Cells* **13**, 161-169

72. Hakak, Y., Lehmann-Bruinsma, K., Phillips, S., Le, T., Liaw, C., Connolly, D. T., and Behan, D. P. (2009) The role of the GPR91 ligand succinate in hematopoiesis. *J Leukoc Biol* **85**, 837-843

73. Zhen, R., Moo, C., Zhao, Z., Chen, M., Feng, H., Zheng, X., Zhang, L., Shi, J., and Chen, C. (2020) Wdr26 regulates nuclear condensation in developing erythroblasts. *Blood* **135**, 208-219

74. Gautier, E. F., Ducamp, S., Leduc, M., Salnot, V., Guillonneau, F., Dussiot, M., Hale, J., Giarratana, M. C., Raimbault, A., Douay, L., Lacombe, C., Mohandas, N., Verdier, F., Zermati, Y., and Mayeux, P. (2016) Comprehensive Proteomic Analysis of Human Erythropoiesis. *Cell Rep* **16**, 1470-1484

75. Trauelsen, M., Rexen Ulven, E., Hjorth, S. A., Brvar, M., Monaco, C., Frimurer, T. M., and Schwartz, T. W. (2017) Receptor structure-based discovery of non-metabolite agonists for the succinate receptor GPR91. *Mol Metab* **6**, 1585-1596

76. O'Neill, L. A. J., and Artyomov, M. N. (2019) Itaconate: the poster child of metabolic reprogramming in macrophage function. *Nat Rev Immunol* **19**, 273-281

77. Smith, C. M., Bryla, J., and Williamson, J. R. (1974) Regulation of mitochondrial alpha-ketoglutarate metabolism by product inhibition at alpha-ketoglutarate dehydrogenase. *J Biol Chem* **249**, 1497-1505

78. Strittmatter, L., Li, Y., Nakatsuka, N. J., Calvo, S. E., Grabarek, Z., and Mootha, V. K. (2014) CLYBL is a polymorphic human enzyme with malate synthase and beta-methylmalate synthase activity. *Hum Mol Genet* **23**, 2313-2323

79. Hunter, G. A., and Ferreira, G. C. (1995) A continuous spectrophotometric assay for 5-aminolevulinate synthase that utilizes substrate cycling. *Anal Biochem* **226**, 221-224

80. Bishop, D. F., Tchaikovskii, V., Nazarenko, I., and Desnick, R. J. (2013) Molecular expression and characterization of erythroid-specific 5-aminolevulinate synthase gain-of-function mutations causing X-linked protoporphyria. *Mol Med* **19**, 18-25

81. Booth, A. N., Taylor, J., Wilson, R. H., and Deeds, F. (1952) The inhibitory effects of itaconic acid in vitro and in vivo. *J Biol Chem* **195**, 697-702

82. Finkelstein, M., Gold, H., and Paterno, C. A. (1947) Pharmacology of itaconic acid and its sodium, magnesium, and calcium salts. *J Am Pharm Assoc Am Pharm Assoc* **36**, 173-179

83. Schranzhofer, M., Schifrer, M., Cabrera, J. A., Kopp, S., Chiba, P., Beug, H., and Mullner, E. W. (2006) Remodeling the regulation of iron metabolism during erythroid differentiation to ensure efficient heme biosynthesis. *Blood* **107**, 4159-4167

84. Zhang, S., Macias-Garcia, A., Ulirsch, J. C., Velazquez, J., Butty, V. L., Levine, S. S., Sankaran, V. G., and Chen, J. J. (2019) HRI coordinates translation necessary for protein homeostasis and mitochondrial function in erythropoiesis. *Elife* **8**

85. Drissen, R., Guyot, B., Zhang, L., Atzberger, A., Sloane-Stanley, J., Wood, B., Porcher, C., and Vyas, P. (2010) Lineage-specific combinatorial action of enhancers regulates mouse erythroid Gata1 expression. *Blood* **115**, 3463-3471

86. Xue, L., Galdass, M., Gnanapragasam, M. N., Manwani, D., and Bieker, J. J. (2014) Extrinsic and intrinsic control by EKLF (KLF1) within a specialized erythroid niche. *Development* **141**, 2245-2254

87. Heideveld, E., Masiello, F., Marra, M., Esteghamat, F., Yagci, N., von Lindern, M., Migliaccio, A. R., and van den Akker, E. (2015) CD14+ cells from peripheral blood positively regulate hematopoietic stem and progenitor cell survival resulting in increased erythroid yield. *Haematologica* **100**, 1396-1406

88. Nagai, J. (1963) Studies on itaconate metabolism. I. Itaconyl-Co-A synthesizing reaction in cell-free extracts of Pseudomonas fluorescens. *J Biochem* **53**, 181-187

89. Robinson, J. B., Jr., and Srere, P. A. (1985) Organization of Krebs tricarboxylic acid cycle enzymes in mitochondria. *J Biol Chem* **260**, 10800-10805

90. Campanella, M. E., Chu, H., and Low, P. S. (2005) Assembly and regulation of a glycolytic enzyme complex on the human erythrocyte membrane. *Proc Natl Acad Sci U S A* **102**, 2402-2407

91. Srere, P. A., and Sumegi, B. (1994) Processivity and fatty acid oxidation. *Biochem Soc Trans* **22**, 446-450

92. Furuyama, K., and Sassa, S. (2000) Interaction between succinyl CoA synthetase and the heme-biosynthetic enzyme ALAS-E is disrupted in sideroblastic anemia. *J Clin Invest* **105**, 757-764

93. Klaeger, S., Gohlke, B., Perrin, J., Gupta, V., Heinzlmeir, S., Helm, D., Qiao, H., Bergamini, G., Handa, H., Savitski, M. M., Bantscheff, M., Medard, G., Preissner, R., and Kuster, B. (2016) Chemical Proteomics Reveals Ferrochelatase as a Common Off-target of Kinase Inhibitors. *ACS Chem Biol* **11**, 1245-1254

94. Marcero, J. R., Piel Iii, R. B., Burch, J. S., and Dailey, H. A. (2016) Rapid and sensitive quantitation of heme in hemoglobinized cells. *Biotechniques* **61**, 83-91

95. Javorfi, T., Erostyak, J., Gal, J., Buzady, A., Menczel, L., Garab, G., and Razi Naqvi, K. (2006) Quantitative spectrophotometry using integrating cavities. *J Photochem Photobiol B* **82**, 127-131

4.6 Figures

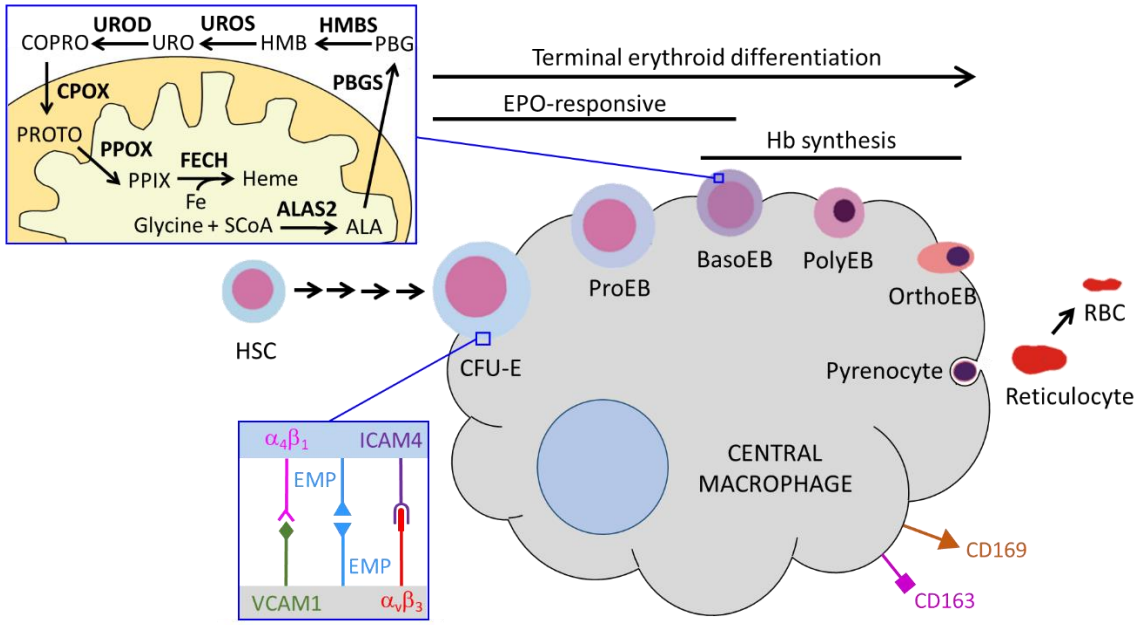

Figure 1. Heme biosynthesis and the erythroblastic island. The terminal steps of erythropoiesis occur while erythroblasts are closely associated with a central macrophage via αβ integrins, vascular cell adhesion protein 1 (VCAM1), erythroblast macrophage protein (EMP), and intercellular adhesion molecule 4 (ICAM4). Heme synthesis in this context is fully activated by the basophilic erythroblast (BasoEB) stage of development. Other abbreviations: HSC = hematopoietic stem cell, CFU-E = colony forming unit-erythroid, ProEB = proerythroblast, PolyEB = polychromatic erythroblast, OrthoEB = orthochromatic erythroblast, SCoA = succinyl-CoA, ALAS2 = aminolevulinic acid synthase 2, PBGS = porphobilinogen synthase, HMBS = hydroxymethylbilane synthase, UROS = uroporphyrinogen III synthase, UROD = URO decarboxylase, CPOX = coproporphyrinogen III oxidase, PPOX = protoporphyrinogen oxidase, PPIX = protoporphyrin IX, FECH = ferrochelatase. Heme synthesis enzymes are in bold.

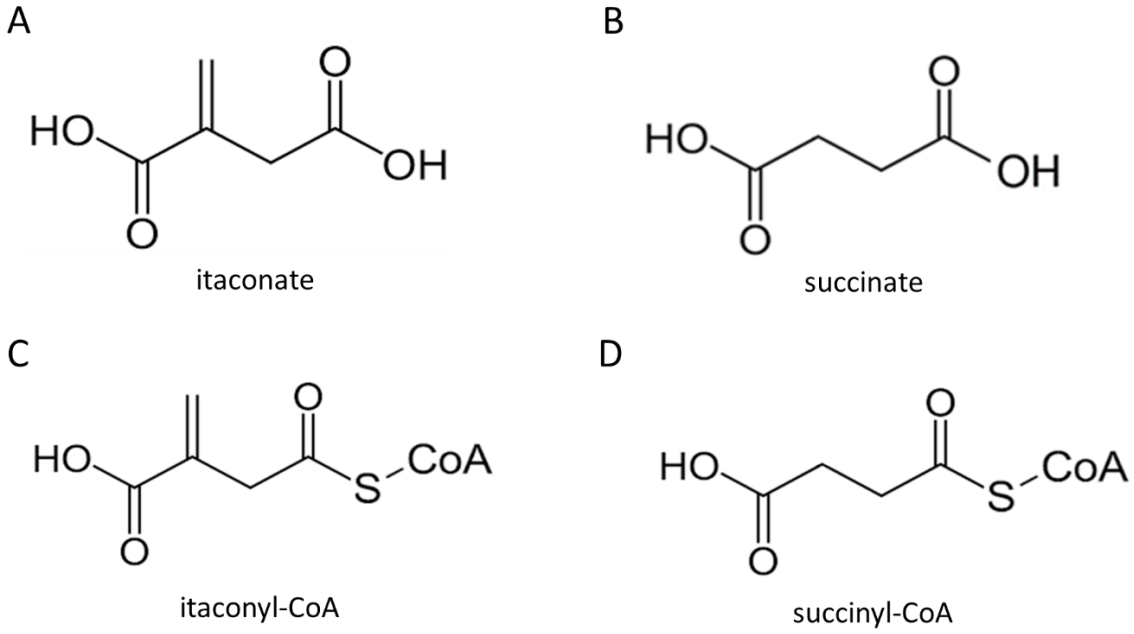

Figure 2. Itaconate and succinate with CoA derivatives. Molecular structures of itaconate (A) and its analog succinate (B) and their respective CoA derivatives itaconyl-CoA (C) and succinyl-CoA (D). The itaconyl-CoA isomer shown is the biologically active form, 3-methylenesuccinic acid.

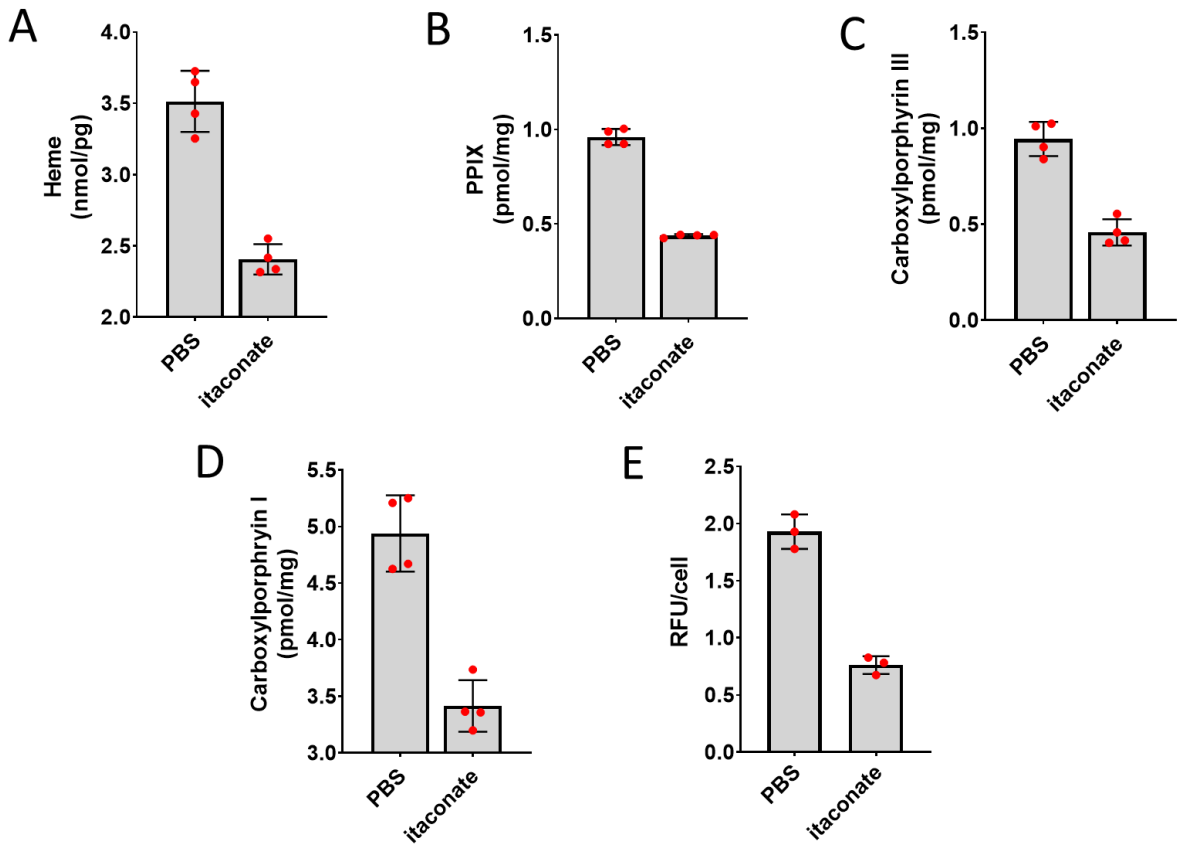

Figure 3. Porphyrin and heme analysis of MEL cells treated with itaconate. Heme (A), protoporphyrin IX (B), and intermediate carboxylated porphyrins (C,D) were determined by HPLC per mass of protein input for wild-type MEL cells differentiated in DMSO media for 72 h. Relative fluorescence of cyclic porphyrins in media from MEL cell cultures overexpressing hsALAS2 over 72 h without DMSO induction (E). Itaconate concentrations were 2.5 mM in all experiments shown here. Specific experimental conditions are provided in the Material and Methods section. Bars represent means ± one SD (n=3-4 biological replicates as indicated). Multiple t-tests combined with Bonferroni analysis produced *p*-values < 0.01 for all PBS vs. itaconate comparisons shown.

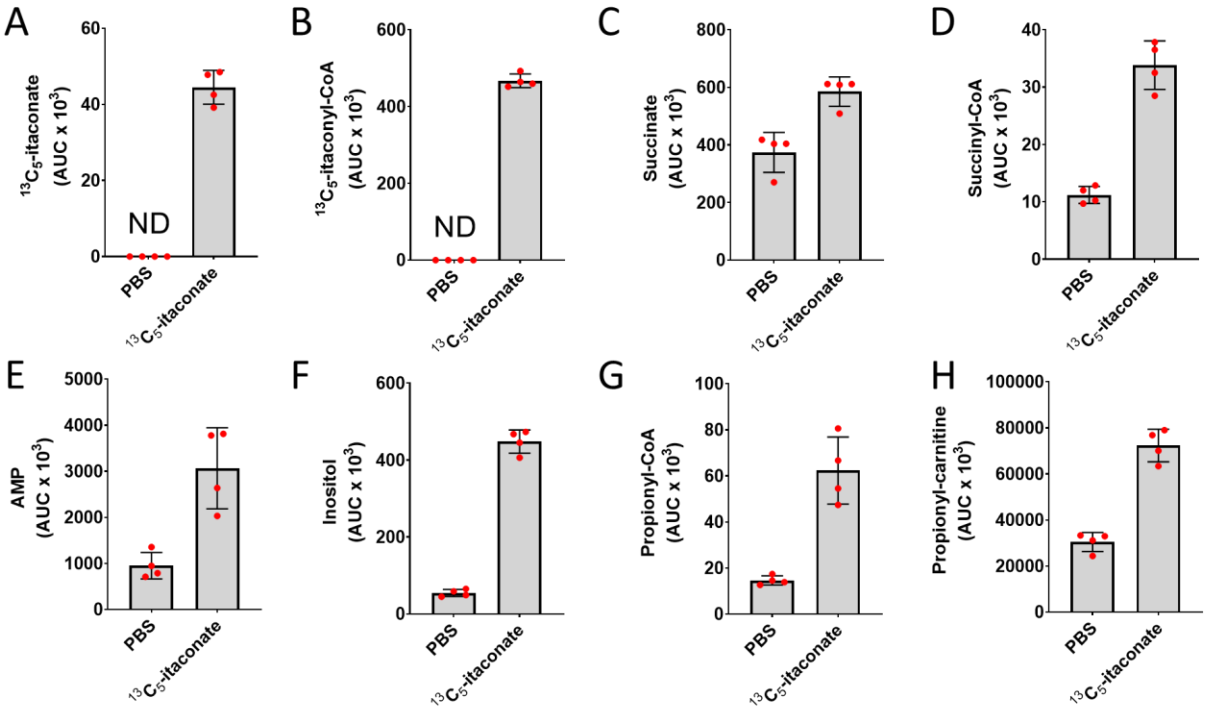

Figure 4. LC-MS analysis of metabolites from differentiating MEL cells treated with labeled itaconate. MEL cultures were induced with DMSO and treated with PBS or 1 mM labeled itaconate for 72 h. Select metabolites targeted by LC-MS analysis appear on the y-axes. Analyses were conducted as described in the Materials and Methods section. Bars represent means ± one SD (n=4 biological replicates). ND = not detected. Multiple t-tests combined with Bonferroni analysis produced *p*-values < 0.01 for all PBS vs. $^{13}C_5$-itaconate comparisons except PBS vs. (D) succinate (0.024) and (H) AMP (0.034).

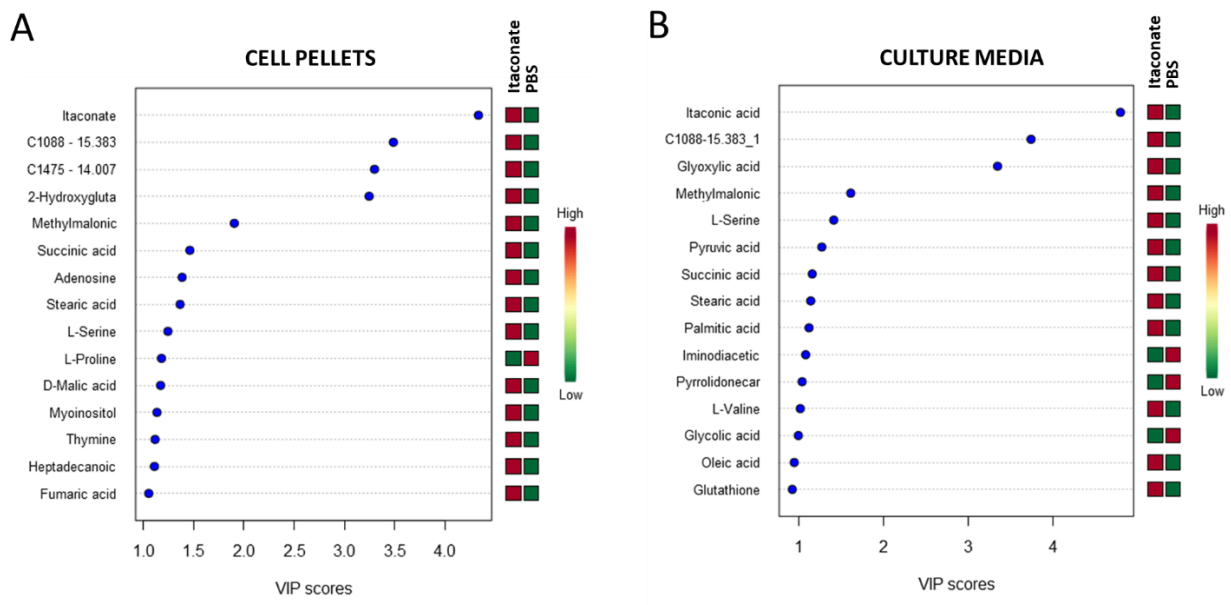

Figure 5. GC-MS metabolomic analysis of differentiating MEL cultures treated with unlabeled itaconate. PLS-DA and associated VIP scores were determined from PCA data by MetaboAnalystR for MEL cells (A) and media (B) in cultures induced with DMSO and treated with PBS or 2.5 mM itaconate for 72 h. Results are based on n=4 biological replicates for each sample set.

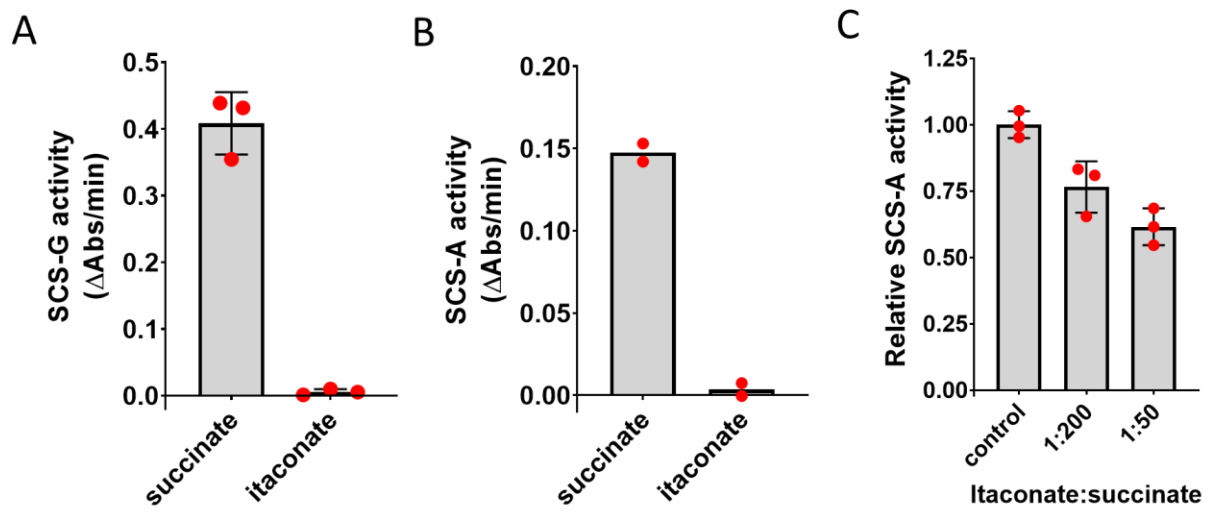

Figure 6. Impacts of itaconate on SCS activity. Succinate but not itaconate at 10 mM concentrations is metabolized by pig heart SCS-GTP (SCS-G) (A) and recombinant SCS-ATP (SCS-A) (B). Itaconate inhibits SCS-A (C) at the indicated ratios using 50 mM succinate in all reactions. Summary bar plots represent mean rates of acyl-CoA formation at 225-235 nm. The corresponding UV scans for (A) and (B) are provided in Figure S7. Bars represent means and error bars = one SD (n=2-3 biological replicates). (A) Student's t-test *p*-value = 0.0001; (C) one-way ANOVA *p*-value = 0.0022 with Bonferroni post-hoc test *p*-values = 0.026, 0.0022, and 0.15 (ns) for control vs. 1:200, control vs. 1:50, and 1:200 v. 1:50, respectively.

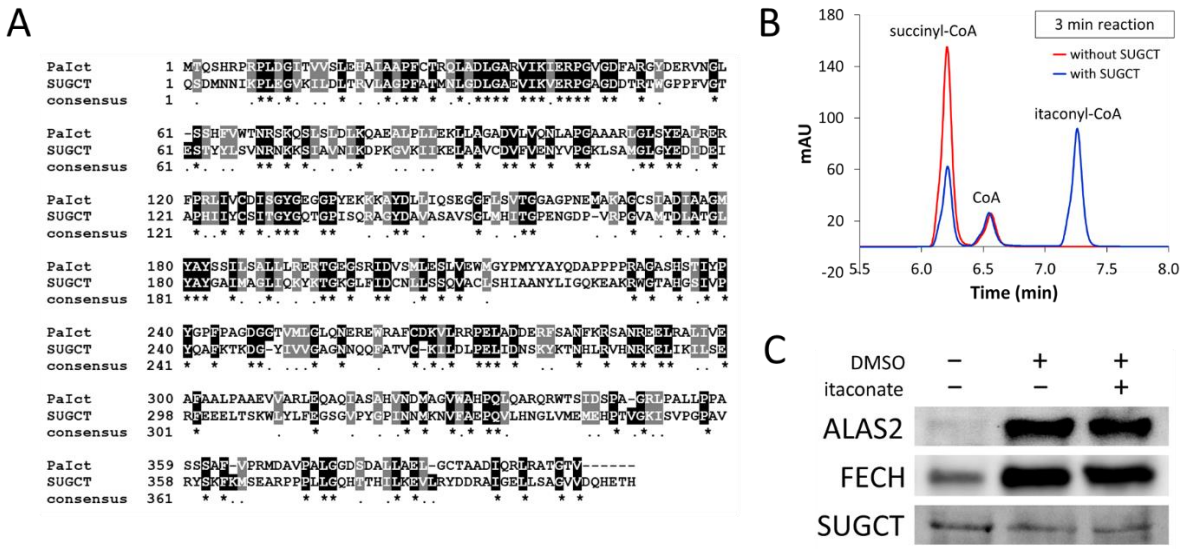

Figure 7. SUGCT converts itaconate to itaconyl-CoA. Human SUGCT is homologous to the *Pseudomonas aeruginosa* itaconyl-CoA transferase (PaIct) (A). Black and gray boxes highlight identical residues and conservative substitutions, respectively. Discontinuous HPLC assays demonstrated that SUGCT generates itaconyl-CoA from succinyl-CoA and itaconate *in vitro* (B). Immunoblotting of MEL mitochondria from cells treated with and without 2.5 mM itaconate and DMSO for 72 h (C). MEL mitochondrial lysates were probed with anti-ALAS2, anti-FECH, and anti-SUGCT primary antibodies. Specific conditions for the HPLC assays and immunoblotting are described in the Materials and Methods. The HPLC chromatogram (B) and western blot (C) shown are representative of n=2 biological replicates.

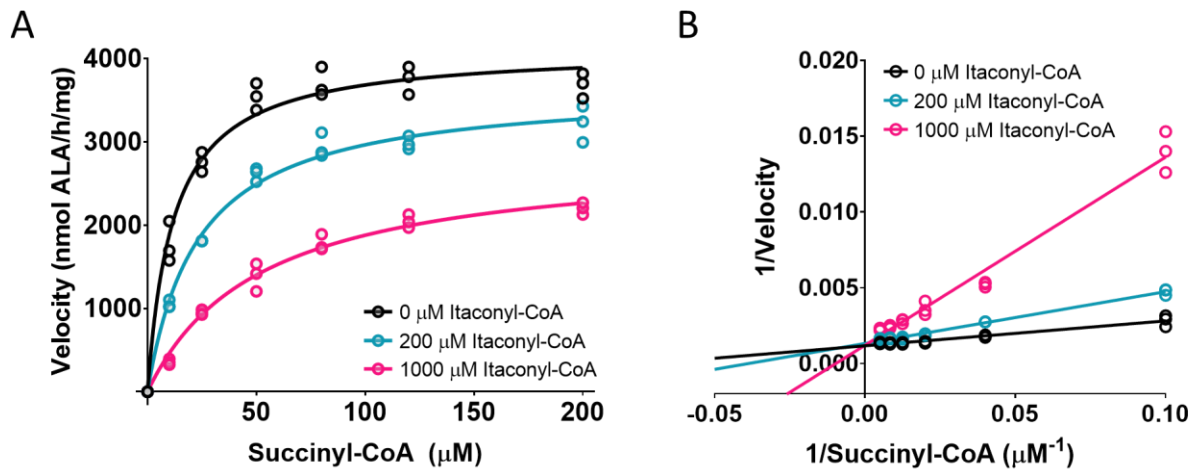

Figure 8. ALAS2 inhibition by itaconyl-CoA. Kinetic progress curves (A) and Lineweaver-Burk plot (B), indicating competitive inhibition of ALAS2 with K_i = 100 ± 20 μM (mean ± SD) for itaconyl-CoA; K_m = 10 ± 2 μM (mean ± SD) for succinyl-CoA. Reactions were conducted as described in the Materials and Methods (n=3 biological replicates from separate protein preparations).

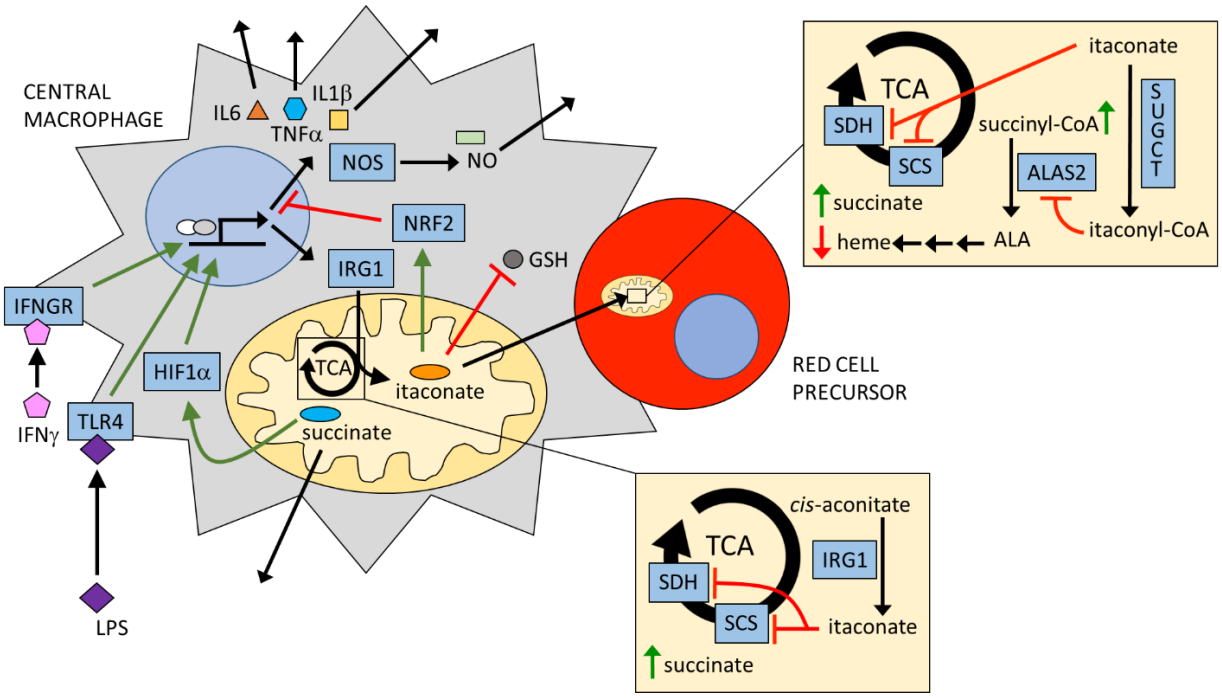

Figure 9. Model of the erythroblastic island during an inflammatory response. IL6 (interleukin 6), TNFα (tumor necrosis factor-alpha), and IL1β (interleukin 1-beta) are proinflammatory cytokines; TLR4 = toll-like receptor 4, IFNGR = interferon-gamma (IFNγ) receptor, GSH = glutathione, NOS = nitric oxide synthase. Specifics details and other abbreviations are provided in the main text.

4.7 Supplementary Information

Supplemental Methods

Cell lines

TF1 hematopoietic cells (ATCC CRL-2003) were maintained in RPMI-1640 media containing 10% FBS, 2 mM glutamine, 1% pen-strep, and 5 ng/mL GM-CSF. GM-CSF was replaced with 2 U/mL human erythropoietin (EPO) (Amgen) to induce erythroid differentiation. TF1 cultures were seeded at 1 x 10^5 cells/mL and differentiated for 4 days in the presence of itaconate, succinate, ALA, MEK inhibitor U0126, and/or SUCNR1 inhibitor compound 4c (gift of Xin Li).

Cells from the adherent RAW264.7 (RAW) blood monocyte/macrophage line (ATCC TIB-71) were grown under the same conditions as uninduced MEL cells (see Materials and Methods in the main text), except that DMEM media containing 4 mM glutamine (Corning) was used instead of DMEM/F12 and 2 mM glutamine. RAW cells were plated at 2 x 10^5 cells/cm^2 and treated with 100 ng/mL lipopolysaccharide (LPS) from *E. coli* (O111:B4) for 24 h to induce an inflammatory phenotype. The RAW-conditioned media was then harvested and clarified by centrifugation and filtration before application to DMSO-induced MEL cells at 20% v/v as indicated.

Spectrophotometric hemoglobin quantitation

Cellular hemoglobinization of TF1 cells was measured as previously described (94) with modifications. Briefly, 10 mL cultures were washed and concentrated in 1.2 mL PBS. Cell counts (Scepter 2.0, EMD Millipore) were made on 1:50 dilutions of the PBS suspensions followed by hemoglobin quantitation of 1-mL samples on the RSM-CLARiTY (Olis) at 411 nm. The empirical Javorfi correction factor (95) was applied to account for the enhanced pathlength

of incident light through the turbid samples. Corrected absorbance values were used in combination with a micromolar extinction coefficient of 0.291 to determine cellular hemoglobin levels.

Recombinant ALAS assays

Discontinuous colorimetric assays were carried out as described in the main text Materials and Methods section. Continuous coupled assays (67) were also used as previously reported to determine whether itaconyl-CoA is an alternative ALAS2 substrate. Coupled reactions were run in 300 μL volumes containing 100 mM MOPS buffer, pH 6.8, 0.2 mM sodium pyruvate, 100 μM PLP, 0.2 mM thiamine pyrophosphate, 0.2 mM NAD^+, 10 mM $MgCl_2$, 1 mM DTT, and 0.12 U pyruvate dehydrogenase from porcine heart (Sigma). Recombinant hsALAS2 (0.5 μM) was assayed in the presence of 500 μM itaconyl-CoA or succinyl-CoA control. Absorbance values for assays run without enzyme were subtracted from those obtained with enzyme to correct for nonenzymatic acyl-CoA hydrolysis during reactions. A millimolar extinction coefficient of 6.22 was applied to determine the corrected rate of NADH and ALA production.

Supplemental Figures

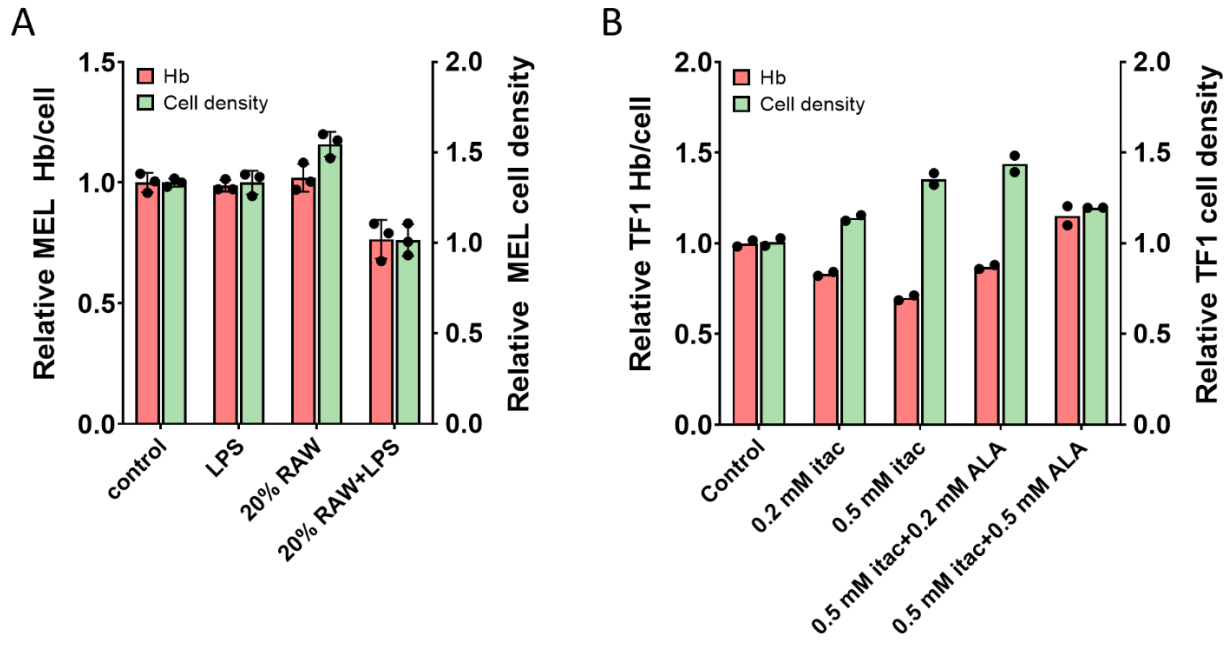

Supplemental Figure 1. Hemoglobinization of erythroblast models treated with LPS-activated macrophage media or itaconate. MEL cells were differentiated with DMSO for 96 h in the presence of 100 ng/mL LPS or media from RAW264.7 cells pretreated with PBS (RAW) or 100 ng/mL LPS (RAW+LPS) for 24 h (A). TF1 cells were induced with EPO for 96 h and treated with itaconate (itac) and/or ALA (B). Experiments were carried out as described in the Supplemental Methods section. Bars represent means (n=2-3 biological replicates) and error bars = one SD. Two-way ANOVA analysis of (C): $p < 0.0001$; Bonferroni post-hoc analysis: $p < 0.001$ for control vs. 20% RAW+LPS, LPS vs. 20% RAW+LPS, and 20% RAW vs. 20% RAW+LPS for relative Hb/cell (rest > 0.99) and $p < 0.02$ for all cell density comparisons except control vs. LPS (> 0.99).

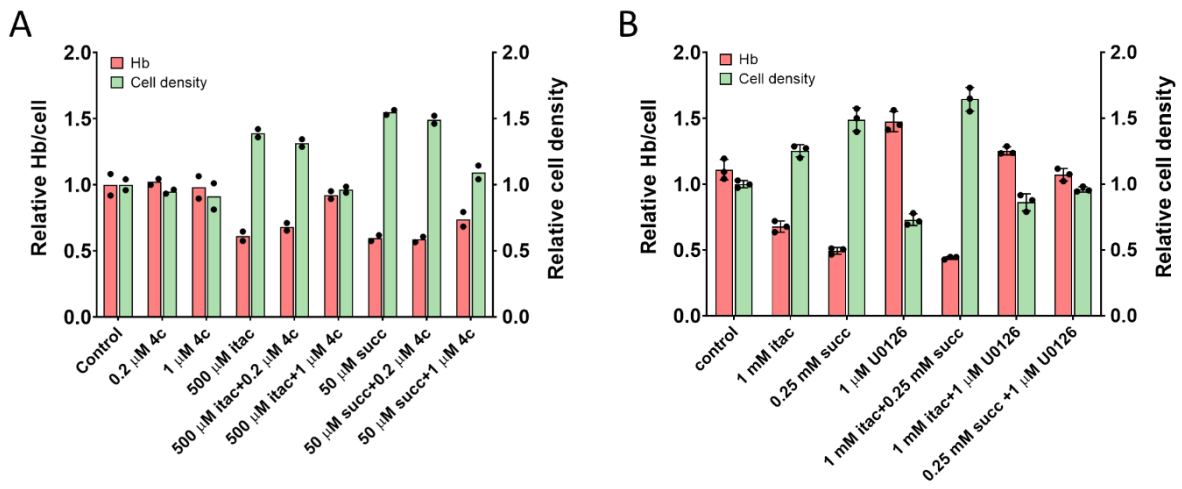

Supplemental Figure 2. Impacts of itaconate on SUCNR1 and MAPK/ERK signaling in TF1 cells. Inhibition of hemoglobinization in EPO-induced TF1 cells by itaconate (itac) is rescued by SUCNR1 antagonist compound 4c (A) and MAPK/ERK pathway inhibitor U0126 (B). Cognate SUCRN1 substrate succinate (succ) was tested for comparison. Experimental details are described in the Supplemental Methods. Bars represent means for n=2 biological replicates (A) or means ± one SD for n=3 (B). Multiple t-tests were used to compare all groups in (B) with Bonferroni post-hoc tests: $p < 0.02$ for all Hb/cell comparisons except control vs. itac+U0126 (0.079) and succ+U0126 (> 0.99) and succ vs. itac+succ (>0.99); $p < 0.01$ for all cell density comparisons except control vs. itac+U0126 (0.29) and succ+U0126 (> 0.99) and succ vs. itac+U0126 (0.38).

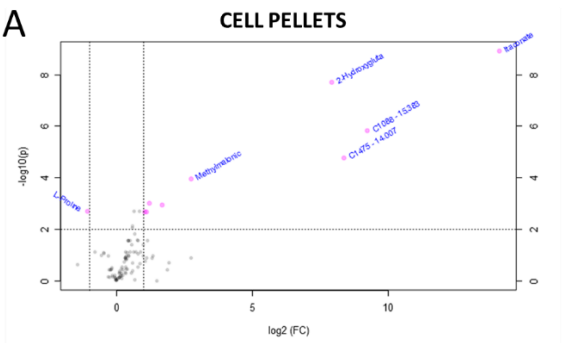

Compound	FC	log_2(FC)	FDR adj. p value	-log10(p)
Itaconate	17631.000000	14.106000	1.22E-9	8.913900
C1088 - 15.383_147	602.130000	9.233900	0.000001	5.826900
C1475 - 14.007_147	331.550000	8.373100	0.000017	4.768800
2-Hydroxyglutaric acid	242.940000	7.924500	1.98E-8	7.702400
Methylmalonic acid	6.674600	2.738700	0.000110	3.956700
Succinic acid	3.179400	1.668800	0.001136	2.944800
L-Serine	2.295500	1.198800	0.000972	3.012200
D-Malic acid	2.128700	1.089900	0.002107	2.676400
Myoinositol	2.034200	1.024400	0.002107	2.676400
L-Proline	0.472450	-1.081800	0.001995	2.700200

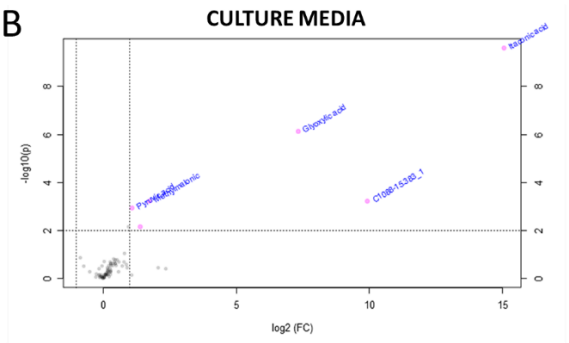

Compound	FC	log_2(FC)	FDR adj. p value	-log10(p)
Itaconic acid	33901.000000	15.049000	2.51E-10	9.601100
C1088-15.383_147	967.720000	9.918500	0.000606	3.217800
Glyoxylic acid	160.510000	7.326500	0.000001	6.125800
Methylmalonic acid	3.341600	1.740500	0.000606	3.217800
L-Serine	2.629600	1.394900	0.007054	2.151600
Pyruvic acid	2.126800	1.088700	0.001164	2.933900

Supplemental Figure 3. Volcano plots derived from GC-MS analysis of MEL cultures treated with itaconate. Differential metabolite analysis for DMSO-induced MEL cells (A) and culture media (B) in the presence or absence of 2.5 mM itaconate over 72 h. C1088 and C1475 are hereto unidentified compounds. Statistics were determined with MetaboAnalystR software, α=0.01 with a minimum 2.0 fold-change (FC) on n=4 biological replicates per group.

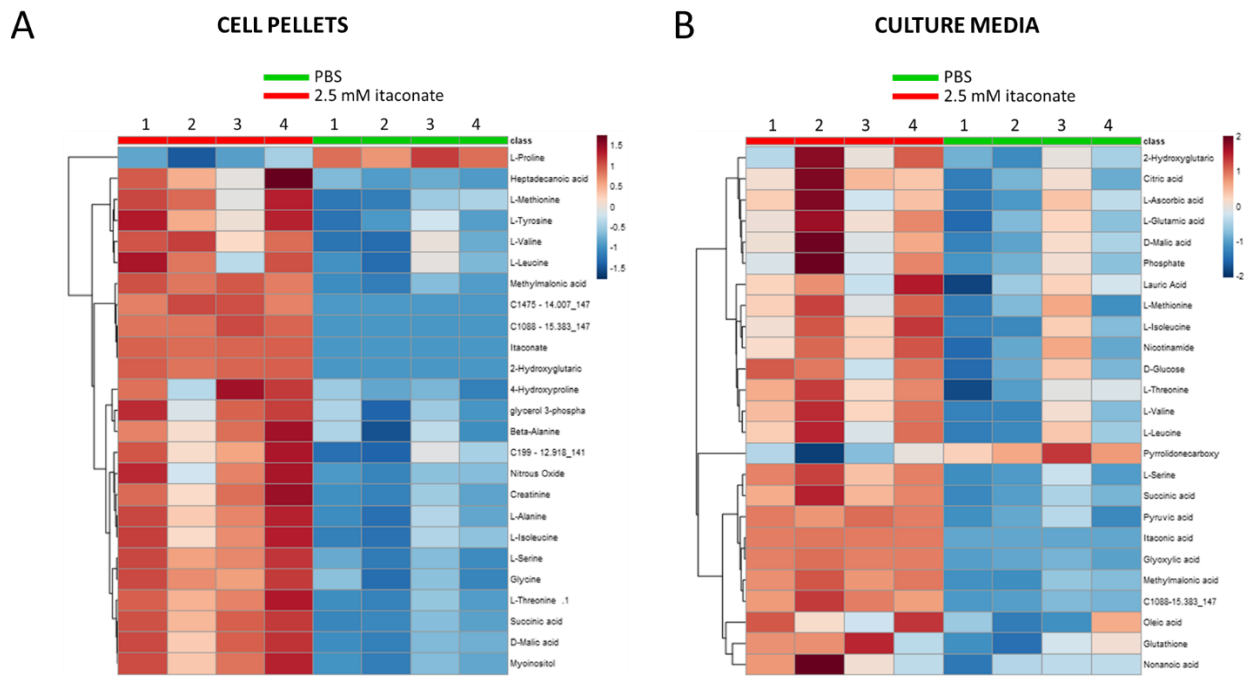

Supplemental Figure 4. Heat maps generated from GC-MS analysis of MEL cultures treated with itaconate. DMSO-induced MEL cells (A) and culture media (B) in the presence of PBS or 2.5 mM itaconate over 72 h. Maps list the 25 most changed metabolites (Student's t-test) between PBS- and itaconate-treated samples. Analysis performed with MetaboAnalystR software on n=4 biological replicates. Numbers at the head of columns indicate the replicate number.

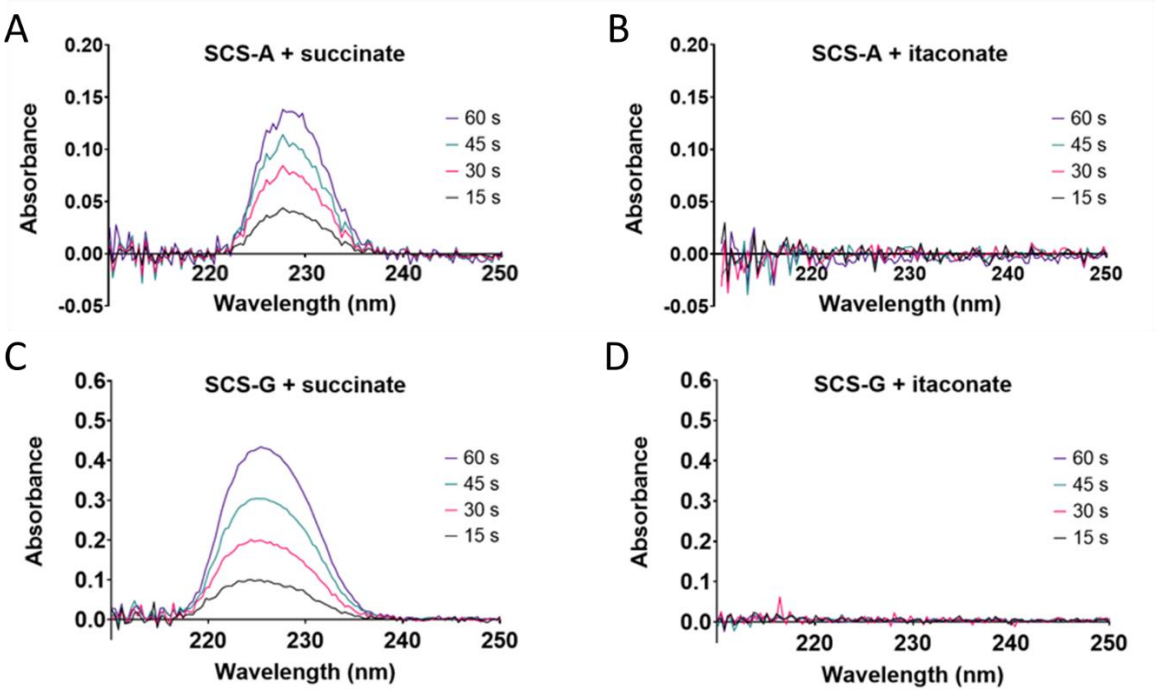

Supplemental Figure 5. SCS activities with succinate or itaconate as substrates.

Recombinant SCS-ATP (SCS-A) and pig heart SCS-GTP (SCS-G) process the canonical substrate succinate (A, C) but not itaconate (B, D). UV scans are representative of n=2-3 biological replicates of reactions conducted as described in the Materials and Methods section.

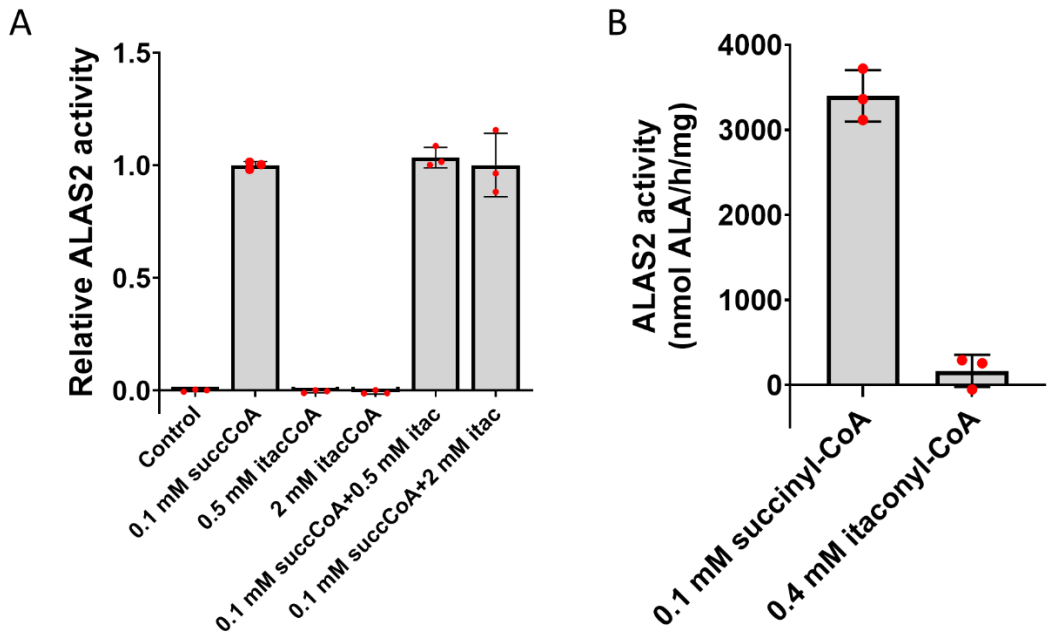

Supplemental Figure 6. ALAS activity assays with itaconate and itaconyl-CoA.

Discontinuous assays (A) and continuous assays (B) for ALAS2 activity in the presence of itaconate and/or itaconyl-CoA with succinyl-CoA substrate as a control. Reactions were prepared as described in the main text Materials and Methods and Supplemental Methods sections. Bars represent means ± one SD (n=3 biological replicates). (A) Multiple t-tests combined with Bonferroni analysis produced *p*-values < 0.0001 except for comparisons between groups with baseline activity (~0) or normal activity (~1). (B) Student's t-test *p*-value = 0.0001.

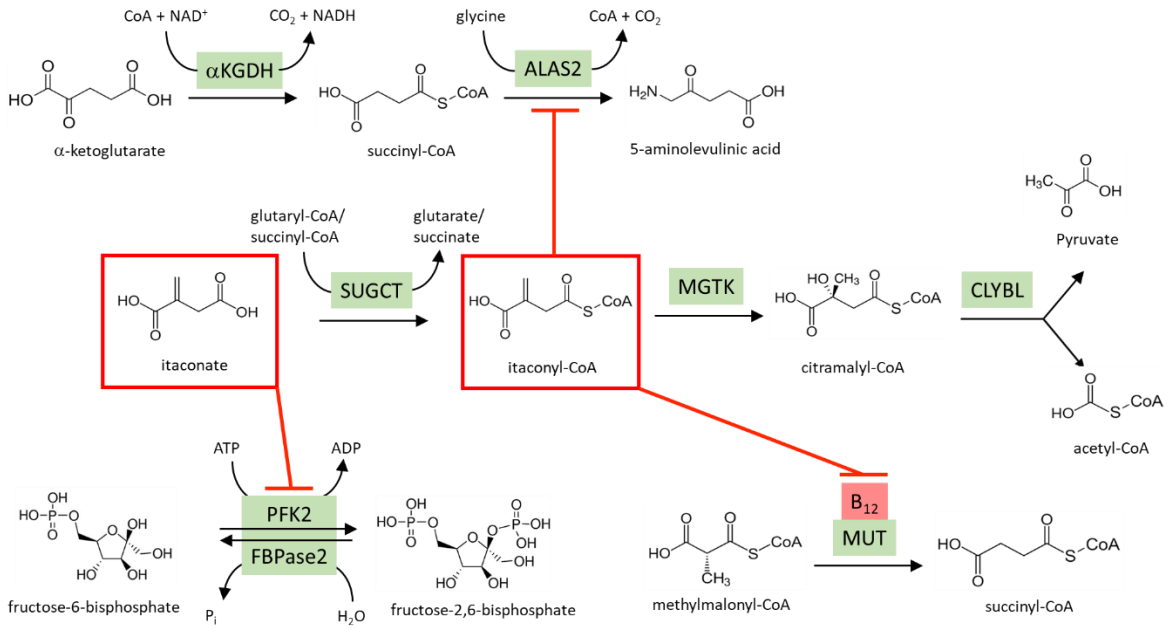

Supplemental Figure 7. Proposed scheme for itaconate metabolism in differentiating erythroblasts. FBPase2 = fructose-2,6-bisphosphatase. Other abbreviations are provided in the main text.

CHAPTER 5

CONCLUDING REMARKS

5.1 Heme Quantitation in Whole Red Cells and Their Progenitors

Accurate determination of heme levels in cells of the erythroid lineage is critical for clinical diagnosis as well as basic research of hematological disease states. Patient heme levels have been reliably measured as hemoglobin using Drabkin's method for many years (1,2), while approaches used in research settings have included radiolabeling with solvent extraction (3), pyridine hemochromagen assay (4), fluorescence analysis (5,6), and the current "gold standard" of high-performance liquid chromatography (HPLC) (7,8). However, each of these methods requires sample destruction and processing with hazardous chemicals prior to the determination of heme.

Here we have presented a protocol from our lab (Chapter 2 and ref (9)) detailing the direct quantitation of heme and hemoglobin in turbid resuspensions of living erythrocyte precursors and mature red blood cells with the CLARiTY spectrophotometer (Olis). Briefly, UV/visible light surrounding the heme Soret wavelengths is generated by a rapid-scanning monochromator (RSM) and converted to isotropic light that is subsequently altered only by sample absorption in an integrating cavity cuvette. The fully diffused light remains trapped within the reflective confines of the cuvette until it encounters the exit port to the detector, therefore increasing the pathlength to several times the dimensions of the cuvette. The enhanced pathlength is inversely related to the detected (apparent) sample absorbance, and this nonlinear

effect is corrected by converting the apparent absorbance to absorbance per centimeter with first principles (10). The resulting sensitivity of the CLARiTY is much superior to that of traditional transmission spectrophotometers. Since there is no need for sample derivatization, accurate and precise heme measurements can be made using this method and combined with downstream analysis (e.g., immunoblotting).

5.2 Erythroid-specific aminolevulinic acid synthase (ALAS2)

ALAS is found in photosynthetic bacteria and non-plant eukaryotes and operates as the rate-limiting enzyme of heme biosynthesis in the mitochondria of higher organisms (11). Two distinct genes encode housekeeping ALAS1 and erythroid-specific ALAS2, on chromosome 3 and the X-chromosome, respectively, in humans (12). Though the catalytic and C-terminal domains of the human isozymes are largely conserved, the unstructured N-terminal domains containing mitochondrial targeting sequences (MTSs) are unique (13,14). The complete structure of mammalian ALAS protein had remained elusive for decades, primarily due to the inability to prepare homogeneous recombinant protein with an intact C-terminal region that is missing in lower organisms. Here (Chapter 3 and ref (15)) we present the crystal structure of human ALAS2 (hsALAS2) (PBD 6HRH, 2.3 Å resolution) and describe the autoinhibitory function of the eukaryotic-specific C-terminal (Ct)-extension therein, including molecular-level explanations for loss- and gain-of-function mutations that result in X-linked sideroblastic anemia (XLSA) and X-linked protoporphyria (XLP), respectively.

ALAS is a homodimeric enzyme that requires pyridoxal 5’-phosphate (PLP) as a cofactor and catalyzes the condensation of glycine and succinyl-CoA to yield ALA. Earlier work in which the structure of *Rhodobacter capsulatus* ALAS was solved identified a conserved mobile

loop over the conserved ALAS active site that undergoes a conformational change to bind succinyl-CoA and release ALA product (16). We now propose that the largely unstructured Ct-extension of hsALAS2 includes a two-turn α-helix (α15) that provides conformational restriction on this active site loop via a salt-bridge network. Engineered mutations of key residues substantiate our hypothesis that the open and closed conformations of ALAS2 are facilitated by disruption and formation of these salt bridge interactions, respectively. Combined with data from molecular dynamics (MD) simulations, we believe that modulation of these interactions during the ALAS2 catalytic cycle are critical for both substrate binding and product release. In XLSA, the characteristic missense mutations stabilize the closed α15-mobile loop state. Oppositely, frameshift mutations in the Ct-extension associated with XLP result in loss of the α15 helix and the autoinhibitory mechanism that contributes to the closed conformational state. An exception is the delG XLP mutant, in which the primary sequence is compromised downstream of the α15 helix. Our kinetic data indicate that the delG enzyme is distinct from other XLP mutants in that it has enhanced catalytic specificities for both substrates.

Moving forward, we postulate that regulatory features of the ALAS2 Ct-extension are important in ALAS1 catalysis and may impact ALAS protein-protein interactions as well. Though the N-terminal domains of ALAS1 and ALAS2 are unique, the catalytic and C-terminal domains are similar. ALAS1 maintains the α15 helix found in the Ct-extension of ALAS2. Unfortunately, ALAS1 has proven difficult to express using recombinant methods that are successful for ALAS2. ALAS2 is distinct from ALAS1 in that it binds the ATP-specific succinyl-CoA synthetase (SCS) subunit (SUCLA2) (17), putatively within the Ct-extension (18). We have previously shown that SCS does not contribute significantly to the production of succinyl-CoA for erythroid heme synthesis (19), perhaps because ALAS2-SUCLA2 binding

stabilizes apo-ALAS2 early in terminal differentiation or prevents the formation of functional SCS enzyme. The ALAS2-SUCLA2 interaction has also been found to be part of a larger heme synthesis metabolon (20) that includes the terminal pathway enzyme ferrochelatase (FECH). Thus some form of feedback loop may be in place and relevant to the ALAS2 Ct-extension. In addition, the established interaction between ALAS2 and the AAA+ protease subunit CLPX (21,22), which enhances PLP loading of ALAS2, may also be relevant and should be investigated further.

Lastly, our structural studies may lead to drug discovery for the treatment of disorders in which cytotoxic porphyrins accumulate due to ALAS2 hyperactivity (XLP) or loss of enzyme function downstream of ALA synthesis found in other porphyrias. Specifically, we have identified small-molecule fragments from crystallography-based screens proximal to the ALAS2 Ct-extension that decrease ALAS2 activity *in vitro*. While our findings to this point have been modest (i.e., significant impacts observed at millimolar fragment concentrations), chemical optimization of inhibitory fragments could generate products of pharmacological significance.

5.3 Impact of Immunometabolite Itaconic Acid on Erythroid Heme Biosynthesis

Induction of mammalian erythroid heme biosynthesis is initiated with upregulation of ALAS2 synthesis during terminal erythropoiesis (23), when dozens of developing red cell precursors are intimately associated with a central macrophage in a bone marrow microniche known as an erythroblastic island (24). It has been previously reported (25) that ALAS2 deficiency contributes to chronic microcytic anemia observed in rheumatoid arthritis (RA) without an alteration in erythroblast iron supply or altered activity of iron-dependent ferrochelatase (FECH), the final heme synthesis pathway enzyme. Separately, bone marrow-

derived macrophages (BMDMs) have been shown to produce millimolar quantities of the succinate analog itaconic acid (methylenesuccinic acid) and to secrete this compound at the outset of an innate immune response (26-28). Itaconate has recently been reported to accumulate in the bronchial tissue during sepsis (28) and in the blood plasma of RA patients (29). In an earlier study utilizing a technique to determine whole-cell hemoglobin (Chapter 2 and ref (9)), we found that itaconate diminishes hemoglobinization and that ALA rescues this effect in the erythroid compartment. Here (Chapter 4) we have proposed that macrophage-derived itaconate is imported by differentiating red cell progenitors in erythroblastic islands and subsequently affects multiple metabolic pathways. In particular, we have determined that heme is reduced at the point of ALAS2 catalysis.

We have cultured erythroid-differentiating murine erythroleukemia (MEL) cells in the presence of itaconate or itaconate-producing macrophage media and found that heme and intermediate porphyrin levels are significantly diminished in all cases. Metabolomic tracing data from these cells have revealed that itaconate is imported and converted to itaconyl-CoA during terminal differentiation. We have also demonstrated that the reverse SCS reaction may not be a valid source of itaconyl-CoA as has been assumed about 50 years (30,31). Instead, succinyl-CoA:glutarate-CoA transferase (SUGCT), the mammalian homolog of the *Pseudomonas aeruginosa* itaconyl-CoA transferase (PaIct), is a putative source of endogenous itaconyl-CoA. SUGCT is expressed in MEL cells and is capable of synthesizing itaconyl-CoA from itaconate and glutaryl-CoA (32) or succinyl-CoA *in vitro*.

In addition to porphyrin deficiency and itaconyl-CoA accumulation in differentiating MEL cells, we have observed increases in the TCA-cycle metabolites succinate and succinyl-CoA. It is enticing to believe that itaconate inhibited succinate dehydrogenase (SDH) as

established elsewhere (33-35) and led to elevated succinate and subsequently succinyl-CoA by the reverse SCS reaction. However, we have demonstrated that itaconate is an inhibitor of reverse SCS activity, pointing to the possibility that succinyl-CoA accumulation occurred at the point of ALAS2 catalysis. Indeed, we have shown that itaconyl-CoA inhibits recombinant hsALAS2 activity without being utilized as an alternative substrate.

Altogether, we provide evidence for a model in which heme synthesis occurring in the context of erythroblastic islands is attenuated at the level of ALA synthesis by the conversion of macrophage-derived itaconate to itaconyl-CoA within developing erythroblasts. The impacts of this mechanism may be linked to anemia associated with chronic disorders such as RA, in which itaconate has been shown to accumulate systemically (29). Further validation of this model will require experiments in a more physiologically-relevant context such as cultured erythroblastic islands and a comprehensive investigation of possible plasmalemmal itaconate transport mechanisms. In addition, the potential impact of the succinate GPCR receptor (SUCNR1) merits attention, as SUCNR1 is expressed in some erythroid progenitors (36) and has been shown to be activated by itaconate (37). Surface plasmon resonance (SPR) and bilayer interferometry (BLI) experiments are currently being conducted and will characterize the binding of itaconyl-CoA to recombinant hsALAS2 more precisely. Our metabolomic data confirm other reports that itaconate impacts glycolysis (38) and B_{12} metabolism (39,40) in addition to heme synthesis. Thus, protein complexes reported along these pathways should also be explored in the presence of itaconate, including the effect of the ALAS2-SUCLA2 interaction. Finally, ALAS2 is a valuable drug target under conditions where cytotoxic porphyrins accumulate. As described for the small-molecule fragments identified in our ALAS2 structure study (Chapter 3), tissue-specific delivery of itaconate to the erythroid compartment could potentially serve to mitigate

porphyrin synthesis in diseases such as XLP or other conditions known to elicit symptoms of porphyria.

From analytical biochemistry to enzyme structure-function to cell culture, the studies described in this dissertation have probed and elucidated multiple aspects of erythroid heme synthesis in mammals. Critically, we have begun to characterize the nature of intrinsic and extrinsic regulation of the first and rate-limiting pathway enzyme ALAS2 in the context of porphyria and inflammation. Future studies will be focused on differentiating the molecular dynamics of wild-type and variant ALAS2 and the housekeeping ALAS1 enzyme. Experiments will include the identification and interrogation of residue-specific ALAS protein interactions. The impacts of small-molecule inhibitors, including the immunometabolite itaconic acid, on ALAS activity will also be investigated in more relevant physiological contexts, with a keen eye on possible therapeutic applications.

5.4 References

1. Drabkin, D. L., and Austin, J. H. (1935) Spectrophotometric studies II. Preparations from washed blood cells; nitric oxide hemoglobin and sulfhemoglobin. *Journal of Biological Chemistry* **112**, 51-65

2. Whitehead, R. D., Jr., Mei, Z., Mapango, C., and Jefferds, M. E. D. (2019) Methods and analyzers for hemoglobin measurement in clinical laboratories and field settings. *Ann N Y Acad Sci* **1450**, 147-171

3. Healey, J. F., Bonkowsky, H. L., Sinclair, P. R., and Sinclair, J. F. (1981) Conversion of 5-aminolaevulinate into haem by liver homogenates. Comparison of rat and chick embryo. *Biochem J* **198**, 595-604

4. Paul, K. G., Theorell, H., and Akeson, A. (1953) The molar light absorption of pyridine ferroprotoporphyrin (pyridine haemochromogen). *Acta Chemica Scandinavica* **7**, 1284-1287

5. Morrison, G. R. (1965) Fluorometric Microdetermination of Heme Protein. *Anal Chem* **37**, 1124-1126

6. Sassa, S. (1976) Sequential induction of heme pathway enzymes during erythroid differentiation of mouse Friend leukemia virus-infected cells. *J Exp Med* **143**, 305-315

7. Bonkovsky, H. L., Wood, S. G., Howell, S. K., Sinclair, P. R., Lincoln, B., Healey, J. F., and Sinclair, J. F. (1986) High-performance liquid chromatographic separation and quantitation of tetrapyrroles from biological materials. *Anal Biochem* **155**, 56-64

8. Sinclair, P. R., Gorman, N., and Jacobs, J. M. (2001) Measurement of heme concentration. *Curr Protoc Toxicol* **Chapter 8**, Unit 8 3

9. Marcero, J. R., Piel Iii, R. B., Burch, J. S., and Dailey, H. A. (2016) Rapid and sensitive quantitation of heme in hemoglobinized cells. *Biotechniques* **61**, 83-91

10. Fry, E. S., Kattawar, G. W., Strycker, B. D., and Zhai, P. W. (2010) Equivalent path lengths in an integrating cavity: comment. *Appl Opt* **49**, 575-577

11. Dailey, H. A., and Meissner, P. N. (2013) Erythroid heme biosynthesis and its disorders. *Cold Spring Harb Perspect Med* **3**, a011676

12. Bishop, D. F. (1990) Two different genes encode delta-aminolevulinate synthase in humans: nucleotide sequences of cDNAs for the housekeeping and erythroid genes. *Nucleic Acids Res* **18**, 7187-7188

13. Lathrop, J. T., and Timko, M. P. (1993) Regulation by heme of mitochondrial protein transport through a conserved amino acid motif. *Science* **259**, 522-525

14. Munakata, H., Sun, J. Y., Yoshida, K., Nakatani, T., Honda, E., Hayakawa, S., Furuyama, K., and Hayashi, N. (2004) Role of the heme regulatory motif in the heme-mediated inhibition of mitochondrial import of 5-aminolevulinate synthase. *J Biochem* **136**, 233-238

15. Bailey, H. J., Bezerra, G. A., Marcero, J. R., Padhi, S., Foster, W. R., Rembeza, E., Roy, A., Bishop, D. F., Desnick, R. J., Bulusu, G., Dailey, H. A., Jr., and Yue, W. W. (2020) Human aminolevulinate synthase structure reveals a eukaryotic-specific autoinhibitory loop regulating substrate binding and product release. *Nat Commun* **11**, 2813

16. Astner, I., Schulze, J. O., van den Heuvel, J., Jahn, D., Schubert, W. D., and Heinz, D. W. (2005) Crystal structure of 5-aminolevulinate synthase, the first enzyme of heme biosynthesis, and its link to XLSA in humans. *EMBO J* **24**, 3166-3177

17. Furuyama, K., and Sassa, S. (2000) Interaction between succinyl CoA synthetase and the heme-biosynthetic enzyme ALAS-E is disrupted in sideroblastic anemia. *J Clin Invest* **105**, 757-764

18. Bishop, D. F., Tchaikovskii, V., Hoffbrand, A. V., Fraser, M. E., and Margolis, S. (2012) X-linked sideroblastic anemia due to carboxyl-terminal ALAS2 mutations that cause loss of binding to the beta-subunit of succinyl-CoA synthetase (SUCLA2). *J Biol Chem* **287**, 28943-28955

19. Burch, J. S., Marcero, J. R., Maschek, J. A., Cox, J. E., Jackson, L. K., Medlock, A. E., Phillips, J. D., and Dailey, H. A., Jr. (2018) Glutamine via alpha-ketoglutarate dehydrogenase provides succinyl-CoA for heme synthesis during erythropoiesis. *Blood* **132**, 987-998

20. Medlock, A. E., Shiferaw, M. T., Marcero, J. R., Vashisht, A. A., Wohlschlegel, J. A., Phillips, J. D., and Dailey, H. A. (2015) Identification of the Mitochondrial Heme Metabolism Complex. *PLoS One* **10**, e0135896

21. Kardon, J. R., Moroco, J. A., Engen, J. R., and Baker, T. A. (2020) Mitochondrial ClpX activates an essential biosynthetic enzyme through partial unfolding. *Elife* **9**

22. Yien, Y. Y., Ducamp, S., van der Vorm, L. N., Kardon, J. R., Manceau, H., Kannengiesser, C., Bergonia, H. A., Kafina, M. D., Karim, Z., Gouya, L., Baker, T. A., Puy, H., Phillips, J. D., Nicolas, G., and Paw, B. H. (2017) Mutation in human CLPX elevates levels of delta-aminolevulinate synthase and protoporphyrin IX to promote erythropoietic protoporphyria. *Proc Natl Acad Sci U S A* **114**, E8045-E8052

23. An, X., Schulz, V. P., Li, J., Wu, K., Liu, J., Xue, F., Hu, J., Mohandas, N., and Gallagher, P. G. (2014) Global transcriptome analyses of human and murine terminal erythroid differentiation. *Blood* **123**, 3466-3477

24. Chasis, J. A., and Mohandas, N. (2008) Erythroblastic islands: niches for erythropoiesis. *Blood* **112**, 470-478

25. Houston, T., Moore, M., Porter, D., Sturrock, R., and Fitzsimons, E. (1994) Abnormal haem biosynthesis in the chronic anaemia of rheumatoid arthritis. *Ann Rheum Dis* **53**, 167-170

26. Strelko, C. L., Lu, W., Dufort, F. J., Seyfried, T. N., Chiles, T. C., Rabinowitz, J. D., and Roberts, M. F. (2011) Itaconic acid is a mammalian metabolite induced during macrophage activation. *J Am Chem Soc* **133**, 16386-16389

27. Michelucci, A., Cordes, T., Ghelfi, J., Pailot, A., Reiling, N., Goldmann, O., Binz, T., Wegner, A., Tallam, A., Rausell, A., Buttini, M., Linster, C. L., Medina, E., Balling, R., and Hiller, K. (2013) Immune-responsive gene 1 protein links metabolism to immunity by catalyzing itaconic acid production. *Proc Natl Acad Sci U S A* **110**, 7820-7825

28. Meiser, J., Kraemer, L., Jaeger, C., Madry, H., Link, A., Lepper, P. M., Hiller, K., and Schneider, J. G. (2018) Itaconic acid indicates cellular but not systemic immune system activation. *Oncotarget* **9**, 32098-32107

29. Daly, R., Blackburn, G., Best, C., Goodyear, C. S., Mudaliar, M., Burgess, K., Stirling, A., Porter, D., McInnes, I. B., Barrett, M. P., and Dale, J. (2020) Changes in Plasma Itaconate Elevation in Early Rheumatoid Arthritis Patients Elucidates Disease Activity Associated Macrophage Activation. *Metabolites* **10**

30. Adler, J., Wang, S. F., and Lardy, H. A. (1957) The metabolism of itaconic acid by liver mitochondria. *J Biol Chem* **229**, 865-879

31. Wang, S. F., Adler, J., and Lardy, H. A. (1961) The pathway of itaconate metabolism by liver mitochondria. *J Biol Chem* **236**, 26-30

32. Marlaire, S., Van Schaftingen, E., and Veiga-da-Cunha, M. (2014) C7orf10 encodes succinate-hydroxymethylglutarate CoA-transferase, the enzyme that converts glutarate to glutaryl-CoA. *J Inherit Metab Dis* **37**, 13-19

33. Ackermann, W. W., and Potter, V. R. (1949) Enzyme inhibition in relation to chemotherapy. *Proc Soc Exp Biol Med* **72**, 1-9

34. Cordes, T., Wallace, M., Michelucci, A., Divakaruni, A. S., Sapcariu, S. C., Sousa, C., Koseki, H., Cabrales, P., Murphy, A. N., Hiller, K., and Metallo, C. M. (2016) Immunoresponsive Gene 1 and Itaconate Inhibit Succinate Dehydrogenase to Modulate Intracellular Succinate Levels. *J Biol Chem* **291**, 14274-14284

35. Lampropoulou, V., Sergushichev, A., Bambouskova, M., Nair, S., Vincent, E. E., Loginicheva, E., Cervantes-Barragan, L., Ma, X., Huang, S. C., Griss, T., Weinheimer, C. J., Khader, S., Randolph, G. J., Pearce, E. J., Jones, R. G., Diwan, A., Diamond, M. S., and Artyomov, M. N. (2016) Itaconate Links Inhibition of Succinate Dehydrogenase with Macrophage Metabolic Remodeling and Regulation of Inflammation. *Cell Metab* **24**, 158-166

36. Hakak, Y., Lehmann-Bruinsma, K., Phillips, S., Le, T., Liaw, C., Connolly, D. T., and Behan, D. P. (2009) The role of the GPR91 ligand succinate in hematopoiesis. *J Leukoc Biol* **85**, 837-843

37. Trauelsen, M., Rexen Ulven, E., Hjorth, S. A., Brvar, M., Monaco, C., Frimurer, T. M., and Schwartz, T. W. (2017) Receptor structure-based discovery of non-metabolite agonists for the succinate receptor GPR91. *Mol Metab* **6**, 1585-1596

38. Sakai, A., Kusumoto, A., Kiso, Y., and Furuya, E. (2004) Itaconate reduces visceral fat by inhibiting fructose 2,6-bisphosphate synthesis in rat liver. *Nutrition* **20**, 997-1002

39. Shen, H., Campanello, G. C., Flicker, D., Grabarek, Z., Hu, J., Luo, C., Banerjee, R., and Mootha, V. K. (2017) The Human Knockout Gene CLYBL Connects Itaconate to Vitamin B12. *Cell* **171**, 771-782 e711

40. Ruetz, M., Campanello, G. C., Purchal, M., Shen, H., McDevitt, L., Gouda, H., Wakabayashi, S., Zhu, J., Rubin, E. J., Warncke, K., Mootha, V. K., Koutmos, M., and Banerjee, R. (2019) Itaconyl-CoA forms a stable biradical in methylmalonyl-CoA mutase and derails its activity and repair. *Science* **366**, 589-593